



TURKISH JOURNAL OF ENGINEERING

EDITOR IN CHIEF

Prof. Dr. Murat YAKAR
Mersin University Engineering Faculty
Turkey

CO-EDITORS

Prof. Dr. Erol YAŞAR
Mersin University Faculty of Art and Science
Turkey

Prof. Dr. Cahit BİLİM
Mersin University Engineering Faculty
Turkey

Assist. Prof. Dr. Hüdaverdi ARSLAN
Mersin University Engineering Faculty
Turkey

ADVISORY BOARD

Prof. Dr. Orhan ALTAN
Honorary Member of ISPRS, ICSU EB Member
Turkey

Prof. Dr. Armin GRUEN
ETH Zurich University
Switzerland

Prof. Dr. Hacı Murat YILMAZ
Aksaray University Engineering Faculty
Turkey

Prof. Dr. Artu ELLMANN
Tallinn University of Technology Faculty of Civil Engineering
Estonia

Assoc. Prof. Dr. E. Çağlan KUMBUR
Drexel University
USA

TECHNICAL EDITORS

Prof. Dr. Roman KOCH
Erlangen-Nurnberg Institute Palaontologie
Germany

Prof. Dr. Hamdalla WANAS
Menoufyia University, Science Faculty
Egypt

Prof. Dr. Turgay CELIK
Witwatersrand University
South Africa

Prof. Dr. Muhsin EREN
Mersin University Engineering Faculty
Turkey

Prof. Dr. Johannes Van LEEUWEN
Iowa State University
USA

Prof. Dr. Elias STATHATOS
TEI of Western Greece
Greece

Prof. Dr. Vedamanickam SAMPATH
Institute of Technology Madras
India

Prof. Dr. Khandaker M. Anwar HOSSAIN
Ryerson University
Canada

Prof. Dr. Hamza EROL
Mersin University Engineering Faculty
Turkey

Prof. Dr. Ali Cemal BENİM
Duesseldorf University of Applied Sciences
Germany

Prof. Dr. Mohammad Mehdi RASHIDI
University of Birmingham
England

Prof. Dr. Muthana SHANSAL
Baghdad University
Iraq

Prof. Dr. Ibrahim S. YAHIA
Ain Shams University
Egypt

Assoc. Prof. Dr. Kurt A. ROSENTRATER
Iowa State University
USA

Assoc. Prof. Dr. Christo ANANTH
Francis Xavier Engineering College
India

Prof. Dr. Bahadır K. KÖRBAHTI
Mersin University Engineering Faculty
Turkey

Assist. Prof. Dr. Akın TATOGLU
Hartford University College of Engineering
USA

Assist. Prof. Dr. Şevket DEMİRCİ
Mersin University Engineering Faculty
Turkey

Assist. Prof. Dr. Yelda TURKAN
Oregon State University
USA

Assist. Prof. Dr. Gökhan ARSLAN
Mersin University Engineering Faculty
Turkey

Assist. Prof. Dr. Seval Hale GÜLER
Mersin University Engineering Faculty
Turkey

Assist. Prof. Dr. Mehmet ACI
Mersin University Engineering Faculty
Turkey

Dr. Ghazi DROUBI
Robert Gordon University Engineering Faculty
Scotland, UK

JOURNAL SECRETARY

Aydin Alptekin
aydinalptekin@mersin.edu.tr

TURKISH JOURNAL OF ENGINEERING (TUJE)

Turkish Journal of Engineering (TUJE) is a multi-disciplinary journal. The Turkish Journal of Engineering (TUJE) publishes the articles in English and is being published 4 times (January, April, July and October) a year. The Journal is a multidisciplinary journal and covers all fields of basic science and engineering. It is the main purpose of the Journal that to convey the latest development on the science and technology towards the related scientists and to the readers. The Journal is also involved in both experimental and theoretical studies on the subject area of basic science and engineering. Submission of an article implies that the work described has not been published previously and it is not under consideration for publication elsewhere. The copyright release form must be signed by the corresponding author on behalf of all authors. All the responsibilities for the article belong to the authors. The publications of papers are selected through double peer reviewed to ensure originality, relevance and readability.

AIM AND SCOPE

The Journal publishes both experimental and theoretical studies which are reviewed by at least two scientists and researchers for the subject area of basic science and engineering in the fields listed below:

- Aerospace Engineering
- Environmental Engineering
- Civil Engineering
- Geomatic Engineering
- Mechanical Engineering
- Geology Science and Engineering
- Mining Engineering
- Chemical Engineering
- Metallurgical and Materials Engineering
- Electrical and Electronics Engineering
- Mathematical Applications in Engineering
- Computer Engineering
- Food Engineering

PEER REVIEW PROCESS

All submissions will be scanned by iThenticate® to prevent plagiarism. Author(s) of the present study and the article about the ethical responsibilities that fit PUBLICATION ETHICS agree. Each author is responsible for the content of the article. Articles submitted for publication are priorly controlled via iThenticate® (Professional Plagiarism Prevention) program. If articles that are controlled by iThenticate® program identified as plagiarism or self-plagiarism with more than 25% manuscript will return to the author for appropriate citation and correction. All submitted manuscripts are read by the editorial staff. To save time for authors and peer-reviewers, only those papers that seem most likely to meet our editorial criteria are sent for formal review. Reviewer selection is critical to the publication process, and we base our choice on many factors, including expertise, reputation, specific recommendations and our own previous experience of a reviewer's characteristics. For instance, we avoid using people who are slow, careless or do not provide reasoning for their views, whether harsh or lenient. All submissions will be double blind peer reviewed. All papers are expected to have original content. They should not have been previously published and it should not be under review. Prior to the sending out to referees, editors check that the paper aim and scope of the journal. The journal seeks minimum three independent referees. All submissions are subject to a double blind peer review; if two of referees gives a negative feedback on a paper, the paper is being rejected. If two of referees gives a positive feedback on a paper and one referee negative, the editor can decide whether accept or reject. All submitted papers and referee reports are archived by journal Submissions whether they are published or not are not returned. Authors who want to give up publishing their paper in TUJE after the submission have to apply to the editorial board in written. Authors are responsible from the writing quality of their papers. TUJE journal will not pay any copyright fee to authors. A signed Copyright Assignment Form has to be submitted together with the paper.

PUBLICATION ETHICS

Our publication ethics and publication malpractice statement is mainly based on the Code of Conduct and Best-Practice Guidelines for Journal Editors. Committee on Publication Ethics (COPE). (2011, March 7). Code of Conduct and Best-Practice Guidelines for Journal Editors. Retrieved from http://publicationethics.org/files/Code%20of%20Conduct_2.pdf

PUBLICATION FREQUENCY

The TUJE accepts the articles in English and is being published 4 times (January, April, July and October) a year.

CORRESPONDENCE ADDRESS

Journal Contact: tuje@mersin.edu.tr

CONTENTS

Volume 7 – Issue 3

RESEARCH ARTICLES

Strengthening of solid beam with fiber reinforced polymers Şemsettin Kiliçarslan, Yasemin Şimşek Türker	166
Buckling performance of thin-walled filled steel columns Abdulkerim İlgün, Ahmad Javid Zia, Sadrettin Sancıoğlu, Hasan Furkan Soydoğan, Münife Hanım Köklü, Semih Arıbaş, Berna Bayram	172
Coordination compounds for rheological and physical-chemical regularity of energy consumption decrease while transporting crude oils Nurullayev Vali Hanaqa, Usubaliyev Baybala Taci, Gurbanov Gusein Ramazan, Abdullayeva Zeynab Arif, Gasimzadeh Aysel Valiyaddin, Hasanova Matanat Maxsud	180
Challenges, threats and advantages of using blockchain technology in the framework of sustainability of the logistics sector Emel Yontar	186
A parametric study on the dynamic lateral earth forces on retaining walls according to European and Turkish Building Earthquake Codes Özgür Lütfi Ertuğrul, Babür Bek Zahin	196
Uranium migration and radioactive characteristics of the Sarıçiçek and Sarıhan Granodiorites Suna Altundaş, Hakan Çınar	208
Comparative analysis of an anchored retaining wall system in a deep foundation excavation: A case study of Sivas Cultural Center Building in Türkiye Mehmet Cemal Acar, Abdullah Kekül	227
Geo-Appraisal of groundwater resource for sustainable exploitation and management in Ibulesoro, Southwestern Nigeria Olumuyiwa Olusola Falowo, Abayomi Solomon Daramola	236
Designing a device for measuring the velocity of liquid flowing in open channels Hüseyin Mutlu, Emre Kaygusuz	259
Investigating the historical building materials with spectroscopic and geophysical methods: A case study of Mardin Castle Lale Karataş	266



Strengthening of solid beam with fiber reinforced polymers

Şemsettin Kiliñarslan *¹, Yasemin Şimşek Türker ¹

¹Suleyman Demirel University, Civil Engineering Department, Türkiye

Keywords

FRP
Reinforcement
Wood Structures
Wood Materials

Research Article

DOI: 10.31127/tuje.1026075

Received: 19.11.2021

Accepted: 18.05.2022

Published: 31.08.2022

Abstract

Timber, concrete and steel are among the traditional building materials used in the construction of buildings. Since concrete is a durable material, it is a building material used in buildings, highways, dams, sidewalks and many other areas. Wood is one of the oldest building materials, and the use of wood and wood-based materials for structural purposes continues to increase. The deterioration of existing wooden structures may result from fatigue and biological attack over time. The cost of replacing the damaged wooden elements is very high, so it seems more appropriate to repair and strengthen the damaged elements. In this study, 20x20x360 mm solid wood beam is reinforced with fiber reinforced polymers and the effect of fiber reinforced polymers on the bending properties of the beam was investigated. In order to determine the bending properties, three-point bending test was applied to the wood beams. As a result of this study, it was determined that the bending properties of wood beam reinforced with fiber reinforced polymer composites were better than the reference samples

1. Introduction

Wood material is an anisotropic, hygroscopic, sustainable and organic material [1-3]. Wood material has many positive properties [4-5]. Wood material is very suitable for use in structural and non-structural areas [6]. However, there are properties that limit the use of wood material in the structural field. The properties are; knots, fiber curl, termites, insects, fungi, biological deterioration, moisture. These undesirable and use-limiting features can be eliminated both during manufacture and use.

Nowadays, there is a rapid increase in the use of wood materials, especially for structural applications. There are some features that limit the use of wood material in the structural area. These features are fiber curl, knots, cracks, difficulty in finding materials in desired shapes and sizes, changes in production methods, use of materials that grow fast but have low resistance properties in production, high waste rate in the use of solid wood material, joining short pieces. Wood material can be strengthened by supporting with fiber-reinforced polymers both to increase the resistance properties of the joints of the structures to be obtained by using wood material, and to overcome the repair difficulties of the damage caused by external factors,

deterioration of the material and earthquakes in previously constructed structures [7-8].

Fiber reinforced polymers generally consist of glass, carbon, graphite, aramid fibers and polymer matrices. Glass is used as the basic raw material in the production of glass fibers. Soda-lime or borax silicates are used in glass fiber production. Additives are added at different rates according to the properties desired to be imparted to the glass [9]. The density of carbon fibers is low compared to metal reinforcement elements; but the resistance properties are higher. carbon fibers; It is produced by processes such as stabilization, carbonization and graphitization [10]. Aramid fibers have high resistance and chemical properties. The tensile strength of aramid fibers is higher than that of steel [11].

Polymer matrices constitute approximately 30-40% of fiber reinforcement elements. During the application of polymer matrices; It undertakes the task of keeping the fibers together, ensuring the desired orientation of the fibers, evenly distributing the load to the fibers and protecting the fibers from environmental effects [10]. Fiber reinforced polymers are produced by combining fibers and polymer matrices under appropriate production conditions. The production process varies according to the desired properties of the final product.

* Corresponding Author

(semsettinkilincarslan@sdu.edu.tr) ORCID ID 0000-0001-8253-9357
(yaseminsimseksdu@gmail.com) ORCID ID 0000-0002-3080-0215

Cite this article

Kiliñarslan, S., & Şimşek Türker, Y. (2023). Strengthening of solid beam with fiber reinforced polymers. Turkish Journal of Engineering, 7(3), 166-171

In structural design, fiber-reinforced polymers are used in the manufacture of new materials, repair of old materials, and structural improvement applications [12-18]. Fiber-reinforced polymers are used in concrete, steel, wooden beams and columns, -I-beam manufacturing, all kinds of strengthening and restoration applications, bridge coatings, reinforcing joints due to their high strength properties [19-21]. FRP composites provide appropriate strength and stiffness, are non-abrasive, and offer excellent ease of installation, reduced long-term maintenance costs, and quick installation in the field [22-24]. It is more convenient to use FRP materials instead of traditional strengthening methods because it requires maintenance and repair over time and its durability is low.

For the successful application of fiber-reinforced polymers in wood material, two different materials must be bonded in a high-quality durable manner [25]. Fiber-reinforced polymer elements can be in the form of strips, plates, rods, and these parts can be assembled with a binder. These reinforcing elements can be placed on the outside of the wood element or on the inside where aesthetic appearance is desired. The fact that the reinforcement element is outside the wood is the most common method used in strengthening works of existing structures [26].

Care must be taken when applying fiber-reinforced polymer elements on wood. First of all, the surface of the wood material should be moisture-free, flat and clean, and the oil and similar substances on it should be cleaned. Wood material should be dry during surface bonding [26].

Nowadays, there are many scientific studies on the longevity and durability of wooden structures. Numerous studies have been carried out on the strengthening of wooden structures with fiber reinforced polymers. When these studies are examined; Pupsys et al. [27], investigated oak wood beams with dimensions of 145 x 145 x 2450 mm strengthened with glass fiber reinforced polymer sheets, and determined that the reinforcement increased the bending properties of oak wood beams. Muratoğlu [28], investigated beams of Eastern beech (*Fagusorientalis* L.) and Scots pine (*Pinus sylvestris*) wood strengthened with carbon fiber reinforced polymers, and determined that the reinforced samples are 108.66 % better bending strength.

Kılınçarslan and Şimşek Türker [29], examined glulam column-beam joint area strengthen with carbon FRP and reported that the values of load carrying capacity, energy consumption and stiffness of strengthened specimens is increased. In addition, found that reinforcement with carbon based FRP fabric increased the strength and durability of the column-beam joints. Wang et al. [30] investigated those bending properties of solid Fir (*Pseudotsuga menziesii* Mirb.) beams reinforced with various fiber-reinforced polymer fabric composites (flax, basalt, E-glass FRP, hybrid FRP) and determined that fiber-reinforced polymers improved the bending properties of wood materials.

Kılınçarslan and Şimşek Türker [14] investigated that effect of reinforcement with carbon-based FRP fabric on load bearing capacity and modulus of elasticity, and stated that ductility and bearing capacity of wood

beams is increased after reinforcement with FRP fabric. Ling et al. [31] examine that Scots pine (*Pinus sylvestris*) beams reinforced with carbon and glass-based polymer fabrics and stated that effect of reinforcement with Carbon-FRP is higher than Glass-FRP. Kılınçarslan and Şimşek Türker [29] investigated that effect of carbon, aramid, basalt and glass-based fiber FRP fabrics on heat treated ash (*Fraxinus excelsior*) beams, and determined that flexural strength and modulus of elasticity increased after reinforced with FRP fabrics of heat-treated wood.

In this study, Ash beams are practically reinforced in a "U" shape from the outer part of the beam with basalt-based polymer fabric used for reinforcement purposes in the market. The beams are subjected to bending test in a universal test device and load-displacement graphs, flexural strength and modulus of elasticity are obtained.

2. Method

Ash (*Fraxinus Excelsior*) is a broad-leaved species that grows in temperate and rarely subtropical and tropical regions of the Northern Hemisphere. This species, which spreads in Europe, Crimea, Caucasus and especially in Britain, is found in Thrace, Eastern and Western Black Sea Region, Marmara and Aegean Region in our country [32]. It spreads on an area of approximately 14410 ha in the forests of our country and its share in the general forest area is less than 1% [33]. Thanks to its smooth trunk and quality wood, it is among the valuable tree species in the forest products sector. In this study, Ash (*Fraxinus Excelsior*) wood species, which is widely used in the production of wood composites and especially for structural purposes, is studied. The Ash beam samples used in the study have been supplied from Nasreddin Forest Products (Naswood) Ltd. in the Antalya region. The wooden beams are manufactured from smooth, knot-free, flawless timber with dimensions of 20x20x360 mm. The image of the cut samples is given in Figure 1.

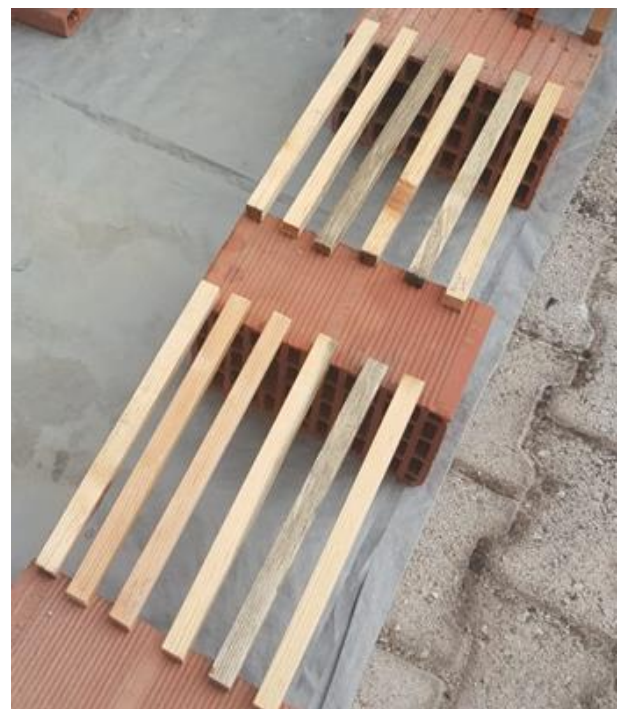


Figure 1. Image of sized samples

Before the beams are tested, all samples have been kept at temperature 20 ± 2 °C and relative humidity $65 \pm 5\%$ conditions until they reached the same equilibrium humidity. After the samples were kept in the air-conditioning cabinet, the humidity levels were checked with an electric humidity meter.

In this study, basalt-based fiber reinforced polymer fabric is used for reinforcement. The technical properties of the FRP fabric used are given in Table 1.

Table 1. The technical properties of basalt fabrics [34]

Structure of the Material	Basalt
Weight (g/m ²)	200
Modulus of Elasticity (GPa)	82
Tensile strength (N/mm ²)	3200
Design Section Thickness (mm)	0,167
Elongation at Break (%)	3,5
Width (mm)	500



Figure 2. U-shaped reinforcement in three regions of the beam

In this study, at least two layers of wrapping are used for the strengthened samples with fiber-reinforced polymer fabrics, due to two layers of wrapping is proposed in the practical use of industry. Roll priming is performed to form a thin film layer (0.1 -0.2 mm) with an epoxy-based primer developed for the MasterBrace® FRP (MasterBrace® P 3500) System.

After the priming process, Developed Epoxy adhesive for MasterBrace® FRP (MasterBrace® SAT 4500) Fibrous Polymer System is used.

Epoxy adhesive is applied to the primed surfaces with a roller to achieve a thickness of 1 mm. As seen in Figure 2, the wrapping process of wooden beams with FRP composites has been performed in a U-shaped reinforcement in three regions of the beam.

After the epoxy adhesive is applied, fibres polymer fabrics cut in appropriate sizes are stretched in the direction of their fibers and adhered to the surface, immediately. Then, it is ensured that the epoxy is absorbed into the fabric and there is not any gap between it and the surface by pressing in the direction of the fibers of the fibrous polymer fabrics with a roller. After the first layer of adhesive is completed, the same operations have been repeated once again, the second layer is wrapped and the wrapping process is completed.

The wrapped beams are kept for 1 week before being subjected to the bending test. Flexural strength tests are carried out on 20x20x360 mm specimens prepared in accordance with TS 2474 (2005) (Figure 3).

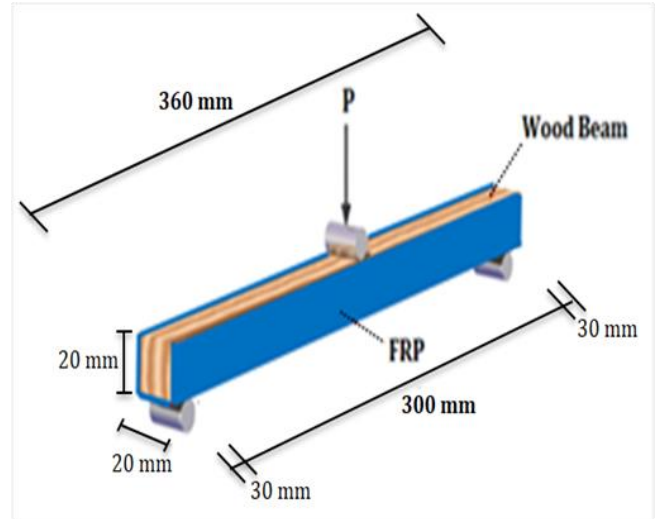


Figure 3. Sample prepared according to the standard for bending test

In the bending tests, the loading speed is set as 6 mm/min constant speed and the experiments are carried out. The span of the support points is taken as 300 mm in the experiments. The three-point bending test experimental setup image is given in Figure 4.



Figure 4. Wrapping process of wooden beams with FRP

The flexural strength and modulus of elasticity are determined as follows, respectively.

$$\sigma_E = \frac{aP_{max}l}{2bh^2} \quad (1)$$

$$E = \frac{\Delta Pl^3}{4bh^2 \Delta f} \quad (2)$$

Where is the σ_E flexural strength (N/mm²), P_{max} is the breaking load (N), l is the space between the support points (mm), b is the width of the specimens (mm) and h

is the height of the specimens (mm), $\Delta P = P_2 - P_1$ is the increase of force in the loading/ deflection curve linear section [N], $\Delta f = f_2 - f_1$ is the deflection increase in the middle of the test specimen's length.

The flexural strength and modulus of elasticity values of the beams are determined and the effect of reinforcement with basalt-based FRP fabric polymers on the flexural properties of wood material is determined.

3. Results

In this study, Ash samples are reinforced with basalt-based FRP fabrics. Reference specimens and reinforced specimens are subjected to the bending test. Load-displacement graphs and values of flexural strength and modulus of elasticity obtained in the study are given in Figure 3, Figure 4 and Figure 5.

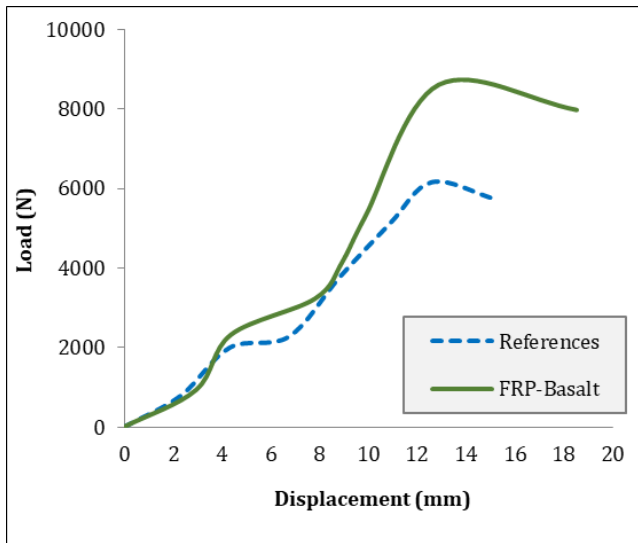


Figure 5. Load-displacement graphs of beams reinforced with reference and basalt-based FRP polymer

It was determined that the load carrying capacity of the basalt-based FRP polymer reinforced sample increased by 40% compared to the reference sample. It was determined that the displacement amount of the reinforced beam increased by 3.32% compared to the reference beams.

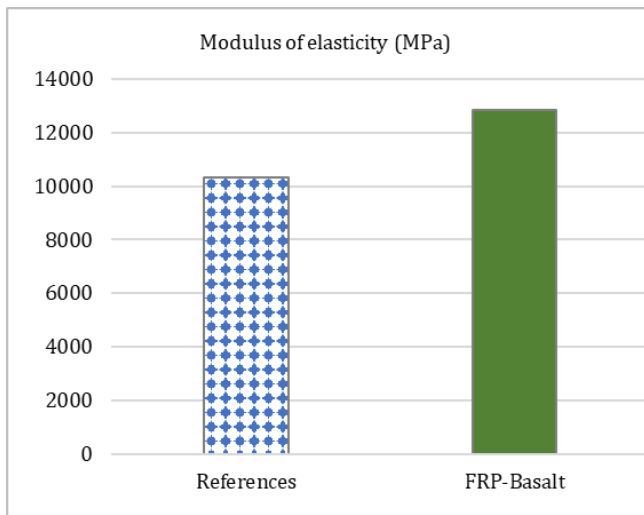


Figure 6. Graphs of modulus of elasticity of beams reinforced with reference and basalt-based FRP polymer

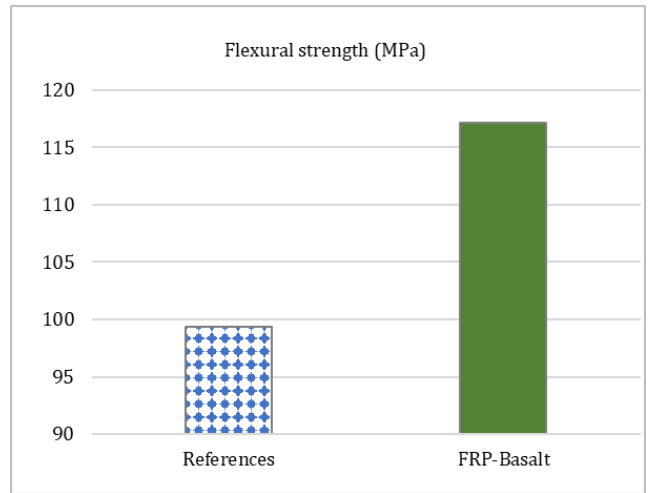


Figure 7. Graphs of flexural strength beams reinforced with reference and basalt-based FRP polymer

When Figure 4 and Figure 5 are examined, it has been determined that the beams reinforced with basalt-based fiber reinforced polymer fabric have flexural strength (117.11 MPa) and modulus of elasticity (12845 MPa). It was determined that the reference beams had flexural strength (99.34 MPa) and modulus of elasticity (10320 MPa). It was determined that the flexural strength value of the reinforced beam increased by 18% and the elasticity modulus value increased by 25% compared to the reference beam.

4. Conclusion

In this study, the effect of basalt-based fiber reinforced polymer fabric on the bending properties of wood material was investigated. Compared to the reference samples, it was determined that strengthening with basalt-based polymers increased the load carrying capacity, displacement amount, flexural strength and modulus of elasticity of wood materials to a certain extent.

Strengthening and joining of wooden materials are generally made with steel elements. However, steel elements detach from wood material over time and are subject to corrosion. Therefore, it reduces the environmental quality over time, harms human health, reduces the usage time of the wooden element and creates environmental problems. Nowadays, most of the historic and existing wooden structures are in need of safe repair and reinforcement. Known repair works, over time, insect failure in different parts of the wooden elements, fungus, rot, etc. Leaving all of the elements that need to be replaced due to reasons from the system can cause important problems in terms of both cost and workmanship and safety of the building. Therefore, it would be more appropriate to replace the damaged elements instead of replacing all the elements used in the building. With the regional change, new combinations (dowel, nail, blotting technique) are formed. Making these combinations does not give the expected result statically. Reinforcing wooden structures with FRP does not take time and provides an aesthetic advantage. For this reason, it is recommended to use basalt-based FRP polymer fabrics used in the study to strengthen the wood material.

Acknowledgement

This study has been prepared within the scope of the thematic area of “Sustainable Building Materials and Technologies” with SDU BAP project with FDK-2019-6950 project code and YÖK 100/2000 doctoral program. The authors thank the SDU BAP unit, YÖK and YÖK100/2000 program staff.

Author contributions

Şemsettin Kılıncarslan: Methodology, Writing-Reviewing, Writing-Original draft preparation. **Yasemin Şimşek Türker:** Methodology, Writing-Reviewing and Editing.

Conflicts of interest

The authors declare no conflicts of interest.

References

- Kılıncarslan, Ş., Şimşek Türker, Y. (2020). Ahşap Malzemelerin İslanabilirlik Özelliği Üzerine Isıl İşlem Uygulamasının Etkisi. *Mühendislik Bilimleri ve Tasarım Dergisi*, 8(2), 460-466.
- Sahin, H. T., Arslan, M. B., Korkut, S., & Sahin, C. (2011). Colour Changes of Heat-Treated Woods of Red-Bud Maple, European Hophornbeam and Oak. *Color Research & Application*, 36(6), 462-466.
- Sahin, C. K., & Onay, B. (2020). Alternative Wood Species for Playgrounds Wood from Fruit Trees. *Wood Research*, 65(1), 149- 160.
- Sahin, C., Topay, M., & Var, A. A. (2020). A Study on Some Wood Species for Landscape Applications: Surface Color, Hardness and Roughness Changes at Outdoor Conditions. *Wood Research*, 65(3), 395-404.
- Şimşek Türker, Y. (2020). Strengthening of Wood Materials Using Composites, 7 th International Conference on Computational and Experimental Science and Engineering (ICCESEN2020), 244-249, Antalya/Turkey.
- Fridley, K. J. (2002). Wood and wood-based materials: Current status and future of a structural material. *Journal of materials in civil engineering*, 14(2), 91-96.
- Foliente, G. C. (1995). Hysteresis modeling of wood joints and structural systems. *Journal of Structural Engineering*, 121(6), 1013-1022.
- Saribiyik, M., & Akgül, T. (2010). GFRP Bar Element to Strengthen Timber Connection Systems. *Scientific Research and Essays*. 5 (13), 1713-1719.
- Özdemir, D., & Mecit, D. (2006). Cam lifleri, *Tekstil ve Konfeksiyon Dergisi*, 1 (1), 281.
- Barragan, O. (2007). Flexural Strengthening of Glued Laminated Timber Beams with Steel and Carbon Fiber Reinforced Polymers, M.S. thesis, Dept. Civil and Environmental Eng., Chalmers University, Göteborg, Sweden.
- Schwartz, M. M. (1984). *Composite Materials Handbook*, 2nd ed. New York, USA, 8, 26-47.
- Fiorelli, J., & Dias, A. A. (2003). Analysis of the strength and stiffness of timber beams reinforced with carbon fiber and glass fiber. *Materials research*, 6, 193-202.
- Fossetti, M., Minafò, G., & Papia, M. (2015). Flexural behaviour of glulam timber beams reinforced with FRP cords. *Construction and Building Materials*, 95, 54-64.
- Kilincarslan, S., & Şimşek Türker, Y. (2019). The Effect of Strengthening with Fiber Reinforced Polymers on Strength Properties of Wood Beams, 2nd International Turkish World Engineering and Science Congress, November 7-10, 2019, Turkey.
- Rescalvo, F. J., Abarkane, C., Suárez, E., Valverde-Palacios, I., & Gallego, A. (2019). Pine Beams Retrofitted with FRP and Poplar Planks. *Mechanical Behavior. Materials*, 12(19), 3081.
- Kilincarslan, S., Şimşek Türker, Y. (2021). Experimental investigation of the rotational behaviour of glulam column-beam joints reinforced with fiber reinforced polymer composites. *Composite Structures*, 262, 113612.
- Donadon, B. F., Mascia, N. T., Vilela, R., & Trautwein, L. M. (2020). Experimental investigation of glued-laminated timber beams with Vectran-FRP reinforcement. *Engineering Structures*, 202, 109818.
- Fletcher, A. (1994). *Advanced Composites-A Profile of the International Advanced Composites Industry*. Elsevier Science, 2 (2), 384-385.
- Van Gemert, D., & Bosch, M. V. (1987). Structural restoration of wooden beams by means of epoxy resin. *Materials and Structures*, 20(3), 165-170.
- Schober, K. U., Harte, A. M., Kliger, R., Jockwer, R., Xu, Q., & Chen, J. F. (2015). FRP reinforcement of timber structures. *Construction and Building Materials*, 97, 106-118.
- Chen, C. J. (1999) Mechanical behavior of fiberglass reinforced timber joints. Ph.D Thesis, N° 1940. Swiss Federal Institute of Technology Lausanne EPFL, Switzerland, 135p.
- Bakis, C. E., Bank, L. C., Brown, V. L., Cosenza, E., Davalos, J. F., Lesko, J. J., Machida, A., Rizkalla, S. H., & Triantafyllou, T. (2002). Fiber-Reinforced Polymer Composites for Construction: State-Of the Art Review, *Journal of Composites for Construction*, ASCE, 6(2), 73-87.
- Harries, K. A., Zorn, A., Aidoo, J., & Quattlebaum, J. (2006). Deterioration of FRP to Concrete Bond Under Fatigue Loading. *Adv Structure Engineering*, 9(6), 77989.
- Kim, Y. J., & Heffernan, P. J. (2008). Fatigue behavior of externally strengthened concrete beams with fiber-reinforced polymers: State of the art. *Journal of Composites for Construction*, 12(3), 246-256.
- Lopez-Anido, R., & Hong, Y. (2003). Fatigue and fracture of the FRPwood interface: Experimental characterization and performance limits. Univ. of Maine, Advanced Engineered Wood Composites Center USA, Rep. 236.
- Steiger, R. (2002). Fibre reinforced plastics (FRP) in timber structures–Investigations and developments. Conference of the eurowood Workshop on Engineered Wood Products– Innovation and Exploitation, Espoo, Finland, 50-53.

27. Pupsys, T., Corradi, M., Borri, A., & Amess, L. (2017). Bending Reinforcement of Full-Scale Timber Beams with Mechanically Attached GFRP Composite Plates. Dept. of Mechanical & Construction Engineering, Northumbria University, July 2017. United Kingdom.
28. Muratođlu, A. (2011). Reinforcement of Wood Building Components with Carbon Fiber Reinforced Polymers (Cfrp) in Restoration: Karabük University, 2011; 1219-1240.
29. Kilincarslan, S., & ŐimŐek Törker, Y. (2021). The Effect of Strengthening with FRP on the Flexural Properties of Heat-Treated Beams, Emerging Materials Research.
30. Wang, B., Bachtiar, E. V., Yan, L., Kasal, B., & Fiore, V. (2019). Flax, Basalt, E-Glass FRP and Their Hybrid FRP Strengthened Wood Beams: An Experimental Study. Polymers, 11(8), 1255.
31. Ling, Z., Liu, W., & Shao, J. (2020). Experimental and theoretical investigation on shear behaviour of small-scale timber beams strengthened with Fiber-Reinforced Polymer composites. Composite Structures, 240, 111989.
32. Yaltırık, F. (1978). Türkiye'deki Doğal Oleaceae Taksonlarının Sistematik Revizyonu. İstanbul Üniversitesi Orman Fakültesi Yayın No: 2404.
33. OGM (2015). Türkiye Orman Varlığı 2015. T.C. Orman ve Su İşleri Bakanlığı, Orman Genel Müdürlüğü, Ankara.
34. BASF, (2022). <https://www.master-builders-solutions.com/tr-tr/products/masterbrace>



© Author(s) 2023. This work is distributed under <https://creativecommons.org/licenses/by-sa/4.0/>



Buckling performance of thin-walled filled steel columns

Abdulkerim İlgün ^{*1}, Ahmad Javid Zia ¹, Sadrettin Sancioğlu ¹, Hasan Furkan Soydoğan ¹, Münife Hanım Köklü ¹, Semih Arıbaş ², Berna Bayram ¹

¹ KTO Karatay University, Department of Civil Engineering, Türkiye

² Arıbaş Metal, Aksaray, Türkiye

Keywords

Axial load
Buckling
Column
FEA

Research Article

DOI: 10.31127/tuje.1092975

Received: 25.03.2022

Accepted: 01.06.2022

Published: 31.08.2022

Abstract

Concrete-filled composite elements have recently gained popularity as beams and columns all over the world. They have advantages similar to reinforced concrete elements, such as the moulding process and the lack of maintenance of the filled concrete, as well as advantages similar to hollow steel elements, such as enhancing compressive strength and bending capacity by using smaller sections. In this paper, the buckling behaviour of thin-walled steel columns with circular cross-section and different filling materials was investigated under uniaxial load. Six different materials (concrete produced using normal aggregate, concrete produced using waste aggregate, waste fine aggregate, waste coarse aggregate, waste iron dust and polyurethane) were used as filling. Filled columns were compared experimentally with hollow thin-walled steel columns that had the same height and diameter. All specimens had the same length (750 mm), same diameter (60.3mm) and the same wall thickness (3mm). Experimental results were compared with analytical results obtained from a calculation done using the national steel design code, Design, Calculation and Construction Principles of Steel Structures 2016. Additionally, columns specimens were modelled in Abaqus software. Conservative and consistent results were obtained from comparing experimental, analytical, and numerical results.

1. Introduction

Concrete and structural steel are the most used materials in construction sector today. If the mechanical properties of these two materials are examined, it is seen that the concrete has high compressive strength with very low flexural capacity. On the other hand, structural steel has both, high flexural capacity and high compressive strength but has a great weakness against fire and buckling problem. To overcome the weakness of these two materials, they are both used together as concrete-filled composite members (CFST) [1]. CFST members have been used widely, recently. Concrete-steel composite columns have numerous advantages and are an interesting alternative for columns made of steel or reinforced concrete. CFST members are more fire resistant than steel structures, additionally, local buckling occurs in steel members, where this problem is mostly prevented in CFSTs [2-6]. CFST columns have higher axial load capacity than reinforced concrete columns [7-8].

1.1. Literature Review

CFST members has been investigated experimentally by some researchers. For example, Han investigated the flexural behaviour of 16 concrete-filled steel beams with a length of 1100 mm and a cross-section of square and rectangular. The beams had the width/depth ratio varying between 1 - 2 and the depth/thickness ratio varying between 20 and 50. Additionally, Han compared experimental results with different standards and codes [9]. Zeghiche and Chaoui investigated 27 concrete-filled steel tubular columns. The main objective of the study was to demonstrate the influence of column slenderness, loading type and compressive strength of the infill concrete on the strength and behaviour of concrete-filled steel tubular columns [10]. Abramski examined 30 CFST columns. In this study, different parameters such as column slenderness factor, various tube thickness, loading type and bond strength between steel and concrete was used [11]. Essopjee and Dundu investigated

* Corresponding Author

*(kerim.ilgun@karatay.edu.tr) ORCID ID 0000-0002-9784-460X
(javid.zia@karatay.edu.tr) ORCID ID 0000-0002-2808-6972
(sadrettin.sancioğlu@karatay.edu.tr) ORCID ID 0000-0002-6095-2164
(furkansoydogan@gmail.com) ORCID ID 0000-0002-2467-6588
(munifehanim.koklu@ogrenci.karatay.edu.tr) ORCID ID 0000-0003-1096-157X
(semiharibas@gmail.com) ORCID ID 0000-0003-3465-3029
(berna.bayram@ogrenci.karatay.edu.tr) ORCID ID 0000-0002-6700-428X

Cite this article

İlgün, A., Zia, A. J., Sancioğlu, S., Soydoğan, H. F., Köklü, M. H., Arıbaş, S., & Bayram, B. (2023). Buckling performance of thin-walled filled steel columns. Turkish Journal of Engineering, 7(3), 172-179

double-skin CFST columns under axial compression until failure. The parameters of this study are the lengths, diameters and strength of the steel tube. Additionally, results obtained from the experimental investigation were compared with international standards and codes such as the South African Standard (SANS) and Eurocode 4 (EC4). Furthermore, experimental results had good agreement with analytical results [12]. Ibanez et al. [13] investigated different cross-sectional shapes CFST stub columns which filled normal and high strength concrete. The test specimens' cross-sections were circular, rectangular and square and also all specimens had equivalent cross-sectional area. Experimental test results compared with Eurocode 4, American, Australian and Chinese codes.

CFST members has been studied theoretically. For instance, Liang and Fragomeni investigated the nonlinear inelastic behaviour of concrete-filled short columns under axial load. The theoretical results obtained from the study were compared with the results obtained from the experimental studies available in the literature [14]. The axial load capacity of CFST columns subjected to concentric and eccentric loads was established by Tan and Nichols. The extent of the experimentally recorded compressive strength increase for the filled concrete owing to steel confinement is proportional to the ratio of steel to a concrete area, according to the findings. As the eccentricity to radius ratio rises, the columns load-carrying capacity and maximum strain drop if the slenderness ratio remains constant [15]. Roder et al. calculated the stiffness and resistance of circular CFST using combined axial and flexural loads. For the evaluation, 122 test specimens were collected from literature observations. The plastic stress method, according to the results, is an effective method for predicting the combined load capacities of circular CFST columns. Furthermore, data shows that current provisions produce ineffective results. The presented models allow for accurate stiffness and resistance predictions [16].

CFST members has been studied numerically using finite element analysis. Abed et al. investigated compressive behavior of CFST's columns subjected to axial load. Three different diameters to thickness ratios and two different compressive strength were used in this investigation as parameters. Axial load capacities obtained from the test were compared with different international codes and standards [17]. Duarte et al. numerically examined short CFST columns filled with rubberized concrete, including rubber particles, in terms of ductility and strength. Short CFST columns with rubberized concrete were compared with same size CFST columns filled with normal concrete. Moreover, columns were modelled numerically to include two types of concrete. Ultimate strengths, load-displacement curves and failure modes were found numerically. Numerical results were compared with experimental results. Furthermore, the results showed good agreement [18]. Hassanein et al. numerically investigated the octagonal cross-sections CFST columns. Finite element model parameters were diameter-wall thickness ratios of steel tube varying from 40 to 200 and compressive strength of filled concrete ranging from 40 to 100 MPa. Finite

element analysis results were compared with existing design codes and standards. Results obtained from numerical analysis were conservative with existing provisions [19]. Al-Ani investigated the axial load capacity of circular CFST stub columns numerically and analytically using finite element analysis via Abaqus software. Finite element analysis results were compared with experimental results in terms of failure load and load-displacement curves. The finite element model and analytical model were consistency with experimental data [20]. Saleh and Al-abboodi numerically investigated CFST stub columns under axial compression using Abaqus software. Investigation parameters for the study were the effects of the concrete grade, steel grade, wall thickness of the steel tube and the cross-sectional shape [21].

In this study, the buckling performance of thin-walled steel columns was experimentally investigated. A total of 13 columns with circular cross-section were used. 2 of 13 specimens were cast as hollow columns and used as reference specimens. The rest were filled with different materials. As filling 6 different materials consisting of waste fine aggregate, waste coarse aggregate, waste iron dust, polyurethane and two types of concrete which, one was produced using normal aggregate and the second one with waste aggregate were used. The main objectives of this study were threefold: first, the investigation of the buckling performance of the thin-walled columns filled with different materials; second, to see the convergence of Turkish national steel design code with axial load capacity obtained from the experimental study [22]. Final, to demonstrate the modelling of concrete-filled composite columns in the Abaqus software that performs Finite Element Analysis (FEA).

2. Materials

2.1. Aggregates

In study, two types (waste and normal) of aggregates have been used in two ways. First as a filling material and second as component of concrete. Sieve analysis has been done to classify the aggregates size. For both types of aggregates, grain diameters were determined as 1-4 mm (fine) and 4-16 mm (coarse). Fine aggregate water absorption rate was calculated as 10.64%, and coarse aggregate water absorption rate was 4.62%. The specific gravity values of fine and coarse aggregates are 2.2 gr/cm³ and 2 gr/cm³, respectively. Summary of aggregate usage details in this study is given in Table 1 and Figure 1.

2.2. Concrete

The mix proportions of the concrete used in the study are described in Table 1. Concrete was produced from both normal aggregate and waste aggregate. Three-cylinder samples were cast from each of the produced concrete. The samples cast were subjected to a compressive strength test after 28 days of curing. According to the test results, the 28-day cubic compressive strength was about 37 MPa. So cylindrical compressive strength can be calculated about 30 MPa

(Figure 2). The slump values were obtained from the slump test and the slump value for both types of concrete were approximately 70 mm.



Figure 1. 1-4 mm (fine) and 4-16 mm (coarse) aggregate



Figure 2. Cubic concrete specimens and compressive test

Table 1. Mix proportions of concrete

Concrete Compressive Strength Type	Cement (%)	Aggregates (%)		Water (%)	Chemical Additives (%)
		Fine	Coarse		
Normal Strength	28.6	14.3	43	13.8	0.3

2.3. Polyurethane foam

The mechanical properties of the polyurethane were obtained from the manufacturer notes. It has a deformation capacity of up to 10% of the total thickness of the material. The average compressive strength shown in the thickness of the material used in the test was 0.516 MPa. The young modulus of polyurethane was between 3-5 MPa.

2.4. Structural steel

The same mechanical properties are expected in each location on the surface of steel columns. Therefore, 2 thin-walled steel profiles used in the experiment were obtained from the same manufacturer. Column

specimens were obtained by dividing the profiles at 750 mm. The structural steel had a diameter of 60.3 mm, a wall thickness of 3 mm and a characteristic yield strength of about 235 MPa (Figure 3).

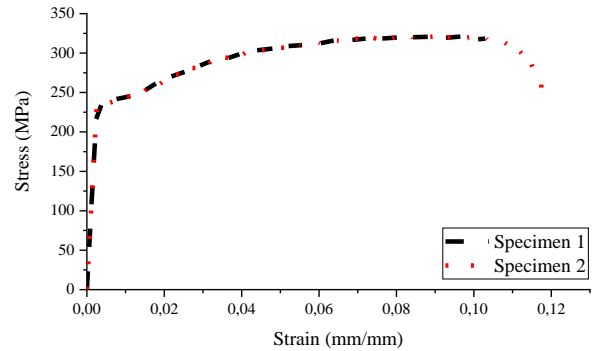


Figure 3. Tensile test results for the steel tube

2.5. Filled columns specimens

In the experimental part of this study a total of 13 CFST column specimens with an identical height and circular cross-section of 750 mm and 60.3 mm were casted in the laboratory. 2 of 13 specimens were consider as reference and cast as hollow columns. From the remaining 11 specimens 2 were filled with concrete produced from normal aggregate, 2 filled with concrete produced from waste aggregate, 2 filled with waste fine aggregate, 2 filled with waste coarse aggregate, 2 filled with polyurethane foam and 1 was filled with waste iron dust. The steel columns were cleaned before filling. Steel plates which had 3 mm thickness were welded under the specimens with fillings, to prevent the discharge of filling materials. In order to place the filling materials homogeneously and without any gaps, the vibration process was applied for 15 seconds. A brief specification of test samples is given in Table 2.

3. Methods

3.1. Experimental study

In this study, thin-walled steel columns filled with different materials were subjected to uniaxial compressive load. In the experiments, a hydraulic press with a capacity of 3000 kN was used to apply the uniaxial load. The applied load and deformations were measured by load-cell and linear variable displacement transducers (LVDT) respectively, which then the data was transferred to a computer by using a data logger. The rotation of specimens was prevented at the supports, and their movement was restricted in the longitudinal and transverse directions. The specimens were capped on both ends with rigid steel caps to distribute the applied load uniformly over the concrete and steel cross-section. A total of 5 LVDTs were used to measure the horizontal and vertical displacements of the columns under the uniaxial load. One LVDT was used to measure the vertical displacement, and the rest were used to measure horizontal displacements. The experimental setup is shown in Figure 4.

Table 2. Specimen labels and material properties

No	Specimens	D (mm)	t (mm)	L (mm)	Infill Materials
1	C-H1	60.3	3	750	-
2	C-H2	60.3	3	750	-
3	C-NC1	60.3	3	750	concrete produced from normal agg.
4	C-NC2	60.3	3	750	concrete produced from normal agg.
5	C-RC1	60.3	3	750	concrete produced from waste agg.
6	C-RC2	60.3	3	750	concrete produced from waste agg.
7	C-RFA1	60.3	3	750	waste fine agg.
8	C-RFA2	60.3	3	750	waste fine agg.
9	C-RCA1	60.3	3	750	waste coarse agg.
10	C-RCA2	60.3	3	750	waste coarse agg.
11	C-P1	60.3	3	750	polyurethane
12	C-P2	60.3	3	750	polyurethane
13	C-ID1	60.3	3	750	iron dust

4. Methods

4.1. Experimental study

In this study, thin-walled steel columns filled with different materials were subjected to uniaxial compressive load. In the experiments, a hydraulic press with a capacity of 3000 kN was used to apply the uniaxial load. The applied load and deformations were measured by load-cell and linear variable displacement transducers (LVDT) respectively, which then the data was transferred to a computer by using a data logger. The rotation of specimens was prevented at the supports, and their movement was restricted in the longitudinal and transverse directions. The specimens were capped on both ends with rigid steel caps to distribute the applied load uniformly over the concrete and steel cross-section. A total of 5 LVDTs were used to measure the horizontal and vertical displacements of the columns under the uniaxial load. One LVDT was used to measure the vertical displacement, and the rest were used to measure horizontal displacements. The experimental setup is shown in Figure 4.

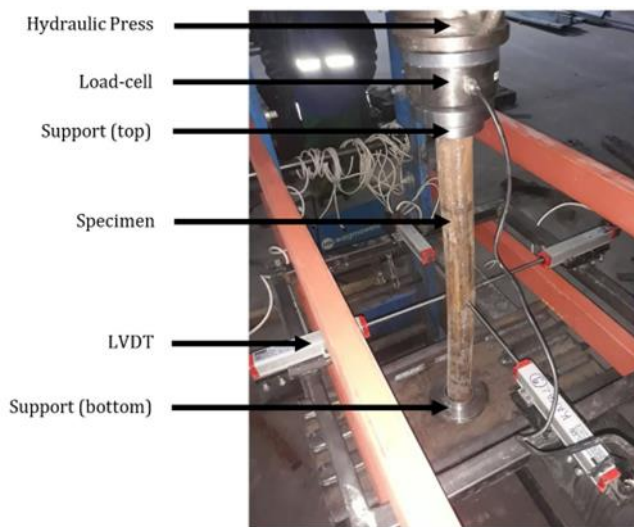


Figure 4. Test setup and instrumentation

In order to consider the behaviour of the filled steel column, 13 specimens were tested with various infill materials and same wall thickness. 60.3 mm diameter circular hollow section (CHS) with 3 mm wall thickness

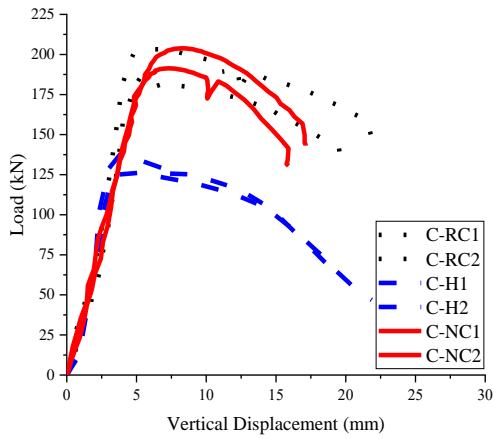
were used for the tests. All the tests have been carried out at the KTO Karatay University Structural Mechanics Laboratory.

The specimens were loaded at 5 kN intervals during the test period. Uniaxial loading was operated manually. All the readings were recorded when both load and displacements had been stabilized. After the failure of the specimen due to local buckling, the loading was not stopped, and the test continued as the vertical displacement reached about 25 mm. Load – displacement curves obtained from the experiment are shown in Figure 6.

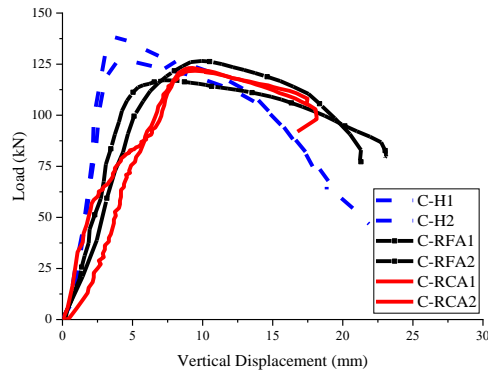
All test specimens of experimental investigations after buckling are given in Figure 5.



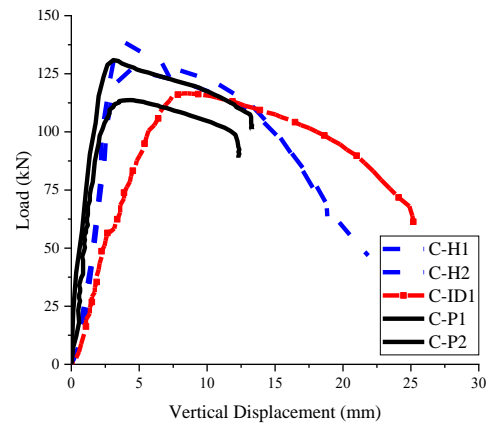
Figure 5. Test specimens after buckling



(a)



(b)



(c)

Figure 6. Experimental test results

4.2. Analytical study

According to [22] section 12, for the plastic stress distribution method, the nominal strength shall be computed assuming that steel components have reached stress of F_y in compression, and concrete components in compression due to axial force have reached stress of $0.85 f_{ck}$. For a circular cross-section filled with concrete, the stress of $0.95 f_{ck}$ is permitted to be used for concrete components in compression due to axial force to account for the effects of concrete confinement.

DCCPSS – 2016 [22] has determined material limits for concrete-filled composite sections that can be used.

For the determination of the available strength, concrete shall have a compressive strength (f_{ck}) of not less than 20 MPa nor more than 70 MPa for normal-weight concrete. The specified minimum yield stress of structural steel used in strength calculation of the composite members shall not exceed 460 MPa. The concrete compressive strength used in the study was 30 MPa and the characteristic yield strength of the structural steel element was determined as 235 MPa.

CFST columns need to be classified for local buckling. The cross-section used in the test was in compact class according to the λ_p limit value given in DCCPSS - 2016 Table 12.1A.

DCCPSS - 2016 Table 12.5 was obtained based on the interaction diagram. According to this table, the axial force formula is given in Equation 1.

$$M_A = 0 ; P_A = A_s F_y + 0.95 f_{ck} A_c \quad (1)$$

where F_y was the yield strength of the structural steel and f_{ck} was compressive strength of the concrete. A_s and A_c were the cross-section areas of steel and concrete, respectively.

4.3. Numerical study

Numerical studies are straightforward and rapid than experimental studies. However, the materials must be defined conveniently to obtain realistic results. There are many programs based on finite element method that can be used to evaluate the numerical analysis of load bearing elements. Abaqus is one of these programs which any structural element can be analyzed numerically in this software [23].

In this paper, Abaqus software was used for concrete-filled column design and analysis. Solid element (C3D8R) in the Abaqus was used to define both the concrete core and the structural steel. Rigid steel caps were modelled with discrete rigid shell elements. These caps were used to distribute the applied load uniformly over the concrete and steel. Concrete-filled column model is illustrated in Figure 7.

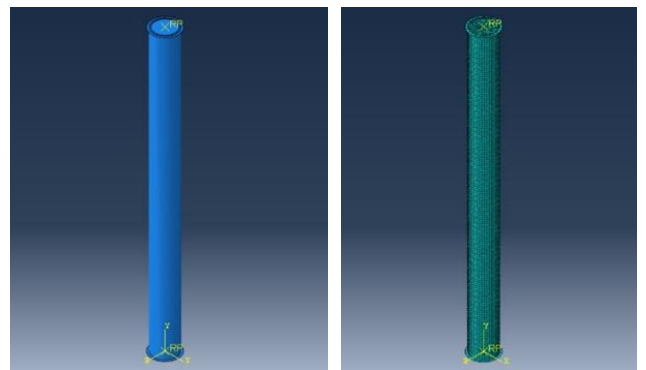


Figure 7. CFST column model in Abaqus

Young modulus was taken as 26600 MPa, and Poisson's ratio of concrete was assumed to be 0.2, in the elastic properties of concrete. To define the plastic properties of concrete "Concrete Damage Plasticity" was used. The compressive and tensile behavior values of

concrete were utilized from [24]. To define the elastic properties of steel, Young modulus was taken as 200 GPa and Poisson's ratio of steel was assumed to be 0.3. The plastic properties of steel were modeled where the yield stress was taken as 235 MPa and the plastic strain was defined as "0" at yielding point. Additionally, ultimate stress and strain was defined as 360 MPa and 0.1, respectively. The properties of materials are shown in Table 3. The interface between the concrete core and steel tube of CFST was modelled in the tangential and normal directions. The friction coefficient was taken 0.3 between steel and concrete (F. H. Abed et al., 2018).

Table 3. Material properties

Elastic/ Plastic	Material parameters	Concrete core	Structural steel
Elastic	Young modulus (MPa)	26600	200000
	Poisson's ratio	0.2	0.3
Plastic	Dilation Angle	31	-
	Eccentricity	0.1	-
	fb0/fc0	1.16	-
	K	0.67	-
	Viscosity parameter	0.0005	-

The numerical study was done with displacement control. The deflection was increased until the vertical displacement reached to 25 mm. Load – displacement curves obtained from the analysis is shown in Figure 8.

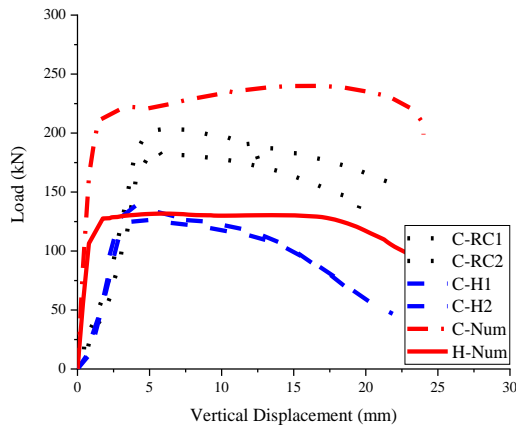


Figure 8. Numerical results

Table 4. Results obtained from the experiment

Specimens	P _{EXP} (kN)	Vertical Displacement (mm)	Increase in Load Capacity (%)	Increase in Vertical Displacement (%)
C-H1	138.601	4.245	-	-
C-H2	126.730	4.388	-	-
Mean Value (C-H1 and C-H2)	132.666	4.317	-	-
C-NC1	191.350	7.266	44.23	68.31
C-NC2	203.836	8.201	53.65	89.97
C-RC1	185.580	5.252	39.89	21.66
C-RC2	203.302	5.683	53.24	31.64
C-RFA1	117.128	9.266	No Increments	114.64
C-RFA2	126.556	9.928	No Increments	129.97
C-RCA1	121.735	9.424	No Increments	118.30
C-RCA2	123.138	9.281	No Increments	114.98
C-P1	130.901	3.094	No Increments	No Increments
C-P2	113.683	4,388	No Increments	No Increments
C-ID1	116.607	10.144	No Increments	134.98

5. Results

To evaluate and compare the obtained results, the mean values of reference specimens have been taken into consideration. Comparing the mean value (C-H1 and (C-H2) and C-NC1 and C-NC2, the axial load capacity had increased by approximately 49%, and the vertical displacement was increase around 79%. Similarly comparing the mean value (C-H1 and (C-H2) and C-RC1 and C-RC2, the axial load capacity had increased by approximately 47% and the vertical displacement increment was around 27%. In the comparison of the reference columns with columns which filled with different aggregates, the axial load capacity had no increments. However, vertical displacement increased by approximately 122% for C-RFA1 and C-RFA2 and 117% for C-RCA1 and C-RCA2. Similarly, the axial load capacity of C-ID1 did not increase but its vertical displacement was increased by about 135%. Unlike other results, neither the axial load capacity nor the vertical displacement value of the C-P1 and C-P2 specimens increased. The results obtained from the experimental study performed as described in the previous sections are summarized in Table 4.

Experimental and analytical results were compared. And, for hollow columns, the prediction success ratio was 96%. Similarly, for C-NC1 and C-NC2, this ratio was 98% and for C-RC1 and C-RC2 was 99%. The prediction success ratio for concrete-filled specimens was 98.6%. Comparisons results are summarized in Table 5.

Numerical results were compared with experimental results. According to comparison, for hollow columns, the ratio of numerical results to experimental results was in the range of 0.959, at the yield point. Similarly, the ratio was 1.110 for concrete-filled columns produced from normal aggregate. Comparisons results are given in Table 6.

Table 5. Comparisons between experimental and analytical results

Specimens	P _{EXP} (kN)	P _{ÇYTHYE} (kN)	P _{ÇYTHYE} /P _{EXP}
C-H1	138.601	126.909	0.915
C-H2	126.730	126.909	1.001
Mean Value (C-H1 and C-H2)	132.666	126.909	0.956
C-NC1	191.350	192.908	1.008
C-NC2	203.836	192.908	0.946
C-RC1	185.580	192.908	1.039
C-RC2	203.302	192.908	0.949
C-RFA1	117.128	-	-
C-RFA2	126.556	-	-
C-RCA1	121.735	-	-
C-RCA2	123.138	-	-
C-P1	130.901	-	-
C-P2	113.683	-	-
C-ID1	116.607	-	-
Mean Value (Filled Specimens)			0.986
Mean Value (All Specimens)			0.971

Table 6. Comparisons between experimental and numerical results

Specimens	P _{EXP} (kN)	P _{NUM} (kN)	P _{NUM} /P _{EXP}
C-H1	138.601	127.250	0.918
C-H2	126.730	127.250	1.004
Mean Value (C-H1 and C-H2)	132.666	127.250	0.959
C-NC1	191.350	219.018	1.145
C-NC2	203.836	219.018	1.075
Mean Value (Filled Specimens)			1.110
Mean Value (All Specimens)			1.035

6. Conclusion

In this study, the axial load capacity of CFST columns with circular cross-section and filled with different materials (concrete produced from normal aggregate, concrete produced from waste aggregate, waste fine aggregate, waste coarse aggregate, polyurethane foam and waste iron dust) were determined experimentally. And the results were compared with analytical and numerical models. The main results obtained from limited number of test specimens are listed below:

- (1) CFST columns have more load-carrying capacities than hollow and filled with different materials columns.
- (2) Vertical displacement increased in CFSTs compared with hollow columns. Load-carrying capacities had no increased infilled with different materials columns compared with hollow columns however vertical displacement increased considerably, except filled with polyurethane.
- (3) Compared experimental and analytical results for CFSTs and hollow columns, ÇYTHYE is successful in prediction of load-carrying capacity (approximately 97%).
- (4) Compared experimental and numerical results for CFSTs and hollow columns, Abaqus software

is successful in modelling, analyzing, and predicting.

- (5) All results compared with each other, results are conservatively and successfully.

Acknowledgement

This study is the further study of the conference paper presented 7th National Structural Mechanics Laboratories Workshop organized by KTO Karatay University Department of Civil Engineering. Thanks to the ABAQUS Inc student version. And the authors thanks to Aribaş Metal for supports.

Author contributions

Abdulkerim İlgün: Investigation, supervision, methodology, funding acquisition. **Ahmad Javid Zia:** Investigation, supervision, writing - original draft writing - review & editing. **Sadrettin Sancioğlu:** Conceptualisation, methodology, investigation, writing - original draft writing - review & editing. **Hasan Furkan Soydoğan:** Methodology, investigation, writing. **Münife Hanım Köklü:** Investigation, analyzing, writing. **Semih Aribaş:** Investigation, writing, funding acquisition. **Berna Bayram:** Investigation, writing.

Conflicts of interest

The authors declare no conflicts of interest.

Abbreviations

CFST	Concrete-filled steel tubes
CHS	Circular hollow section
DCCPSS	Design, Calculation and Construction Principles of Steel Structures
FEA	Finite element analysis
LVDT	Linear variable displacement transducers
A _c	Cross-section area of concrete
A _s	Cross-section area of steel
f _{ck}	Compressive strength of the concrete
F _y	Yield strength of the structural steel
P	Axial load capacity

References

1. Sancioğlu, S. (2020). Experimental and Analytical Investigation of Bending Effects of Concrete Filled Composite Beams. KTO Karatay University.
2. Abed, F., Alhamaydeh, M., & Abdalla, S. (2013). Experimental and numerical investigations of the compressive behavior of concrete filled steel tubes (CFSTs). *Journal of Constructional Steel Research*, 80, 429–439. <https://doi.org/10.1016/j.jcsr.2012.10.005>
3. Lin-Hai Han, Li, W., & Bjorhovde, R. (2014). Developments and advanced applications of concrete- fi lled steel tubular (CFST) structures: Members Concrete Cracks. *Journal of Constructional Steel Research*, 100, 211–228. <https://doi.org/10.1016/j.jcsr.2014.04.016>

4. Lu, Y., Li, N., Li, S., & Liang, H. (2015). Behavior of steel fiber reinforced concrete-filled steel tube columns under axial compression. *Construction and Building Materials*, 95, 74–85. <https://doi.org/10.1016/j.conbuildmat.2015.07.114>
5. Wang, Y. H., Wu, Q., Yu, J., Frank Chen, Y., & Lu, G. B. (2018). Experimental and analytical studies on elastic-plastic local buckling behavior of steel material under complex cyclic loading paths. *Construction and Building Materials*, 181, 495–509. <https://doi.org/10.1016/j.conbuildmat.2018.06.031>
6. Zhu, J. Y., & Chan, T. M. (2018). Experimental investigation on octagonal concrete filled steel stub columns under uniaxial compression. *Journal of Constructional Steel Research*, 147, 457–467. <https://doi.org/10.1016/j.jcsr.2018.04.030>
7. Abramski, M. (2018a). Load-carrying capacity of axially loaded concrete-filled steel tubular columns made of thin tubes. *Archives of Civil and Mechanical Engineering*, 18(3), 902–913. <https://doi.org/10.1016/j.acme.2018.01.002>
8. İlgün, A., Can, H., Bayram, B., Arıbaş, S., Zia, J., & Sancioğlu, S. (2019). Eksenel Yük Etkisi Altında İnce Cidarlı Çelik Kolonların Deneysel Olarak İncelenmesi. *7. Yapı Mekaniği Laboratuvarları Çalıştayı*, 187–192.
9. Han, L. H. (2004). Flexural behaviour of concrete-filled steel tubes. *Journal of Constructional Steel Research*, 60(2), 313–337. <https://doi.org/10.1016/j.jcsr.2003.08.009>
10. Zeghiche, J., & Chaoui, K. (2005). An experimental behaviour of concrete-filled steel tubular columns. *Journal of Constructional Steel Research*, 61(1), 53–66. <https://doi.org/10.1016/j.jcsr.2004.06.006>
11. Abramski, M. (2018b). Load-carrying capacity of axially loaded concrete-filled steel tubular columns made of thin tubes. *Archives of Civil and Mechanical Engineering*, 18(3), 902–913. <https://doi.org/10.1016/j.acme.2018.01.002>
12. Essopjee, Y., & Dundu, M. (2015). Performance of concrete-filled double-skin circular tubes in compression. *Composite Structures*, 133(1), 1276–1283. <https://doi.org/https://doi.org/10.1016/j.compstruct.2015.08.033>
13. Ibañez, C., Hernández-Figueirido, D., & Piquer, A. (2018). Shape effect on axially loaded high strength CFST stub columns. *Journal of Constructional Steel Research*, 147, 247–256. <https://doi.org/10.1016/j.jcsr.2018.04.005>
14. Liang, Q. Q., & Fragomeni, S. (2010). Nonlinear analysis of circular concrete-filled steel tubular short columns under eccentric loading. *Journal of Constructional Steel Research*, 66(2), 159–169. <https://doi.org/10.1016/j.jcsr.2009.09.008>
15. Tan, K., & Nichols, J. M. (2017). Properties of high-strength concrete filled steel tube columns. *Computing in Science and Engineering*, 1(1), 58–77. <https://doi.org/10.22606/mcse.2017.11005>
16. Roeder, C. W., Lehman, D. E., & Bishop, E. (2010). Strength and Stiffness of Circular Concrete-Filled Tubes. *Journal of Structural Engineering*, 136(12), 1545–1553. [https://doi.org/10.1061/\(asce\)st.1943-541x.0000263](https://doi.org/10.1061/(asce)st.1943-541x.0000263)
17. Abed, F. H., Abdelmageed, Y. I., & Kerim Ilgun, A. (2018). Flexural response of concrete-filled seamless steel tubes. *Journal of Constructional Steel Research*, 149, 53–63. <https://doi.org/10.1016/j.jcsr.2018.06.030>
18. Duarte, A. P. C., Silva, B. A., Silvestre, N., de Brito, J., Júlio, E., & Castro, J. M. (2016). Finite element modelling of short steel tubes filled with rubberized concrete. *Composite Structures*, 150, 28–40. <https://doi.org/10.1016/j.compstruct.2016.04.048>
19. Hassanein, M. F., Patel, V. I., Elchalakani, M., & Thai, H. T. (2018). Finite element analysis of large diameter high strength octagonal CFST short columns. *Thin-Walled Structures*, 123(November 2017), 467–482. <https://doi.org/10.1016/j.tws.2017.11.007>
20. Al-Ani, Y. R. (2018). Finite element study to address the axial capacity of the circular concrete-filled steel tubular stub columns. *Thin-Walled Structures*, 126(June 2017), 2–15. <https://doi.org/10.1016/j.tws.2017.06.005>
21. Saleh, S., & Al-Abboodi, İ. (2021). Strength and Behaviour Assessment of Axially Loaded Concrete Filled Steel Tubular Stub Columns. *Turkish Journal of Engineering*, 5(4), 154–164. <https://doi.org/10.31127/tuje.686246>
22. Design, Calculation and Construction Principles of Steel Structures. (2016). Ministry of Environment and Urbanisation.
23. Abaqus. (2010). Abaqus/CAE User Manual. Dassault Systems.
24. Hafezolghorani, M., Hejazi, F., Vaghei, R., Jaafar, M. S. Bin, & Karimzade, K. (2017). Simplified damage plasticity model for concrete. *Structural Engineering International*, 27(1), 68–78. <https://doi.org/10.2749/101686616X1081>



© Author(s) 2023. This work is distributed under <https://creativecommons.org/licenses/by-sa/4.0/>



Coordination compounds for rheological and physical-chemical regularity of energy consumption decrease while transporting crude oils

Nurullayev Vali Hanaqa ^{*1}, Usubaliyev Baybala Taci ², Gurbanov Gusein Ramazan ³, Abdullayeva Zeynab Arif³, Gasimzadeh Aysel Valiyaddin³, Hasanova Matanat Maxsud ²

¹State Oil Company of the Azerbaijan Republic, Republic of Azerbaijan

²Azerbaijan State University of Oil and Industry Scientific-Research Institute "Geotechnological Problems of Oil, Gas and Chemistry", Republic of Azerbaijan

³Azerbaijan State University of Oil and Industry" Head of the department "Oil and gas transportation and storage", Republic of Azerbaijan

Keywords

Asphalt-resin-paraffin deposits
Chemical composition of oil complex
Porous
Structure decomposition
Benzenetetracarboxylic
Balakhany heavy

Research Article

DOI: 10.31127/tuje.1093934

Received: 26.03.2022

Accepted: 18.05.2022

Published: 31.08.2022

Abstract

For the first time, complex compound of zinc (II) 1, 2, 4, 5-benzenetetracarboxylic acid with a porous structure was synthesized. Individuality and chemical formula of a complex compound was determined according to X-ray diffraction, elemental, IR spectroscopy and derivatographic analysis. The process of thermal decomposition of the resulting compound was also studied. It is also found that, despite the fact that the parameters of the unit cell of the crystal are significantly different from the known complex, it retains its layered polymer and porous structure. Recently, high-viscosity oil fields, where non-Newtonian crudes are met, are rapidly developed.

1. Introduction

Oil is a natural multicomponent organic liquid. It is based on a mixture of naphthenic, aromatic and paraffinic hydrocarbons. Oil is a mixture of about 1000 individual substances, of which most are liquid hydrocarbons and heteroatomic organic compounds, mainly sulfurous, nitrous and oxygen, organometallic compounds, the remaining components are dissolved hydrocarbon gases, water, mineral salts, solutions of organic acid salts, etc., mechanical impurities.

The content of all these components can vary widely and depends on the oil field. The oil consists of about 425 hydrocarbon compounds. Any oil under natural conditions consists of a mixture of methane, naphthenic and aromatic hydrocarbons.

It is also found out that formation of these types of connections is directly related to their structures, that is,

when they are in contact with these acids due to their polymeric structures, acid molecules are positioned in interchain spaces. The number of included molecules depends on size and geometric forms of these molecules, that is, their clathrate formation is dependent on the size factor.

In addition to the size factor, pH medium is also of great importance. Depending on pH values, their structures change for easy clathrate formation [1-2]. We have also synthesized and decoded crystal structure of decahydrate complex of copper (II) with 1,2,4,5 - benzenetetracarboxylic (pyromellitic) acid [3].

From the crystal structure it is seen that the complex consists of polymeric nets of parallel planes [2]. The acid anion for coordination impact uses all four carboxyl groups.

The composition of the crystalline compound coordinately bound with copper atoms of water

* Corresponding Author

*veliehet1973@mail.ru) ORCID ID 0000-0002-9608-600X
(ubeybala@gmail.com) ORCID ID 0000-0002-7196-3969
(ebikib@mail.ru) ORCID ID 0000-0003-0167-5707
(abddali@yandex.ru) ORCID ID 0000-0003-0988-4802
(qasimzade92@inbox.ru) ORCID ID 0000-0002-5461-7677
(shyran@yandex.com) ORCID ID 0000-0002-0278-6858

Cite this article

Hanaqa, N. V., Taci, U. B., Ramazan, G. G., Arif, A. Z., Valiyaddin, G. A., & Maxsud, H. M. (2023). Coordination compounds for rheological and physical-chemical regularity of energy consumption decrease while transporting crude oils. Turkish Journal of Engineering, 7(3), 180-185

molecules also includes two molecules of water of crystallization, which by means of hydrogen bonds covering all oxygen atoms bind the layers into a single unit in the form of 3D crystal structure. Wherein one layer of complexes (light) is slightly shifted in the plane (011) with respect to other layer systems (black). Based on the above mentioned, it can be assumed that in the absence of water molecules of crystallization, there would not occur displacement of layers. In this case, large pores in the carcass layers would lie on top of each other and large through columns with ability to include "guest" molecules would be formed. It should be noted that in this structure the interlayer space is also available for the inclusion of appropriate molecules [4].

Thus, the aim of this work is to study the complexation of pyromellitic acid, with further receipt of its non-bonded joints on its basis [5].

2. Method

This work presents the results of the synthesis, physical and chemical and structural and chemical studies of complex compounds of zinc (II) resulting in a weakly acidic medium (pH = 6.8).

As seen in Figure 1, the complex compound is highly crystalline and has a high symmetry. With X-ray indexing unit cell parameters were computed: a = 9,78, b = 19,7, c = 11,76Å.

Comparison of the parameters of the complex compound with parameters of the known complex compounds of copper (II) the crystal structure of which was decoded (a = 9,679 (5), b = 18,17 (2), c = 12,18 Å) showed that they differ respectively by 0.11; 1 and 0,42 Å. As it is seen, the parameters of a and b increase, whereas parameter of c decreases. These values are low, so at the first approach it would be found out that they are isostructural. But the results of the elemental, IR spectroscopy and differential thermal analyzes have not confirmed these isostructural compounds, as elemental analysis results showed that the content of the complex is very different from the complex [6].

Elemental analysis results are presented in Table 1.

Table 1. The results of elemental analysis of the complex compounds of copper and zinc (II)

Found out, %			Composition of compounds	Calculated, %		
H	C	Zn, Cu		Zn, Cu	C	H
-	-	-	Cu ₂ C ₁₀ H ₂₂ O ₁₈	22,81	21,5	3,95
2,31	26,72	29,0	Zn ₂ C ₁₀ H ₁₀ O ₁₂	28,877	26,5	2,20

As it is seen from the table, the compositions of the compounds are very different from each other. The composition of the newly obtained compound has the preliminary chemical formula Zn₂(C₆H₂(COO)₄)(H₂O)₄, whereas the chemical formula of the famous complex is Cu₂(C₆H₂(COO)₄)(H₂O)₁₀.

Decomposition of the complex compounds of zinc (II) begins at 90°C in the temperature range of 90–138°C and is accompanied by a shallow but clear endothermic effect at 110°C and corresponds to the removal of two molecules of water. Experimental loss value of mass is 8 % (calculated 7.95%). Thereafter, in DTA curve there occurs the second endothermic effect in the temperature

range of 138 - 180°C with maximum at 150°C, which corresponds to 1.5 moles of water removal. Experimental loss value of mass is 6% (calculated 5.96%).

Then there occurs the third fuzzy and shallow endothermic effect in the temperature range of 180 – 280 °C with maximum at 240 °C which corresponds to removal of an additional 0.5 moles of water. Here, experimental weight loss of the mass is 2% (calculated 1.99%). Anhydrous intermediate complex is stable up to 400°C which is extremely rare for complex compounds. At 400°C, first slowly, then with high-speed decomposition of anhydrous complex takes place in the temperature range of 400 - 600°C with a single clear exothermic effect with the maximum 520°C. Here the experimental weight loss of the mass is 48% (calculated 48.15%). Since on the curve TG after complete decomposition is not observed weight increase, it can be concluded that oxidation of the zinc ion is due to oxygen atoms of the carboxyl groups. The final product is a ZnO. Experimental mass of the final product is 36% (calculated 35.95%). Below is a diagram of a solid phase transformation of complex compounds:

Since a weight increase is not observed on TG curve after complete decomposition, it can be concluded that oxidation of the zinc ion is due to oxygen atoms of the carboxyl groups. As the final product there remain ZnO. Mass of final experimental product is 36% (calculated 35.95%). Below is a diagram of a solid phase transformation of complex compounds:

IR spectroscopic study also indicates that the frequency at 461; 534; 553 and 590 sm⁻¹ refer to liberational vibrations of water of crystallization or torsional vibrations of water molecules with limited interactions with neighboring atoms [2].

Besides it, absorption bands are observed in IR spectrum of compound at 3550 - 3200 cm⁻¹ (symmetric and asymmetric valent vibrations of OH) and at 1630 - 1600 cm⁻¹ (deformation vibrations of HOH), which are characteristic for water of crystallization.

Absorption bands at 1597, 1548, 1505 (va) and 1457, 1401, 1337 cm⁻¹ (vs) refers to the carboxyl group of an acid anion [7]. Value of the difference value Δ (va - vs) are respectively 140, 146 and 127 cm⁻¹ and it is significantly less than that of ionic compounds, but is in good agreement with the values of bidentate chelate complexes [5].

Thus, the central atom is coordinated to six. Coordination zinc (II) includes four oxygen atoms of two carbonyl groups and two oxygen atoms of water molecules. Coordination polyhedron is octahedron.

As it is seen from the figure, the structure of the complex compound Zn₂(C₆H₂(COO)₄)(H₂O)₄ consists of alternating layers along the axis [2]. The structure is porous and the size of pores is approximately 9 x 16 Å, as in [3]. The layers are stitched together due to hydrogen bonds formed by coordination of water molecules in different layers on the tops of octahedra. It is also possible to assume that the skeleton pores in the structure will be one above the other and, in this case, through columns for the available "guest molecules" will be generated. Thus, one can conclude that a series of non-bonded compounds having practical value can be synthesized on the basis of this compound.

3. Results

The purpose of this article is to study the effect of additives on the rheological properties of the oil field of Azerbaijan Bulla, Balakhany heavy and Surakhany. Additives of Difron 4201 and BAF-1 grades are used as additives [1]. Separation of paraffins, asphaltenes and resins from oil was carried out according to the procedures GOST 11851-85 and GOST 11858-66. The pour point, or the pour point, was determined in the S.D.M. - 530 (Germany), RK 1530-2006 supplied with three cameras for maintenance of temperatures of 0,-17 and 34 °C wasps according to ST. Effective viscosity and shear stress were measured on a rotary rheometer REOTEST-2 using a measuring system standard GOST 26581-85 [2]. The main physicochemical characteristics of oil, such as viscosity, solidification temperature, paraffin content, etc. from Bulla, Balakhany heavy and Surakhani deposits are studied in the work, which are given in Table 2.

Table 2. The main physical and chemical characteristics of oil from the Bulla, Balakhany heavy and Surakhany fields

Indicators	Bulla	Balakhany heavy	Surakhani
Density, at 20 °C kq/m ³	842,1	921,7	859,3
Amount of water, mass %	0,76	0,21	0,79
Chloride Salt Content, mq/l	138,6	38,4	139,5
Amount of mechanical impurities, mass %	0,007	0,009	0,008
Resins content, mass, %	9,6	16,2	14,8
Asphaltenes content, mass, %	0,22	2,8	2,94
Paraffins content, mass, %	13,1	0,31	2,73
Puor point temperature, °C	+12	-33	-21
Viscosity at 20°C mm ² /sec	23,2	160,3	20,2
Fractional composition:			
Overpoint,temperature, °C			
To 200 °C, by volume %	71,5	97,5	78
To 300 °C, by volume %	24,5	16	21
To 350 °C, by volume %	44	32,5	40,5
Final boiling point, °C	63	54	61,5
	341,5	302	328

Table 1 shows that oil from Bulla field belongs to high-paraffinic oil, compared to oil from Balakhana fields heavy and Surakhany. It should also be noted that oil from Surakhany fields has a positive freezing point, which also indicates the presence of a large number of paraffins. It is known that when pumping highly paraffinic oils, paraffin deposition is observed on the inner walls of the pipeline. In order to prevent this phenomenon, a hot pumping method is used when transporting high-paraffin oils. For this purpose, oil is further heated every 25-150 km of pipeline length. Heating oil solves the problem of pumping high-paraffinic oil, but this complicates and increases the cost of its production, transportation and processing. In terms of the dissolution efficiency of ARPS, most often these compositions differ slightly from natural solvents, and in

some cases are even less effective. Natural ARPS removers associated with oil production, such as gas condensate, gas gasoline, a mixture of liquefied petroleum gases, light oil, have become the most widespread. The undeniable advantage of such solvents is their availability. They are usually produced or obtained in oil areas, have a low cost, do not affect further oil processing processes. To increase the effectiveness of ARPS removers, compositions comprising a hydrocarbon solvent and various surfactants are often provided, the addition of which increases the surface activity of the solvents and the dispersion effect of ARPS to the compositions up to 3 wt%. Such surfactants include composite additives, polyalkylbenzene resin (PABR), heavy pyrolysis resin (PR), catalytic cracking thermogasoil (TG), nitrogen-containing block copolymer (BC) of ethylene oxide and propylene oxide with molecular weight of 5000 and phenol-formaldehyde resins [4]. After the reagent was added to the asphaltene-paraffin resin compounds separated from the oil, the results of their electron microscopy were obtained (Figure 3). The results of electron microscopy are of great importance in the analysis of the structural viscosity of oils.

Our studies show that the rheological properties of oils can be improved by selecting a suitable chemical reagent for the group composition.

The results of experimental investigations have shown that reagents BAF-1 (technical conventional name reagents) reduce the viscosity of petroleum such as heavy and crude oil (Balakhany heavy), to facilitate transportation of the subterranean formation from the production site to the refinery or oil storage tanks, increased production, purified oil and oil from the sludge in the tanks.

As is known all these properties of oils (high viscosity, difficulty of transportation, the decline in production, the sludge formation in tanks, etc.) directly related to forming asphaltene-resin-paraffin sediments (ARPS).

X-ray diffraction and electron microscopic studies conducted to elucidate the mechanism of action of reagents us. To conduct the study, two samples of oil (for 300ml) from the same wells taken. To one sample of the oil added 40ml composite reactant solution, and another - left unchanged and distilled to their obtaining the fraction of tar.

As is known, tar is a dry distillate oil at 450-600 °C temperature (depending on the nature of oil) in vacuum condition and atmospheric pressure. The yield of tars depending on the oil's composition is 10-45% (wt.). Resinis a black viscous liquid and formed during the fragmentation of small glittering particles. The composition of the sludge includes paraffin, the naphthenates aromatic hydrocarbons (45-95%), asphaltenes (3-17%), petroleum resin (2-38 %) and the atoms of metals. Depending on the nature of the oil and from the entrance of the transparent fraction of the density of the sludge varies from 0.95 to 1.03 g/cm³, coking 8-26% (weight) and the melting point of the 12-55 °C.

As is known at atmospheric and vacuum distillation the chemical composition of the oils not change.

Therefore, test results obtained for dry and oil products relates directly to oils themselves.

Given the above, the dry product of oil samples subjected to X-ray diffraction and electron microscopy studies. The results are shown in Figures 1, 2, 3 and 4, respectively.

X-ray analysis and electron microscopic images obtained respectively From X-ray diffraction (Fig.1) shows that the dried product sample without reagent pronounced bright consists of three phases between planar distances 4.44, 4.22 and 3.64. On the radiograph (Fig.2) are removed from the dry product oil sample with the reagent, the third phase completely disappears in the first two phases of the maxima are shifted to the low-angle side, i.e., between planar distances increase. This suggests that after the disappearance of the third phase, the structure of 1-st and 2-nd phase changes and their crystallinity increases.

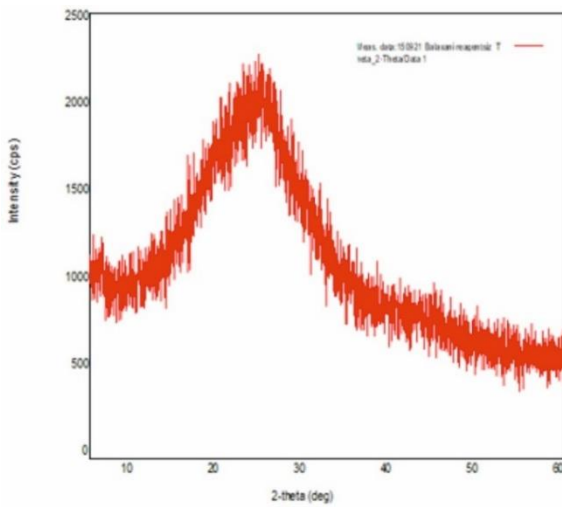


Figure 1. Radiograph of a dry oil sample without reagent

X-ray analysis and electron microscopic images obtained respectively From X-ray diffraction (Fig.1) shows that the dried product sample without reagent pronounced bright consists of three phases between planar distances 4.44, 4.22 and 3.64. On the radiograph (Fig.2) are removed from the dry product oil sample with the reagent, the third phase completely disappears in the first two phases of the maxima are shifted to the low-angle side, i.e., between planar distances increase. This suggests that after the disappearance of the third phase, the structure of 1-st and 2-nd phase changes and their crystallinity increases.

The results of electron microscopic studies reagent less sample (Fig.3) showed that in the dry rest there is the associate consisting of asphaltenes, resins and waxes that worsen the rheological properties of crude oils.

The results of electron-microscopic investigations of the sample with the reagent (Fig.4) indicate that in this associate is fragmented and are distributed evenly in oil, which is in a dissolved state.

4. Discussion

The elemental composition of the obtained compound was defined by gas chromatography method by means of an analyzer CHN30E Carlo ERBA. The content of the metal was calculated on the basis of the

weight loss curve by the quantity of oxide obtained after being heated on derivatograph up to 800° C. X-ray phase analysis was performed on the device Commander Sample ID (Coupled Two Theta/Theta) WL 1.54060. IR spectra were recorded on a device SPECORD-MBO in 400 - 4000 cm-1 area. Derivatograms recorded derivatograph on NETZSCH STA 449F3 STA449F3A-0836-M (range 21 / 10.0 (K / min) / 800).

Synthesis of the compound. The starting materials were C₆H₂(COO)₄, Zn₂(CH₃COO)₂ of qualification 4 (GOST 3759 - 75). The complex is prepared by reacting pyromellitic acid with zinc acetate at a stoichiometric ratio of 1:2. The solution was refluxed until disappearance of the odor of acetic acid, filtered while hot and cooled to room temperature.

The disappearance of the third phase with between planar distance (d = 3,60) reveals that the reactants porous (pore size is ~20A ° BAF-1 with the third phase non-valence form compounds with self-organization and self-construction, i.e., by reacting a reagent with oil arise non-valence skeking interaction between porous polymers and chromatic focal and heteroatom makroassociates third phase. liberated from the third phase of the first and second associates (ARPS) turn into small particles and dissolve in the crude oil. In this regard, and improved rheological properties of oil. An increase in the between planar spacing of the first and second phases shows that their structure changes.

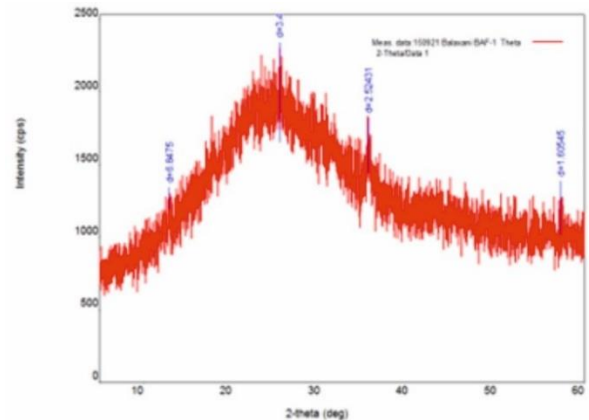
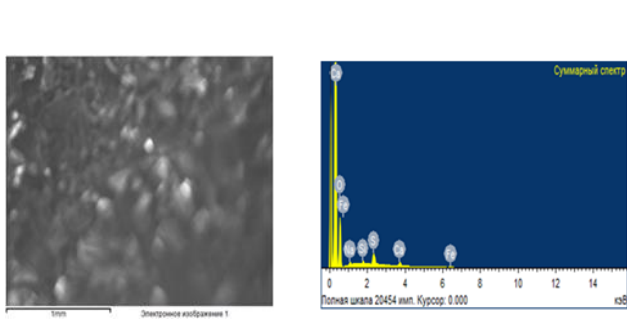


Figure 2. Radiograph of a dry sample oil with reagent

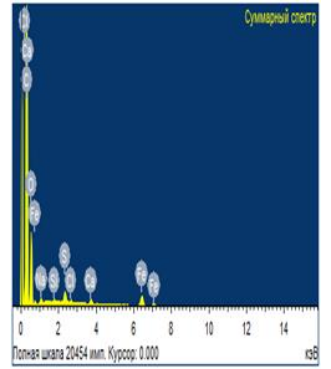
5. Conclusion

According to the results of electron microscopic analysis also clear that in the dry product without reagent paraffin oil associates are in a solid mass, which deteriorate its properties. A dry product oil with a reagent ARPS associates fragmented into small particles, i.e., they uniformly distributed in the oil and therefore improves the rheological properties of oil. This again proves that the reactants form a hetero chromatic non valence compound.

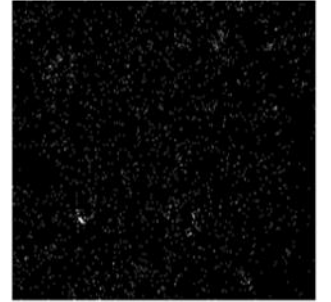
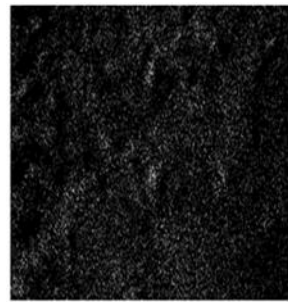
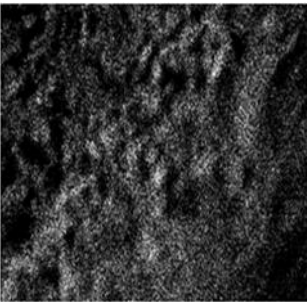
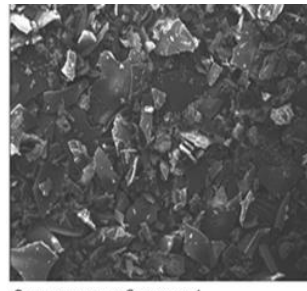
Thus, the research results show that the reagents can solve all the problems arising from paraffin formation, particularly, improve the recovery of oil wells, reducing the viscosity of heavy oils, improve the efficiency of transportation of such crudes and perform effective cleaning oil tanks of oil and petroleum deposits, then is based on the technology of said reactant is multifunctional.



Элемент	Весовой %	Атомный%	Соед. %	Формула
C K	26.84	33.04	98.96	CO ₂
Na K	0.13	0.08	0.17	Na ₂ O
Si K	0.09	0.01	0.06	SiO ₂
S K	0.15	0.07	0.37	SO ₃
Cl K	0.06	0.02	0.00	
Ca K	0.10	0.04	0.14	CaO
Fe K	0.66	0.18	0.85	FeO
O	72.04	66.56		
Итого	100.00			



Элемент	Весовой %	Атомный%	Соед. %	Формула
Na K	8.19	7.84	11.04	Na ₂ O
Si K	9.82	2.99	8.18	SiO ₂
S K	22.95	15.34	55.81	SO ₃
Ca K	10.83	5.95	15.16	CaO
Fe K	7.85	3.01	9.82	FeO
O	47.17	64.88		
Итого	100.00			

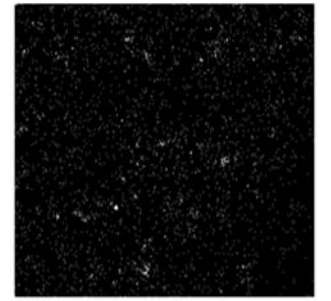
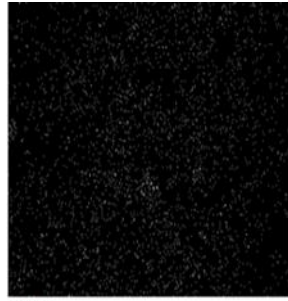


C Kα1_2

O Kα1

O Kα1

Na Kα1_2

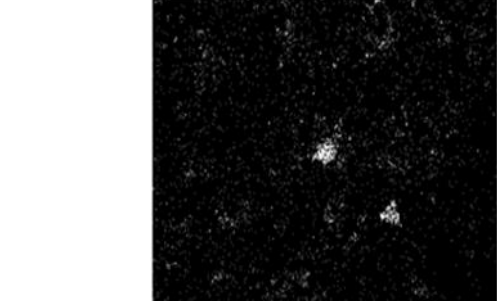
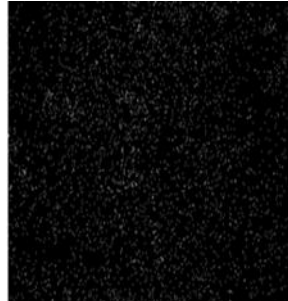


Na Kα1_2

Si Kα1

S Kα1

Ca Kα1



S Kα1

Ca Kα1

Fe Kα1

Figure 3. Electron- microscopic image of a dry oil sample without reagent

Figure 4. Electron microscopic image of a dry sample reagent free oil with reagent

Acknowledgement

The authors gratefully acknowledge the research council of State Oil Company of the Azerbaijan Republic (SOCAR) and Azerbaijan State University of Oil and Industry.

Author contributions

Nurullayev Vali Hanaqa, Usubaliyev Baybala Taci, Gurbanov Gusein Ramazan: Conceptualization, Methodology, Software
Abdullayeva Zeynab Arif, Gasimzadeh Aysel Valiyaddin: Data curation, Writing-Original draft preparation, Software, Validation.
Hasanova Matanat Maxsud: Visualization, Investigation, Writing-Reviewing and Editing.

Conflicts of interest

The authors declare no conflicts of interest.

References

1. Usubaliev, B. T., Taghiyev, D. B., Nurullayev, V. H., Munshieva, M. K., Alieva, F. B., & Safarova, P. S. (2017). Structural and Chemical Research of Coordination Compounds of Hexaaqua Bisbenzol 1,2,4,5-Tetracarbonate Diiron (II) with a Layered-Porous Structure. *Journal of Nanomaterials & Molecular Nanotechnology*, 6 (1), 1-5.
2. Usubaliev, B. T., Taghiyev, D. B., Nurullayev, V. H., Munshieva, M. K., Alieva, F. B., & Safarova, P. S. (2017). Synthesis and Physico-Chemical Studies of Complex Compounds of Iron (II) and (III) With Phthalic Acid. *Journal of Nanomaterials & Molecular Nanotechnology*, 6 (5), 1-4.
3. Usubaliev, B. T., Taghiyev, D. B., Nurullayev, V. H., Munshieva, M. K., Alieva, F. B., & Safarova, P. S. (2017). Synthesis and structural-chemical studies of hexoaquatribenzene - 1, 2, 4, 5- tetracarbon-tetrairon (III) coordinator compound. *Frontiers in Nanoscience and Nanotechnology*, 3 (2), 1-4.
4. Usubaliev, B. T., Munshieva, M. K., Nurullayev, V. H., Alieva, F. B., & Safarova, P. S. (2016). Synthesis and Structural - Chemical Research of Coordination Compounds of Tetraaqua Bisbenzol -1,2,4,5 - Tetracarboksilat Dizinc (II). *Bulletin of Environment, Pharmacology and Life Sciences*, 5 (4), 10-16.
5. Nurullayev, V. H., Usubaliev, B. T., Taghiyev, D. B., Munshieva, M. K., Alieva, F. B., & Safarova, P. S. (2017). Structural and Chemical Research of Coordination Compounds of Hexaaqua Bisbenzol-1, 2, 4, 5-Tetracarbonate Diiron (II) With A Layered-Porous Structure, For Heavy Crude Oil. *International Journal of Nano Studies & Technology*, 2 (1), 123-127.
6. Usubaliev, B. T., Munshieva, M. K., Nurullayev, V. H., Alieva, F. B., Safarova, P. S. (2016). Synthesis, Physical-And Structure- Chemical of Research of Coordinating compounds of Diaquo-1,2,4,5 Benzoltetracarbonat Dimedi (II). *Bulletin of Environment, Pharmacology and Life Sciences*, 5 (3), 12-17.
7. Usubaliev, B. T., Taghiyev, D.B., Nurullayev, V. H., Munshieva, M. K., Alieva, F. B., Safarova, P. S. (2017). Synthesis and Physico-Chemical Studies of Complex Compounds of Iron (II) and (III) With Phthalic Acid. *Journal of Nanomaterials & Molecular Nanotechnology*, 6 (5), 1-4.



© Author(s) 2023. This work is distributed under <https://creativecommons.org/licenses/by-sa/4.0/>



Challenges, threats and advantages of using blockchain technology in the framework of sustainability of the logistics sector

Emel Yontar ^{*1} 

¹Tarsus University, Industrial Engineering Department, Türkiye

Keywords

Blockchain
Logistics
Sustainability logistics
SWOT analysis
Sustainability

Research Article

DOI: 10.31127/tuje.1094375

Received: 28.03.2022

Accepted: 07.07.2022

Published: 31.08.2022

Abstract

Due to the complexity and lack of transparency of traditional supply chains, the introduction and development of blockchain technology is of great interest to the stakeholders involved in the logistics process to improve logistics processes in the supply chain and make them more sustainable. A detailed analysis has been made for the logistics industry in this study, which is discussed to investigate the undeniable benefits of blockchain technology. Today, when we try to determine our application methods in line with sustainable development purposes, it is seen that the logistics industry gains many advantages when it is integrated with blockchain technology. For this purpose, SWOT analysis has been applied as a result of literature review for logistics management, which is one of the sub-activities of supply chain management that applies blockchain technology, and contributes to the application potential in the logistics industry. At this point, some of the strengths that will require the use of blockchain technology in the logistics sector are decentralized structure, effective information sharing, fast response, robust risk management, interprocess integrity, etc. While its weaknesses are low performance, having a complex structure and high energy consumption can be the problem. In addition, some of the opportunities that the sector will gain are the ability to optimize time, solve problems, gain competition, increase sustainability; on the other hand, external threats, cross-integration adoption, new technology, limited data privacy etc. is happening.

1. Introduction

Blockchain technology has the potential to be adapted to every step of the supply chain, from the sourcing of raw materials to the distribution stage and consumers [1-2]. Blockchain, which started to work with financial applications, shows potential for application in many other sectors [3]. One of such areas of interest is supply chain management operations [4] and logistics operations, which is one of its activities. Like all other sectors, logistics sectors are also affected by the radical change of technology. In this context, studies and applications for the use of blockchain technology in the logistics and supply chain sectors have gained importance in recent years in order to digitize the logistics industry and to realize business processes in a more transparent, reliable and traceable way.

Blockchain is known as a distributed database system that records transaction data, managed by consensus mechanism [5]. In 2008, a group under the name of Satoshi Nakamoto announced the crypto currency Bitcoin, in which blockchain technology is a

fundamental element [6], and the concept of blockchain entered the literature.

The typical workflow of using the blockchain for any transaction is shown in Figure 1. Each block contains its own unique ID number and ensures transaction security. All transactions made in the system are verified by users, arranged in order and cannot be undone after being added to the network. This working principle of the blockchain makes it a reliable technology [7]. The application logic of blockchain and supply chains bears great similarities [8].

Logistics management is accepted in the literature as areas where blockchains are suitable. Supply chains are a structure that includes many physical flows involving multiple actors and stakeholders, and information sharing that supports this flow. Transactions can be documented throughout the product lifecycle and a permanent history of the product is created. Blockchain technology: (i) each asset can be recorded at every stage, (ii) all official documents can be tracked (iii) digital assets can be tracked along with physical assets.

* Corresponding Author

^{*}(eyontar@tarsus.edu.tr) ORCID ID 0000-0001-7800-2960

Cite this article

Yontar, E. (2023). Challenges, threats and advantages of using blockchain technology in the framework of sustainability of the logistics sector. Turkish Journal of Engineering, 7(3), 186-195

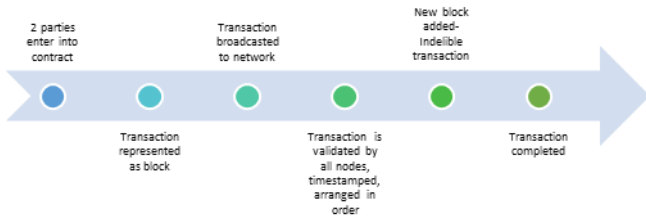


Figure 1. Blockchain work flow representation

According to this statement, the Blockchain supply chain relationship has come to the fore in many studies. Tektaş and Kırbaç [9] conducted a case study on the use of blockchain technology in logistics, and an application study of this case study was carried out in a logistics company using appropriate methodological methods. Kshetri [10] explained how blockchain affects key supply chain management objectives such as reliability, cost, quality, sustainability and flexibility. Agrawal et al. [11] proposed a blockchain-based traceability framework for traceability in the textile and apparel supply chain. Ronaghi [12] establishes a model for assessing the maturity of blockchain technology in the agricultural supply chain. Katsikouli and Wilde [13] examine the use of blockchain technology to manage supply chains in the food and agriculture industries. Reddy et al. [14] conducts a systematic literature review on applications of blockchain technology in the automotive supply chain.

The authors, who dealt with various sectors in their studies, did not ignore the concept of sustainability and focused on supply chain management. Sustainability in supply chain management, while managing the flow of materials, information and capital throughout the supply chain and the cooperation between the enterprises within the chain, simultaneously seeks to set and achieve goals for the three dimensions of sustainable development, which are formed by stakeholders and customer expectations. Di Vaio and Varriale [15] study the relationship between blockchain, operations management and sustainability issues in supply chain management. Yadav and Singh [16] explore the use of blockchain technology to develop effective sustainable supply chain management. Sunmola and Apeji [17] focus on blockchain technology and explore sustainable supply chain visibility and features of blockchains. Kouhizadeh et al. [18] examines the barriers to adopting blockchain technology to manage sustainable supply chains with the DEMATEL technique. Also addressing sustainable development goals, Tsolakis et al. [19] explores the design of blockchain-based food supply chains. Esmaeilian et al. [20] provides an overview of Blockchain technology and Industry 4.0 to drive supply chains towards sustainability.

Based on these explanations, this study explores the advantages, possibilities and application of blockchain technology with special emphasis on blockchain technology in logistics. It is aimed to contribute to the development of blockchain applications in the logistics sector by evaluating the perspective in the literature. Other parts of the work proceed as follows. In Section 2, technical aspects of blockchain technology are discussed and information about blockchain is given. In Section 3, the compatibility of logistics management, which is one

of the supply chain management activities, with blockchain is examined. In Section 4, sustainability was discussed, the relationship between sustainable development goals and blockchain was analyzed and its connection with logistics was matched. In Section 5, the methodology is presented, and in this chapter, the findings of the study are discussed by making a SWOT analysis between sustainable logistics and blockchain. In the last section, comments are made on the findings and suggestions for future studies are presented.

2. Blockchain Architecture

Blockchain is a comprehensive technology that brings together multiple technologies and keeps them integrated. Basically, it includes three important technologies: asymmetric encryption algorithms, distributed data storage and consensus algorithms. In addition to these, the technology of smart contracts is later incorporated into the blockchain technology. Asymmetric encryption algorithm is the encryption technology used for the authentication of ownership, in terms of security [21]. Distributed storage means that every node added has independent and complete data storage. Smart contracts are co-formulated and prepared by network partners. Each participant creates a common smart contract to complete a peer-to-peer transaction or transfer.

Blockchain applications consist of five modules that manage related transactions [22]:

- Block creation module; It contains information and details of transactions located on all nodes and helps add new blocks to the existing supply chain by providing links to the front block.
- Data source module; It ensures that data received by users is not modified or corrupted.
- Reconciliation module; It is used to confirm and verify all transactions to prevent data corruption.
- Transaction module; monitors and manages the steps of a transaction on the blockchain.
- Connection and interface module; Information technology software required for blockchain applications synchronizes and keeps track of transactions.

In summary, blockchain technology has certain advantages when used operationally. Data dominance comes first, and each company has the authority to share only as much data as it wants to share, while keeping its own data. Especially in multi-stakeholder and actor systems such as logistics, it incorporates trust-building mechanisms such as multiple consensus-based approval among all participants. As a result of the blockchain application, it is observed that uncertainty can be reduced and trust between stakeholders is possible. While the blockchain system provides transparency among all stakeholders, it is also possible to create a collaborative environment between all actors. Blockchain, which takes its main power from its ability to make transactions without intermediaries, appears in many areas as a cost-effective technological solution. In

addition to all these, it is possible with blockchain to eliminate fraud and unethical transactions and errors in processes. Blockchain provides a distributed consensus mechanism that ensures participant entities are aware of every event and transaction by creating an irrefutable record in the public ledger.

Blockchain is expected to become an innovative and disruptive force in the future, and some argue that these technologies have great potential to promote sustainable development [23]. The features of blockchain that make it unique and promising for future applications are listed in Figure 2 [24].

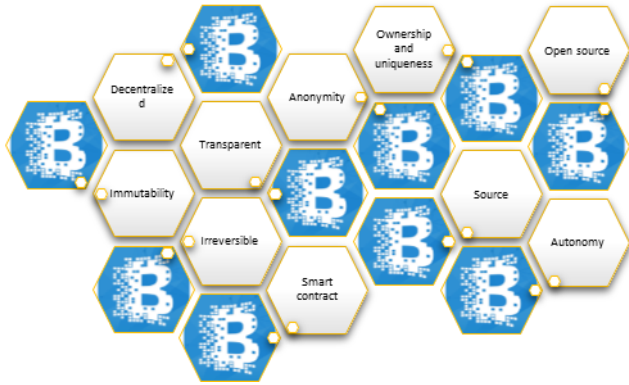


Figure 2. The general characteristics of Blockchain

3. Logistics Management-Blockchain Relationship

Due to the lack of transparency of supply chains, it is seen that stakeholders are open to recognizing and developing blockchain technology in order to make logistics processes in the supply chain sustainable [25].

It is the index of basic factors consisting of the concepts of "right product, right quantity, right form, right time, right source, right way and right price" within the definition of logistics. Remarkably, at the time of product entry, all these factors are affected by the standard and quality of logistics operations. Therefore, these elements can provide basic resources when determining different logistics situations on the basis of sustainability. At the same time, these elements become the basis for key metrics in monitoring operational success or failure. Thus, it is important and comes to the fore that which parameter is sustainable, which parameter is related to the blockchain.

One of the most important reasons why blockchain technology has attracted great interest in sectors such as supply chain is that it emerged as a solution to the trust problem encountered in classical commercial relations [26]. In general terms, in addition to the benefits of blockchain technology such as transaction speed, information sharing and transparency, the main purpose is to increase transaction security.

Blockchain technology provides flexibility by reducing the effects of outages and applying a preventive and proactive approach to risk management [27]. Even in a large manufacturing business, it can provide robust risk management due to its ability to scale according to requirements. IoT and RFID systems are developed when integrated with blockchain technology, resulting in a more secure supply chain. The IoT system is a centralized digital integration network. Blockchain contributes to

the high security of the IoT system in terms of product traceability by enabling end-to-end data transfer for dynamic data storage [28].

Blockchain has significant potential to increase efficiency and help resolve disputes in the logistics industry throughout the entire logistics and settlement process, including trade finance. Blockchain technology is in a position to help alleviate many of the frictions experienced in logistics, including procurement, transport management, tracking and tracing, customs cooperation and trade finance [29]. With the use of smart contracts, a trust protocol will be established between the parties and the parties in the supply chain will become interdependent. In fact, in this case, it can be said that if there is no smart contract, there will be no flow in the supply chain. At the same time, the party that is not connected to any of the parties in the system with a smart contract cannot be included in the supply chain network [30].

It is a reality to experience the bullwhip effect frequently depending on the fluctuation in demand in logistics systems. However, after the establishment of an environment of mutual trust with the mechanisms of the blockchain, projections for the future can be made much healthier. As a result, the problems arising from uncertainty in the entire logistics system will be eliminated, especially if the product planning and management is stable and the expectations of the customers are met. While the main mission of logistics planning specialists is to solve systemic and instant logistics problems, their number will decrease with this technology and their duties will become system monitors. While logistics companies can perform all transactions through online systems, they will also be able to provide better quality and transparent service with multiple approval mechanisms. With this technology, problems such as insurance, delivery, document management and payment can be eliminated.

Hackius and Peterson [31] investigated the general prospects, barriers and advantages of blockchain in logistics and supply chain management. Accordingly, they came to the following conclusions about the potential of the blockchain (Figure 3):

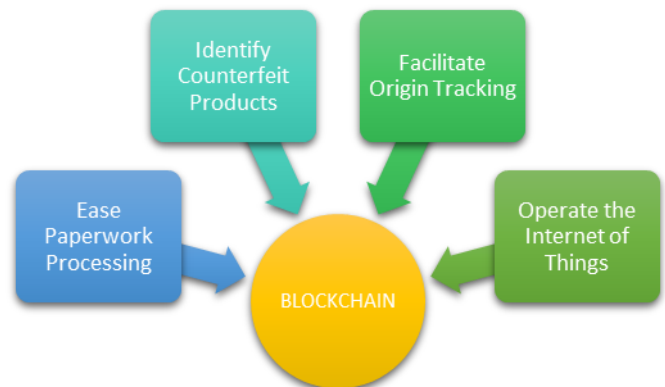


Figure 3. The potential of blockchain technology in logistics

Blockchain technology allows to greatly reduce production and logistics costs, speed up production

processes, reduce intermediaries in production processes, and also prevent forgery in documents and processes. In addition, it is extremely important to apply the blockchain architecture in the logistics sector in terms of digital document management and product tracking. In addition, the immutability, transparency, traceability and trust concepts of blockchain technology will be easily applied in the logistics industry, and the control of products, materials, data and processes with the blockchain will make great contributions to the logistics industry [32]. In the concept of supply chain, the concept of transparency refers to the information contained in a supply network and presented to the stakeholders. In this context, the information flow in the supply chain will be transformed into a more reliable and transparent one with blockchain technology [33]. Sadouskaya [34] examined the effects of blockchain technology on the supply chain and logistics sectors in his study. In the mentioned study, some advantages of blockchain technology on the supply chain are stated as providing reliable information about the product to consumers, providing participation to all parties with a decentralized structure, reducing counterfeiting, minimizing product returns, and also facilitating payment systems.

However, it is possible to list the following among other benefits; (1) locating products; (2) visibility of handling conditions (stacking, relocating, transferring from large containers to smaller containers, renewing or repairing containers, aerating, sieving, mixing and similar operations) without changing the essential qualities of the goods under customs supervision; and (3) between multiple parties in the supply chain to facilitate interaction.

4. Blockchain Sustainability Relationship

Blockchain is a very useful framework for creating sustainable operations in logistics. It helps to create sustainable supply chains with the activities (Figure 4):

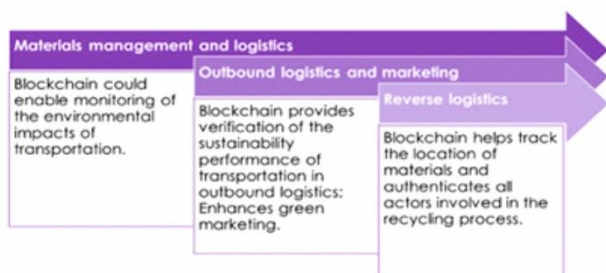


Figure 4. Sustainable supply chains activities at blockchain

It is known that blockchain technology, which is so related to the concept of sustainability, will also benefit the goals of sustainable development. The Sustainable Development Goals are a universal call to action to eradicate poverty, protect our planet and ensure that all people live in peace and prosperity. This call consists of 17 objectives (Figure 5). It provides all countries with clear guidance and objectives to adopt in accordance with their priorities and the environmental challenges facing the world.



Figure 5. Sustainability Development Goals (SDG)

The United Nations published a report on FinTech and the Sustainable Goals in 2016 on the potential contribution of blockchain technology to these goals and discussed how it can help [35].

Blockchain technology can help reduce fraud (Goals 8, 10) and increase food trust (Goals 2, 3, 12) and supply chain traceability (Goals 14 and 15). In addition to these, in researches; Hwang et al. [36] introduced the energy consumer service model that implements blockchain technology, big data, and the IoT, which allows various energy sources to be connected to various users and producers (Goal 7, 17). Looking at these studies in the literature, it is seen that blockchain technology contributes to sustainable development goals. Again, when optimum transportation management is provided, the ability to reduce carbon emission values and then serve a healthy life (Goal 3, 7); Among the advantages of port logistics are reducing the waiting time by making regular voyages and increasing the quality of life in the water (Goal 14).

5. Method

In this section, SWOT analysis for blockchain is made and some articles included its relationship with logistics and sustainability.

SWOT analysis is one of the best-known analysis methods that provides perspective and can be used to evaluate a new technology or trend with its strengths, weaknesses, opportunities and threats [37]. Gould [38] states that SWOT analysis highlights how external opportunities can be exploited and weaknesses are minimized, and how the issue can be protected against external threats, given the strengths of the subject under consideration. The SWOT analysis combines the strengths and weaknesses of the subject under consideration with the opportunities and threats in the external environment.

The four elements of SWOT Analysis express the following meanings [39-40]: Strengths: It is the situations in which the organization is more effective and efficient than its competitors with its capabilities. Weaknesses: Situations where the organization can or should improve is less effective than its competitors. Opportunities: The environment presents to the organization and it is the favorable conditions for the organization to achieve its objectives successfully, the environment for the organization; competitors, developments in the field of information, laws, etc. In this context, organizations should constantly try to

understand and anticipate the environment in order to understand and benefit from opportunities. Threats: These are the negative environmental indicators that occur in the environment and that can end the existence of the organization or stop its development, thus requiring measures to be taken.

Accordingly, SWOT analysis for blockchain technology; It has been brought together and inferences have been made by using the relevant articles. The summary table of blockchain technology is visualized in Figure 6 and explained in detail.

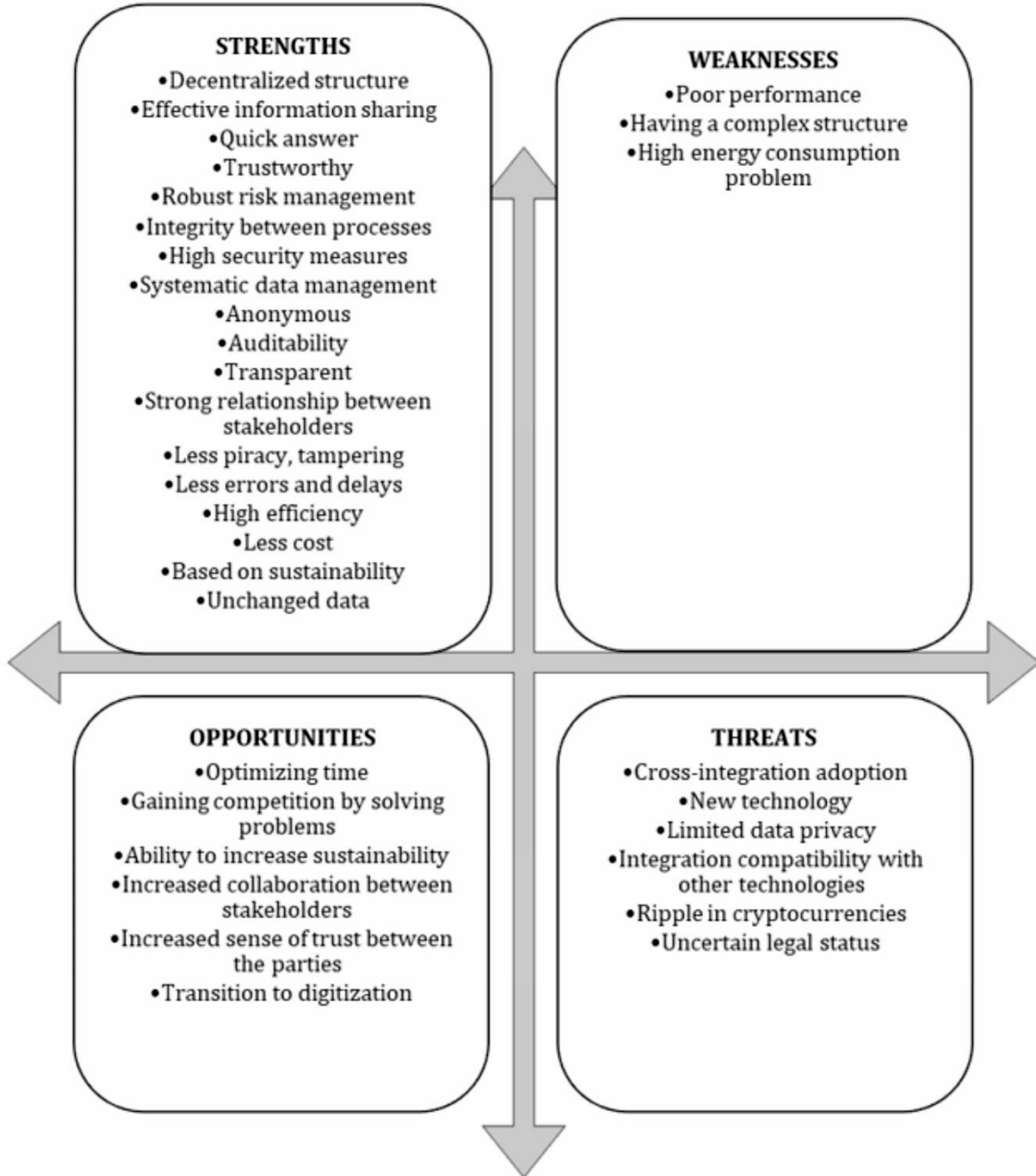


Figure 6. SWOT analysis summary table for blockchain technology

5.1. Strengths

1.It has a decentralized structure. The systems data can be accessed, stored and updated in more than one system [24, 34, 41].

2. It can contribute effectively to knowledge sharing [22, 41]. In this context, the information flow in the supply chain can be made more reliable and transparent with blockchain technology [33].

3. Fast response [10], transaction speed of blockchain technology [22], acceleration of production processes and improvement in response time [42-45].

4. It provides consumers with reliable information about the product, minimizes product returns [34] and has reliability [10].

5. Even in a large manufacturing enterprise, it can provide robust risk management and reduce risk due to its ability to scale according to requirements [10, 27].

6. It includes Asymmetric encryption algorithm, Distributed storage, Consensus algorithm, Smart contracts technologies. Asymmetric encryption algorithms have highest security [21]. In multi-stakeholder and actor systems such as logistics, it incorporates trust-building mechanisms such as multiple consensus-based approval among all participants. The data in the system is protected by encryption algorithms and distributed data storage [46]. Blockchain also helps facilitate real-time order placement and automation of production tasks with smart contract implementation [47].

7. Blockchain system provides transparency among all stakeholders [22, 32]. An identical copy of a blockchain is held by each node in the network, allowing real-time auditing and review of datasets, helping to track the status of an item during a transaction [42, 44, 48, 49, 50].

8. It can strengthen communities by promoting trust and transparency and supporting the development of reputation-based ownership of common resources.

9. It also improves the relations between all stakeholders [7], and at the same time, a collaborative working environment (collaboration) can be created between all actors.

10. By transaction security, widely distributed structure can prevent hacking, vulnerability, compliance with government rules and contract disputes [22].

11. Blockchain is less prone to identity fraud [34,51].

12. Elimination of fraudulent and unethical transactions and errors in processes is possible with blockchain and can significantly reduce human errors [52].

13. With the traceability of blockchain technology, it can be easily applied in the logistics industry and the control of products, materials, data and processes with blockchain will make great contributions to the logistics industry [32,49].

14. It allows companies to improve their supplier selection process [3].

15. It helps them improve the purchasing function [53].

16. It has significant potential to increase efficiency throughout the logistics process and help resolve disputes in the logistics industry [42-44, 50].

17. The more stable the product planning and management is, and the more customers' expectations are met, the more uncertainty-related problems in the entire logistics system can be resolved.

18. It can significantly reduce production and logistics costs, additional costs, transportation costs [4, 45, 52].

19. It helps to track and verify sustainability values, performance in product history [10, 54, 55].

20. It can help implement physical networks for sustainable logistics [56].

21. Blockchain technology can play an important role in tackling climate change by improving carbon emissions, promoting clean energy trade, and increasing climate finance flows with optimum transport management [57].

22. The quality of life in the water can be increased by reducing the waiting time and carrying out the port

logistics in regular voyages and with the optimum occupancy rate.

23. In the logistics industry, blockchain technology can significantly reduce time delays [52].

24. Integrating the supply chain with the blockchain enables increased sustainability with improved product transportation and inventory management [52].

25. It supports the decision making of the logistics operators and enables them to make quick decisions.

26. Data stored on the blockchain is practically immutable due to the need for verification by other nodes and traceability of changes [24, 58].

27. There is process integrity. Users can be sure that the actions described in the protocol are performed correctly and in a timely manner without the need for human intervention [48].

28. It has anonymity, while data transfer takes place between nodes, the identity of the individual remains anonymous [24]. There is also the protection and registration of intellectual property [42-44, 50].

29. The source is always clear. Every product has a digital record on the blockchain proving its authenticity and origin [24].

30. Managing data in the supply chain is becoming more systematic. While calibrating the data, the security of the data increases [42-44, 50].

31. Each of the transactions on the blockchain is verified and recorded with a timestamp. Thus, any user in the network can easily monitor previous records by accessing any node in the distributed network [48, 59].

5.2. Weaknesses

1. There will also be delays in the block production process when large amounts of data are stored. This indicates that it has low performance [60,61].

2. It is emphasized that it is very difficult to change and upgrade the structure and architecture of the blockchain after implementation. It has a complex structure [59,62].

3. Regarding energy consumption, it has been argued that the amount of energy consumed by network nodes and the cost of hardware required to validate new blocks are extremely high [63].

5.3. Opportunities

1. Blockchain technology also creates effective opportunities for optimizing time as well as the cost associated with business documentation and administrative procedures.

2. Eliminating the problems encountered in issues such as insurance, delivery, document management and payment will be eliminated with this technology and will provide a competitive advantage [64-65].

3. It has the ability to potentially improve the environment and significantly increase sustainability

4. Increased cooperation and trust between parties is likely due to data becoming more transparent [26, 43, 52, 66].

5. Blockchain can accelerate the digitization agenda in the industry [59, 65].

5.4. Threats

1. There are barriers to adoption in areas such as data ownership and quality, privacy concerns, technology challenges, and overall integration of sustainability goals [67].

2. It is not yet understood as a new technology [68-70]. Blockchain technology needs to be further developed and understood to unlock its true potential.

3. There is no data privacy on public blockchains. Since there is no privileged user system, every user on the blockchain can access all the information on the blockchain [61]. Such users who are concerned about data privacy should prefer private blockchains [61, 71-72-73].

4. There may be an integration problem [51,72]. Businesses must procure or develop blockchain-based solutions that interoperate with their existing legacy systems or transform their existing systems to be blockchain compatible.

5. Fluctuations in cryptocurrencies, which can become a limitation in accepting blockchain-based payments, can pose a problem [73].

6. The ambiguous legal situation is confusing and obstructive [72]. Regulators have yet to catch up with blockchain innovation, which negatively impacts blockchain adoption by businesses across industries. Digital currencies implementing blockchain have struggled to grant support due to the lack of government and regulatory support [74].

The strengths in the analysis show how the blockchain excels over other traditional methods. In other words, they are the features that make the blockchain advantageous in competition. Weaknesses are also noted, showing how other methods are more obvious than blockchain to provide an objective view. Opportunities and threats show the potential benefits and disadvantages that the external environment can bring to the subject.

6. Conclusion

Digitalization solutions have been entering the sectors with an increasing effect in recent years. Although the newest technology, the blockchain technology, has made a name for itself with the use of crypto money, it is now used in the management of business in many areas. Increasing technological solutions and sectors' interest in these technologies, as well as their compatibility, come to the fore. In blockchain technology, the transaction history is created through a series of linked blocks that can be easily traced through blocks that make the technology transparent and reliable, increasing the trust of the industries in this technology. In particular, its compatibility with companies operating in logistics is discussed in this study. Blockchain has enormous potential for many activities in the functioning from the supplier to the consumer, from the receipt of the order to the delivery of the right product, in the right quantity, in the right conditions, in the right location and at the right time.

From this point of view, in the current study, blockchain applications in the logistics sector were discussed under the title of sustainability and striking strengths were revealed with SWOT analysis. First of all, by talking about what blockchain technology is, its compatibility with supply chain management, which is a logistics and sub-activity related to blockchain, was investigated with a detailed literature review study. In addition, sustainability studies, which are becoming increasingly important and that we are obliged to implement in all areas of our lives, have been examined. The contribution of blockchain technology in terms of sustainable logistics has been shared through SWOT analysis. At this point, the strengths that will require the use of blockchain technology in the logistics sector are as follows; decentralized structure, effective information sharing, fast response, reliable, robust risk management, inter-process integrity, high security measures, systematic data management, anonymous, auditability, transparent, strong relationship between stakeholders, less hacking, tampering, less errors and delay, high efficiency, low cost, sustainability-based, unchanging data. The weak points are as follows; low performance, complex structure and high energy consumption problem. In addition, the opportunities for the sector are as follows; optimizing time, gaining competition by eliminating problems, the ability to increase sustainability, increasing cooperation between stakeholders, increasing trust between parties, transition to digitalization. On the other hand, like every technology, it has external threats; Cross-integration adoption, new technology, limited data privacy, integration compatibility with other technologies, volatility in cryptocurrencies, Uncertain legal situation. As a result, its potential contribution to the logistics sector is undeniably important. In this study, by evaluating the perspective in the literature, it has contributed to the development of blockchain applications in the logistics sector.

After this study, which is considered on the basis of a proposal for future studies, the compatibility of blockchain technology with the logistics sector, an analysis can be carried out on different sectors (Food, energy, etc.). With the findings obtained, field research can be made and an evaluation can be made on a company basis. In this way, inter-sectoral gain can be achieved with accurate and reliable transfer with blockchain technology.

Conflicts of interest

The authors declare no conflicts of interest.

References

1. Goyat, R., Kumar, G., Rai, M. K., Saha, R., Thomas, R., & Kim, T. H. (2020). Blockchain Powered Secure Range-Free Localization in Wireless Sensor Networks. *Arabian Journal for Science and Engineering*, 45(8), 6139-6155.

2. Babich, V., & Hilary, G. (2020). OM Forum— Distributed ledgers and operations: What operations management researchers should know about blockchain technology. *Manufacturing & Service Operations Management*, 22(2), 223-240.
3. Kouhizadeh, M., & Sarkis, J. (2018). Blockchain practices, potentials, and perspectives in greening supply chains. *Sustainability*, 10(10), 3652.
4. Chang, S. E., Chen, Y. C., & Lu, M. F. (2019). Supply chain re-engineering using blockchain technology: A case of smart contract-based tracking process. *Technological Forecasting and Social Change*, 144, 1-11.
5. Swan, M. (2015). *Blockchain: Blueprint for a new economy*. "O'Reilly Media, Inc."
6. Nakamoto, S., & Bitcoin, A. (2008). A peer-to-peer electronic cash system. Bitcoin.–URL: <https://bitcoin.org/bitcoin.pdf>, 4,2.
7. Queiroz, M. M., Telles, R., & Bonilla, S. H. (2019). Blockchain and supply chain management integration: a systematic review of the literature. *Supply Chain Management: An International Journal*.
8. Rodrigues, U. R. (2018). Law and the Blockchain. *Iowa L. Rev.*, 104, 679.
9. Tektaş, B., & Kırbaç, G. (2020). Lojistik sektöründe blokchain teknolojisinin kullanılmasına yönelik bir vaka analizi incelemesi ve lojistik şirketi uygulaması. *Süleyman Demirel Üniversitesi İktisadi ve İdari Bilimler Fakültesi Dergisi*, 25(3), 343-356.
10. Kshetri, N. (2018). 1 Blockchain's roles in meeting key supply chain management objectives. *International Journal of Information Management*, 39, 80-89.
11. Agrawal, T. K., Kumar, V., Pal, R., Wang, L., & Chen, Y. (2021). Blockchain-based framework for supply chain traceability: A case example of textile and clothing industry. *Computers & industrial engineering*, 154, 107130.
12. Ronaghi, M. (2020). A Blockchain Maturity Model in Agricultural Supply chain. *Information Processing in Agriculture*, 1-25.
13. Katsikouli P. and Wilde A. S. (2020), On the Perks and Challenges of Blockchain Technology for Managing Food Supply Chains, Reports, https://backend.orbit.dtu.dk/ws/portalfiles/portal/212676157/Blockchain_in_the_Food_Sector_1.2.pdf.
14. Reddy, K. R. K., Gunasekaran, A., Kalpana, P., Sreedharan, V. R., & Kumar, S. A. (2021). Developing a Blockchain Framework for the Automotive Supply Chain: A systematic Review. *Computers & Industrial Engineering*, 107334.
15. Di Vaio, A., & Varriale, L. (2020). Blockchain technology in supply chain management for sustainable performance: Evidence from the airport industry. *International Journal of Information Management*, 52, 102014.
16. Yadav, S., & Singh, S. P. (2020). Blockchain critical success factors for sustainable supply chain. *Resources, Conservation and Recycling*, 152, 104505.
17. Sunmola, F., & Apeji, D. U. (2020). Blockchain Characteristics for Sustainable Supply Chain Visibility. In 5th NA International Conference on Industrial Engineering and Operations Management, Detroit, Michigan, USA.
18. Kouhizadeh, M., Saberi, S., & Sarkis, J. (2021). Blockchain technology and the sustainable supply chain: Theoretically exploring adoption barriers. *International Journal of Production Economics*, 231, 107831.
19. Tsolakakis, N., Niedenzu, D., Simonetto, M., Dora, M., & Kumar, M. (2021). Supply network design to address United Nations Sustainable Development Goals: A case study of blockchain implementation in Thai fish industry. *Journal of Business Research*.
20. Esmailian, B., Sarkis, J., Lewis, K., & Behdad, S. (2020). Blockchain for the future of sustainable supply chain management in Industry 4.0. *Resources, Conservation and Recycling*, 163, 105064.
21. Diffie, W., & Hellman, M. (1976). New directions in cryptography. *IEEE transactions on Information Theory*, 22(6), 644-654.
22. Min, H. (2019). Blockchain technology for enhancing supply chain resilience. *Business Horizons*, 62(1), 35-45.
23. França, A. S. L., Neto, J. A., Gonçalves, R. F., & Almeida, C. M. V. B. (2020). Proposing the use of blockchain to improve the solid waste management in small municipalities. *Journal of Cleaner Production*, 244, 118529.
24. Dutta, P., Choi, T. M., Somani, S., & Butala, R. (2020). Blockchain technology in supply chain operations: Applications, challenges and research opportunities. *Transportation Research Part E: Logistics and Transportation Review*, 142, 102067.
25. Yli-Huumo, J., Ko, D., Choi, S., Park, S., & Smolander, K. (2016). Where is current research on blockchain technology?—a systematic review. *PloS one*, 11(10), e0163477.
26. Hawlitschek, F., Notheisen, B., & Teubner, T. (2018). The limits of trust-free systems: A literature review on blockchain technology and trust in the sharing economy. *Electronic commerce research and applications*, 29, 50-63.
27. Liu, M., Yu, F. R., Teng, Y., Leung, V. C., & Song, M. (2019). Performance optimization for blockchain-enabled industrial Internet of Things (IIoT) systems: A deep reinforcement learning approach. *IEEE Transactions on Industrial Informatics*, 15(6), 3559-3570.
28. Qiao, R., Zhu, S., Wang, Q., & Qin, J. (2018). Optimization of dynamic data traceability mechanism in Internet of Things based on consortium blockchain. *International Journal of Distributed Sensor Networks*, 14(12), 1550147718819072.
29. Danyal D., 2020 <https://devrimdanyal.medium.com/lojistikte-blockchain-ile-m%C3%BCkemmeli%C4%9Ffeula%C5%9Fmak-114a4468fa7e>
30. Van Engelenburg, S., Janssen, M., & Klievink, B. (2018, July). A blockchain architecture for reducing the bullwhip effect. In *International Symposium on Business Modeling and Software Design* (pp. 69-82). Springer, Cham.
31. Hackius, N., & Petersen, M. (2017). Blockchain in logistics and supply chain: trick or treat?. In *Digitalization in Supply Chain Management and Logistics: Smart and Digital Solutions for an Industry*

- 4.0 Environment. Proceedings of the Hamburg International Conference of Logistics (HICL), Vol. 23 (pp. 3-18). Berlin: epubli GmbH.
32. Akram, A., & Bross, P. (2018). Trust, Privacy and Transparency with Blockchain Technology in Logistics. In MCIS (p. 17).
33. Awaysheh, A., & Klassen, R. D. (2010). The impact of supply chain structure on the use of supplier socially responsible practices. *International Journal of Operations & Production Management*.
34. Sadouskaya, K. (2017). Adoption of blockchain technology in supply chain and logistics.
35. Schinckus, C. (2020). The good, the bad and the ugly: An overview of the sustainability of blockchain technology. *Energy Research & Social Science*, 69, 101614.
36. Hwang, J. M.-I. Choi, T. Lee, S. Jeon, S. Kim, S. Park, S. Park, Energy prosumer business model using blockchain system to ensure transparency and safety, *Energy Procedia* 141 (2017) 194–198, <https://doi.org/10.1016/j.egypro.2017.11.037>.
37. Andersen, B. (2007). Business process improvement toolbox. Quality Press.
38. Gould, R. (2012). Creating the strategy: Winning and keeping customers in B2B markets. Kogan Page Publishers.
39. Ağaoğlu, E., Şimşek, Y., & Altınkurt, Y. (2006). Endüstri meslek liselerinde stratejik planlama öncesi SWOT analizi uygulaması. *Eğitim ve Bilim*, 31(140).
40. Ülgen, H., & Mirze, S. K. (2007). *Çözümlerinde stratejik yönetim*. Arıkan Basım Yayın Dağıtım, 4.
41. Litke, A., Anagnostopoulos, D., & Varvarigou, T. (2019). Blockchains for supply chain management: Architectural elements and challenges towards a global scale deployment. *Logistics*, 3(1), 5.
42. Wang, Y., Han, J. H., & Beynon-Davies, P. (2019). Understanding blockchain technology for future supply chains: a systematic literature review and research agenda. *Supply Chain Management: An International Journal*.
43. Saberi, S., Kouhizadeh, M., Sarkis, J., & Shen, L. (2019). Blockchain technology and its relationships to sustainable supply chain management. *International Journal of Production Research*, 57(7), 2117-2135.
44. Shamout, M. (2019). Understanding blockchain innovation in supply chain and logistics industry. *International journal of innovative technology and exploring engineering*, 8 (6), 309-315.
45. Liang, W., Tang, M., Long, J., Peng, X., Xu, J., & Li, K. C. (2019). A secure fabric blockchain-based data transmission technique for industrial Internet-of-Things. *IEEE Transactions on Industrial Informatics*, 15(6), 3582-3592.
46. Wu, J., & Tran, N. K. (2018). Application of blockchain technology in sustainable energy systems: An overview. *Sustainability*, 10(9), 3067.
47. Sheel, A., & Nath, V. (2019). Effect of blockchain technology adoption on supply chain adaptability, agility, alignment and performance. *Management Research Review*.
48. Abeyratne, S. A., & Monfared, R. P. (2016). Blockchain ready manufacturing supply chain using distributed ledger. *International Journal of Research in Engineering and Technology*, 5(9), 1-10.
49. Saberi, S., Kouhizadeh, M., Sarkis, J., 2018. Blockchain technology: A panacea or pariah for resources conservation and recycling? *Resour. Conserv. Recycl.* 130, 80–81. <https://doi.org/10.1016/j.resconrec.2017.11.020>
50. Narayanaswami, C., Nooyi, R., Govindaswamy, S. R., & Viswanathan, R. (2019). Blockchain anchored supply chain automation. *IBM Journal of Research and Development*, 63(2/3), 7-1.
51. Kshetri, N. (2017). Potential roles of blockchain in fighting poverty and reducing financial exclusion in the global south.
52. Tijan, E., Aksentijević, S., Ivanić, K., & Jardas, M. (2019). Blockchain technology implementation in logistics. *Sustainability*, 11(4), 1185.
53. Rane, S. B., & Thakker, S. V. (2019). Green procurement process model based on blockchain-IoT integrated architecture for a sustainable business. *Management of Environmental Quality: An International Journal*.
54. Cui, P., Dixon, J., Guin, U., & Dimase, D. (2019). A blockchain-based framework for supply chain provenance. *IEEE Access*, 7, 157113-157125.
55. Xu, M., Chen, X., & Kou, G. (2019). A systematic review of blockchain. *Financial Innovation*, 5(1), 1-14.
56. Meyer, T., Kuhn, M., & Hartmann, E. (2019). Blockchain technology enabling the Physical Internet: A synergetic application framework. *Computers & Industrial Engineering*, 136, 5-17.
57. Green, J. Solving The Carbon Problem One Blockchain at A Time. *Forbes*, 2018. Retrieved from <https://www.forbes.com/sites/jemmagreen/2018/09/19/solvingthe-carbon-problem-one-blockchain-at-a-time/#1992bb415f5e>.
58. Bogart S. and K. Rice, "The Blockchain Report: Welcome to the Internet of Value," 2015.
59. Wang, J., Wu, P., Wang, X., & Shou, W. (2017). The outlook of blockchain technology for construction engineering management. *Frontiers of engineering management*, 4(1), 67-75.
60. Lo, S. K., Xu, X., Chiam, Y. K., & Lu, Q. (2017). Evaluating suitability of applying blockchain. Paper presented at the 2017 22nd International Conference on Engineering of Complex Computer Systems (ICECCS).
61. Lu, Q., & Xu, X. (2017). Adaptable blockchain-based systems: A case study for product traceability. *IEEE Software*, 34(6), 21-27.
62. Drescher, D. (2017), *Blockchain basics: a non-technical introduction in 25 steps*, 1st edn, Apress, Berkeley, California.
63. Stilgherrian. (2016), Let's quit the blockchain magic talk. Available online: <http://www.zdnet.com/article/lets-quit-the-blockchain-magic-talk/>
64. Liu, X.; Zhao, M.; Li, S.; Zhang, F.; Trappe, W. (2017) A Security Framework for the Internet of Things in the Future Internet Architecture. *Future Internet*,
65. Tezel, A., Papadonikolaki, E., Yitmen, I., & Hilletoft, P. (2019). Preparing Construction Supply Chains for Blockchain: An Exploratory Analysis. In *CIB World*

- Building Congress Constructing Smart Cities, Hong Kong, China, (Vol. 6).
66. Winfield, M. (2018). Erişim: 01 Nisan 2019, The Legal Frontier: Blockchain and Smart Contracts. In BIMPlus. <http://www.bimplus.co.uk/management/legal-frontier-blockchain-and-smart-contracts/>.
67. Kamble, S., Gunasekaran, A., & Arha, H. (2019). Understanding the Blockchain technology adoption in supply chains-Indian context. *International Journal of Production Research*, 57(7), 2009-2033.
68. Hughes, L., Dwivedi, Y. K., Misra, S. K., Rana, N. P., Raghavan, V., & Akella, V. (2019). Blockchain research, practice and policy: Applications, benefits, limitations, emerging research themes and research agenda. *International Journal of Information Management*, 49, 114-129.
69. Johansson, J., & Nilsson, C. (2018). How the blockchain technology can enhance sustainability for contractors within the construction industry
70. Mendling, J., I. Weber, W. van der Aalst, J. V. Brocke, C. Cabanillas, F. Daniel, and S. Dustdar. (2017). Blockchains for Business Process Management- Challenges and Opportunities. *ACM Transactions on Management Information Systems (TMIS)*, 9(1), 1-16.
71. Nanayakkara, S., Perera, S., & Senaratne, S. (2019). Stakeholders' Perspective on Blockchain and Smart Contracts Solutions for Construction Supply Chains. Paper presented at the CIB World Building Congress.
72. Niranjnamurthy, M., Nithya, B., & Jagannatha, S. (2019). Analysis of blockchain technology: pros, cons and SWOT. *Cluster Computing*, 22(6), 14743-14757.
73. Gatteschi, V., Lamberti, F., Demartini, C., Pranteda, C., & Santamaría, V. (2018). Blockchain and smart contracts for insurance: Is the technology mature enough? *Future Internet*, 10(2), 20.
74. Christopher, C. M. (2014). Whack-a-Mole: Why Prosecuting Digital Currency Exchanges Won't Stop Online Laundering. *Lewis & Clark L. Rev.* 18, 20-25.



© Author(s) 2023. This work is distributed under <https://creativecommons.org/licenses/by-sa/4.0/>



A parametric study on the dynamic lateral earth forces on retaining walls according to European and Turkish Building Earthquake Codes

Özgür Lütfi Ertuğrul^{*1}, Babür Bek Zahin¹

¹Mersin University, Civil Engineering Department, Türkiye

Keywords

Seismic acceleration coefficient
Soil friction angle
Lateral earth forces
Retaining Structures

Research Article

DOI: 10.31127/tuje.1100015

Received: 07.04.2022

Accepted: 09.05.2022

Published: 31.08.2022

Abstract

In the earthquake regulations of many countries, Mononobe-Okabe method was used to determine the seismic lateral earth forces and earth pressure coefficients for the design of retaining structures. However, there are various interpretation differences of this method between earthquake regulations of different countries. In this study, effect of different seismic acceleration coefficients (S_{DS}) and different soil friction angles (ϕ'_d) on the seismic earth forces acting on a high retaining structure were investigated through a parametric study based on the methods described in 2018 Turkish Building Earthquake Code (TBEC-2018) and EuroCode-8 (EC-8). For this purpose, approximately 120 analyzes were carried out by using different parameters and the analysis results were shown in tables and figures. Analyses were performed for yielding rigid retaining walls and anchored walls for the principles defined in the mentioned earthquake codes. It was observed that the seismic lateral force estimations made with TBEC-2018 are higher compared to values calculated according to EuroCode-8. In the calculation of dynamic thrust, unexpected results may occur at some critical values of θ angle which is dependent on the lateral acceleration coefficient.

1. Introduction

Earth retaining structures play an important role in the modern civil engineering infrastructure. In addition to static loads, additional earth forces can affect to the retaining walls during earthquakes. In order to design the retaining structures safely with the rules stipulated in different earthquake codes, dynamic loads created by earthquakes should be taken into account in addition to the static loads. However, due to the complicated nature of soils, it is very difficult to realistically predict the seismic behavior of the retaining structures and to perform an analysis with a loading method with many variables and many unknowns, such as seismic forces and soil inhomogeneity. Therefore, for the estimation of dynamic soil thrust forces, simplified models having different assumptions about soil, wall and ground acceleration should be made in order to be able to analyze the dynamics of the retaining structures under the seismic effect [1]. The effect of seismic loads on the retaining structures depends on the inertia of the structure, the behavior of the soil under the wall and the backfill, the characteristics of the seismic motion that

occur such as the amplitude and frequency of the dynamic load and the natural period of the retaining structure-backfill-foundation subsoil. Besides, retaining wall-soil interaction should be taken into account. Due to the earthquakes that occurred in 1923 in Japan and the collapse of many retaining walls after earthquakes, Okabe [2] and Mononobe- Matsuo [3] explained that the soil pressure can increase with the effect of earthquakes. So called “Mononobe-Okabe Method” is a refinement of the static Coulomb theory in quasi-static conditions. In the Mononobe-Okabe analysis which is basically recommended for dry cohesionless soils, the additional forces that occur due to the effect of horizontal and vertical accelerations in the Coulomb active or passive wedge are calculated and the force balance is rewritten accordingly to obtain the quasi-static soil force [4-5]. The Mononobe-Okabe method has been a reference point for quasi-static methods developed later, and has been included in many regulations including 2018 Turkey Building Earthquake Code (TBEC-2018) [6] and EuroCode8 – Chapter 5. For this reason, it is known that the formulas of TBEC-2018 and EC-8 Chapter 5 are very

* Corresponding Author

(ertugrul@mersin.edu.tr) ORCID ID 0000-0002-1270-3649
(baburbekzahin786@gmail.com) ORCID ID 0000-0001-8362-0667

Cite this article

Ertugrul, Ö. L., & Zahin, B. B. (2023). A parametric study on the dynamic lateral earth forces on retaining walls according to European and Turkish Building Earthquake Codes. Turkish Journal of Engineering, 7(3), 196-207

similar and the results obtained from the analyzes are in good harmony [7].

Eurocode 8 (2004) [8] regulation applies to European Union countries. In this regulation, an equivalent static method is proposed for the earthquake-proof design of retaining structures. With the publication of the (TBEC-2018), it has been observed that new sections have been added and many changes have been made in the section related to the retaining structures in the previous regulation on Buildings to be Constructed in Earthquake Zones (DBYH,2007) [9]. For the earth retaining structures, the calculation of horizontal and vertical static-equivalent earthquake coefficients is now being calculated according to the earthquake acceleration coefficients (S_{DS}) which can be obtained from the new interactive earthquake map of Turkey. In addition, to obtain horizontal and vertical static-equivalent seismic coefficients, the earthquake acceleration coefficient (S_{DS}) can be obtained from the Turkey Earthquake Map (TBEC-2018) which is currently available in [10].

2. Method

Previous Turkish Earthquake Code (TBEC-2007) classifies Turkey into different earthquake zones according to their seismicity and provides the necessary calculation, design and construction rules for the structures in these regions for stability, sufficient strength, durability, rigidity and ductility [11]. Similar philosophy of design is considered in new Turkey Building Earthquake Code 2018 however, earthquake zones approach is replaced with more realistic coordinate-based earthquake parameter maps. In earthquake codes that include earthquake engineering and its practical applications, it is known that structures are not damaged in small earthquakes, the damage to non-structural parts is accepted in medium-sized earthquakes, and structures are damaged beyond repair in large earthquakes, but they are prevented from complete collapse. According to the results obtained from new researches, necessary changes are made in earthquake regulations. The Turkish Earthquake Code has been updated and changed many times until now. In the Turkish Building Earthquake Regulation (TBEC-2018), which entered into force in 2018, it is foreseen that the dynamic soil thrust force will be calculated by the Mononobe-Okabe method. On the other hand, in TBEC-2018, the distributed loads, static and dynamic water forces are included in the calculations, and effect of vertical static-equivalent seismic coefficients (k_v) in gravity direction should also be investigated. The largest of the two soil thrust forces found will give the soil thrust forces to be used in the design. Although the Mononobe-Okabe analysis indirectly indicates that the point on which the total active thrust acts is $H/3$ above the base of the wall having height of H , empirical findings show that the point at which this force acts is higher under dynamic loading conditions. According to TBEC-2018 and EC-8 regulations, the application point of the resultant thrust force will be taken as the midpoint of the wall height ($h=H/2$) for dynamic soil pressures. In this study, approximately 120 analyzes were performed in Excel

computer program by using different earthquake acceleration coefficients (S_{DS}) and soil internal friction angle (ϕ'_d) based on the methods mentioned above for a parametric study. Analysis results are shown in tables and figures.

The terminology and flowchart used in the design of the retaining structures according to the 2018 Turkish Earthquake Code (TBEC-2018) and EuroCode 8 (EC-8), which are currently in force, are given in Figure 1 and Figure 2, respectively. In these forms; k_h and k_v are horizontal and vertical static-equivalent earthquake coefficient, S_{DS} is the design spectral acceleration coefficient (earthquake acceleration coefficient), r is the design coefficient, S_s is the map spectral acceleration coefficient for short period, F_s is the local ground effect coefficient, P_{water} and ΔP_{water} are resultant static and dynamic water pressures, θ is the angle (an angle that depends on horizontal and vertical earthquake coefficients.), γ^* is the soil unit weight, γ is the soil natural unit weight, γ_d is the saturated soil unit weight, γ_{water} is the water unit weight, d_{water} is the submerged height of the wall, β is the angle of inclination of the soil surface behind the wall with respect to the horizontal, ϕ'_d is the design friction resistance angle of the soil (the angle of internal friction of the soil), ψ is the angle of the wall with respect to the horizontal (from the horizontal in front of the wall to the back of the wall), δ_d is the angle of friction between the wall and the soil, K is the total (static+dynamic) earth pressure coefficient, K_a is the active earth pressure coefficient, K_p is the passive earth pressure coefficient, H is the wall height, q surcharge load, P_t is the total static force, P_s is the static and P_d is the dynamic force acting on retaining walls, α is the ratio of design acceleration to gravitational acceleration, S is the soil factor, a_{vg} vertical component of design ground surface acceleration, a_g is the design ground surface acceleration, E_{ws} is the static water pressure, E_{wd} is the hydrodynamic water pressure, γ is the saturated soil unit volume weight, γ_{dry} is the dry unit weight of the soil, H_w is the height of the submerged wall, γ_ϕ is a coefficient for the backfill soil, E_t is the total static force, E_s is the static force and E_d is the dynamic soil thrust acting on the retaining walls. Values of the soil parameters are given in Table 1. A simplified drawing is provided in Figure 3 to depict the angles and the forces acting on the gravity retaining wall.

3. Parametric Analyses

Considering the soil parameters given above, anchored and gravity-type earth retaining structures that can allow displacements were analyzed using the Excel computer program according to the methodology proposed by the TBEC-2018 and EC-8 Regulations.

Obtained static and dynamic thrust forces are summarized in Table 2 to Table 5. Results show that internal friction angle of the soil, ϕ'_d , is an important factor on the horizontal static and dynamic thrust forces acting on the wall. In these tables, K_{as} denotes the static lateral earth pressure coefficient, P_{as} denotes the static lateral force, K_{ad} is the dynamic lateral earth pressure coefficient, E_{ad} is the dynamic earth thrust calculated

according to EC-8 and P_{ad} is the dynamic earth thrust calculated according to TBEC-2018.

In addition, it is seen that the short period design spectral acceleration coefficients (S_{DS}) and the θ angle which is dependent on these coefficients are effective in

the static and dynamic active soil pressure coefficients and the horizontal static and dynamic active thrust forces acting on the wall. As the earthquake acceleration coefficient (S_{DS}) values increase, the horizontal dynamic active thrust forces acting on the wall also increase.

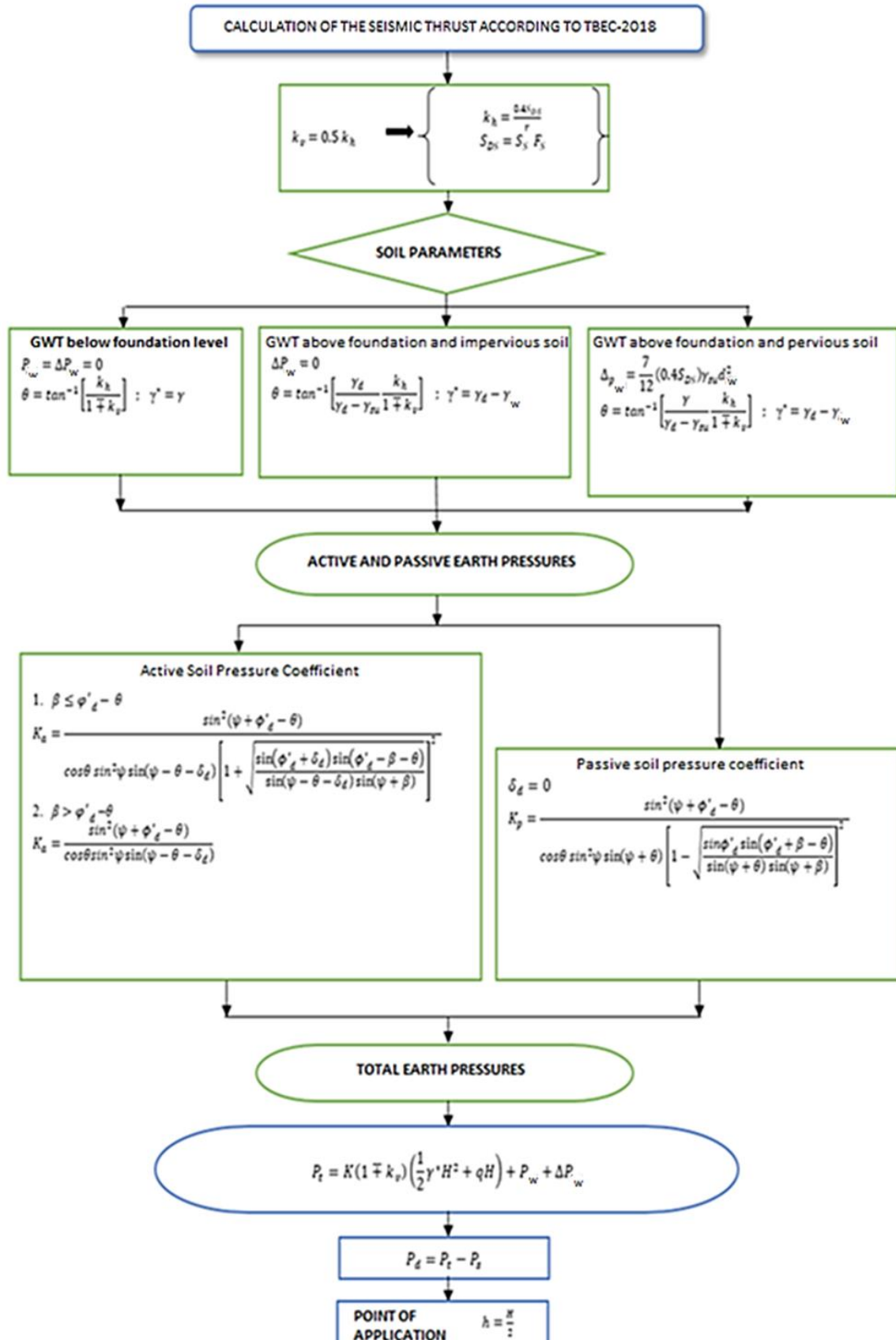


Figure 1. Design Schema according to TBEC-2018

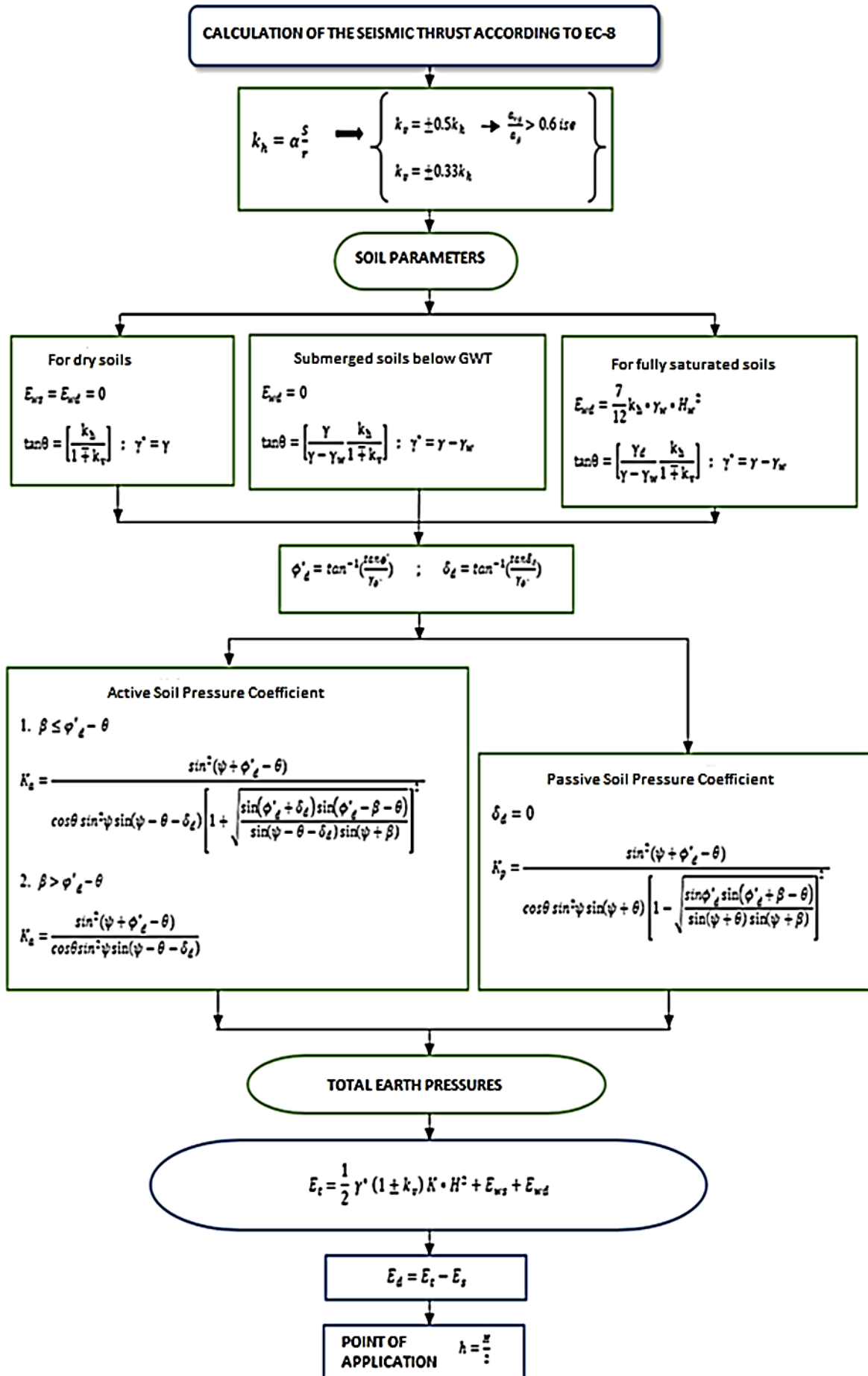


Figure 2. Design Schema according to EC-8

Table 1. Soil parameters

Explanation	Symbol	Value	Unit
Wall Height	H	12	m
Natural Unit Weight of Soil	γ^*	18	kN/m^3
Saturated Unit Weight of Soil	γ_d	21	kN/m^3
Unit weight of water	γ_{water}	10	kN/m^3
Surcharge load	q_s	-	kN/m^2
Angle of the wall surface with horizontal	ψ	90	$^\circ$
Internal angle of friction of the soil	φ'_d	20	$^\circ$
		30	$^\circ$
		40	$^\circ$
Friction angle between soil and wall	δ_d	17	$^\circ$
Angle of the backfill surface with horizontal	β	0	$^\circ$
Angle of wall surface with vertical	θ^*	-	$^\circ$
Permeability coefficient	k_x	10^{-3}	m/sn
Permeability coefficient (Impervious Soils)	k_x	10^{-6}	m/sn

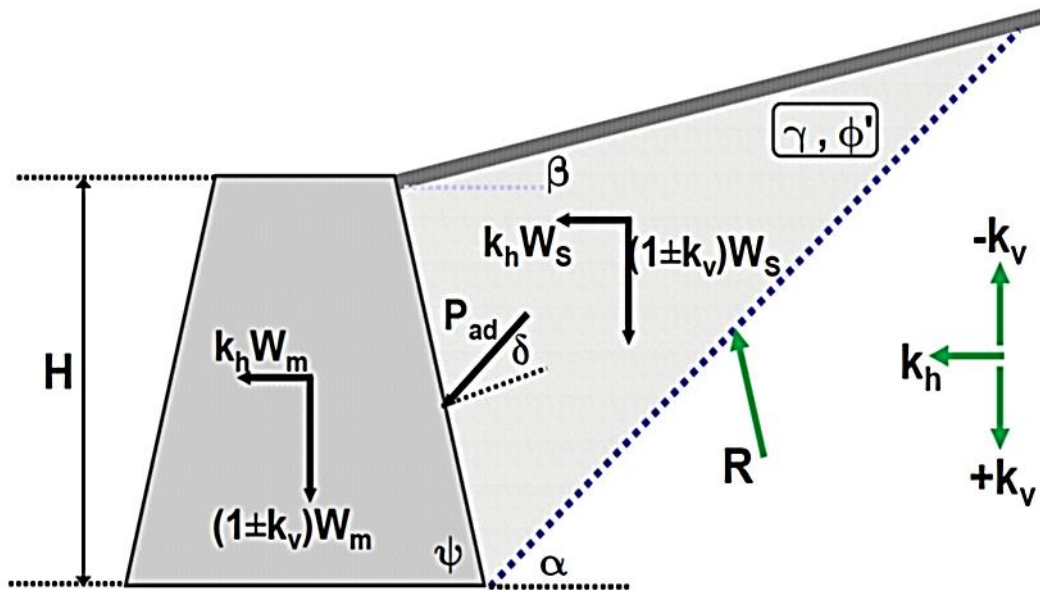


Figure 3. A simplified drawing for the gravity retaining wall (Eurocode-8)

Table 2. A comparison of lateral dynamic earth pressures for anchored walls ($r = 1$) with impermeable backfill

φ'_d	Static			Acceleration Coefficients				θ	K_{ad}	E_{ad} (kN/m)	P_{ad} (kN/m)
	K_{as}	P_{as} (kN/m)	S_{DS}			θ					
				k_h	k_v						
20	0.431	558.387	0.5	0.2	0.1	22.989°	0.983	509.466	610.469		
			0.75	0.3	0.15	33.972°	1.372	715.579	847.811		
			1	0.4	0.2	43.668°	1.936	1001.523	1177.079		
			1.25	0.5	0.25	51.843°	2.805	1423.943	1663.503		
			1.5	0.6	0.3	58.571°	4.273	2109.681	2453.139		
30	0.299	388.072	0.5	0.2	0.1	22.989°	0.477	225.249	273.153		
			0.75	0.3	0.15	33.972°	1.606	954.859	1113.311		
			1	0.4	0.2	43.668°	2.365	1360.146	1580.004		
			1.25	0.5	0.25	51.843°	3.564	1966.983	2278.786		
			1.5	0.6	0.3	58.571°	5.636	2962.693	3425.361		
40	0.200	259.440	0.5	0.2	0.1	22.989°	0.329	177.429	210.509		
			0.75	0.3	0.15	33.972°	0.803	475.884	554.183		
			1	0.4	0.2	43.668°	2.610	1581.294	1827.079		
			1.25	0.5	0.25	51.843°	4.096	2352.169	2714.755		
			1.5	0.6	0.3	58.571°	6.7156	3634.415	4191.279		

Table 3. A comparison of lateral dynamic earth pressures for anchored walls ($r = 1$) with permeable backfill

φ'_d	Static			Acceleration Coefficients			θ	EC-8	TBEC-2018
	K_{as}	P_{as} (kN/m)	S_{DS}			K_{ad}		E_{ad} (kN/m)	P_{ad} (kN/m)
				k_h	k_v				
20	0.431	558.387	0.5	0.2	0.1	19.983°	0.862	591.420	679.385
			0.75	0.3	0.15	30.008°	1.212	859.252	975.070
			1	0.4	0.2	39.289°	1.643	1151.698	1299.099
			1.25	0.5	0.25	47.489°	2.273	1527.839	1719.504
			1.5	0.6	0.3	54.513°	3.258	2050.489	2308.616
30	0.299	388.072	0.5	0.2	0.1	19.983°	0.361	310.336	345.677
			0.75	0.3	0.15	30.008°	1.394	1063.999	1200.805
			1	0.4	0.2	39.289°	1.968	1444.542	1626.278
			1.25	0.5	0.25	47.489°	2.826	1948.686	2194.079
			1.5	0.6	0.3	54.513°	4.198	2669.198	3011.033
40	0.200	259.440	0.5	0.2	0.1	19.983°	0.259	296.210	321.832
			0.75	0.3	0.15	30.008°	0.568	569.917	624.282
			1	0.4	0.2	39.289°	1.601	1277.591	1426.452
			1.25	0.5	0.25	47.489°	3.178	2226.991	2506.974
			1.5	0.6	0.3	54.513°	4.891	3127.126	3530.765

4. Results

In Figure 4 and Figure 5, variation of lateral seismic thrust versus S_{DS} values considering different soil internal friction angles for yielding type anchored walls and gravity walls are compared according to Euro Code 8 and 2018 Turkish Building Earthquake Code (TBEC-2018). Analyses were conducted for $\varphi'_d = 20^\circ, 30^\circ, 40^\circ$.

In the previous earthquake code, Turkey is classified into various seismic regions according to their seismicity and the active ground acceleration coefficient takes values between 0.1 and 0.4 according to these regions.

According to TBEC-2018, S_{DS} values can be estimated using the interactive earthquake maps. For this reason, in order to investigate the effect of the earthquake acceleration coefficient (S_{DS}) on the dynamic thrust forces acting on the earth retaining structures, the variation of the earthquake acceleration coefficients and the dynamic thrust forces according to EC-8 and TBEC-2018 regulations are given in Figure 3 for the anchored walls and the gravity walls. It can be observed that lateral dynamic thrust increase as S_{DS} values increase. This increase is mostly linear for low soil internal friction angle values: On the other hand, the relationship between S_{DS} and P_{AD} becomes nonlinear for higher internal friction angle values. As seen in Figure 4, with the increase of earthquake acceleration coefficient (S_{DS}), active dynamic thrust forces acting on the wall increase according to TBEC-2018 and EC-8 regulations.

The results obtained from both regulations (TBEC-2018 and EC-8) exhibits difference from each other. However, in both methods, with the increase of the soil internal friction angle (φ'_d) the active dynamic thrust forces acting on the wall decrease. As can be seen from the figures, anchored walls ($r=1$) are exposed to greater dynamic soil thrust forces than the gravity-type retaining structures ($r=1.5$) with allowed displacements. With the increase of

earthquake acceleration coefficient (S_{DS}) in dynamically impermeable soils, retaining structures are exposed to greater dynamic soil forces compared to permeable soils. Although additional dynamic water forces are taken into account in dynamically permeable soils, the water behind the wall flows towards the back of the wall and it is thought that the wall is less exposed to the water force. However, anchored walls ($r=1$) are exposed to greater dynamic soil thrust forces than gravity-type yielding retaining structures ($r=1.5$). The reason of this behavior can be considered as the limited displacements of the backfill soils due to the presence of ground anchors. The limited deformations in the soil does not let the soil strength to be fully mobilized. This will increase the lateral dynamic thrust acting on the retaining structure.

Figure 6 and Figure 7 depict the distribution of horizontal dynamic active thrust forces acting on the wall versus soil internal friction angle (φ'_d) for different earthquake acceleration coefficients ($S_{DS}=0.5, 0.75, 1, 1.25$ and 1.5) in anchored walls and gravity type walls according to Euro Code 8 and 2018 Turkish Earthquake Code.

As can be seen from these figures, with the decrease of the soil internal friction angle (φ'_d), the active dynamic thrust forces acting on the wall increase according to TBEC-2018 and EC-8 regulations, and the results obtained from both regulations (TBEC-2018 and EC-8) are similar. The results obtained from the analyzes show that the anchored walls ($r=1$) can be subjected to greater dynamic soil thrust forces than the gravity retaining structures ($r=1.5$).

It is known that the soil internal friction angle (φ'_d) has an inverse relationship with the horizontal thrust force acting on the wall. It is predicted that the horizontal thrust forces acting on the wall will decrease with the increase of the internal friction angle (φ'_d) (Figure 6a, f and Figure 7a, b, g, h, i). Since different internal friction angles were used in the

parametric analyses, calculations were performed by using the formulas suggested for $(\beta \leq \phi'_d - \theta)$ and $(\beta > \phi'_d - \theta)$ cases according to EC-8 and TBEC-2018. With the increase of the internal friction angle (ϕ'_d), the horizontal thrust force acting on the wall increases up to a certain angle (ϕ'_d) and it is seen that the dynamic thrust forces decrease with the increase in the angle (ϕ'_d) which can be observed in Figure 6b, g, h and Figure 6c, d, f, j). However, only the second case $(\beta > \phi'_d - \theta)$ formula is used in Figures 7c, d, e, i and Figure 7e. With the increase in the earthquake acceleration coefficient (S_{DS}), the angle, which depends

Figure 6c, d, f, j). However, only the second case $(\beta > \phi'_d - \theta)$ formula is used in Figures 7c, d, e, i and Figure 7e. With the increase in the earthquake acceleration coefficient (S_{DS}), the angle, which depends

on the horizontal and vertical earthquake coefficients also increases. In calculating the value of the active soil pressure coefficient, the formula for

the first case $(\beta \leq \phi'_d - \theta)$ does not yield results if the angle θ , which depends on the horizontal and vertical earthquake coefficients, exceeds a certain soil internal friction angle.

Therefore, both regulations propose the formula for the second case $(\beta > \phi'_d - \theta)$ to calculate active soil pressure. To be able to determine the active soil pressure, it is necessary to make calculations based on the second situation $(\beta > \phi'_d - \theta)$ according to TBEC 2018 and EC-8, and there is a discrepancy between the results for the values where different formulas are being used. In other words, it was seen that use of the first and second formulas together in the calculation of the active soil pressure coefficient may cause numerical inconsistency thus affecting the results. This leads to the calculation of different dynamic earth pressure values, due to use of different formulas. This is found to be unrealistic and may be considered as a short coming of the TBEC-2018 procedure for the seismic design of the retaining walls.

Table 4. A comparison of lateral dynamic earth pressures for gravity walls ($r = 1.5$) with impermeable backfill

ϕ'_d °	Static		S_{DS}	Acceleration Coefficients		θ °	EC-8 TBEC-2018		
	K_{as}	P_{as} (kN/m)		k_h	k_v		K_{ad}	E_{ad} (kN/m)	P_{ad} (kN/m)
0.75	0.2	0.1	22.989°	0.983	509.466	610.469			
1	0.267	0.133	30.431°	1.227	639.807	760.558			
1.25	0.333	0.167	37.367°	1.536	800.017	945.043			
1.5	0.4	0.2	43.668°	1.936	1001.523	1177.079			
30	0.299	388.072	0.5	0.133	0.067	15.255°	0.232	64.494	88.041
			0.75	0.2	0.1	22.989°	0.477	225.249	273.153
			1	0.267	0.133	30.431°	1.415	848.626	990.981
			1.25	0.333	0.167	37.367°	1.825	1073.893	1250.379
			1.5	0.4	0.2	43.668°	2.365	1360.146	1580.004
40	0.200	259.440	0.5	0.133	0.067	15.255°	0.174	76.949	94.805
			0.75	0.2	0.1	22.989°	0.329	177.429	210.509
			1	0.267	0.133	30.431°	0.588	341.812	399.797
			1.25	0.333	0.167	37.367°	1.163	700.529	812.866
			1.5	0.4	0.2	43.668°	2.610	1581.294	1827.079

Table 5. A comparison of lateral dynamic earth pressures for gravity walls ($r = 1.5$) with permeable backfill

ϕ'_d °	Static		S_{DS}	Acceleration Coefficients		θ °	EC-8 TBEC-2018		
	K_{as}	P_{as} (kN/m)		k_h	k_v		K_{ad}	E_{ad} (kN/m)	P_{ad} (kN/m)
0.75	0.2	0.1	19.984°	0.862	675.420	763.385			
1	0.267	0.133	26.726°	1.097	886.448	993.659			
1.25	0.333	0.167	33.207°	1.339	1089.760	1215.049			
1.5	0.4	0.2	39.289°	1.643	1319.698	1467.099			
30	0.299	388.072	0.5	0.133	0.067	13.158°	0.187	199.747	218.332
			0.75	0.2	0.1	19.984°	0.361	394.336	429.677
			1	0.267	0.133	26.726°	0.704	696.786	765.226
			1.25	0.333	0.167	33.207°	1.562	1320.548	1470.770
			1.5	0.4	0.2	39.289°	1.968	1612.542	1794.278
40	0.200	259.440	0.5	0.133	0.067	13.158°	0.142	221.662	235.988
			0.75	0.2	0.1	19.984°	0.259	380.210	405.832
			1	0.267	0.133	26.726°	0.438	574.742	617.111
			1.25	0.333	0.167	33.207°	0.748	846.188	916.958
			1.5	0.4	0.2	39.289°	1.601	1445.591	1594.452

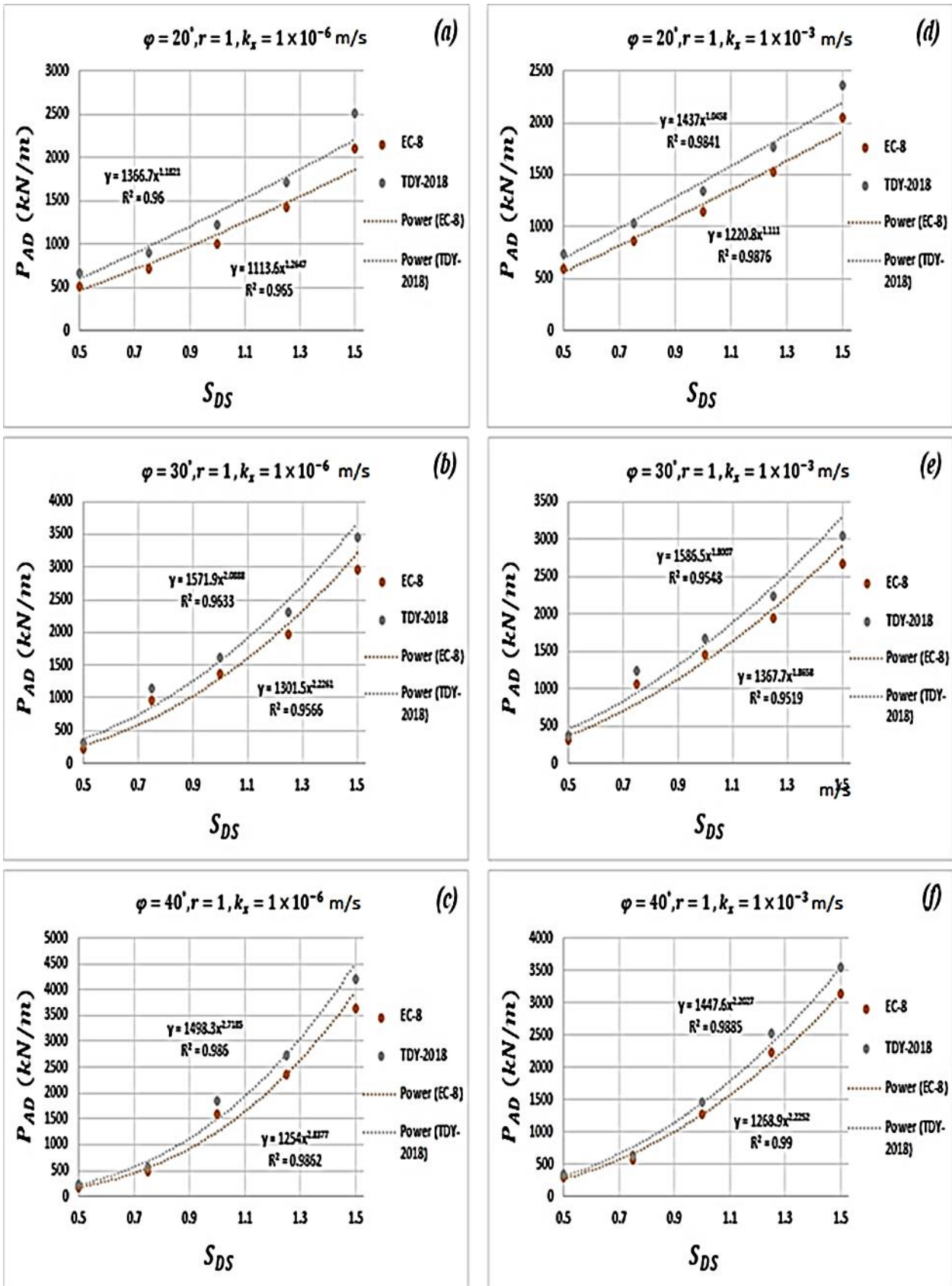


Figure 4. Variation of horizontal dynamic active thrust forces acting on the anchored wall with earthquake acceleration coefficient

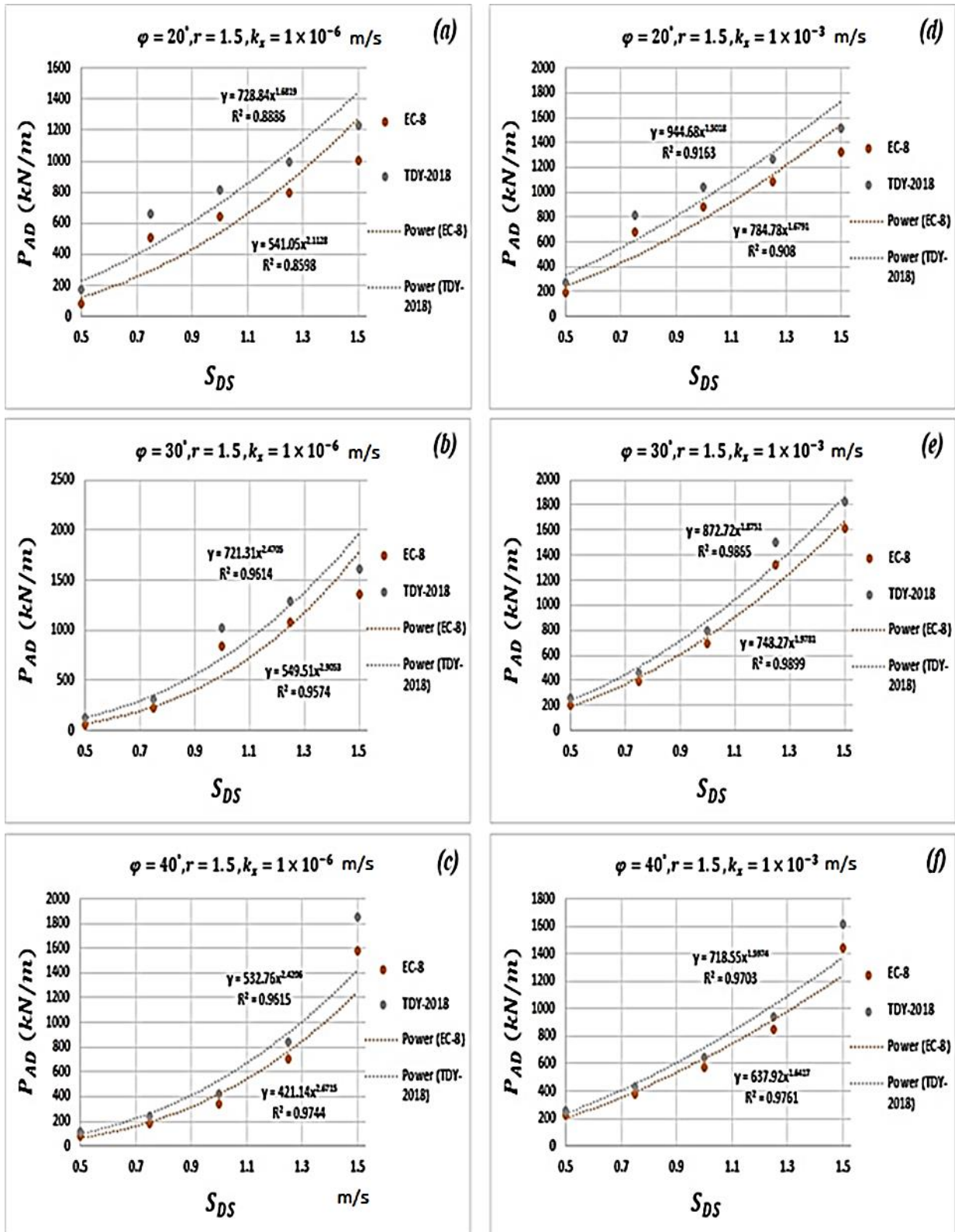


Figure 5. Variation of horizontal dynamic active thrust forces acting on the yielding gravity with the earthquake acceleration coefficient

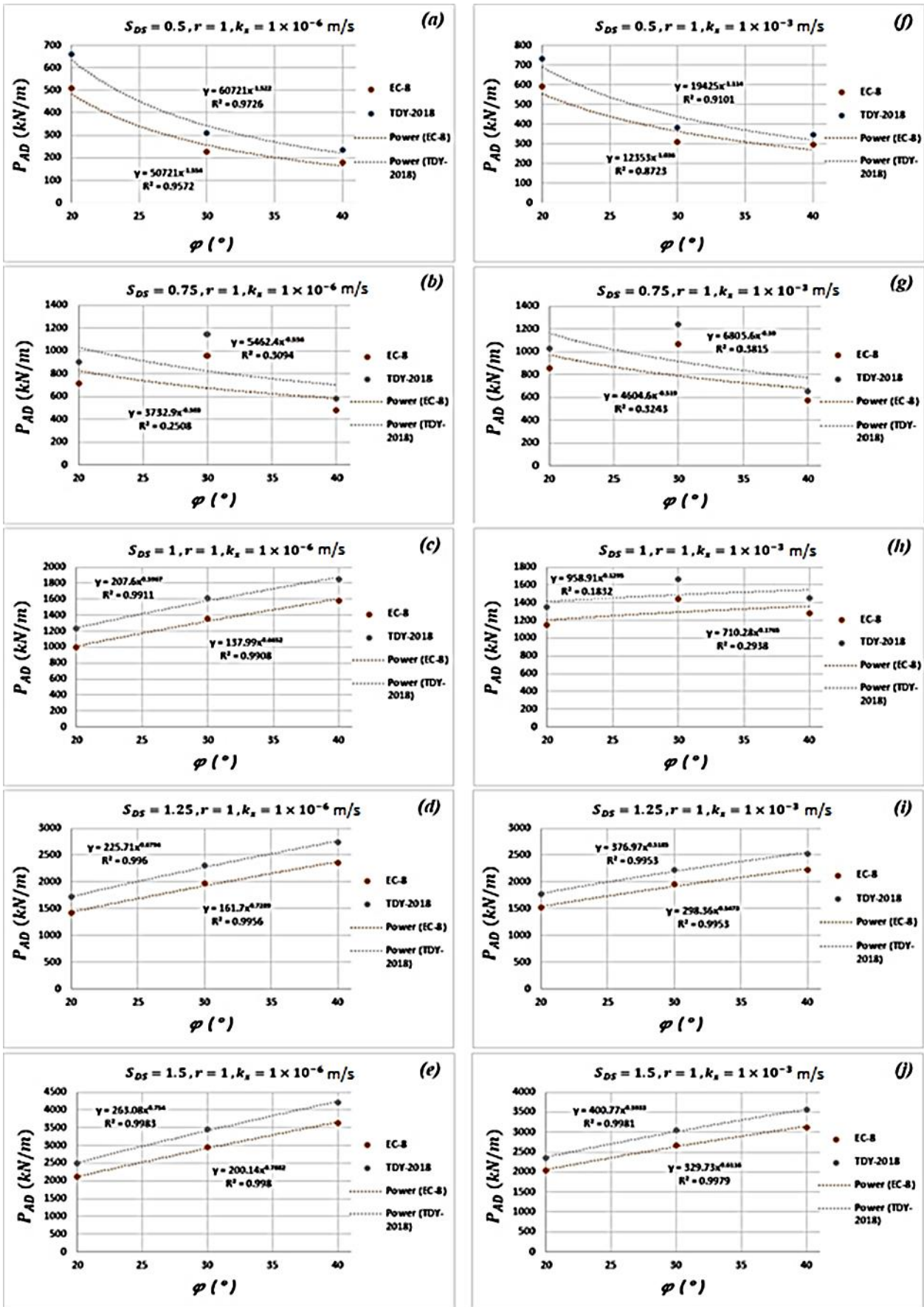


Figure 6. Variation of horizontal dynamic active thrust forces acting on the anchored wall with the internal friction angle of the soil (ϕ'_d)

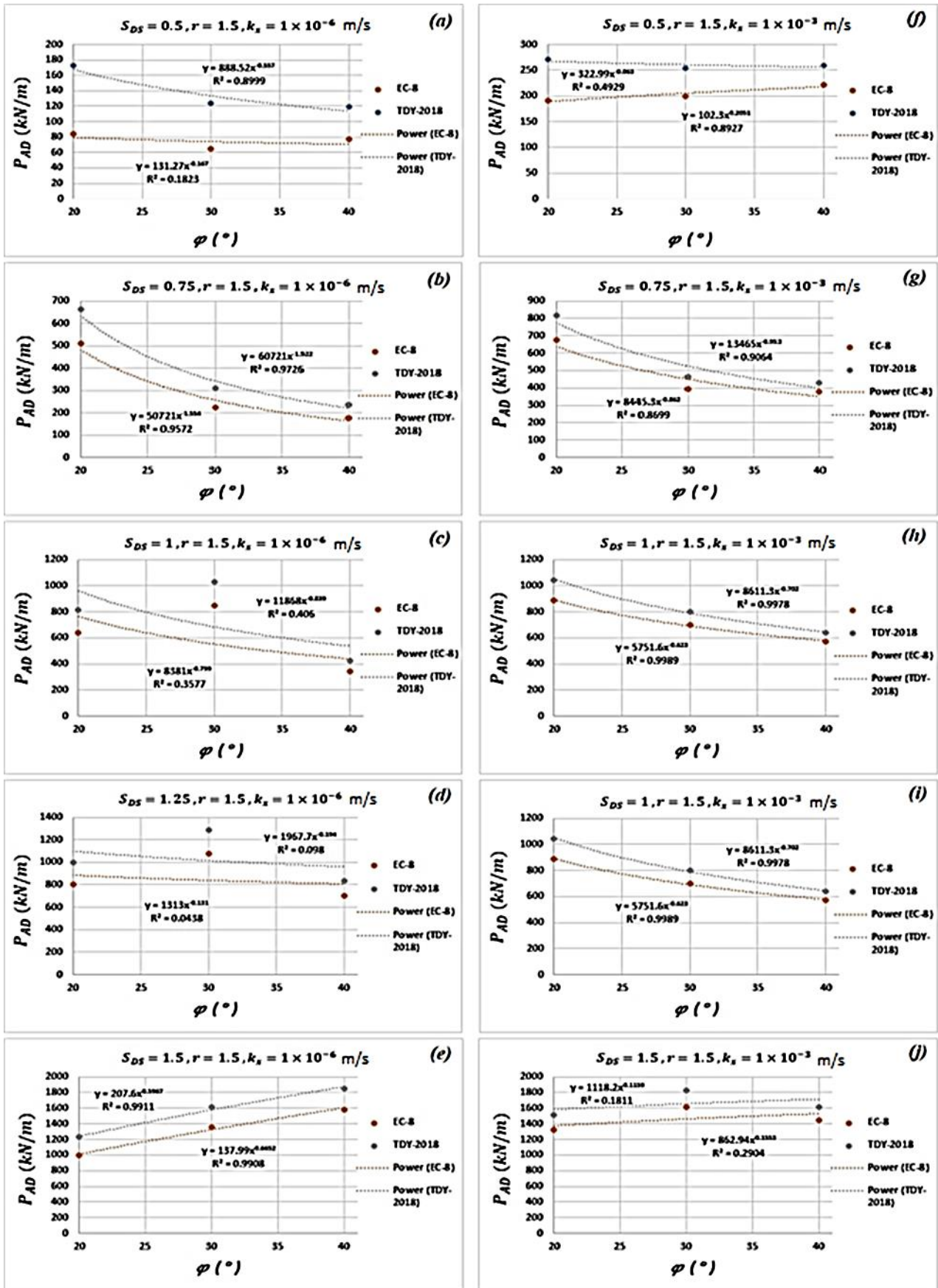


Figure 7. Variation of horizontal dynamic active thrust forces acting on the yielding gravity wall with the internal friction angle of the soil (ϕ_0) according to EC-8 and TBEC-2018 Regulations

5. Conclusion

Mononobe-Okabe method have generally been used to determine the dynamic lateral soil thrust and soil pressure coefficients for the design of retaining structures in various building earthquake codes. However, there are interpretation differences between these regulations in earthquake codes of different countries. In this study, seismic response of anchored walls and yielding gravity retaining walls are investigated according to the procedures suggested by Turkey Earthquake Code 2018 (TBEC-2018) and EuroCode-8 (EC-8). A parametric study was carried out using different earthquake acceleration coefficient (S_{DS}) and different soil friction angles (ϕ'_a) for a 12 m high retaining wall. For this purpose, based on the procedures described in these earthquake codes, approximately 120 analyzes were performed using different parameters and the results of the analyses were shown in the form of tables and figures. The results show that the horizontal static and dynamic forces acting on the wall decrease with the increase of the soil internal friction angle (ϕ'_a). However, in cases where the angle θ , which depends on the horizontal and vertical earthquake coefficient, is larger than the soil internal friction angle (ϕ'_a), dynamic active thrust forces acting on the wall increases with the increase in the soil internal friction angle for the cases ($\theta > \phi'_a$). With the increase in the earthquake acceleration coefficient (S_{DS}), active dynamic thrust forces increase according to the TBEC-2018 and EC-8 regulations, and the results obtained from both regulations are in agreement with each other. It is observed that the soil internal friction angle (ϕ'_a) and earthquake acceleration coefficients (S_{DS}) are important factors due to their effect on the horizontal dynamic active thrust forces acting on the wall. According to EC-8 and TBEC-2018, the dynamic forces can take higher values than the static forces. It is known that the earth pressure coefficients used in TBEC-2018 and EC-8 regulations are based on Mononobe-Okabe method. However, in EC-8, it should be noted that the friction angle between the wall and the ground (δ_a) and the soil internal friction angle (ϕ'_a) values are reduced in the earth pressure calculations according to the equations given in Figure 2. As a further study, it is planned to suggest revised versions of the formulas to prevent illogical earth pressure calculations at critical values where different formulations are being used.

Author contributions

Özgür Lütfi Ertuğrul: Conceptualization, Methodology, Reviewing and Editing, Validation.
Babur Bek Zahin: Data curation, Software, Original draft preparation.

Conflicts of interest

The authors declare no conflicts of interest.

References

1. Bowles, L. E. (1996). *Foundation analysis and design*. New York: McGraw-Hill.
2. Okabe, S. (1926). General theory of earth pressures. J. Japan. Soc.Civil Eng., 12(1), 123-134.
3. Mononobe, N., & Matsuo, M. (1929). On the determination of earth pressures during earthquakes. Proc. World Engrg. Congress, 9, pp. 179-187.
4. Kramer, S. L. (1996). *Geotechnical earthquake engineering*. India: Pearson Education.
5. Das, B. M. and Sobhan, K. (2013). *Principles of geotechnical engineering*. USA: Cengage learning.
6. Türkiye Bina Deprem Yönetmeliği (TBDY). (2018). Ankara: Bakan İşleri Genel Müdürlüğü, Deprem Araştırma Dairesi.
7. Özberk, L. & Kahyaoğlu, M.R. (2018). Dayanma Yapılarının DBYBHY ve TBDY Gore Analiz Sonuçlarının Karşılaştırılması ve Tespitler. Zemin Mekaniği ve Geoteknik Mühendisliği, 17. Ulusal konferansı bildiri kitabı, 1-10. İstanbul
8. Eurocode-8. (2004). Design Of Structures For Earthquake Resistance Of Structures-Part 5: Foundations, Retaining Structures And Geotechnical Aspects. European Standard, European Committee for Standardization.
9. DBYBHY (2007). Deprem Bölgelerinde Yapılacak Binalar Hakkında Yönetmelik. Ankara: Çevre ve Şehircilik Bakanlığı.
10. <https://www.turkiye.gov.tr/afad-turkiye-deprem-tehlike-haritalari>
11. Gürsoy, Ş. (2013). İstinat Duvarlarına Etkiyen Aktif Zemin İtkilerinin Eurocode-8 ve Türkiye Deprem Yönetmeliğine Göre Karşılaştırılması. Karabük Üniversitesi, Gazi Üniversitesi Fen Bilimleri Dergisi, 1(4), 153-160.



© Author(s) 2023. This work is distributed under <https://creativecommons.org/licenses/by-sa/4.0/>



Uranium migration and radioactive characteristics of the Sarıççek and Sarıhan Granodiorites

Suna Altundaş^{*1}, Hakan Çınar²

¹Gümüşhane University, Faculty of Engineering and Natural Sciences, Department of Geophysics Engineering, Türkiye

²Karadeniz Technical University, Faculty of Engineering, Department of Geophysics Engineering, Türkiye

Keywords

Gamma-Ray Spectrometer
Radioelement Composition
F Parameter
Radioelement Ratios
Uranium Migration

Research Article

DOI: 10.31127/tuje.1100375

Received: 08.04.2022

Accepted: 07.07.2022

Published: 31.08.2022

Abstract

The radionuclide concentrations of eU (ppm), eTh (ppm), K (%) and dose rate values were measured in Sarıççek (Gümüşhane) and Sarıhan (Bayburt) granodiorites for a duration of 5 minutes at each of 532 measurement points. The radioelement ratios (eU/eTh, eU/K, and eTh/K) indicating the origins of the rocks, the geochemical indicators (U_{me} , F parameter, and eU-(eTh/3,5) rate) showing the uranium mobility and the radioelement concentrations were calculated and mapped within the study areas. The average K, eU, and eTh concentrations were calculated as 2.98%, 3.15 ppm, and 12.45 ppm for Sarıççek granodiorite, and 1.83%, 2.73 ppm, and 13.6 ppm for Sarıhan granodiorite, respectively. Higher radioactivity values were observed in basaltic, sedimentary, and ultramafic rock combinations within the granodiorite masses. In the classification according to radioelement ratios, it was concluded that the rocks in the study areas formed as a mixture of upper mantle and crustal materials. In both study areas, there was uranium transport from the granodioritic masses into the surrounding rocks, and accordingly, the rocks in the surrounding formations were enriched in uranium. As a result, radioactivity levels, rock formation origins, and uranium transport of both granodioritic masses and rocks in the surrounding formations were determined by evaluation with radioelement concentration values and ratios and migration parameters. The study areas were characterized by associating them with geology in light of radioactive data.

1. Introduction

The natural radioactivity existing on earth has affected all living things directly or indirectly since the formation of the earth. This natural radioactivity includes cosmic rays coming from outer space especially, and the rays emitted as a result of the decay of natural radionuclides in rocks, soil, water, and even the air we breathe. The natural radioactivity level of a place varies depending on the geological structure, geographical location, and radiochemical characteristics of the region. Factors such as rain, snow, low pressure, high pressure, and wind direction also determine the magnitude of the natural radiation level. People are exposed to different types of radiation emitted from these sources in the natural environment in which they live. The most common natural radiation sources are ^{40}K , ^{238}U , ^{226}Ra , and ^{232}Th isotopes [1].

The amounts of these radionuclides, which contribute to environmental radioactivity, in nature may vary according to soil and rock types. Natural

radioactivity in soils and rocks provides the largest contribution to the environmental gamma dose rate. For example, natural radioactivity in volcanic rocks is higher than in sedimentary rocks. The level of radioactivity in sedimentary and phosphate-type rocks is also quite high [2-3]. Granites are very common plutonic rocks in most of the earth. Granites gain prominence radiologically because they contain high proportions of ^{238}U , ^{232}Th , and ^{40}K . Granite rocks spread over large areas in many regions and contain significant levels of Th. As a result of radiometric studies carried out around the world and in Turkey, gamma radiation was measured in areas with very high radiation values [4].

Metamorphic rocks, granitic rocks, sediments containing organic matter, sandstones, and carbonate sedimentary rocks are rock groups rich in uranium, thorium, radium, and radon. The presence of uranium and thorium in igneous rocks is closely related to changes in uranium and thorium concentrations and igneous crystallization of magma. The uranium and

* Corresponding Author

(sunaaltundas@gmail.com) ORCID ID 0000-0002-5840-0352
(cinar@ktu.edu.tr) ORCID ID 0000-0002-6562-1962

Cite this article

Altundaş, S., & Çınar, H. (2023). Uranium migration and radioactive characteristics of the Sarıççek and Sarıhan Granodiorites. Turkish Journal of Engineering, 7(3), 208-226

thorium content in igneous rocks decreases from acidic rocks to basic rocks [5].

The natural radionuclides these rocks contain should be determined and examined radiologically, especially due to the use of granite as a building material inside and outside buildings. In terms of natural radioactivity, although the abundance of natural radioelements in the oceanic crust and the mantle is very low, the content of these elements in granitic rocks is very high. According to geologists, the cause of this is the fractional crystallization of magma and partial melting [6]. Especially high concentrations of radioactivity were detected in igneous rocks such as granite. Granite is distributed over large areas in many regions and contains significant amounts of thorium [7]. The eU (equivalent uranium)/eTh (equivalent thorium) ratio is highly affected by the oxidation process and this process causes uranium (U) migration. This ratio is a very important parameter in determining the oxidation area of U [8]. Since uranium is a mobile element, it can convert from U⁺⁴ to U⁺⁶ during oxidation. U can migrate from one place to another and react with the elements there. The eU/eTh ratio is a very important geochemical parameter for U migration.

Most of the earth-forming rocks, ground, and surficial waters containing these elements have radioactive properties. Both airborne and land-borne gamma-ray spectrometer studies are usually used for purposes such as uranium prospecting, surficial geological mapping, and soil mapping in agriculture, stratigraphic analyses of geological formations, geothermal research, and metallic mining research [9]. There are many scientific studies related to the definition of the natural radiation level in rock and soils [10-11], lithological discrimination-related studies [12-14], radionuclide concentrations in volcanic rocks and granitic plutons [15-19], radioactive areas of mineralization [20-22], possible uranium migration areas and the migration paths in granitic rock [23-27].

In this study, the Sarıççek granodiorite (Gümüşhane) and Sarihan granodiorite and surrounding formations (Bayburt) containing different lithological units located in the Eastern Pontides, Turkey was selected as the study areas. Sarıççek granodiorite, surrounded by Early Eocene volcanic rocks of the Alibaba Formation, is part of the composite E-W-trending Kaçkar Batholith in the Eastern Pontides of Eastern Turkey. The rocks outcropping in the Sarıççek granodiorite are I-type granodiorite rocks and generally change from calc-alkaline composition to high K calc-alkaline composition [28]. Sarihan granodiorite and its surrounding formations located in the Eastern Pontides, Turkey comprises three different lithological units namely, Hozbirikyayla Formation (limestone and sandy limestones), Sarihan granodiorite (consisting of quartz monzodiorite, granodiorite, and quartz diorite), and ophiolitic mélange (andesite, basalt, sandstone, gravelly sandstone) [29]. The pluton has calc-alkaline composition and is characterized by a calc-alkaline granodiorite trend [30].

Within the scope of this study, concentrations of equivalent uranium (eU, in ppm), equivalent thorium (eTh, in ppm), potassium (K, in %) and dose rate values

of the Sarıççek (Gümüşhane) and Sarihan granodiorites (Bayburt) and surrounding formations were investigated using the gamma-ray spectrometry method. An attempt was made to correlate the obtained radionuclide concentration changes with the geology of the study areas. Using the radionuclide concentrations obtained from measurements made in the field, the geochemical element ratios provide information about the origin of the rocks and the migration tendency of the natural radionuclides in the rocks, especially U, was calculated and mapped.

2. Location and geological background of the study areas

2.1. General setting of the study areas

Within the scope of this study, radioactivity measurements were carried out in and around the Sarıççek granodiorite (Gümüşhane) located between 40° 25' 30.61" and 40° 26' 33.94" north latitude and 39° 49' 28.70" and 39° 52' 3.69" east longitude and in Sarihan granodiorite and its surroundings (Bayburt), which is located between 40° 04' 56.03" northern latitude and 39° 57' 28.81" and 40° 08' 56.87" east longitude (Fig. 1).

The Sarıççek granodiorite is located approximately 30 km west of Gümüşhane city (between map sheets H43 b1-b2), southeast of the Eastern Black Sea Mountains (Pontides). The Sarıççek granodiorite has an ellipsoidal shape and is approximately 7x2.3 km in size. The long axis of the granodiorite is in the NE-SW direction. Sarihan granodiorite is approximately 40 km south of Bayburt and on map sheets Trabzon H44 d1-d4. While most of the study area is within the borders of the province of Bayburt, part of the mélange belt is within the borders of the province of Erzincan. This pluton crops out in an area of approximately 40 km².

2.2. Geological Structure

The Pontide Orogenic Belt constitutes an essential part of the Alpine-Himalayan system and geographically corresponds to the Black Sea and Thrace regions in Turkey [31]. The Eastern Pontide Orogenic Belt (Fig. 2), which includes the study areas, was divided into three subunits as north, south, and axis zones from north to south by considering different lithological features and facies changes [32-33].

In the northern zone, in general, Late Mesozoic and Cenozoic granitic rocks and volcanic rocks constitute the dominant lithology. Moving south, the igneous rock-dominated sequence in the north is replaced by a sequence dominated by sedimentary rocks.

In the axis zone, the serpentinized ultramafic masses and Miocene volcanic-sedimentary rocks are the dominant rock lithologies [34]. The areas investigated within the scope of the study crop out in the southern zone of the Eastern Pontide Orogenic Belt (Fig. 3a).

Sarıççek granodiorite (Fig. 3b), which is the second of the studied masses and crops out approximately 30 km west of Gümüşhane city center, close to the northern part of the southern zone, is surrounded by Eocene volcanic rocks [36].

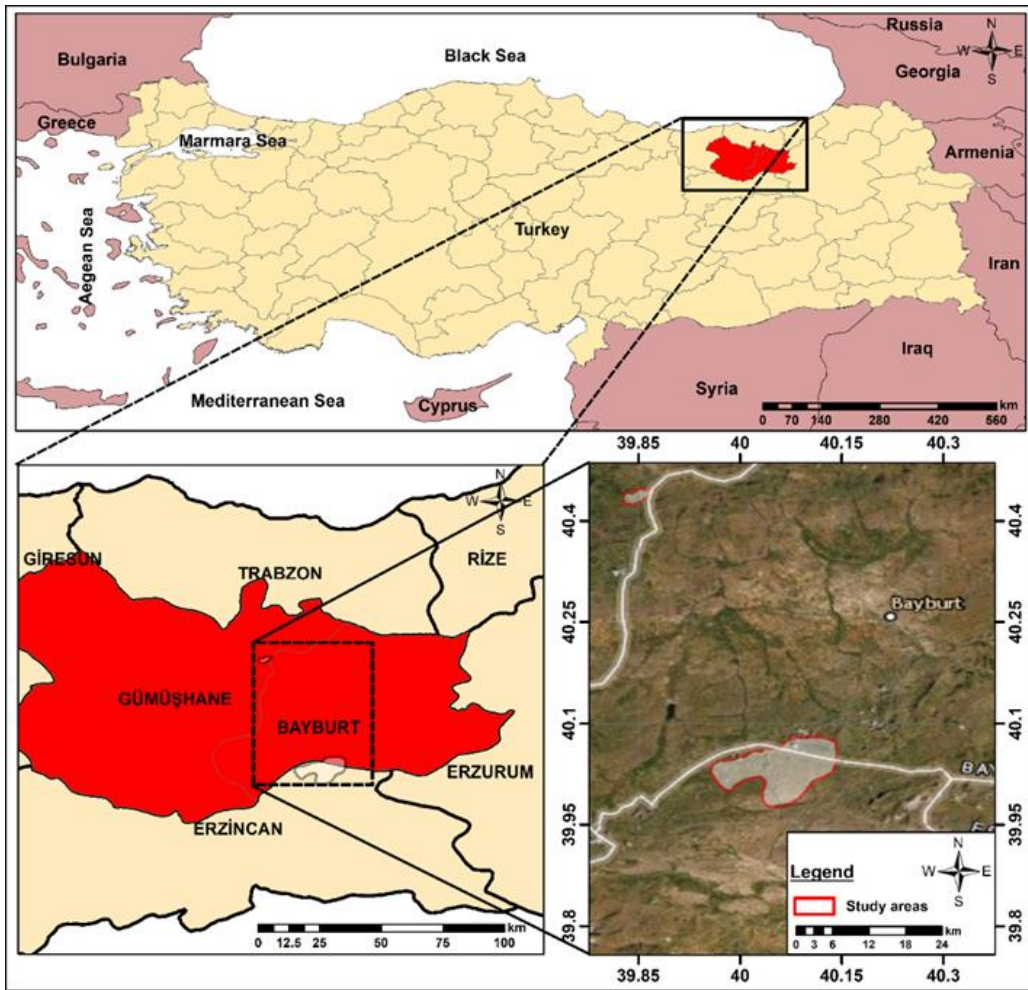


Figure 1. Location map of the studied areas in the Gümüşhane (Sarıçiçek) and Bayburt (Sarıhan)

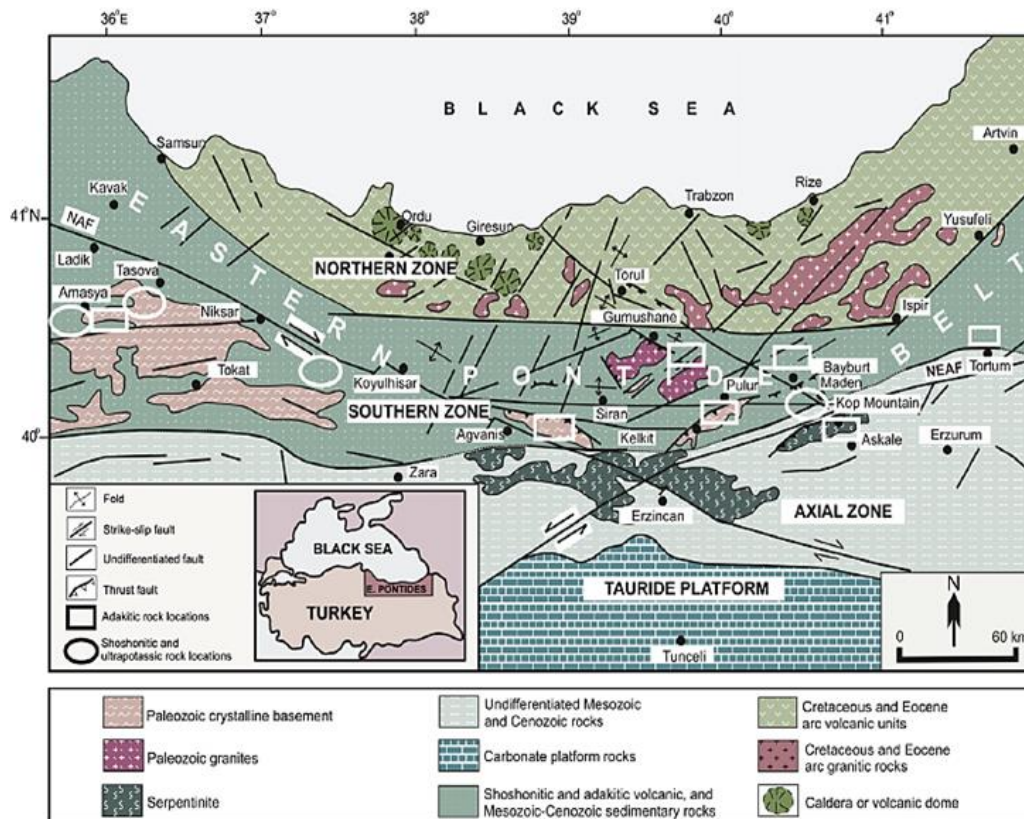


Figure 2. Main tectonic features and zones of the eastern Pontides orogenic belt (NAF: North Anatolian Fault; NEAF: Northeast Anatolian Fault) modified from [35]

In this area, which reflects the typical features of the southern zone, the Eocene Alibaba Formation is represented by a thick volcanic and pyroclastic sequence that developed following the deposition of nummulitic limestones overlying a conglomeratic level at the base. Compared to the Sarihan granodiorite in the south, it contains fewer enclaves, and plagioclase, amphibole, and biotite crystals can be observed macroscopically on hand

samples from the rocks forming this mass. The rocks outcropping in Sariçiçek granodiorite (Fig. 3b) are I-type granodiorite rocks and generally change from calc-alkaline composition to high K calc-alkaline composition [28]. The age of the mass was determined as Lutetian as a result of Ar/Ar dating performed on mafic minerals [36] and U-Pb dating of zircons [37].

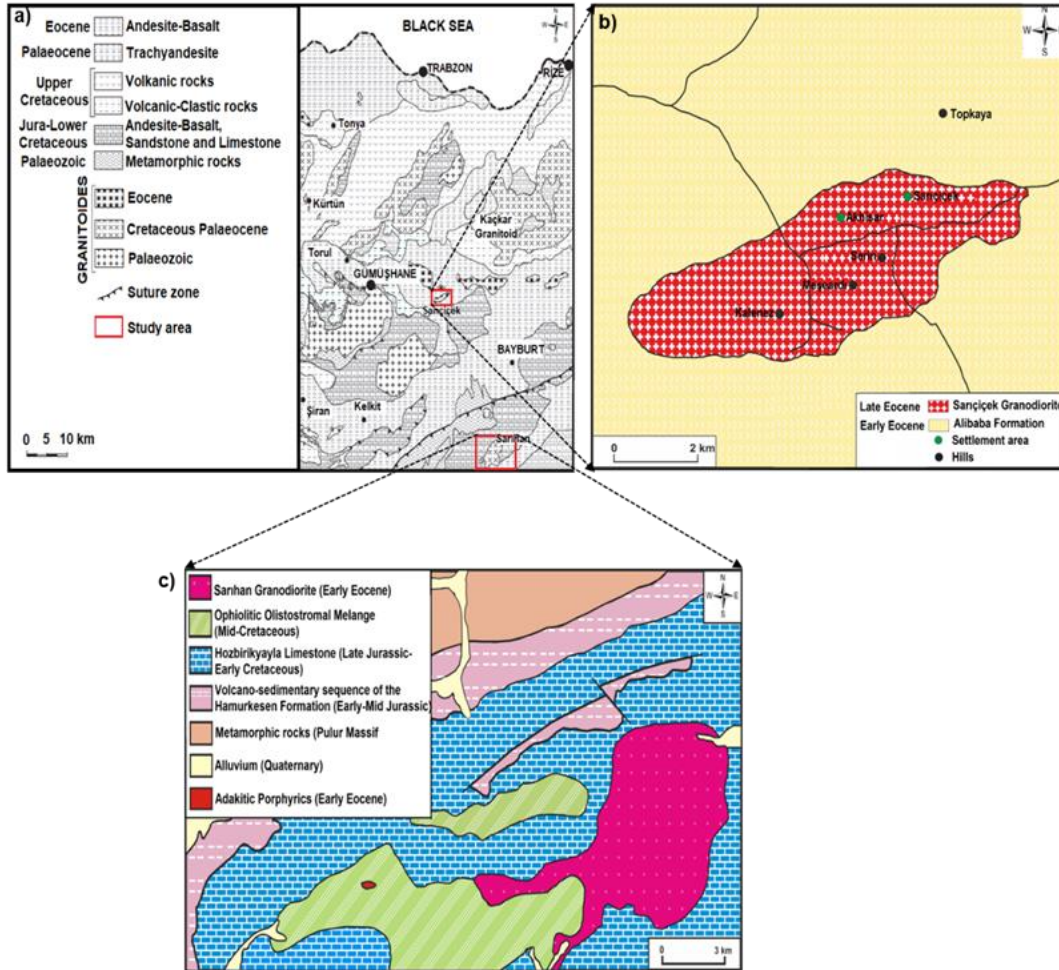


Figure 3. a) The geology map of the studied area modified from [38] b) The Sariçiçek granodiorite and surroundings modified from [28] and c) The Sarihan granodiorite and its relationship with the surroundings rocks modified from [30] and [39]

Sarihan granodiorite (Fig. 3c), which is located in the southern zone and is further south compared to the first study area, is one of the largest intrusive masses with adakitic composition in the Eastern Pontides [39]. Sarihan granodiorite has contacts with the Middle Cretaceous Otlukbeli mélangé and the Late Jurassic-Early Cretaceous Hozbirikyayla Limestone. Traces of contact metamorphism and skarn mineralization are usual, especially along with the contact with limestones [30]. The mass, which presents a rather massive appearance, is characterized by well-developed and unfilled fracture systems. In addition, mafic microgranular enclaves are commonly seen in the mass, indicating magma mixture, and the diameters of the enclaves reach 40 cm in places (Fig. 4). In a study of felsic intrusions cropping out in the Pular massif [38], zircons selected from the samples taken from this mass were aged by the U-Pb dating method, and Early Eocene age of approximately 53

million years was obtained. It was emphasized for the first time that this rock mass has adakitic composition. The Sarihan granodiorite is a metalumin-based, calc-alkaline, and I-type granitoid [40].



Figure 4. Mafic microgranular enclave and Aplite dyke found in Sarihan granodiorite

3. Material and Method

3.1. In-situ Gamma-Ray measurements

Gamma-ray spectrometry has been used for uranium exploration, geological mapping studies, and earthquake monitoring studies [9]. Since the existence of the universe, K, U, and Th radionuclides are found in greater or lesser amounts in rocks within a zone up to a depth of about 10-12 km within the earth's crust. The average concentrations of these elements in the earth's crust are 2.33 % for K, 3 ppm for U, and 12 ppm for Th [41]. The gamma-ray spectrometer used in the study was an instrument designed for natural and artificial radioisotope measurements on cores taken by drilling in the field and laboratories or on rock-soil samples collected from the field. Gamma rays emitted can be measured as a physical property because rocks contain different radioactive elements in different proportions and some minerals contain radioactive elements in different proportions. U, Th, and K elements and their isotopes, which have this radioactive feature and are found in significant proportions in the earth's crust, have

great importance in geological and geophysical research. The isotopes of these elements emit gamma-rays at certain energy levels. With gamma-ray spectrometry, these gamma rays are measured in certain energy ranges. For this reason, gamma-ray spectrometry is an important radiometry technique applied in the investigation of many issues related to the earth. With radioactivity measurements made on soil or rocks, the number of radioactive elements by weight at each point (K (%), eTh (ppm), eU (ppm)) is measured. Determination of uranium and thorium is based on the assumption that the daughter elements are in equilibrium with the parent elements; that is, none of the steps in the decay series were disturbed. Based on this assumption, the amounts of uranium and thorium released are equivalent to the value in equilibrium with the measured radioactivity of the isotopes of thallium or bismuth. For this reason, gamma-ray measurement results are expressed as 'equivalent uranium (eU)' and 'equivalent thorium (eTh)'. There are three important gamma-ray energies from high to low: 2.62 MeV for thorium (^{208}Tl), 1.76 MeV (^{214}Bi) for uranium, and 1.46 MeV (^{40}K) for potassium [42-43].

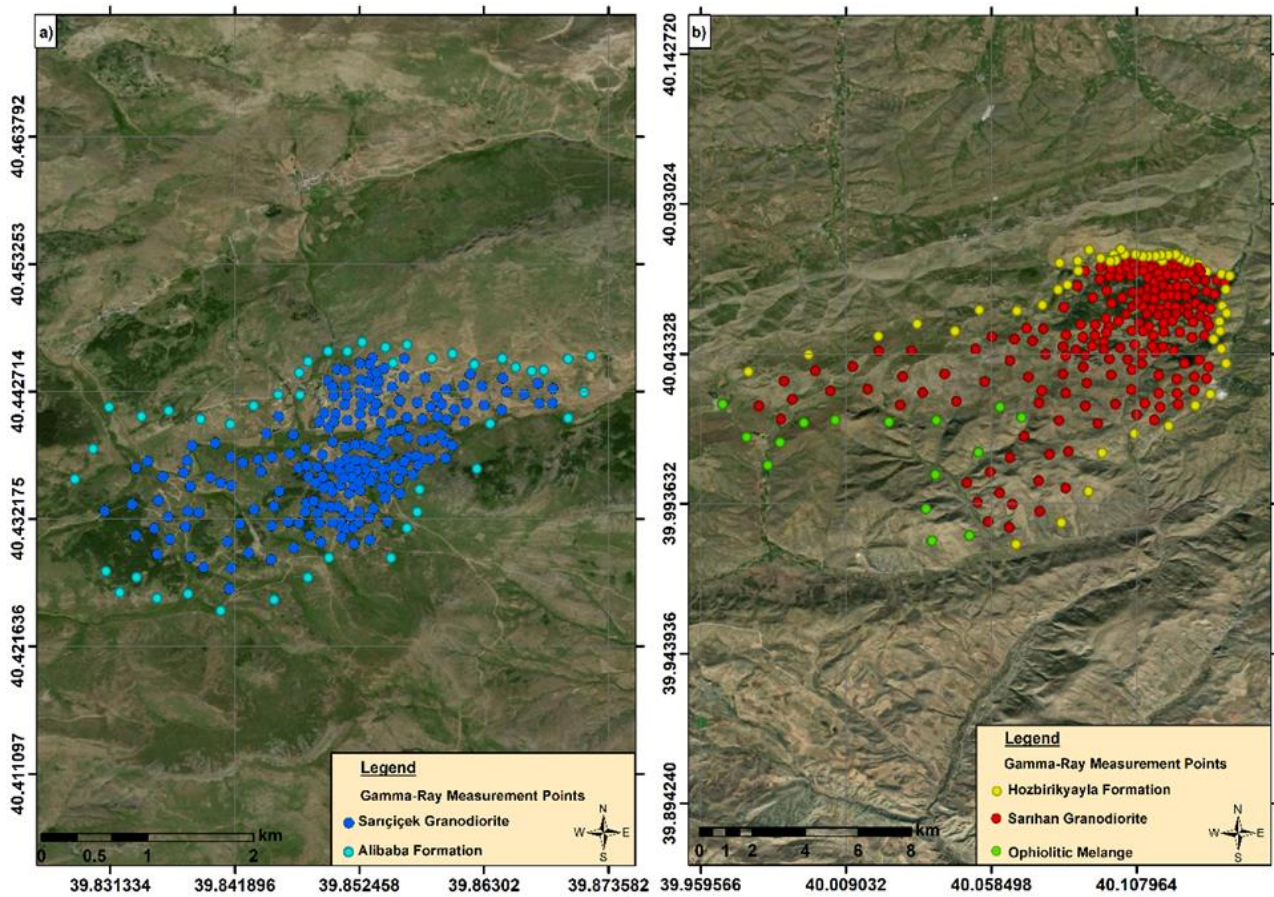


Figure 5. In-situ gamma-ray measurement points in the study areas

In-situ gamma-ray spectrometry measurements were made in and around Sarıçiçek and Sarıhan granodiorites at 532 points in total, forming an irregular grid owing to topographical difficulties. Of these, 265 points were measured on outcropping rock and soils in Sarıçiçek granodiorite and surrounding formations and 267 were measured on Sarıhan granodiorite and its surrounding formations (Fig. 5). The measurement time was set to 5

minutes for each point, and the coordinates of the points were recorded using a handheld GPS. In addition to radiometric parameters (K, eU, eTh, and dose rate) obtained from measurements in the field, the radionuclide ratios (eU/eTh, eU/K, and eTh/K) provide information about the origin of the rocks. Geochemical indicators (U_{me} , F parameter, and eU-(eTh/3,5) rate) showing uranium remobilization in the rocks and the

relationship between radioelement concentrations were calculated and these data were mapped. By evaluating the maps together, the presence of uranium migration can be assessed and the direction of possible uranium migration was determined in the study areas.

3.1.1. Natural radionuclide ratios (K/eTh, eU/eTh, and eU/K)

Some factors that affect radionuclide concentrations, such as soil moisture content, condition of outcropping rock, vegetation, and geometric structure of the land, have a lesser effect on these radionuclide ratios. The radionuclide ratios (K/eTh, eU/K, and eU/eTh) that provide information about the origins of rocks are frequently used in the detailed interpretation of in situ radioactivity measurements. For example, eU/K and eU/eTh ratios are particularly useful to reveal uranium-rich areas [44-45].

3.1.2. Geochemical indicators of uranium remobilization

Uranium, which is a mobile element, migrates from its source to another location. The expected original uranium content was calculated by dividing the eTh content (eTh/eU) ratio by the value (3.5) for granite to understand uranium remobilization in the region [46]. The result is the hypothetical uranium distribution. This helps define the trends of uranium migration. When the eU-(eTh/3.5) values are mapped, it is accepted that negative contour areas indicate uranium-poor areas, while the areas with positive contours show places where uranium enrichment occurs. By subtracting the original uranium content (U₀) from the available uranium content (U_p), the uranium migration value (U_m) for a particular rock can be estimated [47]. The original uranium content (U₀) can be calculated by multiplying the average thorium content by the average regional eU/eTh ratio in various lithological units (U₀=eTh×(regional eU/eTh)).

If the original uranium content (U₀) is known from the available uranium content (U_p) in soil and rocks, we can calculate the uranium migration rate (U_{me} %) using the following equation;

$$\%U_{me} = (U_m/U_p) \times 100 \quad (1)$$

U_{me} (%) values have two states; if U_{me} is >0, this indicates that uranium migration took place within the geological body. If U_{me} <0, it means that uranium migration did not occur within the geological body [48].

High degrees of uranium transfer in the rock is due to the high degree of correlation between eU and eU/eTh ratio. For additional information about the redistribution of radioactive elements, the inverse ratio between the eU/eTh ratio and the eTh content in different lithological units can be used. In deriving the degree of rock alteration, the F parameter was used [49]. The F parameter is given by the following equation:

$$F = K/(eTh/eU) = eU/(eTh/K) = K \times (eU/eTh) \quad (2)$$

Using this parameter, we can describe two specific characteristics of rock environments: one is the uranium abundance relative to eTh/K, and the other is the potassium abundance relative to eTh/eU. Therefore, the use of the F parameter is effective in identifying strong K-alteration zones associated with uranium mineralization [50].

3.2. Gamma-Ray measurements in the laboratory

Rock and soil samples were taken from the study areas to test the sensitivity of the spectrometer and the concentration difference that may occur depending on the detector used between measurements using field and laboratory environment (Fig. 6). Soil samples were taken from a depth of 30 cm from the surface by removing foreign objects such as stones, grass, wood chips, and tree bark. The rock samples were collected from the rock by cleaning the mossy and altered parts of the exposed rocks.



Figure 6. Soil and rock samples collected from the Sariçiçek granodiorite and surroundings

All soil and rock samples taken from the field were left to dry in a laboratory environment for 15-20 days. The dried soil and the rock samples were crushed and after the necessary stages were passed through a 2 mm sieve to create homogeneous samples. Samples were placed into 100 ml plastic measuring cups with a diameter of 55 mm and a height of 65 mm, prepared for the experimental geometry, and kept for one month after the caps were tightly closed [15].



Figure 7. Canberra GC 1519 model HPGe detector

In the spectrometric analysis carried out in the laboratory, only 84 samples were used from the samples

collected from Sarıçiçek granodiorite and surroundings, due to the large number of samples collected. The measurement time was approximately one day. A Canberra, GC 1519 model HPGe detector, which has a resolution of 1.9 keV at 1332.5 keV gamma of ⁶⁰Co and relative efficiency of 15%, was used for radioactivity measurements of the samples (Fig. 7). Gamma spectrometry uses a detector, preamplifier, spectroscopy amplifier, analog-digital converter (ADC) system that converts analog counts into electronic signals, and multi-channel analyzer (MCA). The detector was shielded with cylindrical lead with a thickness 10 cm that contains an inner concentric cylinder of Cu with a thickness of 2 mm in order to reduce the background effects [5]. The sample counting time was determined as 80000 s. The obtained spectra were analyzed using the Genie-2000 program, and the activity concentrations were calculated.

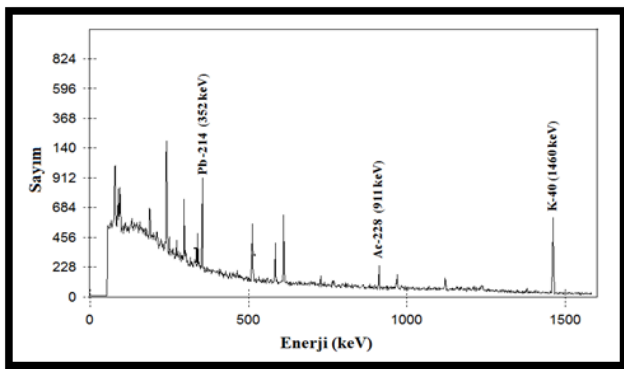


Figure 8. Gamma ray spectrum of a rock sample taken from Sarıçiçek granodiorite

In Fig. 8, the gamma ray spectrum is presented for one of the rock samples from the Sarıçiçek granodiorite measured with the HPGe detector. By using energy calibration, the energy values of the peaks and corresponding radioisotopes were determined. During the study, the energy calibration was checked periodically. Peaks for the decay products of ²³⁸U (²²⁶Ra (186.21 keV), ²¹⁴Pb (351.9 keV), ²¹⁴Bi (609.3 keV)) and ²³²Th series (²⁰⁸Tl (583.1 keV) and ²²⁸Ac (911.1 keV)), ⁴⁰K (1460.8 keV) and ¹³⁷Cs (661.6 keV) were taken into account and the relevant area (ROI) regions were selected for each peak. In addition, the areas of the peaks were marked to give the largest area and the smallest error. Taking into account the detector efficiency, the specific activity concentration of these natural radionuclides, A (Bq.kg⁻¹) was calculated from the following equation.

$$C = \frac{N}{\varepsilon \times P_{\gamma} \times t \times m} \quad (3)$$

N, ε, P_γ, t, and m in this formula represent the net counting rate (counts per second), the detector efficiency, the absolute transition probability of gamma-decay of the nuclide, the counting time (seconds), and mass of the sample in kg [5]. The net areas under the peaks were obtained by subtracting the background

(peak areas from the blank measurement for each calculated element) from the total area.

4. Results and Discussion

4.1. Assessment of In-situ Gamma-ray Data in the Sarıçiçek Granodiorite and Surroundings

The natural radioactivity level of a region varies depending on both the radionuclide concentrations in the soil and rocks in the region and the distance of the area from the sea. While the altitude of the measurement area in Gümüşhane varied between 1900-2200 m, this value varied between 1800 m and 2300 m in the second study area of the Sarıhan granodiorite. This situation is one of the reasons for the high gamma dose ratio values in the regions. Since the altitude from the sea increases in direct proportion to the amount of cosmic radiation, the amount of gamma radiation also increases accordingly. When we examine the geological structure of the region, while Sarıçiçek granodiorite and its surroundings mainly consist of granite, granodiorite, quartz monzonite, and quartz monzodiorite composition rocks, this unit is surrounded by the Alibaba Formation and the rock types contain eU, eTh, and K which exist spontaneously in different proportions.

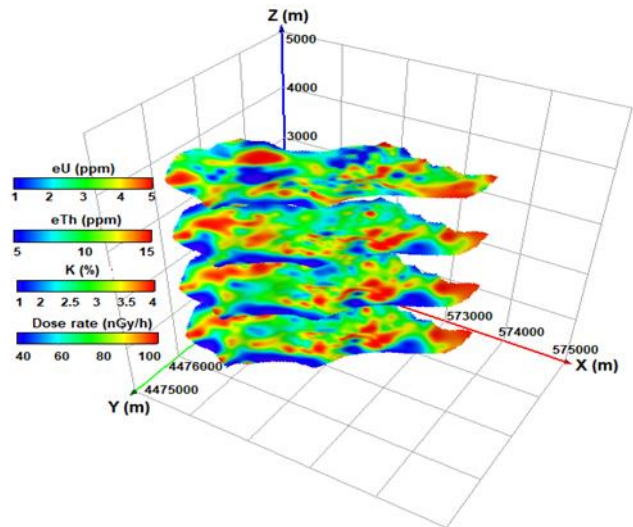


Figure 9. Three-dimensional representation of eU, eTh, K concentrations and dose rate distribution of Sarıçiçek granodiorite and surroundings (Gümüşhane) modified from [15].

The highest concentration and dose rate values (from orange to red) are seen for the Sarıçiçek granodiorite, while the lowest (from dark blue to light blue) values were obtained from the Alibaba Formation surrounding the plutonic mass (Fig. 9). Finally, the medium values defined by a color scale ranging from green to yellow are distributed in the whole area. While the highest concentrations of equivalent thorium, potassium, and dose rate values were recorded in the plutonic mass consisting of granite, granodiorite, quartz monzonite, and quartz monzodiorite composition rocks, the lowest equivalent uranium value was measured in this mass. The lowest concentration values were found in the Alibaba Formation containing basalt, andesites and

pyroclastics. Average values of ^{40}K , ^{232}Th , ^{238}U , and dose rate in the Sarıçiçek granodiorite and surroundings were calculated as 2.98%, 12.45 ppm, 3.15 ppm, and 188.78 nGy/h, respectively.

Areas with high potassium concentration in the Sarıçiçek granodiorite were associated with granitic rocks that contain abundant rock forming minerals such as K-bearing feldspars (orthoclase, plagioclase). The quartz-bearing monzodiorites in the area contain K-poor minerals compared to other rocks [30]. Depending on this result, these low concentration areas were associated with quartz-bearing monzodiorites. While high values in the study area show that K is concentrated with eU and eTh, this increase in K concentration also indicates the presence of altered rocks in the environment.

Although high uranium values were obtained in the Sarıçiçek granodiorite, the highest concentration value was measured for andesitic rocks depending on the mineral content. When we examine the area in general, it can be said that eU, which has a rather irregular change as a result of surface weathering, shows an increasing trend from southwest to northeast. The areas where the eU concentration was low in the pluton can be explained by the transport of U to other places by factors such as surface waters or wind as a result of physical weathering. Areas of high concentration in the plutonic mass may be associated with light-colored rocks with a high content of quartz and therefore high SiO₂ content. In addition, the eTh concentration was measured at low values in some points on the mass, and this situation arises from magmatic rocks or soils that lost their acidic character as a result of weathering.

The eU/eTh ratio for the study area ranged from 0.031 to 1.034, with an average of 0.268. Although high values were observed in the margins and middle parts of the Sarıçiçek granodiorite, it was low in general in the mass. The Alibaba Formation had very high eU/eTh values. The eU/eTh ratio was 0.25 in continental crust [51] and 0.39 in the depleted upper mantle [52]. The eU/eTh values calculated for the study area showed that the rocks did not have completely crustal origin in the area but were a mixture of upper mantle and continental crust rocks. The sections with high eU/eTh ratio (0.4-1) are from the continental crust, and the areas with average values are from the mantle. The K/eU ratio varies in the range from 3280.9 to 53600 with a mean of 10303.21 for the whole area. The variation in K/eU ratios indicates that the melts from different mantle reservoirs were composed of various compositions in terms of source. Average K/eU values were given as 9475, 15607, 27245, and 12367 for the upper, middle, lower and total crusts, respectively [53]. Compared to the values defined

in the study area, areas with the average K/eU ratio (10303.21) are very close to the values given for the upper crust. Therefore, they are associated with the continental upper crust. The calculated K/eTh ratio for all rock and soil samples in the study area ranged from 1121.95 to 8620.69 with an average of 2452.6. Areas with high K/eTh ratio in the Sarıçiçek granodiorite were associated with granites with high K content (Table 1).

To determine whether there was a relationship between the uranium, thorium, and potassium concentrations measured in the study area, the correlation coefficients between these radioelements were calculated and the results are presented in detail below. Graphs showing the relationships between K-eTh, K-eU, and eTh-eU for the Sarıçiçek granodiorite and its surroundings are given in Fig. 10. As a result of the evaluation, the correlation coefficient between K and eTh radioelements was calculated as 0.67, and there was a reliable and linear relationship between the two radioelements. However, since the geological formations in the area contain these radioelements (especially uranium) in different proportions between the K-eU (R²=0.112) and eTh-eU (R²=0.110) ratios, there is a lot of scattering in the graph and there was no relationship between them.

The eTh and K concentrations showed similar increases and decreases in both Sarıçiçek granodiorite and Alibaba Formation rocks (Fig. 9). The variation in eTh and K concentration maps is quite similar. However, the concentration changes in the eU map are independent of these two radionuclides. That is, at the points where eTh and K were high, uranium was low depending on the mineral content. Therefore, a linear relationship was observed between K and eTh in the relationship graphs (Fig. 10), while a dispersed distribution was observed in the graphs of K-eU and eTh-eU, originating from the irregular eU variation.

A potassium composite map was generated (Fig. 11a) combining K in red, K/eTh in green, and K/eU in blue. Three different colors of cyan, blue, red, and green represent different amounts of radionuclides on the K composite map. Despite the low K and eU content, the eTh content is high in the anomaly zones represented by green color in the middle parts of the Sarıçiçek granitoid. In basaltic rocks (blue areas), which are a member of the Alibaba Formation surrounding the granitoid mass, K and eTh are low, and uranium is somewhat higher. These areas, which are high in eTh and eU and low in K especially in the southeast of the study area, are represented by cyan color. The red-colored areas (low eU and eTh and high K) are associated with granitic rocks with high K content.

Table 1. The K, eTh, and eU concentrations and dose rate, ratios of the concentration, and the geochemical indicators of uranium remobilization in the Sarıçiçek granodiorite and surroundings

	K (%)	eTh (ppm)	eU (ppm)	D (nGy/h)	eU/eTh	eU/K	eTh/K	U _{me} (%)	F parameter	eU-(eTh/3,5)
Min.	0,8	0,5	2,9	30,435	0,031	0,186	1,16	-123,3	0,08	-3,98
Max.	5,22	8,9	23,6	153,12	1,034	3,047	8,91	62,36	2,92	6,357
Mean	2,98	3,15	12,45	87,54	0,268	1,09	4,20	-14,70	0,77	-0,402

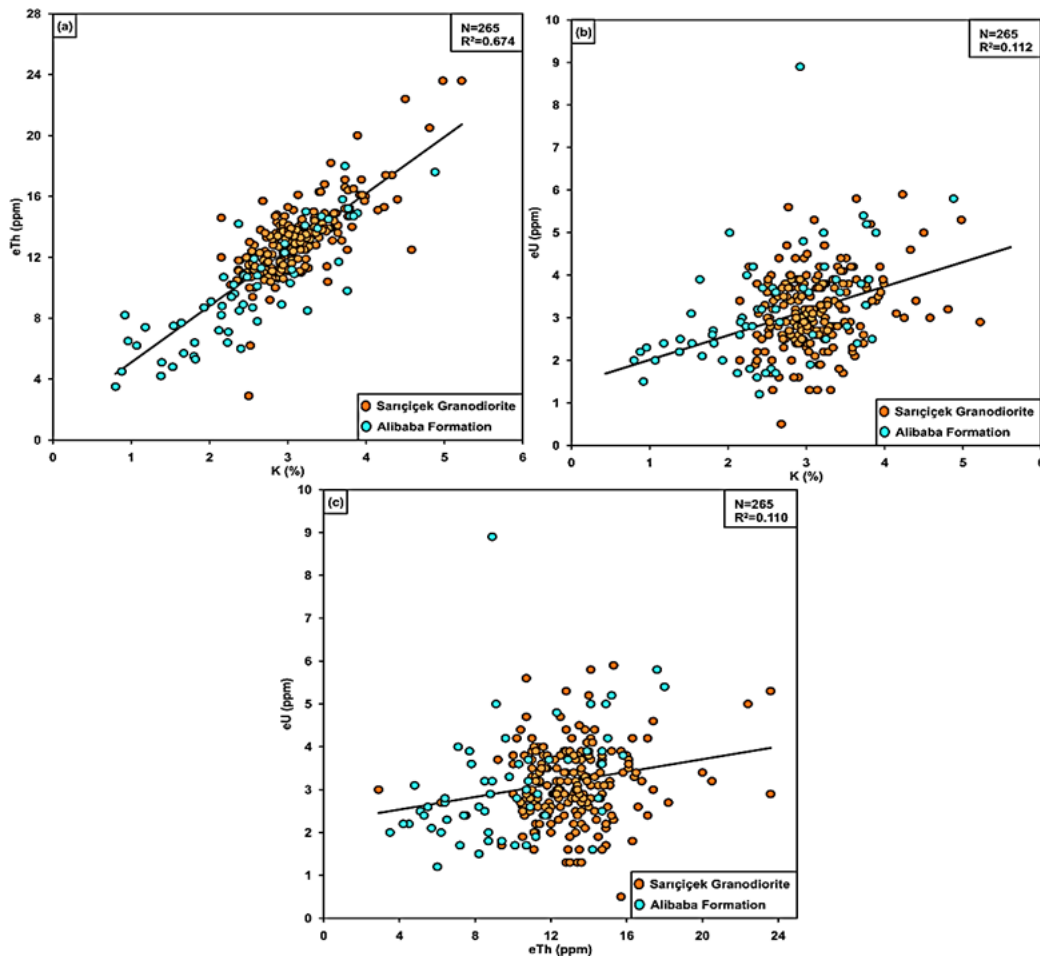


Figure 10. Variation diagrams of the Sarçiçek granodiorite and surroundings: a) K vs eTh, b) K vs eU, and c) eTh vs eU modified from [15]

The eTh composite map is shown in Fig. 11b. Areas that are observed as large inclusions in the north, west, and south parts of the study area represented by blue reflect low K and eTh contents and high eU content, and these areas are associated with basaltic rocks. The high K and eTh values and low eU content in the granitoid mass are shown in yellow. The areas with low eTh with high K and eU contents appear as small scattered points in the study area and are represented by magenta color. These areas were interpreted as areas where soils and rocks with volcanic materials have lost their acidic properties as a result of weathering. The areas (bright green) with high eTh with low K and eU concentrations spread from west to east of the area and are associated with areas where the rocks are concentrated by remaining in the environment and thus contain this element.

When the eU composite map given in Fig. 11c is carefully examined, different colored anomaly zones which consist of inclusions of various sizes were observed throughout the study area. K and eTh have average values in the granitoid, especially where the eU content is very low, and these areas (represented by blue color) are associated with uranium-depleted granitic rocks. There are magenta-colored enclosures (high K and eU, and low eTh) observed in the granitoid mass. These highly concentrated areas are associated with rocks with high quartz content. Finally, the green areas indicate higher eTh concentration than eU and K contents in the rocks as a result of surface weathering in both the

granitoid and the unit surrounding the granitoid. As can be seen from the composite map, uranium, which exhibits irregular change, shows an increasing trend from southwest to northeast.

The eU-(eTh)/3.5 ratio shows small changes towards the inner and marginal parts of the granodiorite (Fig. 12a). As with the eU concentration map, this rate of change has a distribution with high values especially in the marginal parts of the plutonic mass. For the study area, this ratio varies between -3.98 and 6.357, with an average value of -0.402. Negative values in the study area indicate uranium-poor areas, while positive values indicate uranium-rich areas. When the rate change in Fig. 9 and the eU map (Fig. 12a) are evaluated together, the eU concentration was quite low in areas showing negative values (the rate of change was very low), and this rate of change was positive, but rather high, in areas with high eU. Especially in the parts with negative values, this indicates that as the initial U content deteriorates, the radionuclide migrates.

In the mobility diagram (eU (ppm) versus eU-(eTh/3.5)) given in Fig. 12b, most of the data belonging to the Sarçiçek granodiorite are below the zero line. In the Alibaba Formation, which consists of andesite, basalt, and pyroclasts surrounding the granodiorite, most of the data had positive values. The diagram clearly shows that there is uranium transport from the granodiorite to the Alibaba Formation and that these rocks are enriched with uranium.

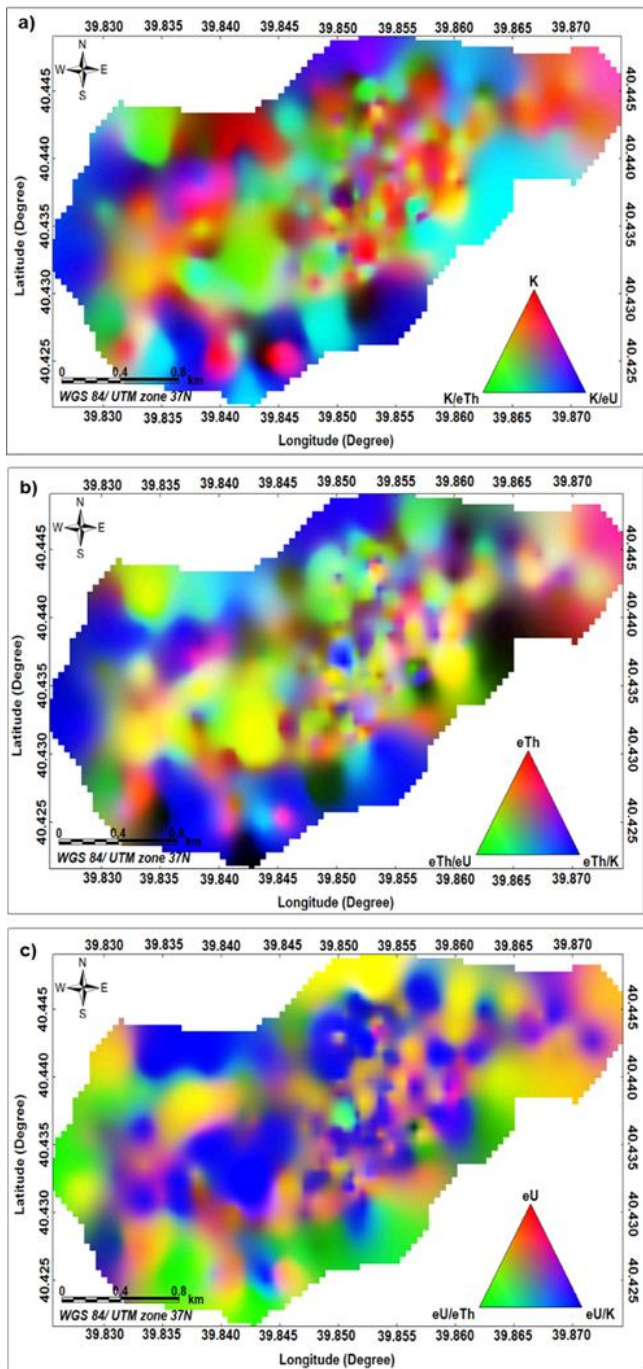


Figure 11. a) K, b) eTh, and c) eU composite image maps for the Sarıçiçek granodiorite and surroundings

The eU migration percentage calculated for Sarıçiçek granodiorite and surroundings ranges from -123.3 to 62.36, with an average of -14.70 (Fig. 12c, Table 1). Positive migration values obtained at the edges and northeast of the granodiorite in the study area indicate that migration is towards the inside of the unit. The fact that the migration percentage calculated for the Alibaba Formation is negative indicates that the U migration is outside the unit. Depending on some situations such as weathering, alteration, magmatic differentiation, sedimentation, and metamorphism, the uranium radionuclide in the environment moves from its environment to another environment, causing an increase and decrease. In the migration distribution map,

there was uranium migration towards the surrounding rocks, especially in the NW of the study area.

The alteration parameter (F), which has a distribution very similar to the eU migration distribution map, was calculated to be high in Sarıçiçek granodiorite (Fig. 12d). This situation indicates that the eU and K concentrations in the granodiorite are high in places and accordingly there is a small amount of uranium enrichment in the area. While the average F parameter for the study area was calculated as 0.77, minimum and maximum values varied between 0.085 and 2.92.

On the ternary map (Fig. 13a), areas with low eU, K, and eTh concentrations are represented by black color and are associated with basalts in the Alibaba Formation. Small inclusions of with especially granite and andesitic rocks, in the northern and western parts of the study area are represented by white color, and these parts correspond to areas with high concentrations of all three radioelements. Areas of high eTh with low K and eU concentrations on the map are shown with green inclusions, while areas with low K and eTh but high eU concentrations in the northeastern and western parts of the study area are represented in blue. The red color corresponds to high K areas with low eU and eTh concentrations. There are magenta-colored enclosures (high K with low U and Th) observed that vary from place to place in the southern, southwestern, and northeastern parts of the study area area. Areas with high contents of K and eTh but low content of eU are characterized by yellow color.

A ternary diagram was plotted for the study area, with each axis representing a radioelement composition. When the measurements taken on the exposed rock and soils with volcanic composition were evaluated, the data were concentrated on the eTh axis in the triangular ternary diagram (Fig. 13b). This situation for the radioelement concentration in the study area varied depending on the lithological units and their mineral content.

4.2. Assessment of In-situ Gamma-ray Data in the Sarihan Granodiorite and Surroundings

In the granodiorite, which has solid appearance, especially in the southern parts, the rocks are easily fragmented and look like soil due to arenization and hydrothermal weathering. Depending on this situation in Sarihan granodiorite, changes have occurred in the contents of radioactive elements. When the concentration and dose rate maps created based on radioactivity measurements of the granodiorite and surrounding rocks are examined together, generally high and moderate inclusions were observed in the granodiorite mass for all three radionuclides (Fig. 14). The lowest concentration values were found in the Hozbirikeyayla Formation (consisting of sandy limestones and limestone) and the ophiolitic olistostromal mélange containing sandstone, gravelly sandstone, basalt, and andesite. The highest radionuclide concentration and dose rate values were obtained in the Sarihan granodiorite containing quartz diorite, granodiorite, and quartz monzodiorite [54].

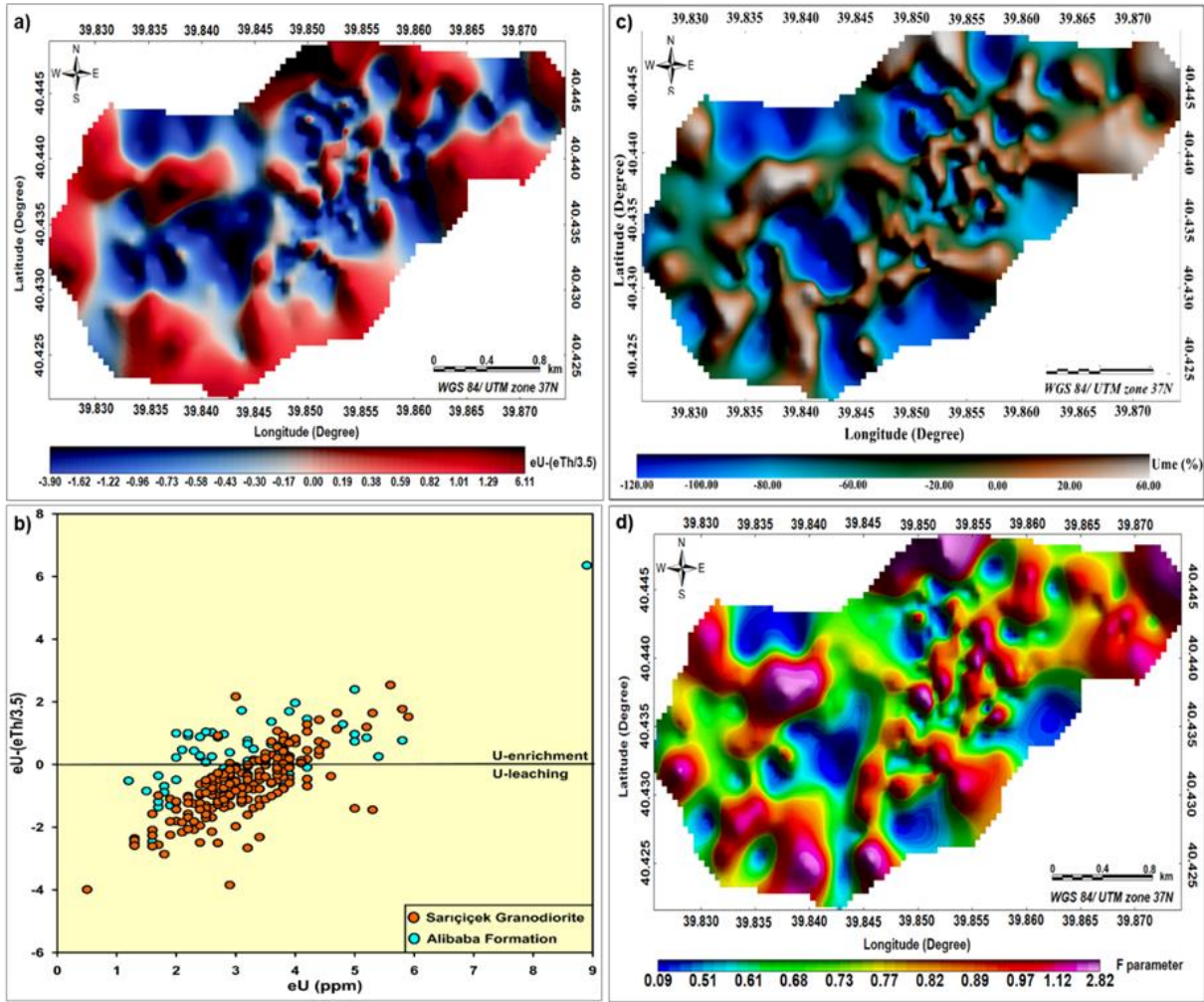


Figure 12. a) $eU-(eTh/3.5)$ uranium mobility, b) eU (ppm) versus $eU-(eTh/3.5)$ plot diagram, c) the uranium migration (U_{me} %), and d) F parameter maps for the Sariçiçek granodiorite and surroundings

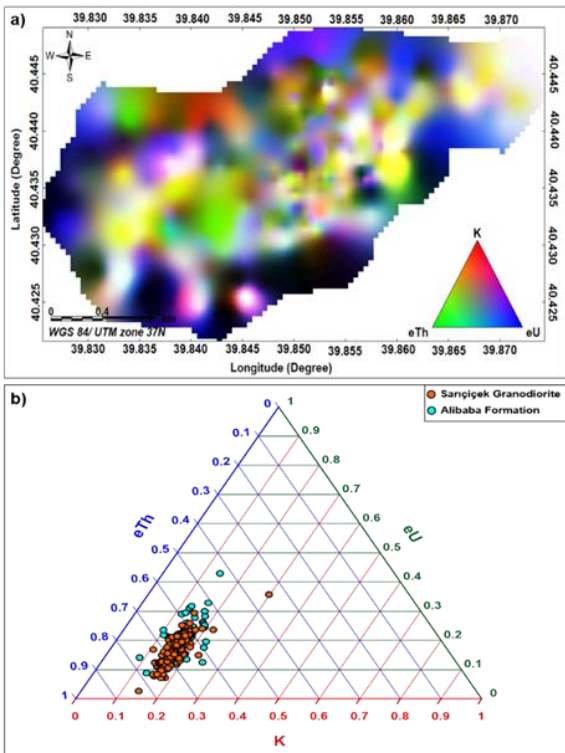


Figure 13. a) Radiometric ternary map, and b) $eU-eTh-K$ ternary diagram for the study area

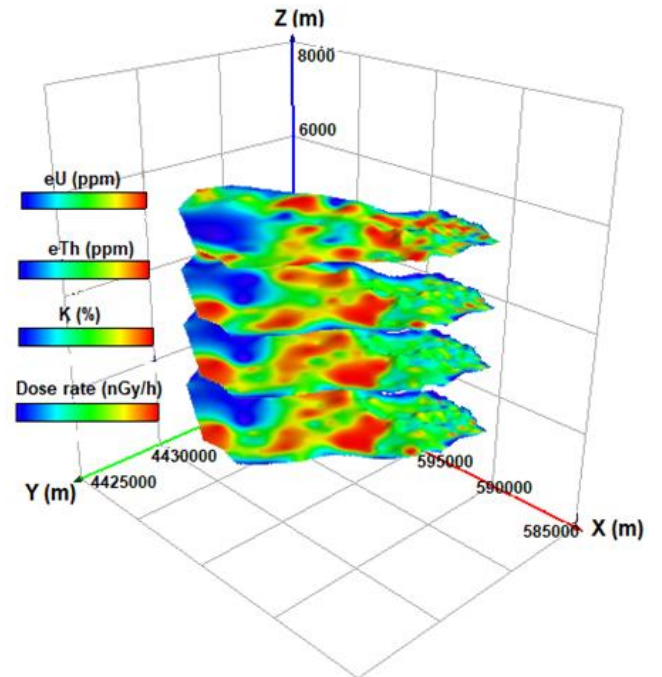


Figure 14. Three-dimensional representation of eU , eTh , K concentrations and dose rate distribution of Sarihan granodiorite and its surroundings (Bayburt) modified from [15]

Potassium is abundant in rock-forming minerals, especially in K feldspars (orthoclase, microcline, and mica (biotite)). The plutonic rock contained 6-18% orthoclase and 1-85% biotite in the Sarihan granodiorite [30]. Accordingly, areas with high K concentration were associated with rocks and soils containing these minerals. The reason why the potassium concentration was very low in the Hozbirikyayla Formation was concluded to be due to the carbonate content in the limestones forming this formation. The low concentration values measured in the study area can be explained by the precipitation of U in organic materials in rocks and soils, or by the transport of U minerals from the environment with the effect of factors such as surface waters or wind as a result of mechanical weathering in the rocks. The eU concentration distribution in the east of the study area was higher than in the west. This situation in the concentration distribution indicates that the element eU may have migrated from west to east.

eTh and K radionuclides were observed at high concentrations in the middle parts of the plutonic mass and places close to the ophiolitic mélangé, while small areas with moderately high values were observed in the northeast. As with these two radionuclides, while the U radionuclide had high-value changes in the middle of the area, it also showed very high concentration changes, especially in the northeast of the study area. The areas where the dose rate and radionuclide concentrations are high were related to K feldspar and the pluton with abundant quartz and accordingly high SiO₂ content. Low radionuclide concentrations and dose rates were observed in the Hozbirikyayla Formation, which contains limestone and sandy limestone surrounding the Sarihan granodiorite from the northwest to southeast.

According to the eU/eTh values given by researchers [51-52], the origin of the rocks in the study area was evaluated. The Sarihan granodiorite and surrounding rocks were classified as continental crustal rocks according to average eU/eTh values. According to the eU/eTh ratio change calculated for the whole area, the rocks in the study area are a mixture of continental crust and depleted upper mantle. The low value (<0.3) region in the center of the study area corresponds to continental crustal rocks, while the values between 0.3-0.5 represent depleted upper mantle origin rocks. The places where the eU/eTh ratio is high corresponded to formation boundaries, especially where limestones are found.

The K/eU ratio for the study area varied between 62.5 and 33000 with an average of 7111.88. According to the K/eU ratio values [53], the average K/eU values for the study area were correlated with the continental upper crust. This ratio was calculated in previous studies [55]. In addition, the average K/eU ratio calculated for the area was also consistent with the K/U ratio (7000) values calculated in previous studies.

The average K/eTh ratio in the study area was 1376.15 and varied between 35.71 and 5000 (Table 2). Areas with a K/eTh ratio of 564.97-833.3 correspond to the mélangé belt, while areas with a K/eTh ratio of 909.1 to 1428.57 correspond to Sarihan granodiorite with high K content and areas with a high ratio (K/eTh=2500-

5000) of limestones. The K/eTh ratio gives information about the structure of mica and feldspars, and the increase in this ratio is accepted as an indicator of the clay ratio.

Statistical evaluations were made for Sarihan granodiorite and surroundings, as for the Sariçiçek granodiorite, to determine correlations between radionuclide concentrations (K, eU, eTh). As seen in the correlation graphs (Fig. 15), although there was a good linear relationship ($R^2=0.817$) between K-eTh, there was almost no relationship between K-eU ($R^2=0.234$) and eTh-eU ($R^2=0.158$). Another reason why no relationship could be observed between the U radionuclide and these two radionuclides may be that the U radionuclide is highly affected by events such as surface weathering in the rocks and displays irregular changes depending on this situation. When the geological formations in the area are evaluated within themselves; while the Hozbirikyayla limestone showed the best K-eTh relationship, no relationship was observed between eTh and eU in the Sarihan granodiorite.

As can be clearly seen from the composite maps prepared for each radionuclide, the color transitions in the map show good agreement with the geological formations in the study area. Radionuclide composite maps consist of the combination of the radionuclide in the rock or soil and the ratios of these radionuclides to each other, as shown in Fig. 16. As can be seen on the map, the equivalent uranium composite values vary according to the rock and soil type. While limestone is represented by green and yellow colors; blue, orange, and magenta colors are dominant within the granitoid. Blue areas on the map show areas associated with low K and eTh and high eU, while yellow represents low eU concentrations overlapping with sandy limestone in the southeast part of the area. There are magenta-colored areas (high K and eU and low eTh) varying from place to place from the southwest to the northeast of the study area (Fig. 16a).

On the map, which shows three distinct color changes of yellow, blue, and green, light colors are dominant especially on the granitoid, and the eTh content is relatively higher than eU and K in these areas. The equivalent thorium composite image map in Fig. 16b shows a blue area (high eU with low K and eTh) which has low content of eTh that coincides with the Hozbirikyayla Formation in the northwestern and southeastern parts of the study area. The areas represented by a dark color indicate rocks with low concentration values for eU, eTh, and K.

The potassium composite map created by using K radionuclide and K/eTh and K/eU ratios is given in Fig. 16c. As with the potassium concentration distribution map shown in Fig. 14, the areas represented by red color are associated with low equivalent thorium and equivalent uranium content versus high potassium content rocks. Potassium variation zones are shown as cyan-colored parts on the potassium composite image map, and these zones are related to rocks that have low K concentrations which coincide with limestones with high carbonate content.

Table 2. The K, eTh, and eU concentrations and dose rate, ratios of the concentration, and the geochemical indicators of uranium remobilization in the Sarihan granodiorite and surroundings

	K (%)	eTh (ppm)	eU (ppm)	D (nGy/h)	eU/eTh	eU/K	eTh/K	U _{me} (%)	F parameter	eU-(eTh/3,5)
Min.	0,01	0,2	0,8	8,038	0,043	0,303	2	-160,47	0,06	-6,3
Max.	4,41	33,6	5,4	158,78	5,91	17,77	17,77	27,65	1,47	3,828
Mean	1,83	13,6	2,73	73,03	0,284	1,92	7,47	-48,44	0,38	-1,164

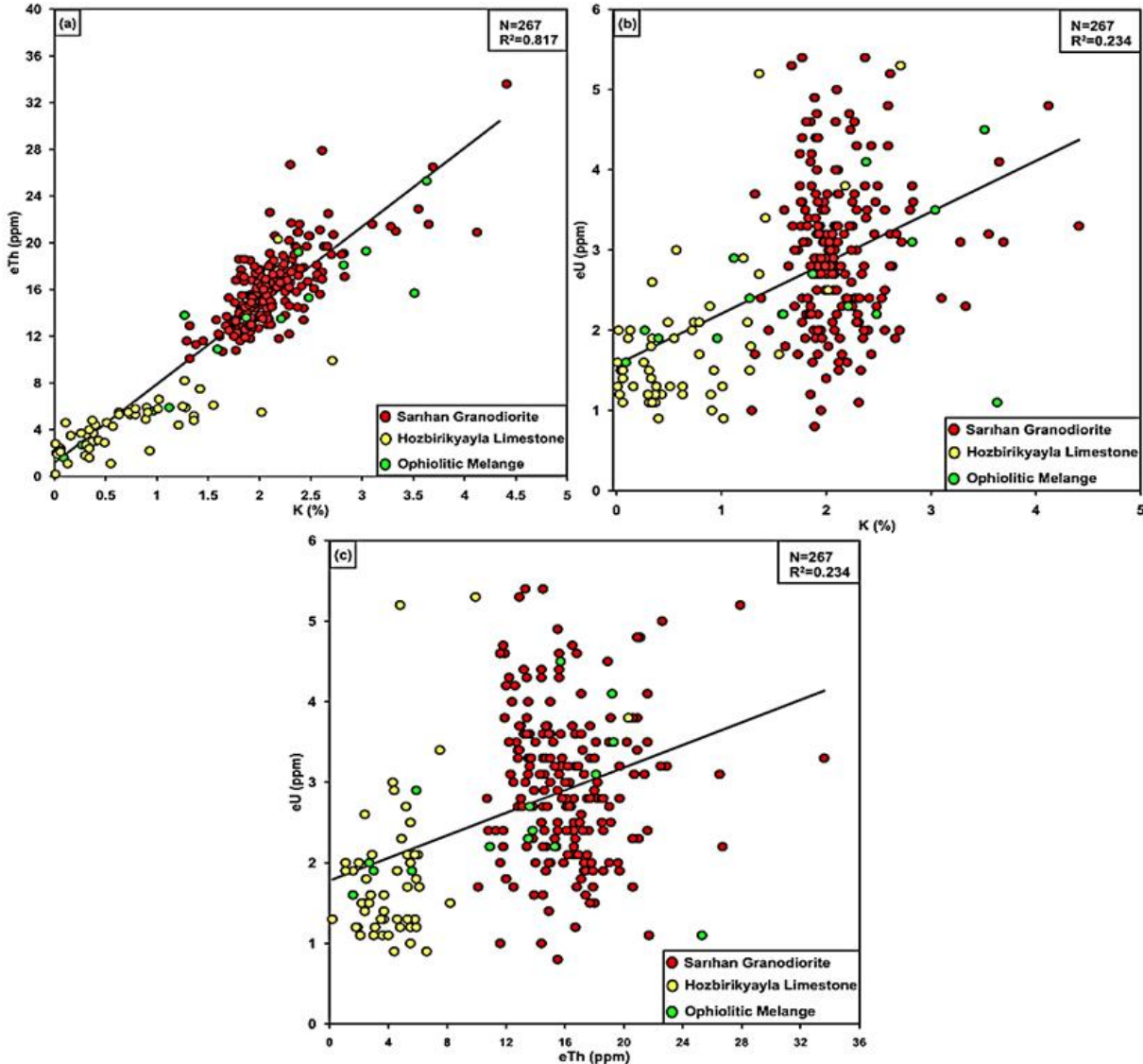


Figure 15. Variation diagrams of the Sarihan granodiorite and surroundings: a) K vs eTh, b) K vs eU, and c) eTh vs eU modified from [15]

In the study area, high $eU-(eTh)/3.5$ values were obtained in the limestone and ophiolitic mélange, as with the other geochemical radionuclide ratios (Fig. 17a). While high and moderate values were observed in the northern part of the Sarihan granodiorite, quite low values were obtained in the middle and southern parts of the plutonic mass. For the study area, this ratio varies between -6.3 and 3.828, with an average value of -1.164. This ratio also represents the original U content in the medium due to the remaining and immobile Th radionuclide. Over time, the U radionuclide, which is exposed to events such as decomposition and alteration in the formation, cannot maintain its original concentration and changes. The mobility diagram for the Sarihan granodiorite and its surroundings is given in Fig. 17b. As with the Sarıççek granodiorite, most of the

values in the granodiorite are negative values. Most values for the Hozbirikyayla limestone are above the zero line and there is uranium enrichment as a result of uranium transport from the granodiorite. There was a partial change in the values of the mélange belt, and increases and decreases were observed in the amount of uranium in the environment depending on the type of rock.

While the percentage of U migration calculated for the Sarihan granodiorite and its surroundings had an average of -48.43, these values varied between -160.47 and 27.645 (Fig. 17c). Positive migration values obtained for the Sarihan granodiorite in the study area show that the migration is towards the inside of the unit. The fact that the migration percentages calculated for the mélange and Hozbirikyayla Formation are negative

indicate that the U migration is outside the unit. While there is a decrease in the U concentration as a result of transport in the environment, it added to the existing U radionuclide in the environment where it was transported, causing an increase in the concentration.

The Efimov (F) parameter was calculated to be high for the Sarihan granodiorite (Fig. 17d). This situation indicates that the eU and K concentrations in the granodiorite are high and accordingly there was U enrichment in the area. While the average F parameter for the entire study area was calculated as 0.381, minimum and maximum values ranged between 0.0057-1.473. Areas with high F values, as in Sariçiçek granodiorite, indicate possible areas for metallic mines. The places where this parameter is high are associated with high-grade alteration zones and indicate areas with K enrichment related to the alteration of mafic minerals in the rocks during potassic alteration [56].

The ternary map for the Sarihan granodiorite and surroundings is given in Fig. 18a. The dark areas represented by low values are related to limestone, and sandy limestones especially in the west to the northeast part of the Hozbirikyayla Formation surrounding the Sarihan granodiorite and the eTh, K, and eU concentrations are low in these areas. The low uranium and high potassium and thorium parts on the map are shown in yellow, while the blue color in the southeast of the area corresponds to low uranium regions. Finally, light magenta color inclusions appearing in places coincide with low thorium and high uranium and potassium concentrations. In addition, areas identified by the light green color indicate uranium enrichment.

The ternary diagram is a diagram created base on certain constant equalization of the sum of three variable data sets, such as potassium, uranium, and thorium (Fig. 18b). This constant variable used in the definition is usually expressed as either 1.0 or 100%. In the study, it was assumed that the K, eU, and eTh variables are equal to 1.0. K, eU, and eTh concentrations measured in different lithological formations such as Sarihan granodiorite, Hozbirikyayla Formation, and ophiolitic mélange belt are given on ternary diagram. According to the diagram, while the Sarihan granodiorite exhibits high thorium values, the mélange belt and Hozbirikyayla formation have higher uranium values than this granitoid.

While the K₂O and SiO₂ contents of the rocks forming the non-adakitic Sariçiçek granodiorite were between 2-4.5% and 58-75%, respectively [28], the K₂O and SiO₂ amounts for the adakitic Sarihan granodiorite were between 2.16-2.76% and 61.16-65.29% [35]. According to the silica content, both Sariçiçek granodiorite and Sarihan granodiorite consist of rocks with a transitional composition (intermediate magma, between 53-65% Si) between felsic and mafic magma. These rocks with felsic magma composition rich in silica (Si) contain significant amounts of potassium, aluminum, and sodium and small amounts of magnesium, iron, and calcium. Adakitic rocks with high silica content and felsic magma composition are associated with high eTh/eU ratios due to low U and high Th content. This situation is explained by the transport and removal of elements such as U, Th, and Rb in the lower crust with the solution (especially the U

radionuclide) during partial melting by many researchers [51].

In the study, the average eTh/eU ratio was calculated as 5.5 for the non-adakitic Sariçiçek granodiorite and as 4.16 for the adakitic Sarihan granodiorite [15]. The average eTh/eU ratios as a result of studies about adakitic rocks around the World were; Panamanian adakites [57] 2.7, Pulur adakites [37] 3.33, Kamchatka adakites [58] 2.8, Arkeen Wawa adakites [59] 4.5, and 3.4-6 in adakites found in volcanic zones in Chile [60]. The average eTh/eU value obtained for Sarihan granodiorite with adakitic character in this study was closer to the mean crustal value (eTh/eU=4.0) [61], while adakitic rocks are generally represented with high eTh/eU values.

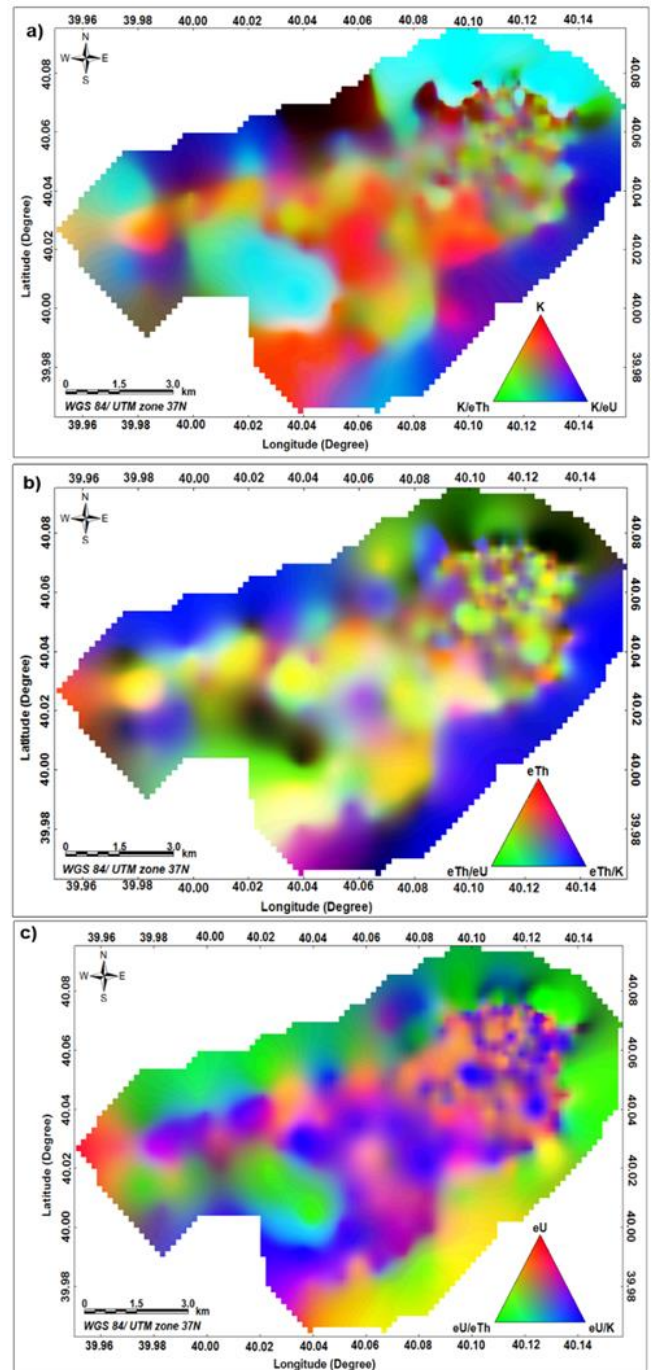


Figure 16. a) K, b) eTh, and c) eU composite image maps for the Sarihan granodiorite and surroundings

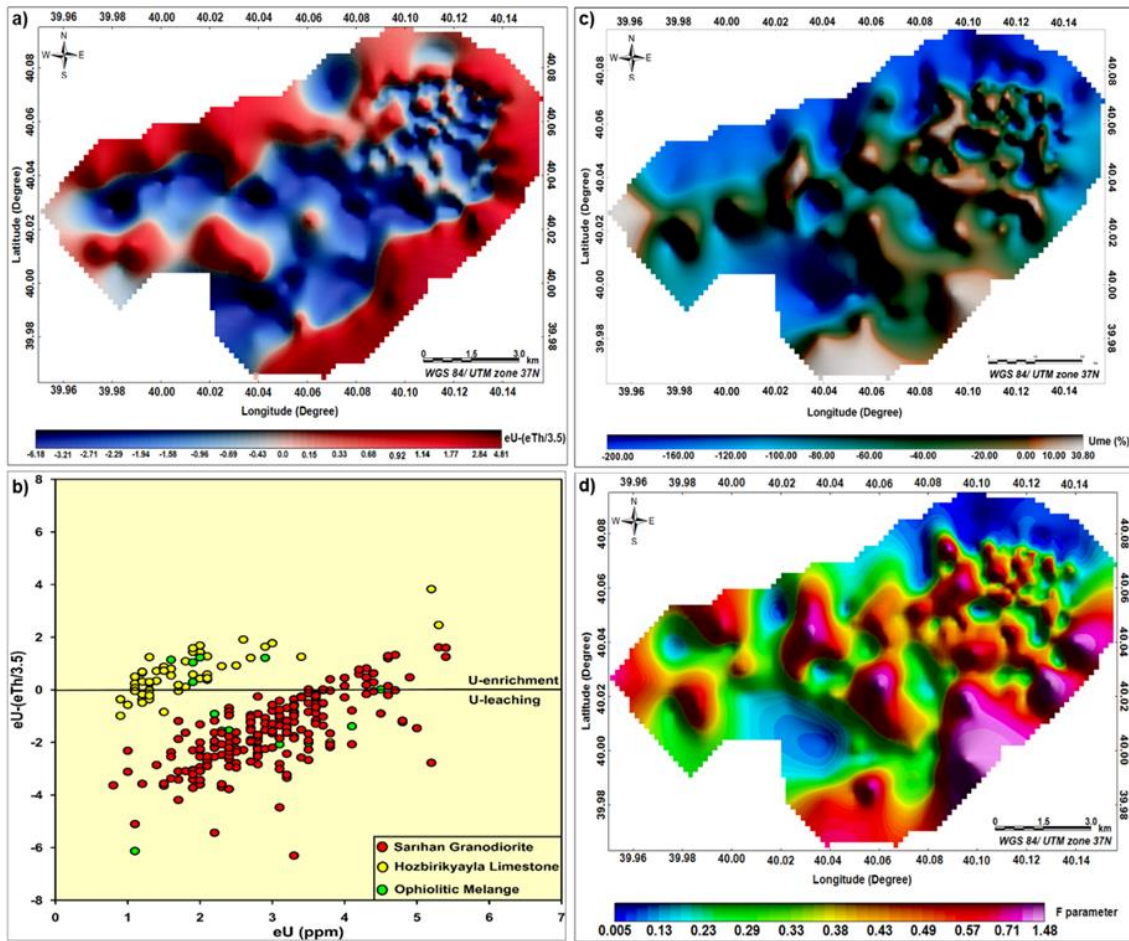


Figure 17. a) eU-(eTh/3.5) uranium mobility, b) eU (ppm) versus eU-(eTh/3.5) plot diagram, c) The uranium migration (U_{me} %), and d) F parameter maps for the Sarihan granodiorite and surroundings

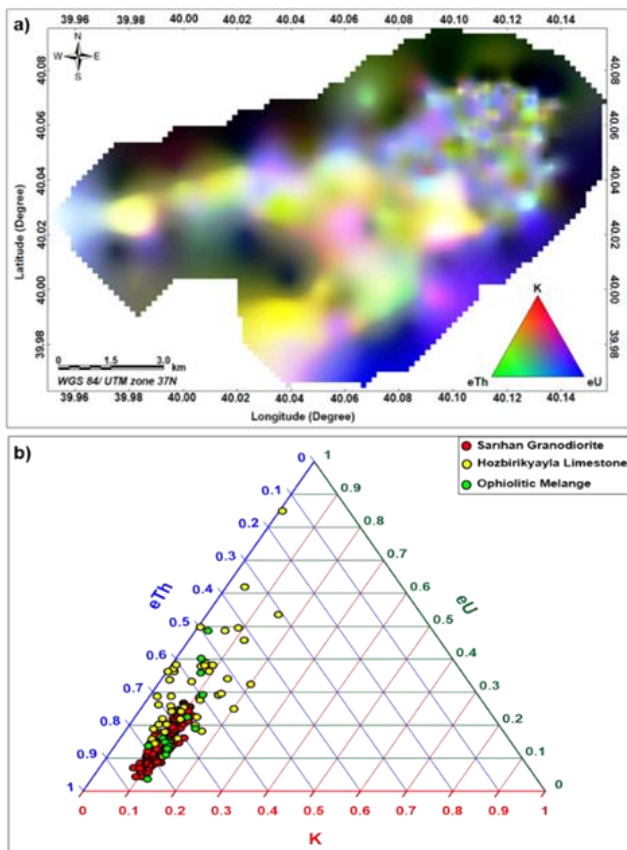


Figure 18. a) Radiometric ternary map, and b) eU-eTh-K ternary diagram for the study area

4.3 Laboratory Gamma Spectrometry Analysis of Samples Collected from Study Area (Gümüşhane)

The relationship between the data measured in the field and the data measured with the system with higher sensitivity in the laboratory was determined as activity unit (Bq/kg). The concentrations of K, eU, and eTh with in-situ measurements were recorded as % and ppm, respectively. Thus, in order to compare in-situ and laboratory measurements, concentration units must be converted into activity units [62]. The conversion factors for K, eU, and eTh in Bq/kg are 313, 12.35, and 4.06, respectively. The average activity concentrations of ^{232}Th , ^{238}U , and ^{40}K radioactive nuclei obtained from laboratory and field measurements (Table 3) for the samples analyzed are shown in Fig. 19. When Fig. 19 and Table 3 are examined together, low differences between the in situ and laboratory results were observed for the ^{238}U activity, while high differences were observed for the ^{40}K activity values.

The ranges of the activity concentrations of ^{238}U , ^{232}Th , and ^{40}K were 6.055-72.86 Bq/kg, 19.48-95.81 Bq/kg, and 287.96-1633.86 Bq/kg for the in-situ measurements, and 6.71-70.89 Bq/kg, 16.08-83.62 Bq/kg, and 208.72-1262 Bq/kg in the laboratory, respectively. The determined radionuclide activity concentrations were compared with studies in the literature for similar rock types [63-67]. As a result, no significant difference was found between in-situ and laboratory measurements.

Table 3. Average activity concentrations of ^{238}U , ^{232}Th and ^{40}K measured in laboratory and in-situ for Sariçiçek granodiorite and its surroundings

Formation	Laboratory Measurements (HPGe detector)			In-situ Measurements (NaI(Tl) detector)		
	U (Bq/kg)	Th (Bq/kg)	K (Bq/kg)	U (Bq/kg)	Th (Bq/kg)	K (Bq/kg)
Alibaba Formation	29.2	37.05	422.436	35.72	45.12	543.71
Sarıçiçek Granodiorite	42.93	51.68	422.81	40.91	54.35	495.71

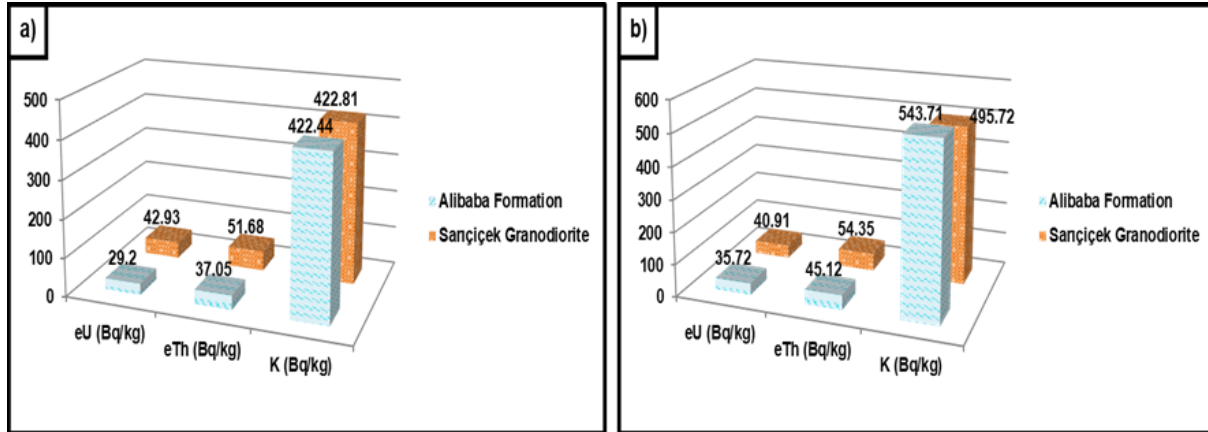


Figure 19. Activity concentrations of ^{232}Th , ^{238}U and ^{40}K obtained from a) HPGe (Laboratory) and b) NaI(Tl) (In-situ) detectors for Sariçiçek granodiorite and surroundings modified from [15]

5. Conclusion

In this study, Sariçiçek (Gümüşhane) and Sarihan granodiorites (Bayburt) and their surrounding formations were examined by using portable spectrometry. The data measured and calculated in the field were represented on maps, which include maps of radionuclide concentrations, radionuclide ratios, composite image, and uranium remobilization maps.

In the radioactivity measurements carried out in the study areas, radionuclide concentrations showed irregular changes in both granodiorites due to the rock (consisting of quartz monzodiorite, granodiorite, and quartz diorite) and mineral differences (quartz, muscovite, sphene, biotite, and K-bearing feldspars (orthoclase, plagioclase)) in the formations. While the highest radionuclide concentrations (eU, eTh, and K) were mostly observed in granodioritic masses, low values were obtained in the formations surrounding these masses. Based on the average eU/eTh, K/eTh, and K/eU data, the rocks in the study area do not entirely have crustal origin, but formed as a result of a mixture of upper mantle and continental crust. It was concluded that the irregular changes in the main, trace, and rare earth elements in the rocks were affected by differentiation during crystallization to a high degree, partial melting events to a partial degree, and also hybridization of two magmas during the formation of the rocks. These results are supported by the results obtained in other studies [40,28].

When the study is evaluated in terms of uranium mobility, positive migration values obtained for the Sariçiçek and Sarihan granodiorites show that the migration is towards the inside of the unit, while the negative values for the surrounding formations indicate that the U migration was outside the units. To summarize uranium migration or transport in the study, uranium transport was not related to chemical weathering but to

the transportation of rock fragments and soil as a result of physical weathering (wind, surface waters, tectonic, etc.) and the accumulation of radionuclides in these units.

There are differences between the data measured in two different environments, as can be seen from the data obtained from the in-situ and laboratory measurements. This may be caused by factors related to the device used for measurement (crystal difference in the detector, crystal volume, calibration) and the measurement time, or external factors (cosmic rays, radioisotope particles in the air, soil humidity, vegetation, etc.) in the area where the measurement is made. During in-situ measurement with a gamma-ray spectrometer, the value measured in each window of the spectrometer; that is, the number of gamma rays is equal to the sum of the gamma rays coming from terrestrial and extraterrestrial sources. As a result of this situation, the *in-situ* results obtained in this study were higher than the laboratory results for ^{238}U , ^{232}Th , and ^{40}K . In brief, there was no significant difference between the results of the in situ measurements with the NaI(Tl) detector and the laboratory analysis made with the HPGe detector for the activity values.

To summarize briefly, nowadays, chemical and petrological variations in rocks can be investigated and mapped quickly and easily, depending on the relationship between geology and radionuclide concentrations, especially in areas where granitic rocks are present, with in situ gamma-ray spectrometry measurements (K, U, and Th concentrations).

Acknowledgement

We would bluntly like to express our gratitude to the reviewers and the editor of the Journal, for their helpful criticism and detailed discussions and suggestions that improved the manuscript. Grateful thanks are offered to the provider of financial support for the research presented here: Karadeniz Technical University

Scientific Research Project (Project no: BTAP-9588). A part of this study was presented as an oral presentation at the congress named International Online Conferences on Engineering and Natural Sciences (IOCENS 2021).

Author contributions

Suna Altundaş: Conceptualization, Methodology, Software Interpretation, Visualization, Writing-Original draft preparation, Field study. **Hakan Çınar:** Investigation, Writing-Reviewing and Editing.

Conflicts of interest

The authors declare that they have no known competing financial interests or personal relationships that could have appeared to influence the work reported in this paper.

References

- Dizman, S. (2006). Measurement of natural radioactivity level in Rize-centre and towns of Rize. Master thesis, Karadeniz Technical University, Graduate School of Natural and Applied Sciences, Trabzon, Turkey.
- Valkovic, V. (1984). Radioactivity in the Environment. Elsevier Science B. V., Netherlands.
- Kathren, R.L. (1984). Radioactivity in the Environment: Sources, Distribution and Surveillance. Harwood Academic Publishers, New York.
- UNSCEAR. (2000). United Nations Sources and Effects of Ionizing Radiation. Volume I: Sources; Volume II: Effects. United Nations Scientific Committee on the Effects of Atomic Radiation, Report to the General Assembly, with scientific annexes. United Nations sales publications E.00.IX.3 and E.00.IX.4. United Nations, New York.
- Apaydın, G., Köksal, O.K., Cengiz, E., & Tıraşoğlu, E., Baltas, H., Karabulut, K., & Söğüt, Ö. (2019). Assessment of natural radioactivity and radiological risk of sediment samples in Karacaören II dam Lake, Isparta/Turkey. *ALKÜ Fen Bilimleri Dergisi*, 28-35.
- Canbaz, B., Çam, N.F., Yaprak, G., & Candan, O. (2010). Natural radioactivity (^{226}Ra , ^{232}Th and ^{40}K) and assessment of radiological hazards in the Kestanbol granitoid, Turkey. *Radiation Protection Dosimetry*, 141,192-198.
- Tzortzis, M., Tsertos, H., Christofides, S., & Christodoulides, G. (2003). Gamma-ray measurements of naturally occurring radioactive samples from Cyprus characteristic geological rocks. *Radiation Measurements*, 37, 221–229.
- Naumov, G.B. (1959). Transportation of uranium in hydrothermal solution as a carbonate. *Geochemistry*, 1, 5-20.
- Aydın, İ. (2004). Radiometric method and Gamma-ray spectrometer in Geophysics.
- Abd El-Mageed, I.A., El-Kamel, H.A., & Abbady, A. (2011). Assessment of natural and anthropogenic radioactivity levels in rocks and soils in the environments of Juban town in Yemen. *Radiation Physics and Chemistry*, 80, 710–715.
- Heikal, M.Th.S., El-Dosuky, B.T., Ghoneim, M.F., & Sherif, M.I. (2012). Natural radioactivity in basement rocks and stream sediments, Sharm El Sheikh Area, South Sinai, Egypt: Radiometric levels and their significant contributions. *Arabian Journal of Geosciences*.
- Youssef, A., Hassan, A., & Mohamed, M. (2009). Integration of remote sensing data with the field and laboratory investigation for lithological mapping of granitic phases: Kadabora pluton, Eastern Desert, Egypt. *Arabian Journal of Geosciences*, 2, 69-82. <https://doi.org/10.1007/s12517-008-0020-2>.
- Azzaz, S., Arnous, M., Elmowafy, A., Salem Kamar, M., Abdel Hafeez, W. (2018). Lithological discrimination and mapping using digital image processing, petrographic and radioactive investigation of Wadi Dahab area, Southeastern Sinai, Egypt. *Middle East Journal of Applied Sciences*, 8, 444-464.
- Bayoumi, M.B., & Emad, B.M. (2020). Mapping and Lithological discrimination using digital image processing and radioactive investigations of Wadi Um Gheig area, Central Eastern Desert, Egypt. *Middle East Journal of Applied Sciences*, 10, 737-754. <https://doi.org/10.36632/mejas/2020.10.4.65>.
- Altundas, S. (2016). Investigation of Sarıçiçek and Sarıhan Granodiorites using in-situ Gamma-Ray Spectrometer and Magnetic Susceptibility Methods. PhD thesis (in Turkish with an English abstract), Karadeniz Technical University, Trabzon.
- Pourimani, R., Zare, M.R., & Ghahri, R. (2014). Natural radioactivity concentrations in Alvand granitic rocks in Hamadan, Iran. *Radiation Protection and Environment*, 37, 132-140. <https://doi.org/10.4103/0972-0464.154866>.
- Papadopoulos, A., Altunkaynak, S., Koroneos, A., Ünal, A., & Kamacı, Ö. (2016). Distribution of natural radioactivity and assessment of radioactive dose of Western Anatolian plutons, Turkey. *Turkish Journal of Earth Sciences*, 25, 434-455. <https://doi.org/10.3906/yer-1605-4>.
- Maden, N., Akaryalı, E., & Çelik, N. (2019). The in situ natural radionuclide (^{238}U , ^{232}Th and ^{40}K) concentrations in Gümüşhane granitoids: implications for radiological hazard levels of Gümüşhane city, northeast Turkey. *Environmental Earth Sciences*, 78, 330. <https://doi.org/10.1007/s12665-019-8333-x>.
- Yalcin, F., Ilbeyli, N., Demirbilek, M., Yalcin, M.G., Gunes, A., Kaygusuz, A., & Ozmen, S.F. (2020). Estimation of Natural Radionuclides' Concentration of the Plutonic Rocks in the Sakarya Zone, Turkey Using Multivariate Statistical Methods. *Symmetry*, 12, 1048. <https://doi.org/10.3390/sym12061048>.
- Saleh, G.M., Kamar, M.S., Rashed, M.A., & El-Sherif, A.M. (2015). Uranium Mineralization and Spectrometric Prospecting along Trenches of Um Safi area, Central Eastern Desert of Egypt. *Geoinformatics & Geostatistics: An Overview*, 3, 1. <https://doi.org/10.4172/2327-4581.1000128>.
- Awad, H.A., Zakaly, H.M.H., Nastavkin, A.V., El-Tohamy, A.M., & El-Taher, A. (2021). Radioactive

- mineralization on granitic rocks and silica veins on shear zone of El-Missikat area, Central Eastern Desert Egypt. *Appl. Radiation Isotopes*, 168. <https://doi.org/10.1016/j.apradiso.2020.109493>.
22. Hassan, S.M., Youssef, M.A.S., Gabr, S.S., & Sadek, M.F. (2022). Radioactive mineralization detection using remote sensing and airborne gamma-ray spectrometry at Wadi Al Miyah area, Central Eastern Desert, Egypt. *The Egyptian Journal of Remote Sensing and Space Science*, 25, 37-53. <https://doi.org/10.1016/j.ejrs.2021.12.004>.
 23. Attia, T.E., & Shendi, E.H. (2013). Uranium migration history in the igneous and metamorphic rocks of Solaf-Umm Takha area, based on multi-variate statistical analysis and favorability indices, central south Sinai, Egypt. *IOSR Journal of Applied Geology and Geophysics (IOSR-JAGG)*, 1, 9-20. <https://doi.org/10.13140/2.1.1438.9444>.
 24. Dessouky, O., & Ali, H. (2018). Using Portable Gamma-Ray Spectrometry for Testing Uranium Migration: A Case Study from the Wadi El Kareim Alkaline Volcanics, Central Eastern Desert, Egypt. *Acta Geologica Sinica*, 92, 2214-2232. <https://doi.org/10.1111/1755-6724.13724>.
 25. Sundararajan, N., Pracejus, B., Al Khirbash, S., Al Hosni, T., Ebrahimi, A., Al-lazki, A., & Al-Mushani, M. (2019). Radiometric Surveys for Detection of Uranium in Dhofar Region, Sultanate of Oman. *Sultan Qaboos University Journal for Science [SQUJS]*, 24, 36-46. <https://doi.org/10.24200/squjs.vol24iss1pp36-46>.
 26. Khatlab, M.R., Tawfic, A.F., & Omar, A.M. (2021). Uranium-series disequilibrium as a tool for tracing uranium accumulation zone in altered granite rocks, *International Journal of Environmental Analytical Chemistry*, 101(12), 1750-1760. <https://doi.org/10.1080/03067319.2019.1686495>.
 27. Akingboye, A.S., Ademila, O., Okpoli, C.C., Oyeshomo, A.V., Ijaleye, R.O., Faruwa, A.R., Adeola, A.O., & Bery, A.A. (2022). Radiogeochemistry, uranium migration, and radiogenic heat of the granitic gneisses in parts of the southwestern Basement Complex of Nigeria. *Journal of African Earth Sciences*, 188. <https://doi.org/10.1016/j.jafrearsci.2022.104469>.
 28. Karshi, O. (2002). Petrographic, mineralogical and chemical findings for magma interactions in granitoid rocks: Dölek and Sarıçiçek plutons (Gümüşhane, NE-Turkey). PhD Thesis, Karadeniz Technical University, Institute of Science, Trabzon.
 29. Aydın, A., Ferre, E.C., & Aslan, Z. (2007). The Magnetic Susceptibility of Granitic Rocks as a Proxy for Geochemical Composition: Example from the Saruhan Granitoids, NE Turkey. *Tectonophysics*, 441, 85-95.
 30. Aslan, Z. (2005). Petrography and Petrology of the Calc-Alkaline Sarıhan Granitoid (NE Turkey): An Example of Magma Mingling and Mixing. *Turkish Journal of Earth Sciences*, 14, 185-207.
 31. Ketin, İ. (1966). Tectonic Units of Anatolia. *Journal of MTA*, 66, 20-43.
 32. Bektaş, O., Yılmaz, C., Taslı, K., Akdağ, K., & Özgür, S. (1995). Cretaceous rifting of the eastern Pontide carbonate platform (NE Turkey): the formation of carbonates breccias and turbidites as evidences of a drowned platform. *Geologia*, 57(1-2), 233-244.
 33. Bektaş, O., Şen, C., Atıcı, Y., & Köprübaşı, N. (1999). Migration of the Upper Cretaceous subduction-related volcanism toward the back-arc basin of the eastern Pontide magmatic arc (NE Turkey). *Geological Journal*, 34, 95-106.
 34. Eyüboğlu, Y., Dudas, F.O., Santosh, M., Xiao, Y., Yi, K., Chatterjee, N., Wu, F.Y., & Bektaş, O. (2016b). Where are the remnants of a Jurassic Ocean in the Eastern Mediterranean Region. *Gondwana Research*, 33, 63-91. doi:10.1016/j.gr.2015.08.017.
 35. Eyüboğlu, Y., Chung, S.L., Santosh, M., Dudasi, F.O., & Akaryali, E. (2011). Transition from shoshonitic to adakitic magmatism in the eastern Pontides, NE Turkey: implications for slab window melting. *Gondwana Res.*, 19, 413-429.
 36. Karşlı, O., Chen, B., Aydın, F., & Şen, C. (2007). Geochemical and Sr-Nd-Pb isotopic compositions of the Eocene Dölek and Sarıçiçek Plutons, Eastern Turkey: implications for magma interaction in the genesis of high-K calc-alkaline granitoids in a post-collision extensional setting. *Lithos*, 98, 67-96.
 37. Eyüboğlu, Y., Santosh, M., Dudas, F.O., Akaryali, E., Chung, S.L., Akdag, K., & Bektaş, O. (2013a). The nature of transition from adakitic to non-adakitic magmatism in a slab-window setting: A synthesis from the eastern Pontides, NE Turkey. *Geoscience Frontiers*, 4, 353-375.
 38. Güven, İ.H. (1993). Geological and metallogenic map of the Eastern Black Sea Region, 1:250000 Map, MTA, Trabzon.
 39. Eyüboğlu, Y., Chung, S.L., Dudas, F.O., Santosh, M., Akaryali, E. (2011a). Transition from shoshonitic to adakitic magmatism in the Eastern Pontides, NE Turkey: Implications for slab window melting. *Gondwana Research*, 19, 413-429.
 40. Aslan, Z. (1998). Petrography, Geochemistry and Petrology of Saraycık-Sarıhan Granitoid (Bayburt) and Surrounding Rocks and Geochronology of Sarıhan Granitoid. PhD thesis, Karadeniz Technical University, Trabzon.
 41. IAEA. (1974). Instrumentation for uranium and thorium exploration, International Atomic Energy Agency Technical reports series No. 158, Vienna.
 42. Killeen, P.G., & Cameron, G.W. (1977). Computation of in situ potassium, uranium and thorium concentrations from portable gamma-ray spectrometer data. In: Report of activities, part A, Geological Survey of Canada, 77-1A, 91-92.
 43. GF Instruments. (2009). Gamma Surveyor User Manual. GF-Instruments: Brno, Czech Republic.
 44. Darnley, A.G. (1973). Airborne Gamma-Ray Techniques-Present and Future; Uranium Exploration Methods. International Atomic Energy Agency, Proceedings of a Panel, Vienna, 67-108.
 45. Boyle, R.W. (1982). Geochemical prospecting for thorium and uranium deposits. *Development Economic Geology* 16, Elsevier, Amsterdam.
 46. Clark, S.P., Peterman, Z.E., & Heier, K.S. (1966). Abundance of U, Th and K. In *Handbook of Physical constants*. Geology Society of America, 97, 521-541.

47. NMA. (1999). A report of work progression during II sub-stage (December, 1998-February, 1999) on uranium evaluation in Abu-Zeneima Area, Sinai, Egypt. Confidential Report, NMA, Cairo, Egypt.
48. Youssef, M.A.S., Sabra, M.A.M., Abdeldayem, A.L., Masoud, A.A., & Mansour, S.A. (2017). Uranium migration and favourable sites of potential radioelement concentrations in Gabal Umm Hammad area, Central Eastern Desert, Egypt. *NRIAG Journal of Astronomy and Geophysics*, 6, 368-378.
49. Efimov, A.V. (1978). Multiplikativniy pokazatel dlja vydelenija endogennyh rud aerogamma-spectrometricheskim dannym, in *Metody rud-noj geofiziki: Lenigrad, Nauchnoproizvodstvennoje objedinenie. Geofizika Ed.*, 59-68.
50. Asfahani, J., Aissa, M., & Al-Hent, R. (2010a). Aerial Spectrometric Survey for Localization of Favorable Structures for Uranium Occurrences in Al-Awabed Area and its Surrounding (Area-3), Northern Palmyrides-Syria. *Applied Radiation and Isotopes*, 68, 219-228.
51. Rudnick, R.L., & Fountain, D.M. (1995). Nature and composition of the continental crust: A lower crustal perspective. *Reviews of Geophysics*, 33, 267-309.
52. Sun, S.S., & McDonough, W.F. (1989). Chemical and isotopic systematics of oceanic basalts: implications for mantle composition and processes. In: Saunders AD, Norry MJ (Eds.), *Magmatism in the Oceanic Basins. Geological Society of London Special Publication*, 42, 313-345.
53. Taylor, S.R., & McLennan, S.M. (1985). *The Continental Crust: Its Composition and Evolution*. Blackwell, Oxford.
54. Çınar, H., Altundaş, S., Çelik, N., & Maden, N. (2017). In situ gamma ray measurements for deciphering of radioactivity level in Sarihan pluton area of northeastern Turkey. *Arabian Journal of Geosciences*, 10(19). <https://doi.org/10.1007/s12517-017-3225-4>.
55. Davies, G.F. (1999). Geophysically constrained mantle mass flows and the ^{40}Ar budget: a degassed lower mantle. *Earth Planet. Sci. Lett.*, 166, 149-162.
56. Akaryalı, E., (2010). Geological, mineralogical, geochemical and genetic investigation of the Arzular (Gümüşhane Northeast-Turkey) gold deposit, Ph.D. Thesis, Karadeniz Technical University, Institute of Science and Technology, Trabzon.
57. Defant, M.J., Jackson, T.E., Drummond, M.S., De Boer, J.Z., Bellon, H., Feigenson, M.D., Maury, R.C., & Stewart, R.H. (1992). The geochemistry of young volcanism throughout western Panama and southeastern Costa Rica: an overview. *J. Geol. Soc. (Lond.)*, 149, 569-579.
58. Kepezhinskas, P., McDermott, F., Defant, M., Hochstaedter, A., Drummond, M.S., Hawkesworth, C.J., Koloskov, A., Maury, R.C., & Bellon, H. (1997). Trace element and Sr-Nd-Pb isotopic constraints on a three component model of Kamchatka arc petrogenesis. *Geochim. Cosmochim. Acta*, 60, 1217-1229.
59. Polat, A., & Kerrich, R. (2001). Magnesian andesites, Nb-enriched basalts and adakites from late-Archaean 2.7 Ga Wawa greenstone belts, superior Province, Canada. Implications for late Archaean subduction zone petrogenetic processes. *Contrib. Mineral. Petrol.*, 2141, 36-52.
60. Sigmarsson, O., Martin, H., & Knowles, J. (1998). Melting of subducting oceanic crust from U-Th disequilibria in austral Andean lavas. *Nature*, 394, 566-569.
61. Galer, S.J.G., & O'Nions, R.K. (1985). Residence time for thorium, uranium and lead in the mantle with implications for mantle convection. *Nature*, 316, 778-782.
62. IAEA. (1989). Construction and use of calibration facilities for radiometric field equipment. In: *Proceedings of IAEA technical reports series 309, International Atomic Energy Agency, Vienna*.
63. Działuk, A., Malczewski, D., Żaba, J., & Dziurawicz, M. (2018). Natural radioactivity in granites and gneisses of the Opava Mountains (Poland): a comparison between laboratory and in situ measurements. *J. Radioanal Nucl. Chem.* 316, 101-109.
64. Hassan, N.M., Kim, Y.J., Jang, J., Chang, B.U. & Chae, J.S. (2018). Comparative study of precise measurements of natural radionuclides and radiation dose using in-situ and laboratory γ -ray spectroscopy techniques. *Sci. Rep.* 8, 14115.
65. Kranrod, C., Chanyotha, S., Pengvanich, P., Kritsanuwat, R., Ploykrathok, T., Sriploy, P., Hosoda, M., & Tokonami, S. Comparative study of natural radionuclides measurements and radiation dose assessment using vehicle-borne and laboratory gamma-ray spectroscopy techniques in Thailand.
66. Al-Masri, M.S., & Doubal, A.W. (2013). Validation of in-situ and laboratory gamma spectrometry measurements for determination of ^{226}Ra , ^{40}K and ^{137}Cs in soil. *Applied Radiation and Isotopes*, 75, 50-57.
67. Arogunjo, A.M., Farai, I.P., & Jibiri, N.N. (2002). Comparison of in situ and laboratory gamma-ray spectroscopy of terrestrial gamma radiation in Ibadan, South Western Nigeria. *Global Journal of Pure and Applied Sciences*, 8, 505-509.





Comparative analysis of an anchored retaining wall system in a deep foundation excavation: A case study of Sivas Cultural Center Building in Türkiye

Mehmet Cemal Acar*¹, Abdullah Kekül²

¹Kayseri University, Vocational School of Technical Sciences, Türkiye

²İller Bank, Sivas Regional Directorate, Türkiye

Keywords

Anchored pile
Retaining wall
Deep excavation
Lateral deformation
Plaxis 2D
GGU-Retain

Research Article

DOI: 10.31127/tuje.1103007

Received: 13.04.2022

Accepted: 24.07.2022

Published: 31.08.2022

Abstract

Modeling the surface element and support system in deep excavation pits and investigating the deformation mechanism is an important issue. In this study, alternative solution methods for an anchored bored pile model are compared and discussed, and it is aimed to contribute to the studies to be carried out in the deep excavation area. A numerical analysis of retaining wall design is examined in the case of the Sivas cultural center building's deep excavation using Plaxis 2D and GGU-Retain software. Measured field data and simulated results are discussed. As a result, the bending moment and lateral deformation reach a maximum when the foundation pit is excavated to the bottom. It can be said that the lateral deformation value found with Plaxis 2D is within the allowable limits, closer to the field data, and provides sufficient quality. The research results will provide theoretical and practical knowledge for designing and constructing similar deep excavation pits for the optimal strategy.

1. Introduction

The recent increase in demand for the urban area and intensive construction have led to increased high-rise buildings and deep foundation excavations. It can be dangerous for the buildings around the excavation area and the people working in the excavation pit due to the horizontal displacement of the retaining wall during deep excavation and may cause significant damage. A retaining wall and a supporting system are needed to prevent such possible damage in deep pits. Retaining walls can support steeply, near-vertically, or vertical sloped soils [1].

In this study, bored piles are used as the retaining wall, and anchors are preferred to support them. Prestressed anchors balance the soil pressure and control the wall's lateral deformation. Since the ground conditions in each region differ and vary according to the depth, it is impossible to design a retaining wall in a deep excavation pit with the instructions. In contrast, retaining wall design and construction require extensive engineering effort.

Plaxis 2D [2] and GGU-Retain [3] software have been widely used to simulate and consider variable soil conditions and are well-known calculation methods in deep excavations walls. Today, an anchored bored pile retaining wall system is increasingly used in geotechnical engineering due to its convenient structure that does not cause significant vibration or shakes to surrounding structures and its successful support capability. Maleki et al. [4] analyzed the hardening soil (HS) constitutive model for deep excavations supported by an anchored retaining wall system in various dry or unsaturated soils using Plaxis 2D [5]. They proposed a single practical relationship that predicts the maximum horizontal displacement of the pile top with high accuracy for deep excavations.

In another study, deformation problems related to the interaction between excavation pit and adjacent buildings are examined. They stated that it is impossible to accurately determine a structure's response to excavation-related deformation due to the variability of many factors affecting horizontal and vertical deformations in structures. The article analyzed the

* Corresponding Author

(acar@kayseri.edu.tr) ORCID ID 0000-0002-3241-5353
(abdullahkekul@gmail.com) ORCID ID 0000-0002-7011-9467

Cite this article

Acar, M. C., & Kekül, A. (2023). Comparative analysis of an anchored retaining wall system in a deep foundation excavation: A case study of Sivas Cultural Center Building in Türkiye. Turkish Journal of Engineering, 7(3), 227-235

various risk factors that cause deformations by monitoring the historic building [6]. Consequently, the structure's deformations must be estimated based on continuous monitoring and approximate calculations.

Wang et al. [7] studied the stress and deformation characteristics of composite soil nailing wall and anchored soldier pile wall combined retaining system during excavating 31.4 m deep. They analyzed the construction process of foundation excavation using simulation software and monitoring data. The research proved that the lateral displacement of retaining piles increases with excavation depth. Chen et al. [8] researched the pile anchor support system for a deep foundation in a congested area of Changchun by monitoring and calculating lateral deformation with Plaxis 2D [5]. The results showed that the maximum horizontal displacement in the pit could be reduced by over 50%, 40%, and 30%, respectively, using the combination of soil nailing wall and pile anchor compared with a single support solution. Yang et al. [9] showed that when using a single prestressed anchor in foundation pit engineering, the closer the anchor rope's position is to the foundation pit's center, the greater the anchor stress. Through the field inspection, Shen et al. [10] investigated the performance of a deep foundation pit supported by suspended piles in soil and rock strata for a subway station in Qingdao Metro Line 3 in China. Many site-measured data are analyzed to investigate the horizontal displacement of piles at different depths under different construction stages. The maximum horizontal displacement of the ground is found to be 6 mm. They also proved that early application of prestressed anchor cables during construction increases the project cost, while the excessive late application may destroy the foundation pit.

Raddatz and Taiba [11] compared the horizontal deformations of the piles obtained from the GGU-Retain and Plaxis 2D software in gravelly soil with the deformations obtained from the field. As a result, they found that the model performed with Plaxis 2D provides the most closer deformation values with the results measured at the site in the final phase. Oróstegui and Villalobos [12] conducted a situation analysis to design a steel-profile wooden shoring (solder pile wall) on silty clay soil with no groundwater. The research showed that the GGU-Retain program could successfully model multi-story underground car parks with deformation control. Bilgehan and Kiliç [13] investigated the landslide problem affecting 30 buildings in the Taşova and Alparslan regions of Amasya province using GGU software. As a result, the total amount of slip is calculated according to the type of soil layers, and comparisons are made by taking field deformation measurements. Ruiz et al. [14] analyzed using GGU software and Plaxis 2D for a 2.3 m high road fill project sitting on 8 m deep soft clay soil. These programs calculate a sufficient safety factor for overall stability, and the analysis results are compared with deformation values measured after the landslides. They proved that the deformation results obtained from both programs are close to each other, and both are on the safe side according to the field deformation data.

Although current research results have revealed various aspects of deep foundation pit support engineering, there is a lack of professional research on lateral displacement in anchored bored pile walls and the impact of different software on design. Therefore, this study explores ways to achieve quality engineering design and construction of anchored wall systems.

2. Description of case study

The project is located close to İstasyon Street, one of the most heavily used streets of the Sivas province in T (Fig 1). The location map shows that the project is 100 meters from the Sivas State Hospital.



Figure 1. Sivas Cultural Center Building Location

Sivas Cultural Center building project consists of 3 basement floors, one ground floor, and two normal floors. The architectural view of this 6-story project is shown in Figure 2. The total closed construction area of the project is 22127 m², the base floor area is 6060 m², and the excavation pit depth is 12.5 m.

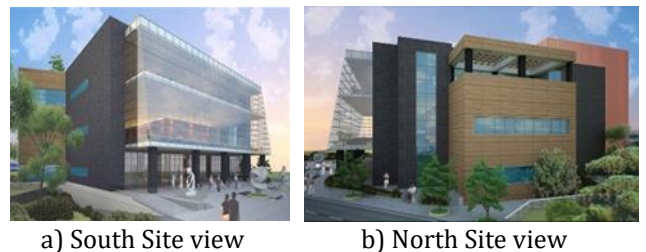


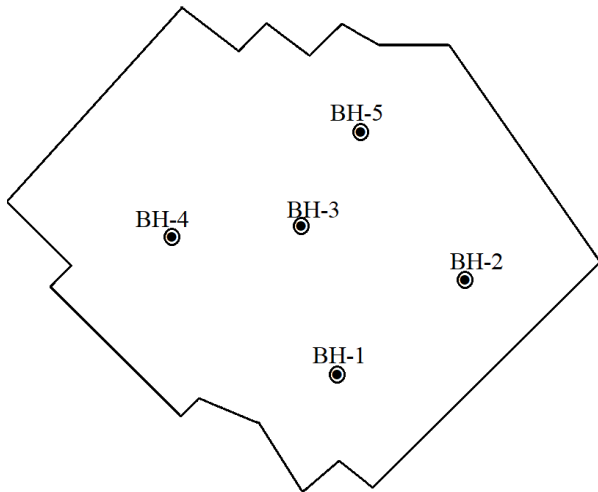
Figure 2. Outside views of the project

2.1. The soil profile and field exploration studies

Brown and light grey clays are encountered in the study area and its surroundings. Five boreholes are drilled during soil exploration to determine the soil properties, and the location plan of the drillings in the field is shown in Figure 3.

The soil exploration area has a flat topography, consisting of various fillings at 0.50 m from the surface, brown clay at 0.50-7.00 m, a 10-15 cm pebbly band at about 6 m levels, and CH clay at 7.00-22.00 m. There is no water or stream around the building site. The groundwater level is about 15 m. The geotechnical

parameters obtained from the field and laboratory test results and used in the model are given in Table 1.



BH-1 39°44'42.7" N; 37°00'33.3"E
 BH-2 39°44'22.9" N; 37°00'33.9"E
 BH-3 39°44'43" N; 37°00'33" E
 BH-4 39°44'44" N; 37°00'30" E
 BH-5 39°44'45" N; 37°00'32" E

Figure 3. Bore Hole Layout Plan

According to the Unified Soil Classification System, the soil class is CH, stiff clay (Table 1). As a result of the tests performed at 5 boreholes, the SPT-N impact values are observed as 6 cm for 50 impacts. For the average soil parameters, the SPT-N 50, internal friction angle 7 degrees, cohesion c, 150 kPa, unit weight 19 kN/m³, elasticity modulus 50 MPa, modulus of subgrade reaction coefficient 40000 kN/m³ are calculated.

3. Numerical Simulation Analysis

First, one anchor point is used vertically, and then it is started to determine the horizontal anchor spacing. Each anchor point consists of 4 anchor cables. The safe working load of each selected rope is 625 kN. The ropes' root length L_k is 9 m, each with a 1.524 cm (0.6 inches) diameter. The pre-tensioned rope's total length is found to be L=17m. These values are for anchor horizontal spacing s=2m. The breaking value for four ropes with a diameter of 1.524 cm is 1043kN. The safe working load is 626 kN, 0.6 times the breaking value. In the project, since the total load on an anchor point is 520 kN, the rope is on the safe side below the breaking value. The safety factor for the ropes against pulling is 2.3, i.e., greater than 2.0 and safe. Numerical analyzes are carried out in phases with Plaxis 2D and GGU-Retain computer programs for the deep excavation model. Static pressure analysis is performed at each stage, except for the addition of the seismic increase between the second and fourth phases.

3.1. Modeling with the GGU Retain

Geometry was created as in Fig. 4 by entering the slope information in the 'Active berms' menu of the GGU Retain program. There is no construction around the excavation area, but the surcharge load effect of 10 kN/m² has been considered since there may be live loads. Since a single row anchor is used in the model, the anchor information and the bored pile starting elevation are entered. For this reason, a single row of anchors is defined at the 3.80m elevation from the anchor's menu. Thus, the geometry and dimensioning of the model are completed using the GGU-Retain program (Fig 4).

Table 1. Soil parameters obtained from boreholes

Boring/Pit Hole No	SAMPLE		Water Content (%)	Unit Weight (kN/m ³)	Dry Unit Weight (Mg/m ³)	Specific Gravity (Gs)	Atterberg Limits			Sieve Analysis (Percent Passing)		Hydrometer	USCS	TRIAXIAL COMPRESSION TEST			
	Sample No	Depth (m)					LL	PL	PI	No.4	No.200			C _u (kPa)	φ _u (Deg)	C' (kPa)	φ' (Deg)
BH-1	UD	12.00	17.3	19.8	1.59	2.67	75.2	27	78.2	20.9	67.7	CH	151	7			
BH-1	SPT	12.45					76.2	25	51.3		93.2	CH					
BH-2	UD	4.50	26.3	20	1.4		52.9	24	29		81.3	CH	160	7			
BH-2	SPT	10.50					64.1	25	39.1		90.4	CH					
BH-3	UD	7.50	23.3	19.4	1.42	2.7	57.7	24.4	31.7		92.3	CH	158	8			
BH-3	SPT	13.50					56.1	24.3	31.7		93.8	CH					
BH-4	UD	12.00					57.8	26.7	31.1		94.9	CH					
BH-4	SPT	15.00					58	21.3	36.7		94.7	CH					
BH-5	UD	4.50	29.3	18.6	1.24	2.65	76.3	26.4	49.9	1.5	95.3	CH	166	6			
BH-5	SPT	12.00					104.6	31.4	73.2		95.4	CH					

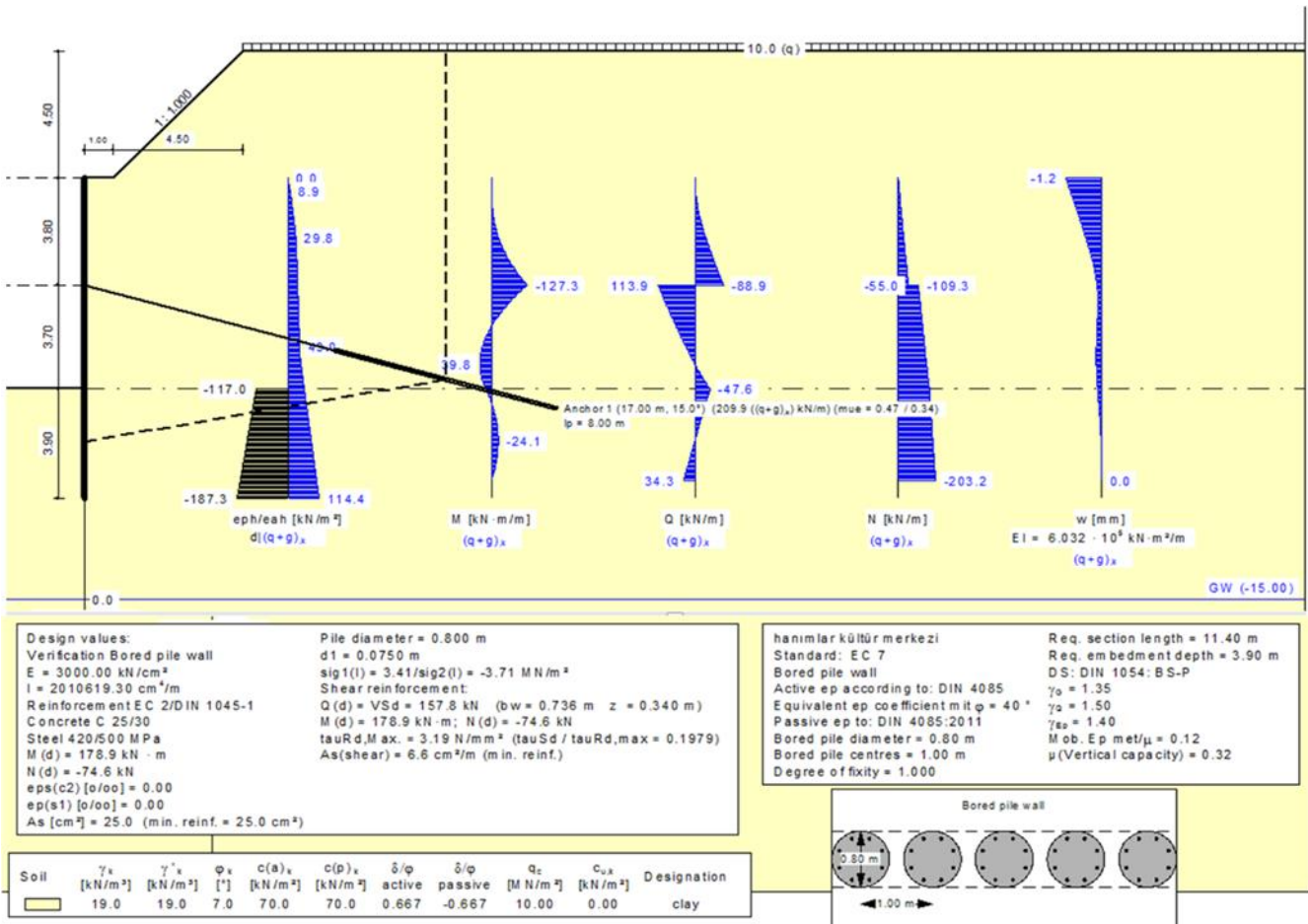


Figure 4. GGU-Retain analysis results of the model

3.2. Modeling with the Plaxis 2D

The set of model parameters is presented in Table 2. After the excavation geometry is determined, the excavation and manufacturing phases of the project are created using the 'Initial conditions' command of the Plaxis 2D program. In Phase1, the initial conditions and then the slope excavation is defined. Fig. 5 is the data entry window of the Plaxis program. Fig 6 is the slope (berm) excavation construction view in the field.

In Fig 7, bored piles are manufactured in the deep excavation of the Sivas Cultural Center building, and in Fig 8, bored piles are connected to the cap beam.

Table 2. Soil parameters used for HS model in Plaxis 2D

Soil Parameters/Units	Symbol	Values
Soil type	CH	Clay
Unit weight (kN/m ³)	γ	19
Cohesion (kPa)	C	150
Friction Angle (Degree)	ϕ	7
Dilation Angle (Degree)	ψ	0
Secant stiffness (kPa)	E_{Ref}^{50}	50000
Tangent stiffness (kPa)	E_{Oed}^{Ref}	50000
Unloading/Reloading stiffness (kPa)	E_{UR}^{Ref}	150000
Power for stress level dependency of stiffness	m	1
Interface reduction factor	R_{int}	0.9
Earth pressure coeff. at rest	K_0^{nc}	0.38

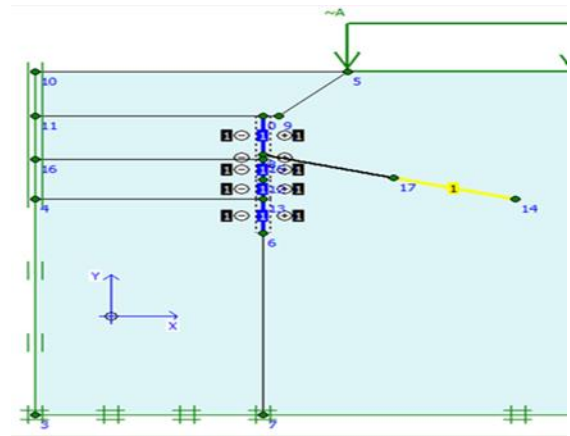


Figure 5. Phase1- Model with Plaxis 2D



Figure 6. Phase1-Slope excavation in the field



Figure 7. Phase 1 Bored pile construction



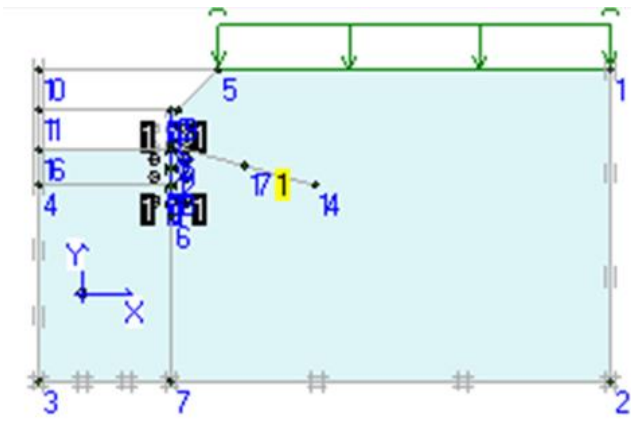
Figure 8. Phase 1 Capping beam construction

In Phase 2, the model is created, and the bored pile is activated. Next, the soil layer is excavated up to the anchor level. Phase 2 is shown in Fig 9(a). In this 2nd phase of the project, the anchor holes are drilled, and the anchor ropes are inserted into the drilled holes with the protection cover (Fig 9(b)).

In Phase 3, cement mortar is injected into the anchor root zone (bonded length), breast beam reinforcements are connected, and concrete is poured. Fig.10 shows these production steps in the field.

After the production of the breast beam is completed, the anchor heads are placed, and the pre-tensioning process is applied. The stages are defined in phase 3 in the Plaxis 2D program. The pre-tensioned anchor application to the ground model is included in the calculations in phase 3 (Fig 10).

Phase 4 includes excavation from the anchor level to the excavation floor level. Phase 4 can be seen in Fig 11. The excavation process is completed, and the analysis phase begins. Figure 12 shows the completed excavation area.



a) Phase 2-Plaxis 2D Model



b) Phase 2-Excavation up to the anchor level at the site

Figure 9. Phase 2-Excavation up to anchor level and activation of bored piles



a) Phase 3-Anchor and breast beam



b) Phase 3-Anchor Head



c) Phase 3-Prestressing

Figure 10 Phase 3-Breast beam construction, placement of anchor heads, and prestressing at the site

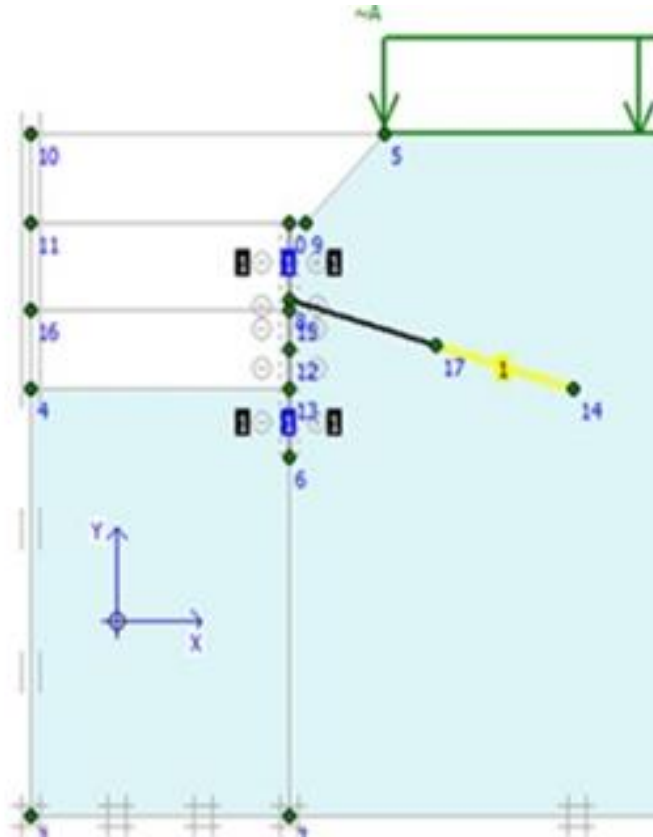


Figure 11. Phase 4-Reaching the excavation base level



Figure 12. Phase4-Excavation completed

4. Results and Discussion

The model of the anchored wall system is designed with Plaxis 2D software with the hardening soil (HS) method and GGU-Retain software with the subgrade reaction modulus method (SRM). The results of the research are discussed in detail.

4.1. Analysis Results with Plaxis 2D

The maximum bending moment in the vertical elements of the shoring system is 155,48 kNm/m, as given in Fig 13. This value is multiplied by the pile

spacing, $S=1.00$ m, and the bending moment affecting the bored pile is included in the calculations. According to this bending moment, the piles are equipped with 80 cm diameter and 16 BC III class longitudinal reinforcements with 20 mm diameter.

The shear force value used in bored pile reinforcement calculations, 164.39 kN/m, is taken from the bored pile shear force diagram shown in Fig. 14.

In phi-c reduction analysis, the system's number of safety factors (Msf) is determined. The Msf value of this design is around 1.7 and remains on the safe side as this value is above 1.5.

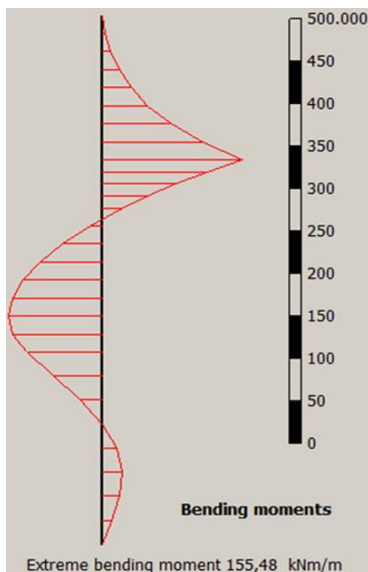


Figure 13. Maximum bending moment

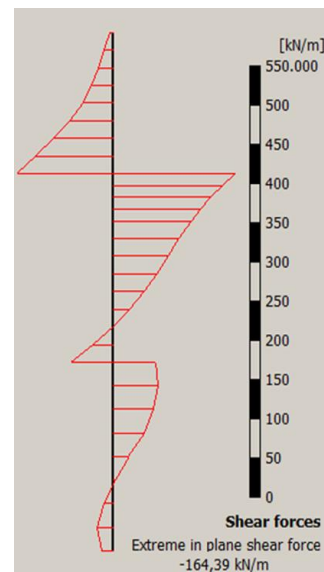


Figure 14. Maximum plane shear force

4.2. Analysis Results with GGU-Retain

A bored pile system with 80 cm diameter and 100 cm spacing is used in the GGU-Retain model. Since there is no construction near the excavation area, a 4.5m-4.5m slope (berm) was made around the excavation to save cost and manufacturing time before the piles were driven.

In the system, which is solved with a single row of anchors, the excavation depth is 12 m, including the sloped part (berm). Anchor intervals are determined as 2 m horizontally. The safe maximum moment capacity of the pile section is calculated as 178.9 kN.m, whereas the maximum moment value acting on the cross-section is 127 kN.m. The pile length is 11.40 m in total, 3.90 m of which is buried under the excavation pit depth.

The stability analysis of slopes is checked with the GGU-Slope [15] program. The circles are tightened where slip may occur, and the most critical slip surface is found. Slope stability analysis is performed with utilization factor. The μ_{max} (Utilization Factor) parameter used in the calculations shows the risk of global failure. FS (Factor of safety) can be examined using GGU-Slope [15] software, but here μ_{max} is the inverse of FS, i.e., equal to 1 over FS. It is found that the model is safe in terms of slope stability, with the μ_{max} value being the highest at 0.76, which is less than 1. There is no global failure problem (Fig.?)

Soil	ϕ_x [°]	c_x [kN/m ²]	γ_x [kN/m ³]	max ψ_A [°]	Designation
clay	7.00	150.00	19.00	80.00	clay

Example 21 Schulze/Simmer 94 Grundbau 1
 Initial calculation data
 Unfavourable slip circle:
 $\mu_{max} = 0.76$
 $x_m = -0.31$ m $y_m = 7.17$ m
 $R = 18.09$ m
 Partial factors:
 - $\gamma(\phi') = 7.00$
 - $\gamma(c') = 1.50$
 - $\gamma(c_u) = 1.50$
 - $\gamma(\text{Unit weights}) = 1.90$
 - $\gamma(\text{Permanent actions}) = 1.00$
 - $\gamma(\text{Variable actions}) = 1.30$
 Maßstabsfaktor Porenwasserdruck = 0.050

Fig. 15 Slope stability analysis

4.3. Discussion and comparison of numerical simulation results with field data

Field maximum horizontal deformation monitoring data are compared with numerical simulation results. After completing the anchored wall system, the maximum horizontal displacement (d_{hmax}) at the top of the pile in the field is measured as 9 mm.

The maximum allowable lateral displacement of the top of the anchored pile is calculated using different approaches in the literature [16-19]. Generally accepted in the literature, in anchored wall applications, for stiff clay soils (i.e., undrained cohesion is more than 50 kPa), the allowable d_{hmax} over H ratio varies between 0.2% and 0.9% for clays ranging from stiff to soft (H is the excavation depth.). The maximum allowable lateral

deformation is calculated as 15 mm using the FHWA (1999) [16] criterion. The maximum lateral deformation value at the top of the pile is measured as 9mm in the field, which is below the allowable limit (15 mm).

The Plaxis 2D using HS theory is a finite element method. This method allows us to consider the soil-structure interaction, including anchors, and determine the soil's stresses and strains throughout the excavation. This method models the plastic volumetric strain in soil compression quite successfully. With Plaxis 2D, the maximum horizontal deformation value allowed at the top of the wall is calculated as 12.41 mm. (Figure 16.). This result shows acceptable consistency with the FHWA [16] criteria of 15mm and closer to the field value of 9mm. During the installation of this anchor, the soil mass is subjected to unloading and loading with increasing excavation depth, and the actual behavior of the soil becomes elastoplastic. It can be said that the Hardened Soil model in Plaxis 2D accurately reflects this elastoplastic behavior of the soil considering lateral deformations.

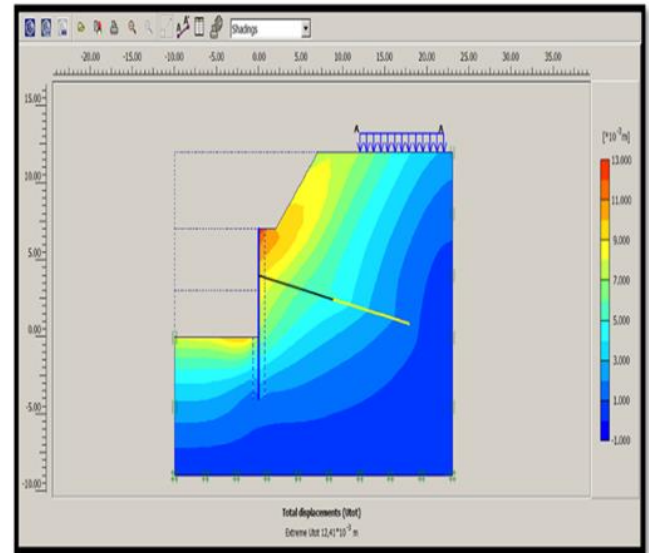


Figure 16. Total Lateral displacement

GGU-Retain uses a calculation method based on SRM (also called the Winkler method). The cohesion value of the stiff clay soil is given as 150 kPa in the geotechnical report. The maximum lateral deformation value at the top of the retaining wall is calculated as 1.2mm, even when the cohesion value is accepted as 70 kPa with applying the safety factor. The GGU-Retain program underestimates the maximum lateral deformation from the field value and Plaxis 2D. GGU-Retain creates a balance between the sliding and holding forces acting on the excavation wall, considering the density of the soil, the internal friction angle, the cohesion, and the concrete-soil friction. For example, calculating the required embedment depth of anchored bored piles takes an initial embedment length value and then iteratively calculates the optimal depth. According to the authors, the inaccuracy of the subsoil reaction method is that it is challenging to choose the appropriate value of the subsoil reaction coefficient accepted throughout the calculations, and it is also assumed to be constant. In

reality, there is a non-linear relationship between soil pressure and displacement.

5. Conclusion and Recommendations

In this research, a comprehensive numerical study is carried out to analyze the anchored bored pile retaining wall design in the case of the Sivas cultural center building's deep excavation. The proposed anchored wall system model is designed with two different programs: Plaxis 2D with HS and GGU-Retain with SRM. Retaining wall design in deep excavations, one of the essential branches of geotechnical engineering, is a very diverse, complex, and comprehensive engineering task. The quality of the project mainly depends on whether the maximum lateral deformation caused by the foundation pit excavation is within a permissible limit. After the retaining wall was completed, the maximum d_{max} was measured at 9 mm at the top of the pile. This deformation value is calculated with Plaxis 2D and GGU-Retain programs as 12.45mm and 1.2mm, respectively.

The maximum lateral deformation value found with both GGU-Retain and Plaxis 2D was within the allowable limits, and both programs' solutions remained on the safe side. However, in GGU calculations, it was observed that the maximum lateral deformations were much smaller than PLAXIS 2D. In addition, with PLAXIS 2D, the deformation value is much closer to the field data and provides sufficient quality. Considering that this low deformation value is due to the high cohesion value of the stiff clay, the authors used an undrained cohesion value of 70 kN/m² instead of 150 kN/m² in the GGU-Retain program, and even in this case, the lateral deformation was calculated as 1.2 mm. As a result, Plaxis 2D solution method was preferred instead of GGU-Retain for the wall design.

This anchored wall project is implemented in a foundation pit with a relatively shallow excavation depth. To better understand the differences in the GGU-Retain and Plaxis 2D programs, it needs to be confirmed by further studies that take into account the actual effective parameters of the soil and the deformation behavior of the wall with increasing excavation depth. In addition, another critical point is that the construction of a safe and economic retaining wall will be possible with a comprehensive subsoil investigation. The proposed HS method for designing an anchored pile retaining wall is based on soil parameters obtained from a geotechnical report. Therefore, the accuracy of the determined parameters depends on the subsoil investigation that reveals the actual ground behavior in the field.

Finally, it can be concluded that Plaxis 2D, using the Hardening Soil theory, can be used with high accuracy for deep excavation pits in hard clay soil.

Acknowledgement

This article is adapted from the Master thesis of the second author under the first (corresponding) author's advisement.

Author contributions

Mehmet Cemal Acar: Conceptualization, Methodology, Software, Data curation, Writing-Original draft preparation. **Abdullah Kekül:** Visualization, Investigation, Software, Validation. Writing-Reviewing and Editing.

Conflicts of interest

The authors declare no conflicts of interest.

References

1. Terzaghi, K., Peck, R. B., and Mesri, G. (1967). *Soil Mechanics in Engineering Practice*, John Wiley and Sons, Inc., New York, NY, USA.
2. PLAXIS. 2D (2006). *Plaxis user manual (version 8.6)*. Delft University of Technology & Plaxis BV, the Netherlands.
3. GGU-Retain (2020). *Manual version 13*. Civilserve GmbH, Steinfeld, Germany.
4. Maleki, J., Pak, A., Yousefi, M., & Aghakhani, N. (2022). A comprehensive FE study for design of anchored wall systems for deep excavations. *Tunnelling and Underground Space Technology*, 122, 104340.
5. Plaxis 2D (2015). *plaxis user manual*, delft university of technology & plaxis bv, the Netherlands.
6. Dmochowski, G., & Szolomicki, J. (2021). Technical and Structural Problems Related to the Interaction between a Deep Excavation and Adjacent Existing Buildings. *Applied Sciences*, 11(2), 481.
7. Wang, S., Li, Q., Dong, J., Wang, J., & Wang, M. (2021). Comparative investigation on deformation monitoring and numerical simulation of the deepest excavation in Beijing. *Bulletin of Engineering Geology and the Environment*, 80(2), 1233-1247.
8. Chen, A., Wang, Q., Chen, Z., Chen, J., Chen, Z., & Yang, J. (2021). Investigating pile anchor support system for deep foundation pit in a congested area of Changchun. *Bulletin of Engineering Geology and the Environment*, 80(2), 1125-1136.
9. Yang, Z., Li, S., Yu, Y., Liu, X., & Hu, Y. (2020). Study on the variation characteristics of the anchor cable prestress based on field monitoring in a foundation pit. *Arabian Journal of Geosciences*, 13(23), 1-10.
10. Shen, Y. S., Yin, J., Zhu, D. S., Kumah, D., Guo, W. F., & Hudu, A. A. (2021). Performance of a deep foundation pit supported by suspended piles in soil and rock strata: a case study. *Arabian Journal of Geosciences*, 14(21), 1-13.
11. Raddatz, D., & Taiba, O. (2017). Anchored piles in Santiago's gravel: modeling results for displacement curve. *Revista de la Construcción. Journal of Construction*, 16(3), 457-467.
12. Oróstegui, P., Villalobos, F. (2010). Design And Construction of An Anchored Soldier Pile Wall For A Large Underground Car Park. *Electronic Journal of Geotechnical Engineering*, Vol. 19: 59-63.
13. Bilgehan, R. P., Kiliç, R. (2008). The Landslides Threatening Taşova Town (Central Anatolia, Türkiye) And Their Environmental Impacts. *Environmental Geology*, 55(1), 179.

14. Ruiz, E. F., Hems, P. S., & Vidal, D. M. (2013). Numerical Analysis of Reinforcement Strains at Failure for Reinforced Embankments over Soft Soils. *Soils and Rocks*, 36(3), 299-307.
15. GGU-Slope (1999) Slope failure calculations with circular and polygon slip planes. Braunschweig, Germany.
16. FHWA-IF-99-015 (1999). Geotechnical Engineering Circular No.4: Ground Anchors and Anchored Systems, U.S. Department of Transportation, Federal Highway Administration, Washington D.C.
17. Clough GW, O'Rourke, T.D. (1990). Construction induced movements of in-situ walls. In: Design and Performance of Earth Retaining Structure, Proceedings of Specialty Conference, Geotechnical Special Publication No.25, ASCE, New York.
18. Carder, D.R. (1995). Ground movements caused by different embedded retaining wall construction techniques, Transport. Res. Lab. Rep., 172, Berkshire, U.K.
19. Long, M. (2001). Database for retaining wall and ground movements due to deep excavations. *Journal of Geotechnical and Geoenvironmental Engineering*, 127(3), 203-224.



© Author(s) 2023. This work is distributed under <https://creativecommons.org/licenses/by-sa/4.0/>



Geo-Appraisal of groundwater resource for sustainable exploitation and management in Ibulesoro, Southwestern Nigeria

Olumuyiwa Olusola Falowo ^{*1}, Abayomi Solomon Daramola ¹

¹ Rufus Giwa Polytechnic Owo, Ondo State, Department of Civil Engineering Technology, Nigeria

Keywords

Ibulesoro
Irrigation indices
Water quality index
Groundwater exploration
GWPIV

Research Article

DOI: 10.31127/tuje.1107329

Received: 22.04.2022

Accepted: 03.08.2022

Published: 31.08.2022

Abstract

Groundwater exploitation requires better understanding of the resource availability and quality/vulnerability. Geophysical techniques, pumping test, hydraulic measurement, borehole logging and quality test analysis have been used in Ibulesoro, southwestern Nigeria, to understanding the hydrogeological system in terms of groundwater availability, aquifer delineation, and evaluate the groundwater physico-chemical and biological contents. The study utilized multi-criteria evaluation techniques (GWPIV) to assess the overall aquifer potential/vulnerability. The geology of the area comprises granite, migmatite, migmatite gneiss, biotitic granite, and gneiss. The main water-bearing unit was the weathered layer and fractured basement, which are usually unconfined aquifer. The hydraulic conductivity and formation factor is related by $y = 0.239e^{0.0519x}$ with correlation coefficient of 0.0961. The average hydraulic conductivity and transmissivity are 0.52 m/d and 5.78 m²/d respectively. The hydrogeological parameters viability increases southwardly, just as groundwater movement/flow is due south. The average thickness of the weathered layer and overburden are 8.6 m and 16.1 m respectively, with dominant resistivity in the range of 80 – 200 ohm-m. The best drilling points (migmatite/gneiss geologic units) are where the fractured basement underlies the weathered layer which most not necessarily exceed 30 - 35 m. The average depth to basement rock is 16.1 m. The obtained GWPIV varied from 1.12 to 1.71, with an average of 1.30 suggesting low potential but good for drinking and irrigation uses in its present state, however highly vulnerability to contamination, as the vadose zone thickness (5.68 m avg.), AVI (0.57 avg.), and LC (0.0818 mhos avg.) all point to the low protective capability. The water types is mixed Ca-Mg-Cl. The mechanism controlling the groundwater quality falls in the mixed zone, which indicates contribution from soil/rock-water interaction, precipitation, and evaporation; while carbonic weathering is more active than the silicate weathering process.

1. Introduction

Advancement and management of groundwater resources is becoming critical in the face of worldwide water scarcity challenges [1]. Ibulesoro is one of the fastest-growing towns in Ondo State's Ifedore Local Government Area in terms of infrastructure, health facilities, housing and estate development, groundwater development, and the emergence of small/micro businesses and industries in the previous ten years. As a result of the boundary shared with FUTA, the staff prefer settling down in the town, hence the population of the town is growing geometrically. However, due to a lack of

treated water from a government-owned well, many residents in the town rely on shallow wells/borehole. But data on these boreholes are usually not available, since many don't carry out hydrogeological survey before drilling operation, which generally leads to unsuccessful/failed boreholes. These abandoned boreholes are typically not backfilled, and they might serve as a route for contaminants to reach an aquifer (if the not cased). For solid and liquid wastes, many have turned to waste disposal sites, which pose a clear threat to water quality. This can lead to ground subsidence, landslides, and other issues. As a result, water resource development and management need to take operate

* Corresponding Author

(solageo2018@gmail.com) ORCID ID 0000-0003-3425-9072
(yomidams02@gmail.com) ORCID ID 0000-0002-0309-2399

Cite this article

Falowo, O. O., Daramola, A. S. (2023). Geo-Appraisal of groundwater resource for sustainable exploitation and management in Ibulesoro, Southwestern Nigeria. Turkish Journal of Engineering, 7(3), 236-258

within a framework of legitimate duties, privileges, and limits [2]. The study's goals were to identify and delineate geological sequences and factors in terms of capacity and value with the mandate to improving groundwater management and development. This study used a combination of geoelectric measures, hydrogeological, borehole logging, and groundwater quality to define the current state of the aquifer system in the area for drinking and irrigation uses [3-4]. Since aquifer permeability, underlying strata lithology, temporal variations in the source and configuration of recharged water, hydrology, and human impacts all influence the occurrence and movement of groundwater resources [5-8].

For decades, the mining and petroleum industries have relied on geophysical surveys. This survey's utility has been demonstrated in the exploration of shallow near-surface/subsurface groundwater supplies [9-13]. The most frequent approaches are dc resistivity, seismic refraction, and gravity and magnetics methods [14-16]. The magnitude and character of the geologic resources below the surface can be determined indirectly using geophysical methods. The depth to/of the basement rocks, as well as the thickness of subsurface faults. Dc electrical resistivity (ER) is the most widely used of the several electrical geophysical methods in hydrogeology [7,17,18]. The ER is a direct current that is delivered to the ground via two metal electrodes. The ground voltage is measured between two metal electrodes that are also driven in the ground. The resistivity of the earth materials between the electrodes can be calculated by the current flowing through the ground and the potential differences or voltage between the electrodes. The expression in equation 1 equals electrical resistivity (R).

$$R = \frac{A \Delta V}{L I} \tag{1}$$

- A = Cross sectional area of current flow
- L = Length of the flow path
- ΔV = Voltage drop
- I = Electrical current

The unit of ER is in ohm-m or ohm-ft units. The four electrodes utilized are: A- +current electrode, B is - current electrode, M-potential electrodes, and N-potential electrodes. If XY denotes the distance between Electrode X and Electrode Y, equation (1) can be written as:

$$R = \left(\frac{2\pi}{\frac{1}{AM} - \frac{1}{BM} - \frac{1}{AN} + \frac{1}{BN}} \right) \frac{\Delta V}{I} \tag{2}$$

The resistivity derived in equation 2 is an apparent resistivity (R) because the earth materials are nearly homogeneous and electrically isotropic. Schlumberger array arrangement is employed in this investigation. It's a linear array of close-together potential electrodes. AB is usually configured to be equal to or larger than five times MN. Equation (3) gives the apparent resistivity:

$$R = \frac{\pi \left(\left(\frac{AB}{2} \right)^2 - \left(\frac{MN}{2} \right)^2 \right) \frac{\Delta V}{I}}{MN} \tag{3}$$

The electrical sounding indicates the depth-dependent differences in apparent resistance. The distance between the potential electrodes and the current electrodes increases as the electrode spacing is increased in electrical sounding. This implies deeper penetration of current into the earth, measuring apparent resistance as it does so.

Hydraulic characteristics of earth materials and groundwater are typically determined in hydrogeological research [19]. This usually entails digging exploratory wells and observing and analyzing pumping test data in order to calculate hydraulic conductivity, transmissivity, storability, safe yields, and hydraulic gradient, among other things. The goal of an exploratory well is to gather data on the geology of the subsurface aquifer. Aquifer tests are often used to analyze the physical qualities of aquifers, in addition to reporting the various geological layers encountered (well logs). Step-down tests are frequently performed before these tests to know the appropriate discharge rate. As a result, one of the focuses of this study is the ability to pump the required volume of water at the lowest cost, taking into account investment, operation, and maintenance [20-21].

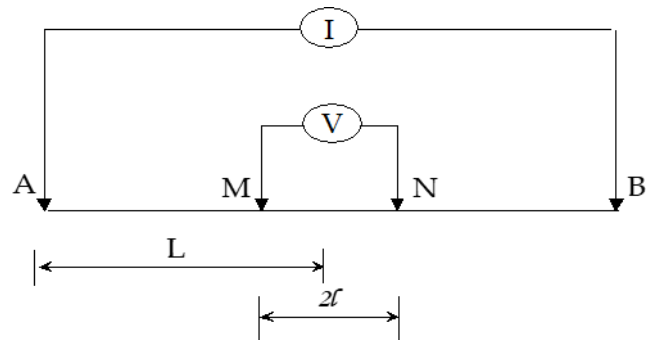


Figure 1. Schlumberger Electrode Configuration.

Safeguarding the water quality in an aquifer is a crucial aspects of groundwater management, and this is done by determining the vulnerability potential [22] from septic tanks, sanitary landfills, municipal wastewater land treatment systems, waste injection wells, toxic chemical disposal sites, cemeteries, mine tailings, mine drainage, water softener regeneration salts, oil field brine, agricultural chemicals and fertilizers, and accidental oil [23-27]. Several approaches for assessing aquifer vulnerability have been presented; among these, index methods such as DRASTIC, GOD, and IRIH are the most extensively utilized [28-29]. S-model aquifer vulnerability assessment is a less expensive option to index models. The protective capacity of the vadose zone is examined in the S-model (e.g., AVI, LC, etc.) by defining the lithological configuration and depth using ER sounding. Because of the development of computer programs, electrical resistivity, which involves the computation of longitudinal conductance, is now used in groundwater research [30]. Furthermore, the water quality index (WQI) is gaining in favor around the

world for monitoring groundwater quality [26,31-34]. The water quality index describes the quality of water in terms of an index number that shows the water's complete quality for any anticipated purpose. It's a mathematical method for changing vast quantities of data on water quality into a distinct number that specifies the water quality level. In fact, establishing WQI in a given area is an important step in land use and water resource management planning. Typically, WQI is calculated from the standpoint of its appropriateness for human drinking.

Aquifers can play a variety of roles in the general development of a region's water resources, including supplying water to wells (supply function) and transporting water from one point to another (pipeline function). An aquifer's unsaturated zone can serve as a waste treatment system. This is known as the aquifer's filter-plant function [35-36]. The unsaturated zone, on the other hand, can do greatly more than serve as a physical filter for germs and viruses. Heavy metals and phosphorus are also effectively removed. Water can also be improved by passing through the saturated zone. Groundwater can serve as an energy source (groundwater heat pump) as well as a storage medium [37].

Groundwater contamination or susceptibility has recently piqued the interest of many researchers throughout the world [16,38-44], because of the significance role it plays in overall wellbeing of humans. Water pollution, according to the World Health Organization, is a change in the composition of water caused by human activities, either directly or indirectly.

Drinking water contaminated with viruses can cause illnesses such as hepatitis, cholera, giardiasis, typhoid, methemoglobinemia, and other complications, especially in infants and newborns who have a low immune system. It can also lead to a loss of water supply, a deteriorated surface water system, high clean-up costs, high prices for alternate water sources, and/or significant health issues. The chemical composition of groundwater is determined by a number of elements, including the frequency of precipitation, the length of time rain water stays in the root zone, and so on. As a result, groundwater contamination is almost entirely due to human activities, particularly in locations where population density is high and land use is intensive. The identification of aquifer recharge zones is an important part of mitigating groundwater pollution, and in such area the protection is very vital.

The motivation for this study was bored out of the need to assist the inhabitant of Ibulesoro in the area of groundwater exploration and exploitation so as to forestall incessant drilling of abortive borehole. Many existing literatures basically centered study of this nature on one or two techniques, with may not give comprehensive results desired, even though cost also may be a major hindrance. Hence this study incorporates aquifer properties, the quality of its water content, and its vulnerability to vertical contamination to decipher the nature of the aquifer and its geochemistry.

2. Method

2.1. Study Area

Ibulesoro is a town in Ondo State, Nigeria, in the Ifedore Local Government. Araromi, Iwoye, Oju oja, Olubule, Ayetoro, and Imogun are the six quarters that make up Ibulesoro. Longitude 0732900 – 0733900mE and Latitude 0809400 – 0809000mN are the coordinates for this location. It is around 80 km² in size. The location can be reached via the Akure – Ilesha Highway and the Akure – Aule Road (Fig. 2). The people's primary occupation is farming. The landscape is steep and moderate sloping, with topographical elevations ranging from 350 to 388 meters (Fig. 2), and the area is bordered by isolated hills/ridges of various geological formations. The tropical rainforest climate which the fall within, is divided into two seasons: wet (March – October) and dry (November – February). When it comes to rainfall frequency and severity, the months of June through September are high, thus leading to high soil saturation, soil erosion and flooding. July and September are the wettest months in the area, with periodic, strong downpours. During the downpour, rainfall of more than 42 mm can be recorded in a single day. The yearly rainfall is 1500 mm, and the average temperature ranges from 18 to 33 degrees Celsius [45]. Because sunshine duration/intensity is short (2.7 to 2.9 hours per day) and evaporation is minimal (between 3 and 4 mm per day) from June to September, relative humidity can reach 90 percent [45].

2.2. Geology and Hydrogeology

The study region is defined by crystalline rock from southern Nigeria's Precambrian basement complex. Migmatite-gneiss, gneiss, biotite gneiss, biotite granite, and granite are the geological units found in the area. The most common is migmatite gneiss, while biotite granite is porphyritic and medium to coarse grained. Granites are found in low-lying outcrops as intrusive. Fractures, veins (pegmatitic, quartzo-feldspathic, and quartz veins), joints, and faults (Figures 3 & 4) can be found with NW-SE and NE-SW structural trends. The rock units are outcropped in various areas. Hydrogeologically, groundwater accumulation is a function of weathering, overburden thickness, degree and nature of fracturing rocks, infiltration/percolation, and aquifer hydraulic capabilities. Secondary porosity and permeability of basement bedrock generated by cracks, joints, faults, and sheared basement bedrock are responsible for such groundwater production. Groundwater yield can also be enhanced by the presence of pegmatitic, quartz, and quartzo-feldspathic veins. The weathered layer and unconfined/confined fractured basement are the area's primary water-bearing units. The aquifer's transmissivity and potentiometric surface, the amount of precipitation that is not lost through evapotranspiration and runoff; the coefficient of permeability of surficial deposits and other strata in the aquifer's recharge area; are some of the factors which determines the volume of recharged water capable of moving downward to the aquifer.

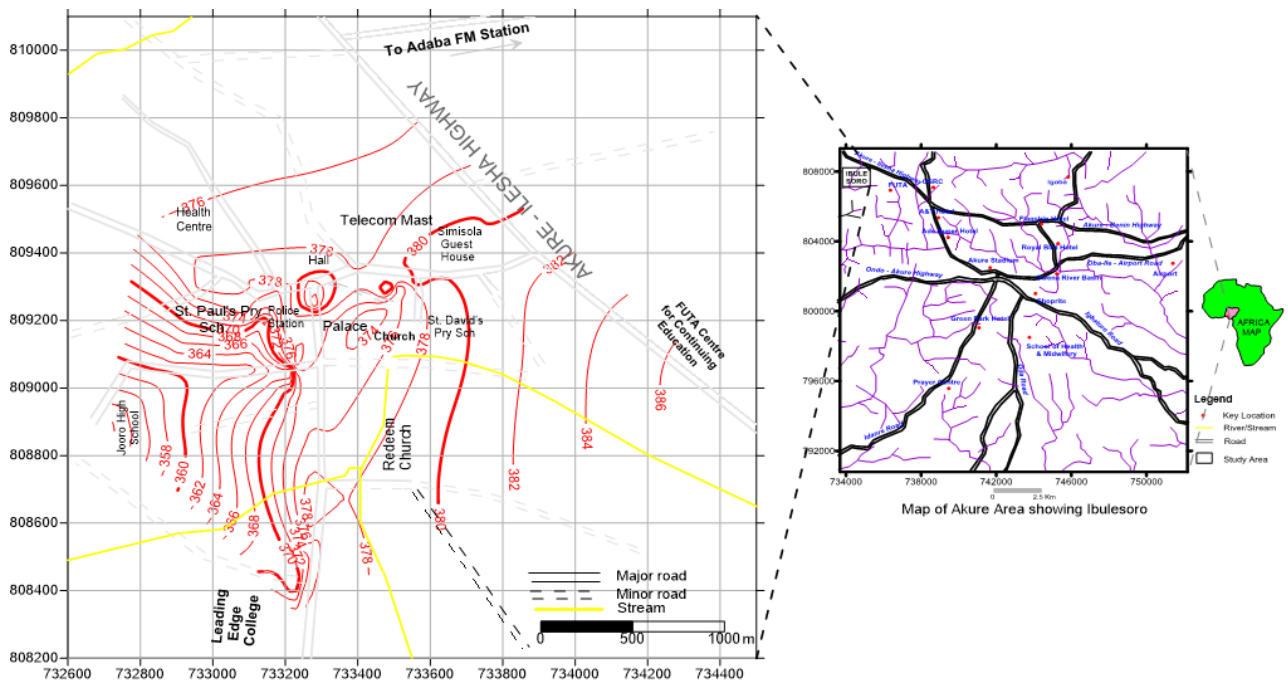


Figure 2. Location map and the topographical variation across the study area

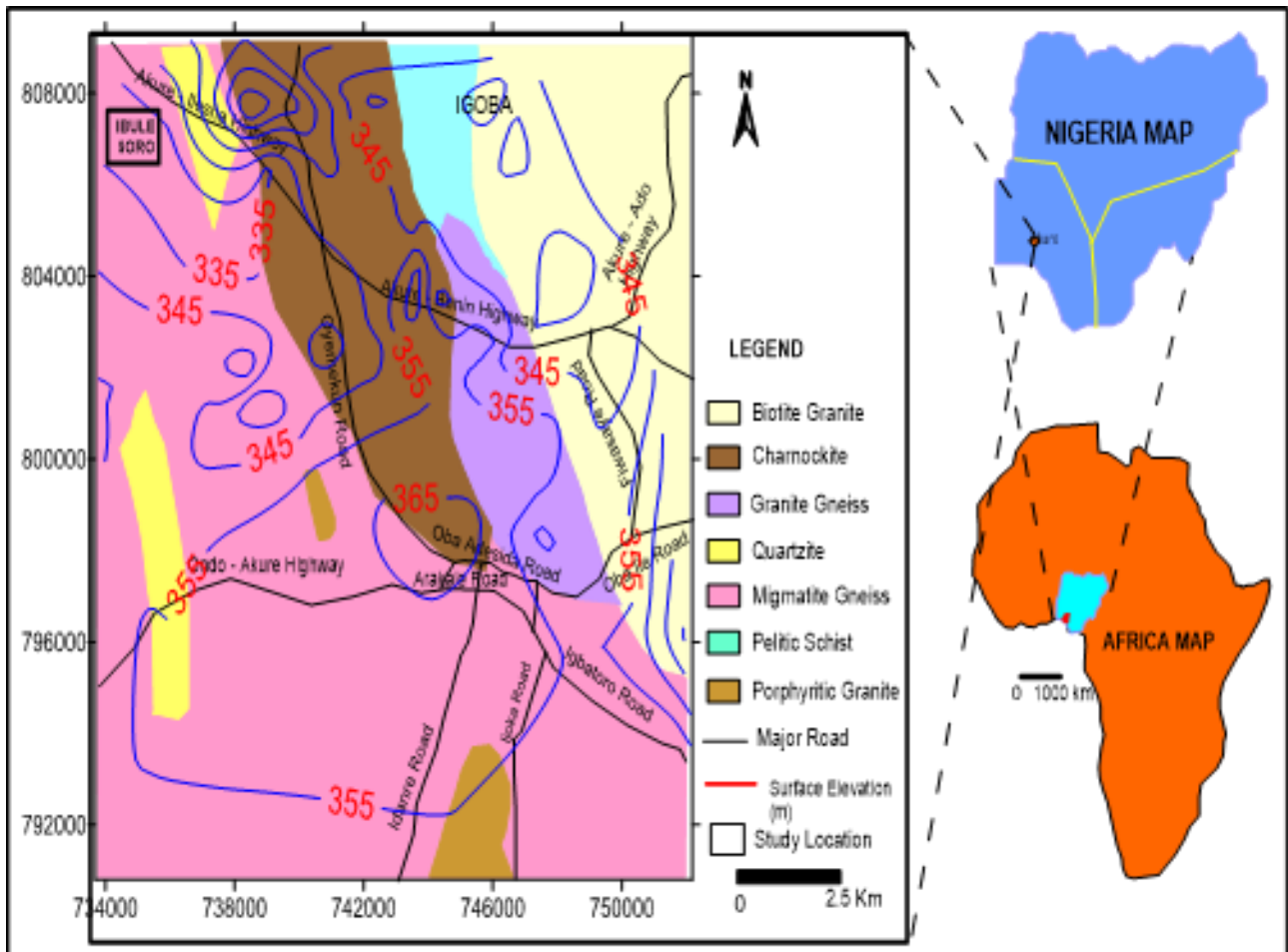


Figure 3. Geological Map of Akure with overlay of elevation variation (modified after [44, 46])



Figure 4. Field Pictures of Geologic units observed varying from migmatite, granite gneiss, granite, biotite gneiss/granite from boulders, low lying, and ridges. The Gneiss shows conspicuous banding; and also, presence of veins especially on migmatite

The study methods employed electrical resistivity, borehole drilling, water quality analysis, and hydrogeological measurements. The data acquisition map is shown in Figure 5. The electrical resistivity utilized the vertical electrical sounding method (VES) data using Schlumberger array using Telford et al. [14] outlined methodology/procedure [16, 44], with current spacing of 100 m. The data collected were processed and interpreted using combination of curve matching and computer iterative modeling [47]. Several hydrogeophysical maps which include depth to aquifer, aquifer thickness, overburden, hydraulic and transmissivity maps were generated. The VES stations were chosen based on geology, topography, the presence of existing water wells/boreholes, and accessibility. The nature and thickness of the overburden, fracture contrast, reflection coefficient, formation factor, traverse resistance, hydraulic conductivity, transmissivity,

longitudinal conductance, and AVI were all combined to produce a groundwater potential map for the area. Equation (4) was used to get the reflection coefficient.

$$r = \frac{(\rho_n - \rho)(n - 1)}{\rho_n + \rho(n - 1)} \quad (4)$$

Where r is reflection coefficient, ρ_n is the layer resistivity of the nth layer and $\rho_{(n-1)}$ is the layer resistivity overlying the nth layer. The fracture contrast was calculated using equation (5).

$$F_c = \frac{\rho_n}{\rho_n - 1} \quad (5)$$

The traverse resistance was calculated using equation (6).

$$T = \sum_{i=1}^n \rho_i h_i \quad (6)$$

where T is traverse resistance, ρ and h are resistivity and thickness of the nth layer respectively. The longitudinal conductance and aquifer vulnerability index (AVI) were used to measure the susceptibility or protective capability of the vadose zone/overburden material to pollution/contamination. These approaches combine or reflect texture, structure, thickness, level of organic carbon, mineral composition of the clay, permeability, geology, and other hydrogeologic factors intrinsic properties [16]. The longitudinal unit conductance (equation 7) was used to predict the water's contamination susceptibility using geoelectrical characteristics [48-49].

$$LC = \sum_i \frac{h_i}{\rho_i} \quad (7)$$

where LC is longitudinal conductance, h_i and ρ_i are the thickness and resistivity of nth layer respectively.

The AVI method measures hydraulic resistance (c) to vertical flow [20] using the thickness of the water bearing units and hydraulic conductivity as shown in equation (8).

$$c = \sum d_i / K_i \quad (8)$$

for layers 1 to i. The interpretation of “c” was done using Table 1. In addition, data was gathered from four existing boreholes, and twenty five (25) water wells. The static water level was calculated using these wells. VES

was located or conducted in fifteen (15) of these well locations for the purpose of correlation.

Table 1. Relationship of hydraulic resistance (c) and Aquifer Vulnerability index

Hydraulic resistance (c)	Log (c)	Vulnerability
0 – 10	<1	Extremely high
10 – 100	1 – 2	High
100 – 1,000	2 – 3	Moderate
1,000 – 10,000	3 – 4	Low
>10,000	>4	Extremely low

Pumping tests were used to assess the hydraulic properties of the wells and boreholes, as this is one of the most effective approaches to determine or estimate the physical qualities of water bearing layers [20]. The ultimate goal is to find a suitable drilling point/location with the lowest pumping cost, pumping water free of sand and silt, a well/borehole with the lowest operating and maintenance costs, and a well/borehole with a long and economical lifetime. The ease with which liquid flows through a medium is measured in hydraulic conductivity (K). Unlike intrinsic conductivity, which characterizes the water transmitting capabilities of a porous media, it incorporates both medium and flow attributes (equation 9):

$$T = Kh \quad (9)$$

where T is transmissivity, K is hydraulic conductivity, and h is thickness of the water bearing unit. The formation factor (Fm) was computed for each of the geological units in the area.

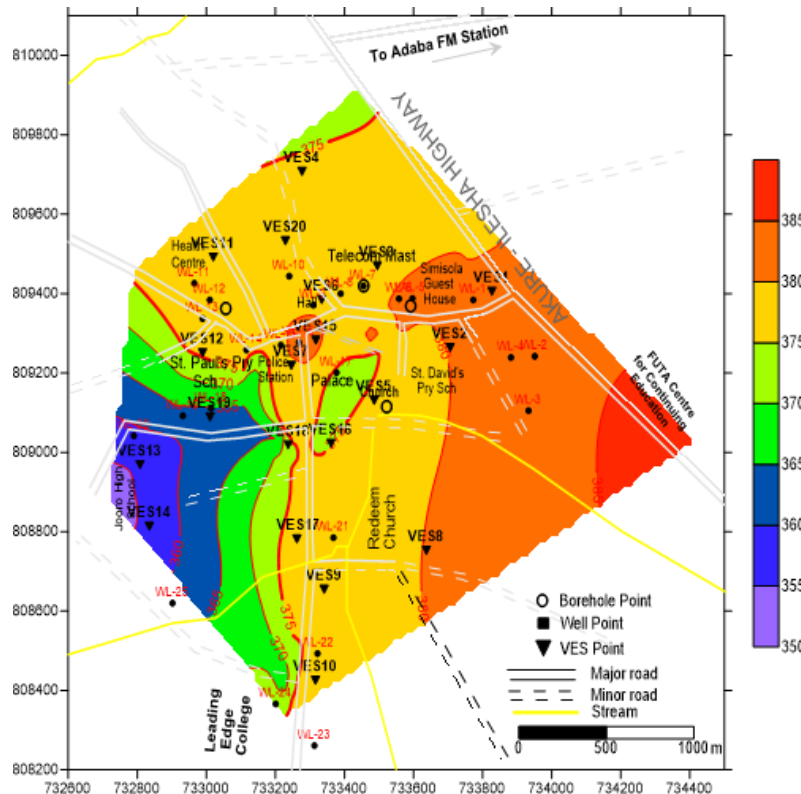


Figure 5. Data Acquisition map showing the locations of the VES, collected water samples, drilled borehole, and hydrogeological measurements from 25 wells

The Fm considers all of the characteristics of the material that affect electrical current flow, such as diagenetic cementation, pore shape, and porosity [7]. In this study, the obtained Fm was associated (r^2) with hydraulic conductivity. The Formation factor was calculated using Equation (10). A conductivity meter was used to measure the conductivity (in mhos) of the water at the site and convert it to ohm-m. The hydraulic conductivity of aquifers with no well/borehole data was calculated using a hydraulic conductivity and formation factor regression equation that was generated. Since a regression expression was built between the two; for each of the formations, transmissivity was estimated as well for all the VES stations.

$$Fm = \frac{\text{average aquifer water resistivity}}{\text{resistivity of water at site}} \quad (10)$$

The easiest way to determine aquifer parameters like K and T is to use data from well pumping tests. These characteristics play a role in regulating the water moving naturally through an aquifer as well as the resistance to fluid extraction. A global positioning system was used to assess SWL from twenty-five open wells. The GPS was used to determine the elevation of the well locations in relation to sea level, while the well's meter rule was lowered into the various wells until it reached the bottom, at which point the measurement was taken at the depth to the well's bottom. Hydraulic head and water column thickness are two more metrics taken. The measurement was taken twice, while the average values were recorded.

Before the rainy season began, ten groundwater samples were obtained at random with polythene bottles to ensure that effluents from runoff did not affect the quality of open wells, less than 10 meters deep. Pre-cleaning of the polythene bottles included Using non-ionic detergents, water, and then de-ionized water for the final rinse [50]. The water wells' locations were geo-referenced accordingly. Standard methodologies and techniques were used to analyze physical, chemical, and biological properties in samples delivered to the lab. At the time of collection, the samples' color, smell, turbidity, taste, appearance, pH, and total dissolved solids (TDS) were measured using a digital multimeter along with the samples' temperature using a mercury-in-glass thermometer. The electrical conductivity of the samples was measured using a digital conductivity meter. The total alkalinity was calculated using the titrimetric method (TA). Total Hardness was determined using EDTA (Ethylene Diamine Tetra Acetic Acid) as a titrant in a PH-10 buffer solution. The content of chlorine was determined using Mohr's method. Calcium, magnesium, potassium, and sodium were determined using a visible spectrophotometer; sulphate, bicarbonate, and nitrate were determined using the calometric method (digital titration). All of the testing were carried out according to APHA guidelines [51]. The ionic balance error (IBE) was calculated using equation (11), and the analytical precision for ion measurements (in meq/l) was determined to be +7%. The value is often within the acceptable range of 10%. As a result, the information can

be used for any purpose to interpret the quality of groundwater (drinking purpose and irrigation).

$$IBE = \frac{(TCC+TCA)}{TCC-TCA} \times 100 \quad (11)$$

where, TCC = total concentration of cations; TCA = total concentration of anions

The biological parameters that were tested were total coliform and E. coli. The American Public Health Association's [51] procedures for collecting and analyzing water samples were rigorously followed. A Piper diagram was used to represent and compare the water quality analyses in the research area. Data was subjected to statistical analysis using correlation and principal component analysis to better understand the nature of groundwater and the correlations between recorded characteristics (PCA).

One of the most successful methods for expressing information about water quality to concerned citizens and policymakers is the water quality index. It has become a critical metric for assessing and managing groundwater around the world, procedure developed by Sakati and Sarma [52] was adopted in this study, by assignment of weight (w_i) to each parameter measured in the water samples according to their relative importance in the overall quality of water for drinking purpose. In this study, a maximum weight of five (5) was assigned to NO_3^- , K^+ , Fe^{2+} , TDS, Cl^- , E-Coli, and total coliform; four (4) to pH, EC and Mn^{2+} ; three (3) was assigned to Ca^{2+} , Mg^{2+} , HCO_3^- , and SO_4^{2-} ; while Na^+ , turbidity, and total hardness (TH) assigned a weight of two (2); temperature and Alkalinity assigned a weight of one (1). Equations (12)-(14) were used in calculating WQI for the samples.

$$W_i = \frac{w_i}{\sum_{i=1}^n w_i} \quad (12)$$

where, W_i is the relative weight, w_i is the weight of each parameter and n is the number of parameters.

$$q_i = \frac{C_i}{S_i} \times 100 \quad (13)$$

where, q_i is the quality rating, C_i is the concentration of each chemical parameter in each water sample in milligrams per liter, S_i is the World Health Organization water standard for each chemical parameter in milligrams per liter.

$$WQI = \sum_{i=1}^n SL_i \quad (14)$$

where SL_i is the product of W_i and q_i . According to Rao and Nageswararao [41], the suitability of WQI values for human consumption was applied in this investigation, as shown in Table 2.

Table 2. Water Quality Indices Rating

WQI values	Rating
0-25	Excellent
26-50	Good
51-75	Bad
76-100	Very Bad
100 & above	Unfit

Permeability Index (PI), Magnesium ratio (MR), Kelly ratio (KR), percent Na, salinity hazard utilizing EC values, sodium absorption ratio (SAR), and residual sodium carbonate (RSC) in meq/l were calculated for irrigation purposes using equations (15)-(20), and the results were rated with standard values [23,53].

$$SAR = \frac{Na^+}{\sqrt{\frac{Ca^{2+} + Mg^{2+}}{2}}} \quad (15)$$

$$\%Na^+ = \frac{(Na^+ + K^+)}{(Ca^{2+} + Mg^{2+} + Na^+ + K^+)} \times 100 \quad (16)$$

$$PI = \frac{Na^+ + \sqrt{HCO_3^-}}{Ca^{2+} + Mg^{2+} + Na^+} \times 100 \quad (17)$$

$$RSC = (HCO_3^- + CO_3^{2-}) - (Ca^{2+} + Mg^{2+}) \quad (18)$$

$$MR = \frac{Mg^{2+}}{Ca^{2+} + Mg^{2+}} \quad (19)$$

$$KR = \frac{Na^+}{Ca^{2+} + Mg^{2+}} \quad (20)$$

3. Results

3.1. Electrical resistivity

Table 3 summarizes the geoelectric characteristics and inferred lithologies, whereas Figure 6 shows the different types of curves. As is typical of the subterranean complex terrain, the individualities of the geoelectric curves differed substantially. They range from three layer A-type (15%), H-type (10%), and K-type (5%), to four layer HA-type (10%), KH-type (40%), HK-type (15%), and five layer HKH-type (5%). The KH-type is the most common, with the four layer curve types accounting for 65 percent of all curve types. This indicates the degree of heterogeneity within weathered profile and fracturing of the basement rocks [10].

Three to five geologic sequences were discovered by the geoelectric interpretations. geologic sequence, as follows: topsoil (25–222 ohm-m; 89 ohm-m avg.), thicknesses (0.5 – 1.2 m; 0.9 m avg.), composed of clay, and sandy clay. Below the topsoil is a layer composed of clay/sandy clay/clay sand (33-320 ohm-m; 150 ohm-m avg.), thicknesses (2.2 – 7.5 m; 3.9 m avg.); the weathered layer, which is composed of clay/sandy clay and clayey sand (29–365 ohm-m; 96 ohm-m avg.), thicknesses (2.3 – 17.5 m; 9.1 m avg.); the partly weathered/fractured layer (25–412 ohm-m; 250 avg.), thicknesses (6.1 – 11.5 m; 8.6 m avg.); and the fresh basement (221–9540 ohm-m; 1861 ohm-m avg.). The depth to the basement rocks ranged from 5.7 to 32.5 m (16.1 m avg.). The water bearing units is basically found in the weathered layer, and confined/unconfined fractured basement which were only delineated in few places.

The spatial distribution of the weathered layer's resistivity and thickness map (Fig. 7a) revealed a

prominent resistivity in the 80–200 ohm-m range, corresponding to a clay/sandy clay water bearing unit, whereas resistivity range of 150 - 300 ohm-m (sandy clay/clay sand) was observed in the extreme northern part. The isopach map of the weathered layer (Fig. 7a) revealed overlapping values across the study area in the range of 6 – 15 m. On the southwestern flank, however, noticeable low thicknesses less than 10 m are observed. The overburden thickness of all VES curves ranges from 5.7 to 32.5 m (Fig. 7b and Table 4), with an average of 16.1 m. The spatial distribution of the overburden thickness (Fig. 7c) decreases northward; while higher values greater than 14 m are seen in the central – southern part. In reality, the presence of a thick aquiferous geologic unit does not necessarily suggest a large water yield, as important characteristics like resistivity, hydraulic gradient, sorption, hydraulic conductivity, transmissivity, and so on still play a role [6].

Table 4 shows that the traverse resistance (TR) ranges from 161.1 to 21896.1 ohm-m² (avg. 2202.9 ohm-m²). Aquifer transmissivity and traverse resistance can be correlated. Transmissivity increases as the TR increases. The average value of 2202.9 ohm-m² is less than 5000 ohm-m² expected of productive aquifer with high safe yield and transmissivity. The fracture coefficient (Fc) ranged from 0.15 – 265, with an average of 32.70 (Table 4). A good water bearing unit must be able to possess low fracture contrast/coefficient in the range of 0 – 20. Consequently, the groundwater potential in the study area on the basis of Fc is low. The reflection coefficient (Rc) is also linked to groundwater yield, as a low Rc indicates a high-density water-filled fracture with a high yield/potential. Table 4 shows the Rc values obtained for this investigation, which vary from -0.32 to 0.99. (0.65 avg.). Lower Rc favours availability of groundwater at reasonable economic supply. The groundwater potential appears to be low based on Table 5 rating, using Rc and overburden thickness.

3.2 Hydraulics

The K and T values for all the VES stations were estimated from the relationship of hydraulic conductivity (x-axis) and formation factor (y-axis) and obtained from twelve wells which were dug besides the VES locations. The relationship established is $y = 0.239e^{0.0519x}$ with correlation coefficient of 0.0961. The hydraulic conductivity of the water bearing units vary from 0.22 to 1.22 m/d and an average of 0.52 m/d; the transmissivity ranges from 1.08 to 18.18 m²/d and an average of 5.78 m²/d (Table 4).

Using Tables 6 and 7, the geological units fall within soil of clay-sand mixture depicting semi-permeable soil material. The spatial distribution of K and T (Fig. 7 c,d) shows that transmissivity is higher in the south with relatively high K-values, while the central part is moderate. Hence the hydrogeological parameters increase southwardly. The information obtained from the wells are presented in Table 8. The static water level which is invariably the thickness of the vadose water zone, varies from 3.9 – 7.9 m with an average of 5.68 m. The total depth of the wells varies from 5.8 m to 10.5 m and an average depth of 7.9 m, with water column of 1.3

– 3.7 m (2.2 m avg.). The obtained K and T ranged from 0.13 – 0.84 m/d (0.41 m/d avg.) and 0.77 – 16.9 m²/d (6.66 m²/d avg.) respectively. These values are very close to values estimated for all the VES stations. The

measured pore water resistivity varied from 34.84 – 53.48 ohm-m (43.12 ohm-m avg.), while groundwater formation factor (Fm) ranges from 0.59 to 11.33, with average value of 4.02.

Table 3. Summary of the VES Results obtained in the study area

Location		Elevation	VES	RESISTIVITY (Ohm-meter)					THICKNESS (m)				DEPTH (m)			Curve	
East	North	(m)	NO.	ρ_1	ρ_2	ρ_3	ρ_4	ρ_5	h_1	h_2	h_3	h_4	d_1	d_2	d_3	d_4	Type
733827	809406	381	1	78	365	1032			0.9	17.5			0.9	18.4			A
733706	809264	380	2	71	45	815	3281		1.1	4.9	26.5		1.1	6.0	32.5		HA
733495	809470	378	3	69	221	1480			0.8	4.9			0.8	5.7			A
733277	809708	375	4	98	254	69	2132		1.0	3.2	15.5		1.0	4.2	19.7		KH
733486	809131	375	5	101	189	68	2248		0.8	7.5	13.8		0.8	8.3	22.1		KH
733334	809385	378	6	78	155	36	9540		1.2	3.5	14.9		1.2	4.7	19.6		KH
733246	809219	378	7	87	122	59	1099		1.0	4.2	12.2		1.0	5.2	17.4		KH
733637	808753	380	8	126	320	98	1247		0.9	2.6	13.3		0.9	3.5	16.8		KH
733341	808655	378	9	56	147	658			1.0	15.5			1.0	16.5			H
733316	808426	376	10	25	211	98	2003		0.8	2.2	8.9		0.8	3.0	11.9		KH
733020	809492	376	11	84	155	369			0.7	5.9			0.7	6.6			K
732989	809251	376	12	63	29	356	221		0.9	3.6	11.5		0.9	4.5	16.0		HK
732808	808969	356	13	45	148	654			1.2	6.8			1.2	8.0			A
732835	808814	356	14	56	101	29	2332		1.2	6.1	9.2		1.2	7.3	16.5		KH
733317	809283	381	15	45	230	63	1983		0.6	2.8	7.1		0.6	3.4	10.5		KH
733361	809023	374	16	73	40.4	286	3262		0.8	3.9	12.5		0.8	4.8	17.2		HA
733262	808782	376	17	89	33	159	25	1425	0.5	2.7	4.9	6.1	0.5	3.2	8.1	14.2	HKH
733237	809019	373	18	92	47	661	341		1.1	2.3	5.3	6.8	1.1	3.4	8.7	15.5	HK
733011	809089	363	19	158	99	752	412		1.0	4.5	7.9	9.9	1.0	5.5	13.4	23.3	HK
733229	809533	377	20	222	79	1498			0.8	13.5			0.8	14.3			H

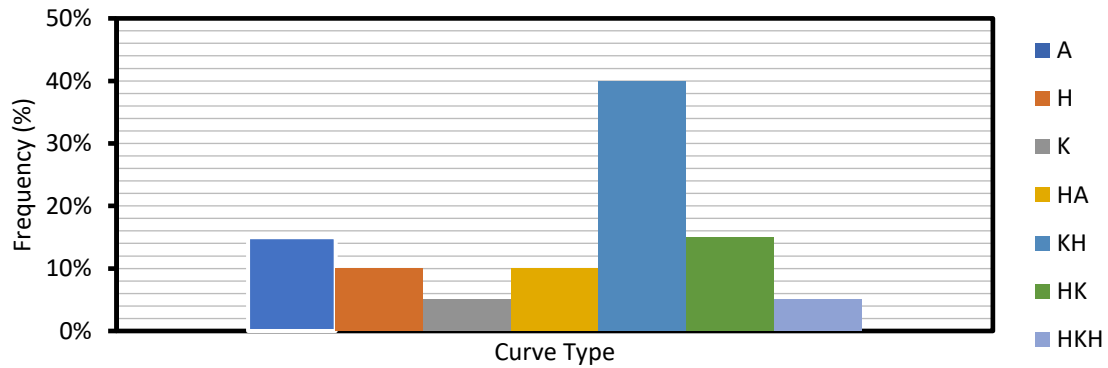


Figure 6. Curve types obtained from ves interpretation

Table 4. Summary of geoelectrical/hydraulics characteristics, vulnerability and groundwater potential index values of the Water Bearing units in the Study

VES No.	Overburden (m)	TR (ohm-m ²)	FC	RC	K (m/d)	T (m ² /d)	LC (ohm-m) ⁻¹	Log (c)	GWPIV	GWPIV Rating
1	18.4	6457.7	2.83	0.48	0.36	6.25	0.0595	0.40	171	Moderate
2	32.5	21896.1	4.03	0.60	0.25	6.63	0.1569	0.64	158	Moderate
3	5.7	1138.1	6.70	0.74	0.22	1.08	0.0338	0.56	128	Low
4	19.7	910.8	30.90	0.94	0.26	4.03	0.0228	1.21	127	Low
5	22.1	1498.3	33.06	0.94	0.29	4.06	0.0476	1.46	127	Low
6	19.6	636.1	265.00	0.99	1.22	18.18	0.0380	0.59	134	Low
7	17.4	599.4	18.63	0.89	0.29	3.59	0.0459	1.25	131	Low
8	16.8	945.4	12.73	0.85	0.60	7.98	0.0153	0.77	131	Low
9	16.5	2334.5	4.48	0.64	0.67	10.39	0.1233	0.17	148	Low
10	11.9	1356.4	20.44	0.91	0.65	5.79	0.1332	0.09	112	Low
11	6.6	973.3	2.38	0.41	0.59	3.48	0.0464	0.07	126	Low
12	16	161.1	0.62	-0.23	0.63	7.25	0.1384	0.15	133	Low
13	8	1060.4	4.42	0.63	0.61	4.15	0.0726	0.29	122	Low
14	16.5	683.3	80.41	0.98	0.32	2.97	0.0818	1.36	117	Low
15	10.5	1118.3	31.48	0.94	0.60	7.50	0.1382	0.75	112	Low
16	17.2	216.0	11.41	0.84	0.63	3.84	0.1075	0.88	125	Low
17	14.2	912.7	0.15	0.97	0.64	4.35	0.1183	-0.11	116	Low
18	15.5	209.3	0.52	-0.32	0.29	2.92	0.0609	0.58	133	Low
19	23.3	603.5	0.55	-0.29	0.60	2.70	0.0518	0.22	133	Low
20	14.3	347.8	123.23	0.98	0.63	8.51	0.1433	0.10	114	Low

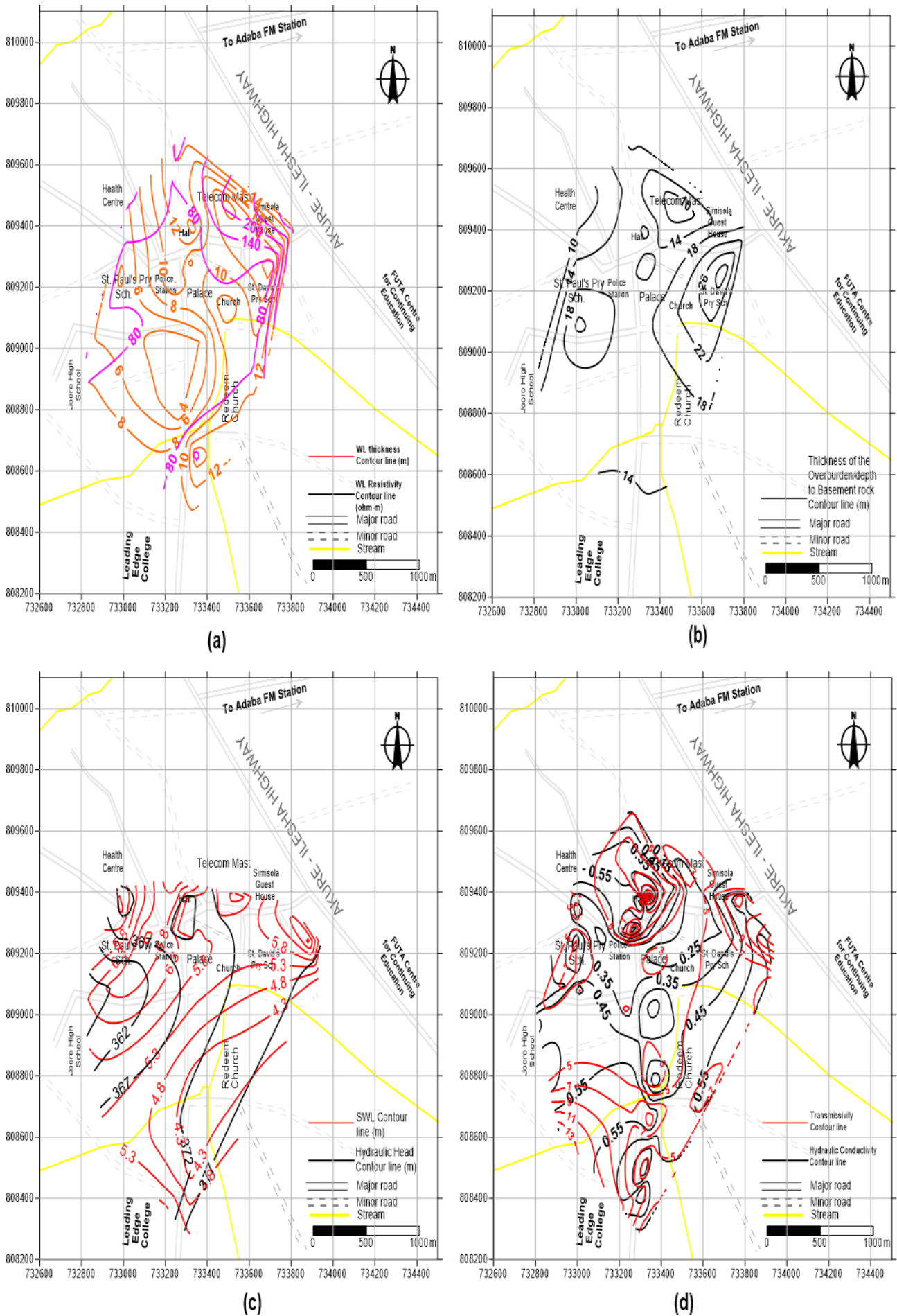


Figure 7. Spatial Distribution of (a) weathered layer thickness and resistivity (b) overburden thickness (c) static water level and hydraulic head (d) hydraulic conductivity and transmissivity

Table 5. Longitudinal unit conductance, overburden thickness, and reflection coefficient with corresponding protective rating

Total Longitudinal unit Conductance (mhos)	Rating of overburden's aquifer protective capacity	Overburden Thickness (m)	Reflection Coefficient	Groundwater Yield
<0.10	Poor	>15	>0.5	High
0.1 – 0.49	Weak	>15	<0.5	Medium
0.5 – 0.99	Moderate	<15	>0.5	Low
1.0 – 4.99	Good	<15	<0.5	Very Low
5.0 – 10.0	Very good			
>10.0	Excellent			

Table 6. Order of magnitude of K for different kinds of rock [54]

Geological Classification	K (m/d)
Unconsolidated Materials	
Clay	$10^{-8} - 10^{-2}$
Fine sand	1 - 5
Medium sand	$5 - 2 \times 10^1$
Coarse sand	$2 \times 10^1 - 10^2$
Gravel	$10^2 - 10^3$
Sand and gravel mixes	$5 - 10^2$
Clay, sand, gravel mixes	$10^{-3} - 10^{-1}$
Rock	
Sandstone	$10^{-3} - 1$
Carbonate rock with secondary porosity	$10^{-2} - 1$
Shale	10^{-7}
Dense solid rock	$<10^{-5}$
Fractured weathered rock (Core samples)	Almost 0 - 3×10^2
Volcanic rock	Almost 0 - 10^3

Table 7. Classification of Water Bearing Geological Units based on Coefficient of Permeability [54]

Class	K (m/d)	Examples
Extremely permeable	>10	Coarse sandstone, limestone and fissured crystalline rocks, pebbles, gravels
Semi-permeable	10-0.1	Fine grained sands, loams, slightly jointed crystalline rocks
Impermeable	<0.1	Clays, marls, compact igneous rocks

High formation factor corresponds to productive aquifer with good water yield. Therefore, based on this, the groundwater yield/potential in the area is low.

3.3 Borehole logging

The nature of parent rock, depth, amount and pattern of weathering, the sand/clay ratio, and the degree of fracturing, fissuring, and jointing all influence the occurrence of groundwater. Figure 8 shows the columnar section of the four drilled boreholes (BH-1 - BH-4) in the area. The column depicts five geological units based on physical observation/inspection of cuttings during drilling. The sections revealed that DBH-1 comprises four units: clay-sand mixture, sandy clay, fractured basement, fresh basement (gneiss), delineated at depth boundaries of 2.5 m, 25 m and 32.5 m respectively.

BH-2 has four unit, consisting of clay-sand mixture, clayey sand grading to clayey soil, sandy clay, fresh basement (granite), with lithological depth boundaries of 1.5 m, 16 m, and 39.9 m respectively. BH-3 consists of clayey sand, sandy clay, clay sand mixture, fractured basement, and fresh basement (migmatite gneiss) corresponding to geologic depth boundaries of 3 m, 6 m, 24 m, and 30 m. BH-4 is characterized by alternation of clay – sand mixture, clayey sand, clay sand grading stiffly to clayey soil, sandy clay, clay sand grading stiffly to clayey soil, sandy clay, and fresh basement (which is granitic); at lithological boundaries of 2 m, 8 m, 15 m, 32 m, and 40 m depth respectively. It was observed from the result of the drilling activity that most of productive boreholes were not drilled beyond the depth range of 30 – 35 m; therefore, this might be the reason why BH-2 and BH-4 failed and characterized with low yield. It was also observed that boreholes drilled on migmatite/migmatite gneiss, and gneiss tend to be productive than granite, even though the fractured/partly weathered layer proved to be the difference between this geological units in the study area. Consequently, the combined weathered zone and fractured basement (unconfined aquifer) is the best groundwater configuration for productive exploitation and development in the area as revealed by the geologic sections (Fig. 8).

3.4 Vulnerability Assessment

The vulnerability of the water bearing units were assessed by AVI and LC as shown in Table 4. The calculated longitudinal unit conductance values (in mhos) of water bearing units using resistivity parameters ranged from 0.0153 to 0.1569 mhos with an average of 0.0818 mhos. Hence using Table 1, the groundwater protective capacity varies from poor – weak, while taking the average value, the protective capacity is poor. The calculated AVI values range from - 0.11 – 1.46, with an average of 0.5715. Therefore, using Table 2, the groundwater in the study area is extremely vulnerable to pollution.

3.5 Groundwater Quality

The geochemistry of groundwater may have an impact on how useful aquifer systems are as water supplies. Without prior treatment, the types and concentrations of dissolved elements in an aquifer system's water determine whether the resource is suitable for drinking water, industrial uses, irrigation, livestock watering, and other uses [55-57]. Tables 9 and 10 reflect the findings of the examinations of the water

samples. The analysis's range and mean concentrations are compared to WHO [58] criteria. The usefulness of water for many uses is influenced by the earth's temperature. The groundwater's temperature ranges between 27.5 and 27.8°C, with a mean of 27.6°C. A generally moderate temperature is shown by the range of values. All of the water samples have a clear look and are tasteless, odorless, and colorless. The average turbidity of water is 9 NTU, which is higher than the WHO-recommended limit of 5 NTU and ranges from 2 to 16 NTU. This shows that the groundwater has a high suspended matter content, including clay, silt, fine organic matter particles, and similar stuff [59-61]. The pH plays a vital role to react with acidic or alkaline. It is controlled by CO₂ - CO₃²⁻ - HCO₃⁻ equilibrium. The combination of CO₂ with H₂O (water) forms H₂CO₃ (carbonic acid), which affects the pH of water. Based on pH, which ranges from 1 to 14, water can be categorized as acidic or alkaline. The groundwater's pH has been measured to range from 4.7 to 5.6. The water is classified

as having an acidic condition according to the pH scale because H⁺ is more than OH⁻ (Table 11) in the water [7, 24].

The ability of a material to carry electrical current is measured by its electrical conductivity (EC). Strong acids like Cl⁻, SO₄²⁻, and NO₃⁻ have high conductivity compared to weak acids like HCO₃⁻ and CO₃²⁻, which have low conductivity. EC ranges from 149 to 391 S/cm (avg. of 234 S/cm). The enrichment of salts in water increases with increasing EC. Using Table 12, the water can be categorized as Type I (EC less than 1500 S/cm), which is characterized by low salt enrichment, low infiltration, high runoff, and high topography. This type of water is assumed to be a recharge water. Total dissolved solids (TDS), which includes any organic matter and some water of crystallization, are a measure of the total salt concentration of dissolved ions from soils and rocks in water. The solubility and type of rocks the water has come into contact with affect the volume and makeup of dissolved solids.

Table 8. Summary of well Information, Sample locations, and measured properties

Well No.	Easting (mE)	Northing (mN)	Elevation (m)	Well Depth (m)	SWL (m)	Water Column (m)	Hydraulic Head (m)	K (m/d)	T (m ² /d)	Pore water Resistivity (Ohm-m)	Aquifer Resistivity (Ohm-m)	Formation Factor
WL-1 (VES 1)	733773	809384	381	10.2	6.6	3.6	373	0.67	12.33	47.17	365	7.74
WL-2	733951	809242	382	8.3	5.1	3.2	377	0.52	16.90	49.50	-	-
WL-3	733933	809105	383	7.7	4.0	3.7	379	0.68	3.88	40.82	-	-
WL-4	733882	809239	382	9.4	7.5	1.9	375	0.72	14.18	34.84	-	-
WL-5	733597	809388	381	6.8	5.2	1.6	376	0.22	4.86	46.73	-	-
WL-6	733558	809387	380	6.7	4.4	2.3	376	0.15	2.94	43.67	-	-
WL-7 (VES 3)	733455	809419	378	7.2	5.2	2	373	0.48	8.35	42.37	-	-
WL-8	733389	809400	377	7.1	5.8	1.3	371	0.61	10.25	37.17	-	-
WL-9 (VES 6)	733310	809371	378	6.9	5.5	1.4	373	0.23	3.80	38.91	36	0.93
WL-10 (VES 15)	733240	809444	377	10.5	7.9	2.6	369	0.58	6.90	39.06	63	1.61
WL-11 (VES 11)	732965	809426	377	7.5	4.8	2.7	372	0.47	3.10	45.05	369	8.19
WL-12	733010	809384	378	6.8	5.0	1.8	373	0.32	5.12	35.97	-	-
WL-13	732989	809337	378	6.5	4.7	1.8	373	0.15	1.20	44.05	-	-
WL-14 (VES 12)	733116	809258	376	9.3	7.5	1.8	369	0.19	3.14	38.31	221	5.77
WL-15 (VES 7)	733216	809270	378	8.6	6.6	2	371	0.66	6.93	50.51	59	1.17
WL-16	733268	809277	383	7.8	5.6	2.2	377	0.84	14.45	53.48	-	-
WL-17 (VES 5)	733377	809201	374	8.1	6.0	2.1	368	0.15	2.13	49.75	68	1.37
WL-18	733014	809111	364	9.9	7.2	2.7	357	0.43	6.67	42.37	-	-
WL-19 (VES 19)	732932	809092	364	8.4	6.9	1.5	357	0.33	7.69	36.36	412	11.33
WL-20 (VES 13)	732790	809042	358	8.3	6.1	2.2	352	0.25	3.58	50.25	148	2.95
WL-21 (VES 17)	733368	808785	377	5.8	3.9	1.9	373	0.17	1.34	42.37	25	0.59
WL-22 (VES 10)	733322	808493	376	6.7	4.1	2.6	372	0.13	0.77	37.59	98	2.61
WL-23	733313	808261	385	6.9	5.4	1.5	380	0.27	1.22	45.87	-	-
WL-24	733201	808366	373	9.5	5.9	3.6	367	0.48	9.98	38.46	-	-
WL-25	732902	808620	375	7.2	5.2	2	370	0.66	14.78	47.39	-	-

Table 9. Result obtained from the physical parameters measured/examined

Well No.	Temp (°C)	pH	TDS (mg/l)	EC (µS/cm)	Colour	Taste	Odour	App.	Turb. (NTU)
WL-1	27.6	5.40	262	391	Colourless	unobjectionable	unobjectionable	Clear	2.0
WL-4	27.7	4.79	102	149	Colourless	unobjectionable	unobjectionable	Clear	6.0
WL-8	27.8	5.56	137	204	Colourless	unobjectionable	unobjectionable	Clear	12.0
WL-10	27.8	5.20	109	162	Colourless	unobjectionable	unobjectionable	Clear	8.0
WL-12	27.5	4.80	158	236	Colourless	unobjectionable	unobjectionable	Clear	14.0
WL-17	27.6	5.18	176	262	Colourless	unobjectionable	unobjectionable	Clear	16.0
WL-19	27.6	5.45	185	242	Colourless	unobjectionable	unobjectionable	Clear	9.5
WL-20	27.5	4.68	123	198	Colourless	unobjectionable	unobjectionable	Clear	5.8
WL-21	27.5	5.50	155	205	Colourless	unobjectionable	unobjectionable	Clear	10.4
WL-22	27.8	4.95	138	290	Colourless	unobjectionable	unobjectionable	Clear	8.8

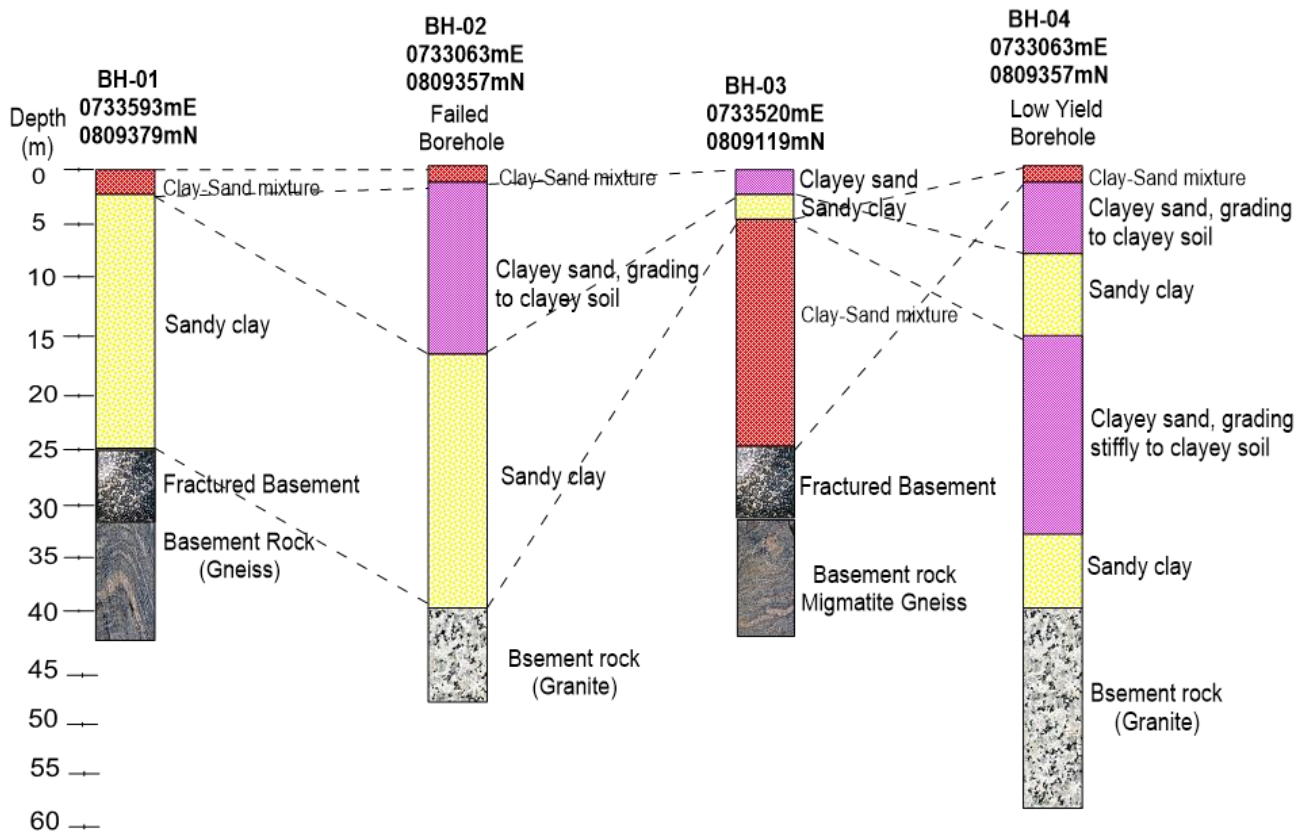


Figure 8. Columnar sections of borehole with drilling information for BH-1 to 4

Table 10. Summary of the analyzed chemical and biological parameters

Well No.	TA	TH	HCO ₃ ⁻	Ca ²⁺	Mg ²⁺	Cl ⁻	Na ⁺	K ⁺	SO ₄ ²⁻	NO ₃ ⁻	Fe	Mn	E-Coli	Total coliform	WQI (%)
WL-1	16	198	16.1	42.5	22.5	37.0	24.1	12.2	5.7	0.86	0.06	0.03	0	8	31
WL-4	12	64	12.7	14.4	6.23	18.0	11.0	12.5	5.2	2.44	0.08	0.02	0	6	25
WL-8	18	113	18.4	25.7	12.0	21.0	13.7	8.9	6.8	5.28	2.06	0.03	1	14	96
WL-10	9	86	9.3	16.8	29.5	15.6	10.1	7.3	8.8	1.86	0.03	0.01	0	7	27
WL-12	10	98	14.8	25.7	8.30	23.0	15.0	11.2	9.9	6.74	0.04	0.02	1	12	42
WL-17	14	176	10.0	29.7	6.33	26.0	16.9	9.8	11.2	9.36	0.06	0.02	1	18	52
WL-19	22	87	10.5	26.5	14.2	19.8	12.4	12.3	5.5	2.65	0.15	0.01	0	8	34
WL-20	17	98	14.2	17.7	19.0	24.5	13.3	9.5	11.3	1.84	0.08	0.01	1	10	32
WL-21	11	102	12.8	19.5	12.8	16.8	19.7	6.7	10.5	1.36	0.04	0.01	0	5	27
WL-22	15	122	8.6	22.6	18.3	21.9	22.8	8.3	7.6	1.11	0.09	0.02	0	6	29

Note: All units are in mg/l except the biological parameters in CfU/100ml

High TDS is typically brought on by the impact of anthropogenic origin with regard to discharge water at topographic lows, while low TDS is typically brought on by the influence of rock-water interaction with regard to recharge water at topographic highs [24]. The value of TDS ranges from 102 mg/l to 262 mg/l (155 mg/l avg.). Therefore, using Table 13, the water is fresh with TDS less than 1000 mg/l. Total alkalinity is a gauge of how effectively calcium carbonate can neutralize acid in water (CaCO₃). The TA ranges from 9 to 22 mg/l (14.4 mg/l on average). The suggested WHO acceptable threshold of 200mg/l is met by this range of results. The samples' total hardness (TH), which ranges from 64 to 198 mg/l (114 mg/l on average), varies greatly. Scale develops in pipes, water heaters, and boilers due to hard water. The

amount of soap lather increases with TH. The study area's water is classified as either soft or hard according to TH, as shown in Table 14. However, the water samples' TH and TA (average readings) both fall within the 400 mg/l and 200 mg/l, respectively, WHO-recommended permitted limits.

Table 11. Classification of pH [24]

pH Range	Type	Dominance of ions
1 - 7	Acid	H ⁺ is more than OH ⁻
7	Neutral	Equal amounts of H ⁺ and OH ⁻
7 - 14	Basic	OH ⁻ is more than H ⁺

Table 12. Classification of EC [24]

EC Range ($\mu\text{S}/\text{cm}$)	Type	Enrichment of salts	Topography	Runoff	Infiltration	Water type
<1,500	I	Low	High	High	Low	Recharge water
1,500 – 3,000	II	Medium	Moderate	Medium	Medium	-
>3000	III	High	Low	Low	High	Discharge water

Table 13. Classification of TDS [7]

TDS range (mg/l)	Classification
<1,000	Fresh
1,000 to 10,000	Brackish
10,000 to 100,000	Saline
>100,000	Brine

Table 14. Classification of TH [7]

TH Range (mg/l)	Classification
<75	Soft
75-150	Moderately hard
150 – 300	Hard
>300	Very hard

The main component of most rocks is calcium (Ca^{2+}), which is typically derived from minerals like plagioclase, pyroxene, and amphiboles. Another source of calcium in groundwater is the presence of carbon dioxide in the soil zone. Ca^{2+} ranges between 14.4 and 42.5 mg/l (24.1 mg/l on average), which is still within the safe range of 75 mg/l suggested by the WHO. The groundwater's calcium content is derived from calcium feldspars found in the rocks in the research area. Basic igneous rocks, volcanic rocks, and metamorphic rocks all include magnesium (Mg^{2+}), which is generated from minerals including olivine, hornblende, serpentine, biotite, augite, and others. Magnesium in groundwater can also come from the sea, mining, and industrial waste. From 6.23 to 29.5 mg/l (14.9 mg/l), Mg^{2+} is present. This value range still falls within the permitted range of 50 mg/l. Sodium (Na^+) is under the WHO limit (50 mg/l) for drinking water as it ranges from 10.1 to 24.1 mg/l (15.9 mg/l on average). An important source of potassium (K^+), which ranges between 6.7 and 12.5 mg/l (9.9 mg/l on average), is found in orthoclase feldspar, nepheline, leucite, and biotite. Other sources of potassium include chemical fertilizers. K^+ 's generally lower content may be caused by clay minerals absorbing it. As a result, the K^+ for drinking water is within the WHO limit (75 mg/l). It ranges from 8.6 to 18.4 mg/l (12.7 mg/l on average) of bicarbonate (HCO_3^-). This value range is within the permissible range of the WHO guideline of 500 mg/l. The principal source of HCO_3^- in the groundwater is probably soil CO_2 . Organic material breakdown also releases carbon dioxide for solution. Sulphate (SO_4^{2-}) levels in the examined water samples range from 5.2 to 11.3 mg/l (8.3 mg/l on average). The reported mean value complies with the 100 mg/l WHO standard for drinking water. Within the permitted limit of 250 mg/l, the chloride (Cl^-) is dissolved from the rocks and soils in the research region, with values ranging from 15.6 to 37 mg/l (22.4 mg/l on average). The water samples have nitrate (NO_3^-) concentrations ranging from 0.86 mg/l to 9.36 mg/l (3.4 mg/l). Nitrate is a compound that is produced when organic matter decomposes and is found in sewage, nitrate fertilizers, and soil. Since the NO_3^- level is less than 10 mg/l, it is most likely coming from suspected nitrate

fertilizers as well as soil nitrate. However, the outcomes are in line with the WHO's advice.

Manganese and iron heavy metal concentrations in the water were 0.01 to 0.03 mg/l (av. 0.018 mg/l average) and 0.03 to 2.06 mg/l (avg. 0.269 mg/l average), respectively. These cation and heavy metal values are extremely low and fall under the WHO standards of 0.1 mg/l and 0.3 mg/l, respectively. The biological quality test revealed an E. coli concentration of 0 to 1 CFU/100 ml and a total bacterial count of 5 to 18 (9 avg.). These average values are below the stipulated limits of 3 Cfu/100 ml for E. coli and 10 Cfu/100 ml for total coliform, respectively. Although the total bacteria count is high. The trilinear diagram of the water samples, shown in Figure 9, is a useful tool for separating information for a critical analysis with regard to the sources of dissolved ions in water and changes in water character [62].

The majority of the water in the study area falls into zone 4 (Fig. 9b), which is classified as "strong acids exceeded weak acids," and no cation-anion pair (Ca-Mg-Cl water type) exceeds 50%. However, only a small percentage of samples (less than 20%) are of non-carbonate hardness (secondary alkalinity) exceeds 50%. (Ca-Cl water type). For the purpose of understanding the mechanisms that control the groundwater chemistry with respect to atmospheric precipitation (rainfall), rock-water interaction, and evaporation, Gibb's diagrams were used to relate the ratios of the cations ($\text{Na}^+ + \text{K}^+ : \text{Na}^+ + \text{K}^+ + \text{Ca}^{2+}$) and anions ($\text{Cl}^- : \text{Cl}^- + \text{HCO}_3^-$) that are plotted against TDS. From Figure 10, the chemistry of the water falls in the mixed zone, which indicates contribution from soil/rock-water interaction, precipitation, and evaporation (Fig. 10 a,b) and carbonic weathering is more active than the silicate weathering process (Fig. 10c). The calculated values of WQI vary from 25 % to 96 % (39.5 % avg.). The spatial distribution of WQI across the study area (Fig. 11) showed that southern generally part is characterized with WQI values less than 50%. This signifies that excellent/good water types characterized the south while the northern area is poor.

According to Table 15, the results of a correlation analysis using Pearson correlation show that there is a strong positive correlation between some of the chemical parameters, including Ca and TH ($r = 0.87$), TH and Cl ($r = 0.85$), TH and Na ($r = 0.72$), TH and Mn ($r = 0.56$), HCO_3 and Fe ($r = 0.61$), HCO_3 and Mn ($r = 0.58$), Ca and Cl ($r = 0.87$), Ca and Na ($r = 0.62$), Na and Cl ($r = 0.62$), Mn and Cl ($r = 0.62$) and Fe and Mn ($r = 0.53$). These chemical parameters had a strong positive connection, which suggests that they came from the same source. The untypical anthropogenic cause is clearly indicated by the negative positive association between Mg and NO_3 ($r = -0.64$), SO_4 and K ($r = -0.57$), and Mg and SO_4 in general.

Groundwater data are subjected to principal component (PC) analysis in order to better understand

the correlations between them and the likely sources of significant ions. The data set underwent an analysis of five components (Table 16). With an eigenvalue of 3.67, the principal component 1 (PC-1) explains 31% of the groundwater variance overall. TH, Ca, Cl, Na, and Mn are

some of the parameters that are heavily and positively loaded on this factor. This relationship demonstrated that the precipitation of all these variables in the water samples is due to a single source.

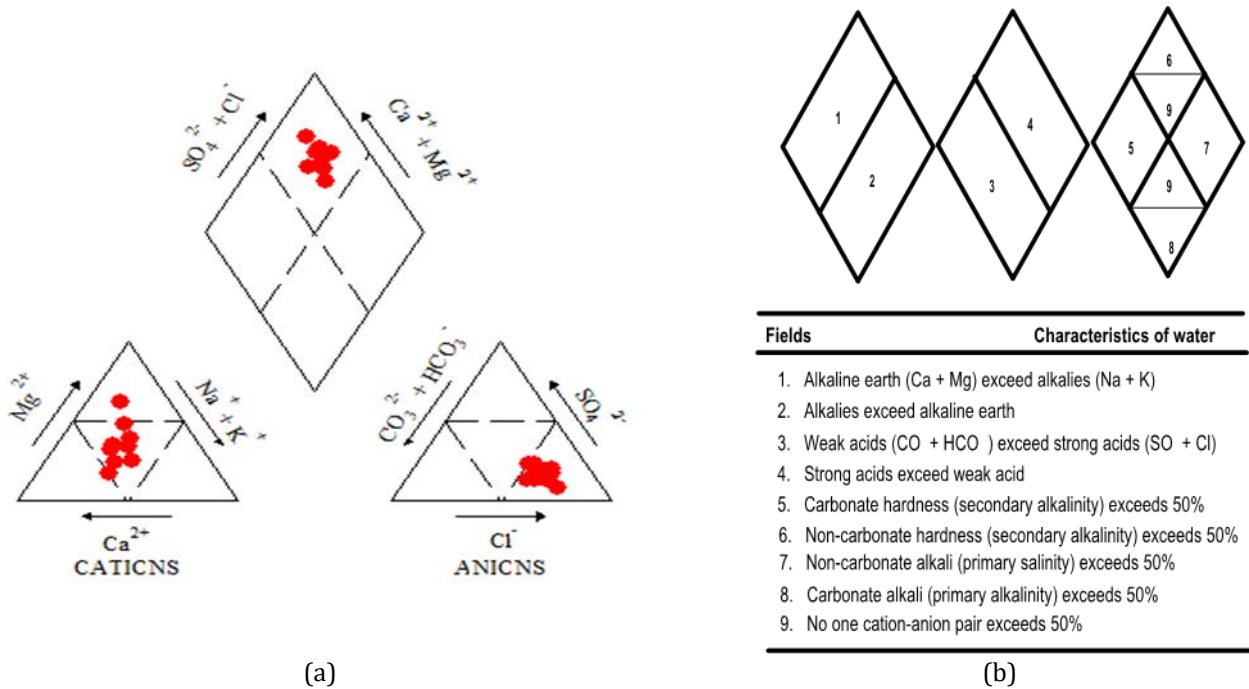


Figure 9. (a) Piper's Trilinear Diagram for Water Samples (b) showing a predominant Zone 4 Water Type

Mineral dissolution, weathering, and anthropogenic pollution have all been assigned to this component. The PC-2's eigenvalue is 2.08, which represents 17% of the overall variance. The following parameters— HCO_3 , Fe, and Mg—are heavily and favorably weighted on this component. This component might be caused by precipitation or mineral dissolution as a result of the interaction between rocks and water. The eigenvalue of PC-3 is 1.89, accounting for 16% of the overall variance. Because of the deterioration of organic materials and anthropogenic contamination, this component is heavily and favorably loaded with NO_3 .

The PC-4's eigenvalue is 2.16, and its overall variance is 18%. The two main factors that are heavily and favorably coupled with this factor are TA and K. This component is due to weathering and anthropogenic contamination.

3.6 Irrigation Water Assessment

By lowering osmotic pressure in plant structure cells, excessive dissolved ion concentrations in irrigation water have a physical and chemical impact on plants and agricultural soil. Therefore, the electrical conductivity (EC), percent sodium absorption ratio (SAR), sodium (percent Na^{+}), permeability index (PI), residual sodium carbonate (RSC), magnesium ratio (MR), and Kelly ratio are frequently used to determine the danger of salinity (KR). The results are shown in Table 17 and the comparison of these indices to the common criteria is shown in Table 18.

Electrical conductivity was used to compute the salinity risk (C), which ranged from 149 to 391 S/cm (234 S/cm), suggesting a low salinity hazard that is safe for irrigation. A crucial chemical indicator for determining how suitable a water source is for irrigation is the salt content or alkali hazard for crops, which is expressed in sodium adsorption ratio. Important calcium and magnesium ions are those that tend to offset the effects of sodium. When SAR concentrations are too high, the physical structure of the soil is destroyed [23]. Soil particles absorb sodium, which is then bound to them. When dry, the soil becomes compact and hard, making it impenetrable to water penetration. A risk occurs when sodium replaces the adsorbents that hold calcium and magnesium because it weakens the structure of the soil. The analyzed water samples' percent SAR ranges from 34.39 to 86.44. (63.72 avg.). Generally speaking, the values are unsuitable for irrigation when using the average value. The percent Na^{+} is inversely proportional to permeability of soils. The range of the percent Na^{+} obtained, which corresponds to excellent water, is 16.09 to 39.33 (28.86 on average). Additionally, the Wilcox plot [63] of the water samples (Fig. 12) demonstrates that the irrigation water is "excellent to good."

Na^{+} , Ca^{2+} , Mg^{2+} , HCO_3^{-} and Cl^{-} concentrations have a big impact on permeability. It is very crucial for plant growth. Plant growth is inhibited when permeability in the soil zone is low. The degree of permeability in the soil is measured using the permeability index (PI). Permeability index is a word used to describe the soil's degree of permeability (PI) The water samples' PI ranges

from 22 to 45. (35 avg.). The groundwater samples fall into the "suitable - marginal" group, taking the average value, it means that the groundwater is marginal or moderate for irrigation, according to the classification of PI in Table 16. The difference between carbonates ($\text{HCO}_3^- + \text{CO}_3^{2-}$) and alkaline earths ($\text{Ca}^{2+} + \text{Mg}^{2+}$), which is measured in meq/l, is known as residual sodium carbonate (RSC). Alkaline earths that are precipitated by carbonates have an impact on water quality by raising the percentage of Na^+ . This is more prevalent when carbonates are present in excess compared to alkaline earths. The excess carbonates combine with Na^+ to form NaHCO_3 , which affects soil structure. The RSC values range between -4 to -1 (-2.3 avg.). Therefore, on the basis of RSC, the irrigation water quality in the area is generally "marginal/suitable".

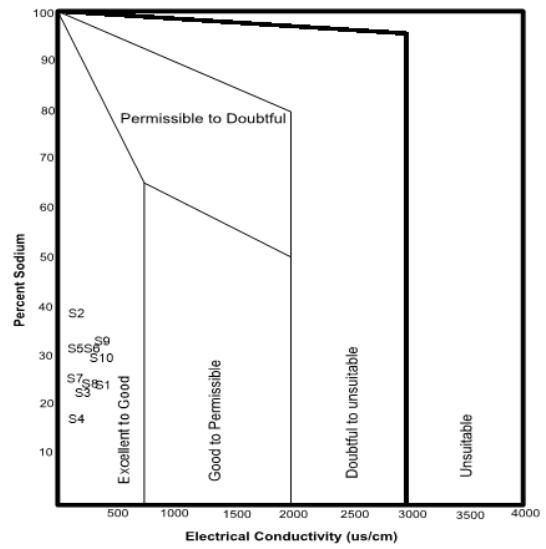


Figure 12. Wilcox Plot of Sampled water

Table 15. Correlation matrix of chemical parameters in water samples from the study area

Parameter	TA	TH	HCO ₃	Ca	Mg	Cl	Na	K	SO ₄	NO ₃	Fe	Mn
TA	1											
TH	0.16	1										
HCO ₃	0.18	0.15	1									
Ca	0.36	0.87	0.32	1								
Mg	-0.03	0.09	-0.17	0.06	1							
Cl	0.30	0.85	0.38	0.87	0.10	1						
Na	0.05	0.72	0.05	0.62	0.10	0.62	1					
K	0.38	0.10	0.24	0.40	-0.35	0.46	-0.09	1				
SO ₄	-0.39	0.08	-0.14	-0.23	-0.06	-0.10	0.01	-0.57	1			
NO ₃	-0.08	0.23	0.08	0.18	-0.64	0.06	-0.20	0.12	0.38	1		
Fe	0.36	-0.02	0.61	0.07	-0.14	-0.08	-0.16	-0.13	-0.24	0.23	1	
Mn	0.13	0.56	0.58	0.62	-0.21	0.60	0.41	0.34	-0.42	0.25	0.53	1

Table 16. Varimax orthogonal rotated factor loadings from PCA of the Analyzed parameters

Variable	Factor 1	Factor 2	Factor 3	Factor 4
TA	0.13	0.24	-0.08	0.61
TH	0.96	0.06	0.07	-0.07
HCO ₃	0.19	0.77	0.12	0.17
Ca	0.89	0.15	0.07	0.28
Mg	0.12	-0.09	-0.86	-0.12
Cl	0.91	0.06	0.04	0.27
Na	0.82	-0.04	-0.23	-0.11
K	0.18	-0.13	0.38	0.87
SO ₄	0.04	-0.21	0.26	-0.84
NO ₃	0.10	0.15	0.90	-0.22
Fe	-0.13	0.96	0.06	0.05
Mn	0.56	0.62	0.20	0.26
Eigen value	3.67	2.08	1.89	2.16
% Variance	31.0	17.0	16.0	18.0
Cumulative % variance	37.0	81.0	100.0	59.0
Interpretation of process	Mineral dissolution, Weathering and anthropogenic pollution	Mineral dissolution and precipitation	Organic matter degradation and anthropogenic pollution	Weathering/anthropogenic pollution

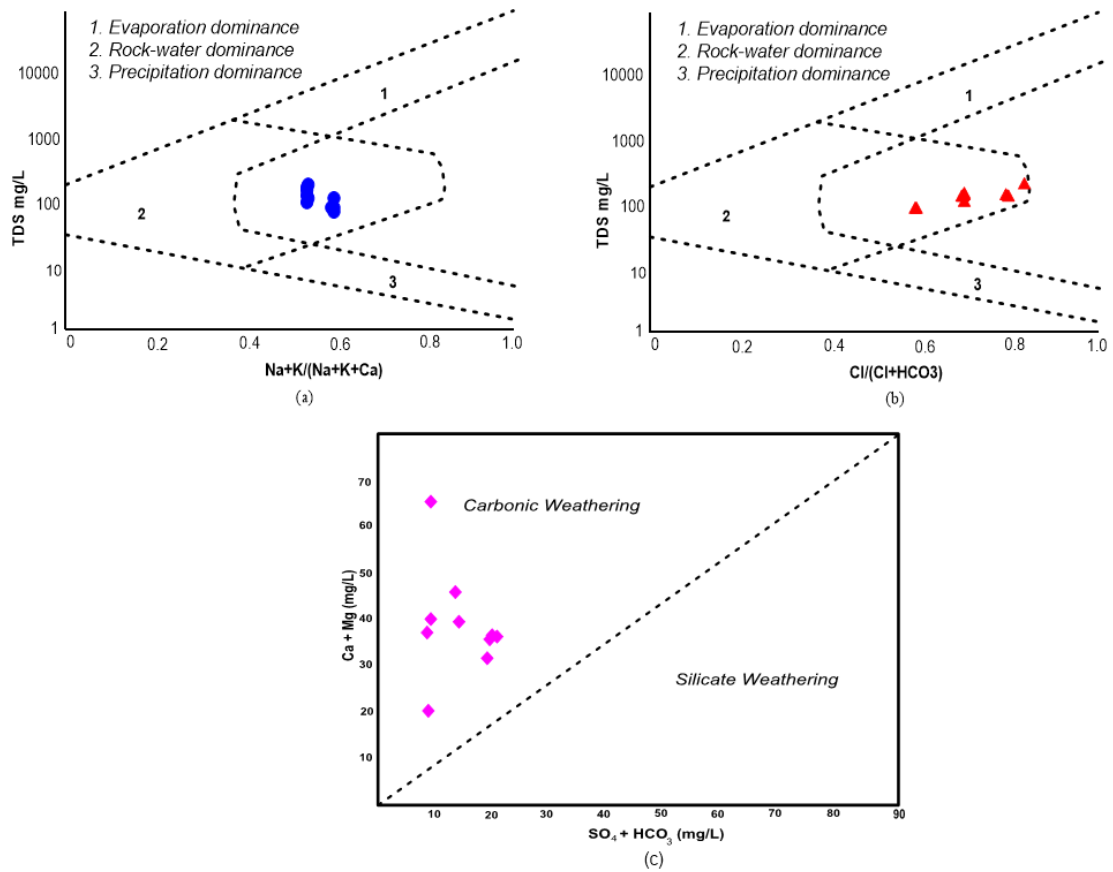


Figure 10. Mechanisms controlling groundwater chemistry in the study area showing a mixed domain (a&b) and (c) carbonic weathering prevalence

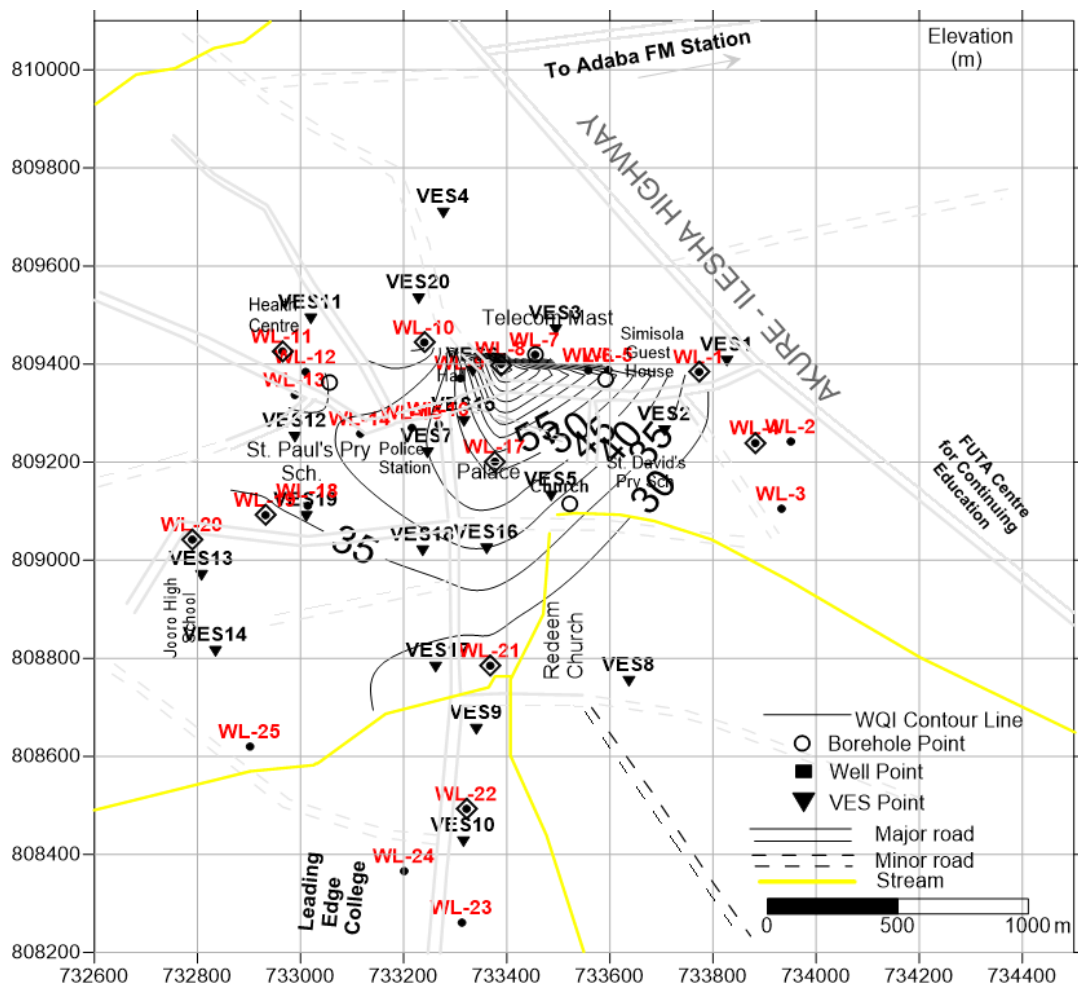


Figure 11. The distribution of WQI values across the study area

Table 17. Results of the Irrigation Indices/parameters obtained from the well water samples

Well No.	PI (%)	RSC	MR	KR	%SAR	%Na	EC
WL-1	27	-4	47	0.26	74.39	25.51	391
WL-4	45	-1	42	0.39	60.99	39.33	149
WL-8	32	-2	43	0.26	55.94	26.62	204
WL-10	22	-3	74	0.13	34.39	16.09	162
WL-12	40	-2	35	0.33	65.83	32.33	236
WL-17	42	-2	26	0.37	73.46	32.98	262
WL-19	28	-2	47	0.22	48.34	25.53	242
WL-20	33	-2	64	0.24	52.31	25.14	198
WL-21	44	-2	52	0.42	85.14	33.67	205
WL-22	37	-3	57	0.38	86.44	31.38	290

Table 18. Irrigation Indices and their categorization [23]

Parameter	Sample range	Classification
Na% (meq/l)	0 – 20	Excellent
	20 – 40	Good
	40 – 60	Permissible
	60 – 80	Doubtful
	>80	Unsuitable
SAR (meq/l)	0 – 10	Excellent (suitable for all types of crops and soil except for those crops sensitive to Na) Good (suitable for coarse textured or organic soil with permeability) Fair (harmfully for almost all soils) Poor (unsuitable for irrigation)
	10 – 18	
	18 – 26	
	>26	
RSC (meq/l)	<1.25	Good
	1.25 – 2.50	Medium
	>2.50	Bad
EC (µs/cm)	<250	Low salinity hazard (good)
	250 – 750	Medium salinity hazard (moderate)
	750 – 2250	High salinity hazard (poor)
	>2250	Very high salinity hazard (very poor)
PI (meq/l)	>75%	Suitable
	25 – 75%	Marginal
	<25%	Unsuitable
MR (meq/l)	<50	Suitable
	>50	Unsuitable
KR (meq/l)	<1.0	Good
	>1.0	Not Good

The magnesium ratio is a proportion that compares magnesium to alkaline earths (Ca²⁺ + Mg²⁺). Magnesium degrades soil structure in water with high salinity and higher Na⁺. More Mg²⁺ can make soil more acidic in equilibrium, which has an impact on crop production [4]. The water samples have MRs that range from 26 to 74 (48.7 on average) and are appropriate for irrigation. Kelly ratio, which compares the concentration of Na⁺ to that of Ca²⁺ and Mg²⁺, is used to categorize the quality of irrigation water. If the KR is less than one, irrigation is appropriate; if it is greater than one, irrigation is not appropriate. The computed KR values for the water samples range from 0.13 to 0.42. (0.3 avg.)

3.7 Groundwater potential index value

Therefore, using multi criteria parameters as rated in Table 19, where all the measured parameters are rated and weighted based on their significances in groundwater accumulation. The parameters were

derived from VES, borehole logging, pumping test and hydraulics measurement. The summation of these parameters resulted into generation of groundwater potential index values (GWPIV) which was used in developing groundwater potential map for the area. All the parameters: weathered layer thickness (WT), weathered layer resistivity (WR), overburden thickness (OT), traverse resistance (TR), transmissivity (TM), reflection coefficient (RC), fracture contrast (FC), formation factor (FM), water quality index (WQI), aquifer vulnerability index (AVI), and longitudinal conductance (LC) were summed up (equation 21) by attaching different weights (w) and ratings (r) based on their significance on groundwater accumulation/storage and exploitation.

$$GW = f(WT, WR, OT, TR, TM, RC, FC, LC, AVI)$$

Therefore, the GWPIV was determined using Eq. 21.

$$GWPIV = WT_w WT_r + WR_w WR_r + OT_w OT_r + TR_w TR_r + TM_w TM_r + RC_w RC_r + FC_w FC_r + LC_w LC_r + AVI_w AVI_r \quad (21)$$

The GWPIV obtained ranges from 112 – 171 with an average of 130 indicating a low potential. The developed groundwater potential map (Fig. 13) showed

predominant low potential across the study except a small zone in the northeast which showed better hydrogeological prospect.

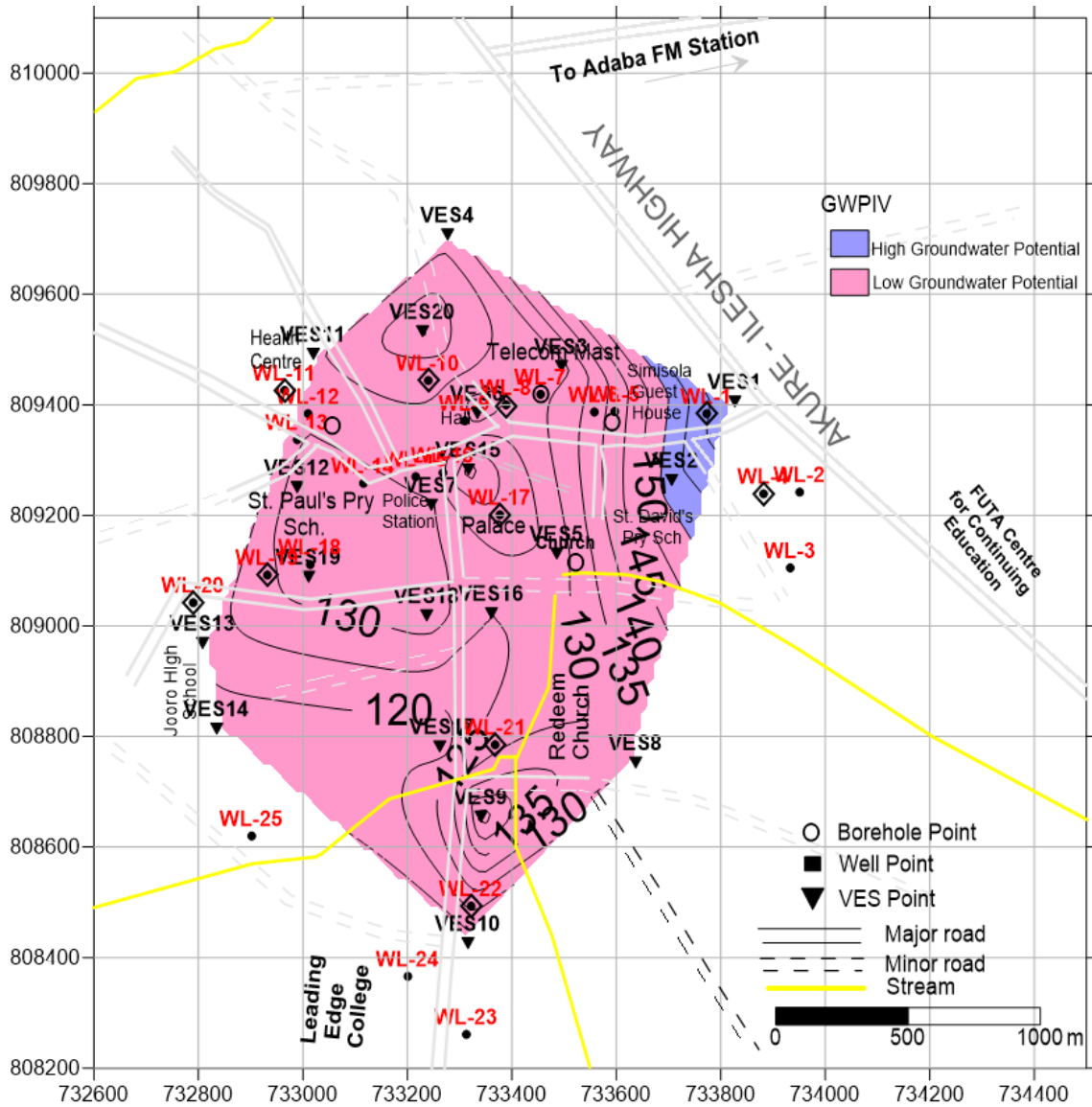


Figure 13. Groundwater Potential map developed for the study area using GWPIV

4. Conclusion

Findings revealed maximum of five geologic sequence comprising topsoil (25–222 ohm-m), thicknesses (0.5 – 1.2 m), composed of clay, and sandy clay; a layer composed of clay/sandy clay/clay sand (33–320 ohm-m), thicknesses (2.2 – 7.5 m); the weathered layer, which is composed of clay/sandy clay and clayey sand (29–365 ohm-m), thicknesses (2.3 – 17.5 m); the partly weathered/fractured layer (25–412 ohm-m), thicknesses (6.1 – 11.5 m); and the fresh basement (221–9540 ohm-m). The depth to the basement rocks ranged from 5.7 to 32.5 m. The overburden thickness ranges from 5.7 to 32.5 m. The weathered layer and the fractured basement are the main water bearing units in the research region, according to the groundwater assessment of Ibulesoro. In most locations, the aquifer system is unconfined, meaning that the saturated thickness is equal to the difference between the free

water table and the aquiclude. It is more prevalent where there is a combination of the two. As a result, the saturated thickness of an unconfined aquifer is not constant but rather variable due to changes in the water table's position over time. The obtained K and T for the aquifers ranged from 0.13 – 0.84 m/d and 0.77 – 16.9 m²/d respectively. The measured pore water resistivity varied from 34.84 – 53.48 ohm-m, while groundwater formation factor (Fm) ranged from 0.59 to 11.33. The groundwater's physicochemical and biological characteristics met the World Health Organization's requirements for potable water. The groundwater's irrigation indices also met requirements for being acceptable for irrigation, with the exception of RSC, which is over the advised standard. The groundwater was rated by the GWPIV as low and extremely prone to contamination. Ca-Mg-Cl-mixed water is the most common form. The study has contributed to knowledge by given baseline information about aquifer

characteristics, in order to enhance the success rate of borehole drilling and groundwater development in the area. However, the limitation experienced in the course of data acquisition was that, the area was built-up, consequently this limitation did not allow extensive spread/stretch of the current electrodes during VES survey. Therefore, this calls for other methods adaptable

and versatile to groundwater investigation in rugged or built-up area, such as seismic method, remote sensing (which can further help in understanding the fault/fracture), borehole logging (e.g., caliper logging), ground penetrating radar. These methods integrated with GIS are recommended for further studies.

Table 19. Muti-criteria Parameters and its probability rating and weights for selected measured parameters in relation to groundwater evaluation

1	Parameter	Range	Weight	Remark	Rating
	Weathered Layer Thickness (m)	0 – 10	1	Low	0.06
		10 – 20	2	Moderate	
		>20	3	High	
2	Weathered Layer Resistivity (ohm-m)	0 – 100	1	Very Poor	0.06
		100 – 200	2	Poor	
		200 - 300	3	Moderate	
		>300	5	Good	
3	Overburden Thickness (m)	0 – 15	1	Low	0.09
		15 – 30	2	Medium	
		>30	4	High	
4	Transverse Resistance	0 – 5000	1	Low	0.06
		5000 – 10000	3	Fair	
		>10000	5	High	
5	Transmissivity	0 – 10	1	Low	0.11
		10 – 20	2	Moderate	
		>20	3	High	
6	Reflection Coefficient	<0.1	3	High	0.04
		0.1 – 0.5	2	Moderate	
		0.5 – 1.0	1	Low	
7	Fracture Constrast	0 - 20	3	High	0.04
		20 – 50	2	Moderate	
		>50	1	Low	
8	Apparent Formation Factor	0 – 3	1	Low	0.04
		3 – 5	3	Fair	
		>5	5	Good	
9.	Longitudinal Conductance	0.10 – 0.50	1	High	0.50
		0.50 – 0.75	3	Moderate	
		0.75 – 1.0	5	Low	
10	Aquifer vulnerability index	<1 - 2	1	Extremely high	0.50
		2 – 3	3	Moderate	
		>3	5	Extremely low	

Acknowledgement

The author is grateful to Federal Water Resources, Akure, Ondo State, Nigeria for assistance rendered during analysis of water samples.

Author contributions

Olumuyiwa Olusola Falowo: Conceptualization, Methodology, Software, Field study, Visualization, Investigation, Writing-Reviewing, Editing, and Data Analysis. **Abayomi Solomon Daramola:** Data curation, Writing-Original draft preparation, Software, Validation, Field study, Data interpretation, and Proof-reading

Conflicts of interest

The authors declare no conflicts of interest.

References

- Hordon, R. M. (1977). Water supply as a limiting factor in developing communities; endogenous Vs. exogenous sources. *Water resources Bulletin*, 13: 933-939.
- Sellers, J. H. (1973). Tax implications of groundwater depletion. *Groundwater*, 11, 4, 27-35.
- Dalila, Z., Boudoukha, A., Abderrahmane, B., & Lahcen, B. (2017). Water Quality Assessment for Drinking and Irrigation Using Major Ions Chemistry in The Semiarid Region: Case of Djacer Spring, Algeria, *Asian Journal of Earth Science*, 10:9-21. <https://doi.org/10.3923/Ajes.2017.9.21>
- Collins, R., & Jenkins, A. (1996). The Impact of Agricultural Land Use on Stream Chemistry in the Middle Hills of the Himalayas, Nepal. *Journal of*

- Hydrology, 185, 71-86. [http://doi.org/10.1016/0022-1694\(95\)03008-5](http://doi.org/10.1016/0022-1694(95)03008-5)
5. Davis, S. N., & Dewiest, R. J. M. (1967). *Hydrogeology*, John Wiley and Sons, 463.
 6. Domenico, P. A., & Schwartz, F. W. (1990). *Physical and Chemical Hydrogeology*. John Wiley & Sons, New York, 824.
 7. Fetter, C. W. (1990). *Applied Hydrogeology*, 2nd Edition CBS Publisher & Distributor, 592.
 8. Ndatuwong, L. G., & Yadav, G. S. (2015). Application of geo-electrical data to evaluate groundwater potential zone and assessment of overburden protective capacity in part of Sonebhadra district, Uttar Pradesh. *Environmental earth sciences*, 73(7), 3655-3664. <http://doi.org/10.1007/s12665-014-3649-z>.
 9. Akinrinade, O. J., & Adesina, R. B. (2016). Hydrogeophysical investigation of groundwater potential and aquifer vulnerability prediction in basement complex terrain—a case study from Akure, Southwestern Nigeria. *Materials and Geoenvironment*, 63(1), 55-56. <http://doi.org/10.1515/rmzmag-2016-0005>
 10. Bayewu, O. O., Oloruntola, M. O., Mosuro, G. O., Laniyan, T. A., Ariyo, S. O., & Fatoba, J. O. (2017). Geophysical evaluation of groundwater potential in part of southwestern Basement Complex terrain of Nigeria. *Applied Water Science*, 7(8), 4615-4632. <https://doi.org/10.1007/s13201-017-0623-4>
 11. Egbueri, J. C. (2018). Assessment of the quality of groundwaters proximal to dumpsites in Awka and Nnewi metropolises: a comparative approach. *International journal of energy and water resources*, 2(1), 33-48. <https://doi.org/10.1007/S42108-018-0004-1>
 12. Selvam, S. (2016). 1D Geoelectrical Resistivity Survey for Groundwater Studies in Coastal Area: A Case Study from Pearl City, Tamil Nadu. *Journal of the Geological Society of India*, 87, 169-178. <http://dx.doi.org/10.1007/s12594-016-0385-x>
 13. Mogaji, K. A., & Omobude, O. B. (2017). Modeling of geoelectric parameters for assessing groundwater potentiality in a multifaceted geologic terrain, Ipinsa Southwest, Nigeria – A GIS-based GODT approach, *NRIAG Journal of Astronomy and Geophysics*, 6:2, 434-451. <https://doi.org/10.1016/j.nrjag.2017.07.001>
 14. Telford, W. M., Geldart, L. P., Sheriff, R. E., & Keys, D. A. (1976). *Applied Geophysics*. Cambridge University Press, London, U. K.
 15. Walton, W. C. (1991). *Principles of Groundwater Engineering*. Lewis Publishers, Inc., Chelsea, MI.
 16. Obiora, D. N., Ibuot, J. C., & George, N. J. (2016). Evaluation of aquifer potential, geoelectric and hydraulic parameters in Ezza North, southeastern Nigeria, using geoelectric sounding. *International journal of environmental science and technology*, 13(2), 435-444. <https://doi.org/10.1007/s13762-015-0886-y>
 17. Anomohanran, O. (2013). Geophysical Investigation of Groundwater Potential in Ukelegbe, Nigeria. *Journal of Applied Sciences*, 13, 119-125. <http://dx.doi.org/10.3923/jas.2013.119.125>
 18. Hussain, Y., Ullah, S. F., Hussain, M. B., Martinez-Carvajal, H., & Aslam, A. Q. (2016). Protective Capacity Assessment of Vadose Zone Material by Geo-Electrical Method: A Case Study of Pakistan. *International Journal of Geosciences*, 7, 716-725. <http://dx.doi.org/10.4236/ijg.2016.75055>
 19. Hamill, L., Bell, F.U. (1986). *Groundwater Resources Development*. Britain Library Cataloguing in Publication Data London, 151 – 158.
 20. Kruseman, G. P., & de Ridder, N. A. (1994). *Analysis and Evaluation of Pumping Test Data*, International Institute for Land Reclamation and Improvement, AA Wageningen, The Netherlands, Second Edition (Completely Revised).
 21. Logan, J. (1964). Estimating transmissivity from routine production tests of water wells. *Groundwater*, 2(1), 35-37. <https://doi.org/10.1111/j.1745-6584.1964.tb01744.x>
 22. El-Naqa, A., & Al-Shayeb, A. (2009). Groundwater Protection and Management Strategy in Jordan. *Water Resources Management*, 23, 2379-2394. <https://doi.org/10.1007/s11269-008-9386-x>
 23. Singh, S. N., Janardhana, R., & Ramakrishna, Ch., (2015). Evaluation of Groundwater Quality and its Suitability for Domestic and Irrigation Use in Parts of the Chandauli-Varanasi Region, Uttar Pradesh, India *Journal of Water Resource and Protection*, 7, 572-587. <http://dx.doi.org/10.4236/jwarp.2015.77046>
 24. Rao, N. S. (2017). *Hydrogeology- Problems with Solutions*. PHI Learning Private Limited, 265.
 25. Paramaguru, P., Anandhan, P., Chidambaram, S., Ganesh, N., Neolian, M., Devary, N., Vesudevan, U., Rakesh, R. G., & Pradeep K. (2016). Appraisal of Groundwater Quality in the Cuddalore District of TN, India, *International research journal of earth sciences*, 4(6), 23-30.
 26. Walski, T. M., & Parker, F. L. (1974). Consumers' water quality index. *Journal of the Environmental Engineering Division*, 100, 259-611.
 27. Hem, J. D. (1989). *Study and Interpretation of the chemical characteristics of natural waters*. U.S. Geological survey water supply paper 2254, 3rd Edition.
 28. Napolitano, P., & Fabbri, A. (1996). Single-Parameter Sensitivity Analysis for Aquifer Vulnerability Assessment Using DRASTIC and SINTACS. In: *HydroGIS 96: Application of Geographical Information Systems in Hydrology and Water Resources Management*, Proceedings of Vienna Conference, IAHS Pub., Vienna, 235, 559-566. http://hydrologie.org/redbooks/a235/iahs_235_05_59.pdf
 29. Aller, L., Bennet, T., Leher, J. H., Petty, R. J., & Hackett, G. (1987). DRASTIC: A Standardized System for Evaluating Groundwater Pollution Potential Using Hydro Geological Setting. *EPA*, 35, 600-622. <https://link.springer.com/article/10.1007/s11269-008-9319-8>
 30. Zhu, X., & Ierland, E. C. V. (2012). Economic modeling for water quantity and quality management: A welfare program approach, *Water Resource Management*, 26, 2491-2511

31. Dalkey, N. C. D. (1968). An objective water quality index, The Rand Corporation Harkins. Journal - Water Pollution Control Federation, 46, 588–591.
32. Sateesh, B., Sateesh, S., Kumar, K., & Reddy, N. (2017). Assessment of Groundwater Quality for Irrigation Use and Evolution of Hydrochemical Facies in the Yeshwanthapur Sub-Basin, Warangal Dist. IOSR Journal of Applied Geology and Geophysics (IOSR-JAGG), 5(4) Ver. I, 14-20. <https://doi.org/10.9790/0990-0504011420>
33. Harkins, R. D. (1974). An objective water quality index. Journal–Water Pollution Control Federation, 46, 588–591.
34. Couillard, D., & Lefebvre, Y. (1985). Analysis of water quality indices. Journal of Environmental Management, 21, 161–179.
35. Brutsaert, W., Gross, G. W., & Mc Gehee, R. M. (1975). C.E. Jacob's study on the prospective and hypothetical future of the minning of the groundwater deposited, 13; 492-505.
36. Coulibaly, H., & Rodriguez, M. J. (2004). Development of performance indicators for Quebec small water utilities. Journal of Environmental Management, 73(3), 243–255. <https://doi.org/10.1016/j.jenvman.2004.07.003>
37. Gass, T. E., & Lehr, J. (1977). Groundwater energy and the groundwater heat pump. Water well journal, 31(4), 42-47.
38. Khrisat, H. T., & Al-Bakri, J. (2019). Assessment of Groundwater Vulnerability in Azraq Catchment in Fuhais-Jordan Using DRASTIC Model. Open Journal of Geology, 9, 364-377. <https://doi.org/10.4236/ojg.2019.97024>
39. Jain, C. K., Bandyopadhyay, A., & Bhadra, A. (2010). Assessment of Ground Water Quality for Drinking Purpose, District Nainital, Uttarakhand, India. Environmental Monitoring and Assessment, 166, 663-676. <http://doi.org/10.1007/s10661-009-1031-5>
40. Saeedi, M., Abessi, O., Sharifi, F., & Meraji, H. (2009). Development of groundwater quality index. Environ Monit Assess, 10pp. <http://doi.org/10.1007/S10661-009-0837-5>.
41. Rao, G. S., & Nageswararao, G. (2013). Assessment of ground water quality using water quality index. *Archive of Environmental Sciences*, 7(1), 1-5.
42. Kalaivanan, K., Gurugnanam, B., Pourghasemi, H. R., Suresh, M., & Kumaravel, S. (2017). Spatial Assessment of Groundwater Quality Using Water Quality Index and Hydrochemical Indices in the Kodavanan Sub-Basin, Tamil Nadu, India. *Sustain Water Resour Manag*. <https://doi.org/10.1007/S40899-017-0148-X>
43. Li, P., Qian, H., & Wu, J. (2010). Groundwater Quality Assessment Based on Improved Water Quality Index in Pengyang County, Ningxia, Northwest China. *E-Journal of Chemistry*, 7(S1): S209-S216. <https://doi.org/10.1155/2010/451304>
44. Ojo, J. S., Olorunfemi, M. O., Aduwo, I. A., Bayode, S., Akintorinwa, O. J., Omosuyi, G. O., & Akinluyi, F.O. (2014). Assessment of surface and groundwater quality of the Akure metropolis, Southwestern Nigeria. *Journal of Environment and Earth Science*, ISSN 2225-0948, 4(23), 19.
45. NIMET. (2012). Nigeria Meterological Agency. Nigeria Climatic Data: Abuja, Nigeria. www.nimetng.org
46. Nigeria Geological Survey Agency (NGSA). (2006). Published by the Authority of the Federal Republic of Nigeria.
47. Orellana, E., & Mooney, H. M. (1966). Master Tables and Curves for Vertical Electrical Sounding over Layered Structures. Interciencia, Madrid, Spain.
48. Zohdy, A. A. R., Eaton, G. P., & Mabey, D. R. (1974). Application of surface geophysics to groundwater investigations. United State Geophysical Survey, Washington.
49. Loke, M. H. (1997). Electrical Imaging surveys for Environmental and Engineering Studies. A partial guide to 2-D and 3-D surveys. Minden Heights, 11700, Penang, Malaysia.
50. Gibb, J. P., Schuller, R. M., Griffin, R. A. (1981). Procedures for the Collection of Representative Water Quality Data from Monitoring Wells. Cooperative Groundwater Report No. 7, Illinois State Water Survey and Illinois State Geological Survey, Champaign, Illinois.
51. APHA, (1998). America Public Health Association. Standard Methods for the Examination of Water and Waste Water. 18th Edition, Washington D. C, 4-17.
52. Kakati, S. S., & Sarma, H. P. (2007). Studies on water quality index of drinking water of Lakhimpur District. *Indian Journal of Environmental Protection*, 27(5), 425-428.
53. Haque, S., Sadique, A. B. M., Mazharul, M. I., Zakia, S., Nargis, A., & Masud, H. (2017). Assessment of Irrigation Water Quality of Pabna District (North-Western Part) of Bangladesh for Securing Risk-Free Agricultural Production, *American Journal of Water Science and Engineering*, 3(6), 67-71. <http://doi.org/10.11648/j.ajwse.20170306.11>
54. Bell, F. G. (2007). *Engineering Geology*, Second Edition. Elsevier, 581pp.
55. Mgbenu, C. N., & Egbueri, J. C. (2019). The hydrogeochemical signatures, quality indices and health risk assessment of water resources in Umunya district, southeast Nigeria. *Appl Water Sci*. <https://doi.org/10.1007/s13201-019-0900-5>
56. Raju, N. J., Ram, P., & Dey, S. (2009). Groundwater Quality in the Lower Varuna River Basin, Varanasi District, Uttar Pradesh, India. *Journal of the Geological Society of India*, 7, 178-192. <http://dx.doi.org/10.1007/s12040-008-0048-4>
57. Vasanthavigar, M., Srinivasamoorth, K., Vijayaragavan, K., Rajiv, G. R., Chidambaram, S., Anandhan, P., Mani, V. R., & Vasudevan, S. (2010). Application of Water Quality Index for Groundwater Quality Assessment: Thirumanimuttar Sub-Basin, Tamilnadu, India. *Environmental Monitoring and Assessment*, 171, 595-609. <http://dx.doi.org/10.1007/s10661-009-1302-1>
58. WHO, (2011). *Guidelines for Drinking Water Quality*, 3rd Ed. World Health Organization, Geneva, 2011.
59. Egbueri, J. C., Mgbenu, C. N., & Chukwu, C. N. (2019). Investigating the hydrogeochemical processes and quality of water resources in Ojoto and environs using

- integrated classical methods. *Model Earth Syst Environ.* <https://doi.org/10.1007/s40808-019-00613-y>
60. Igbemi, A., Nwaogazie, I. L., Akaranta, O., & Abu, G. O., (2019). Water Quality Assessment by Pollution Indices in Eastern Obolo Coastline Communities of Nigeria. *American Journal of Water Resources*, 7(3), 111-120. <http://doi.org/10.12691/ajwr-7-3-4>
61. Ochungo, E. A., Ouma, G. O., Obiero, J. P. O., & Odero, N. A. (2019). Water Quality Index for Assessment of Potability of Groundwater Resource in Langata Sub County, Nairobi-Kenya. *American Journal of Water Resources*, 7(2), 62-75. <http://doi.org/10.12691/ajwr-7-2-4>.
62. Piper, A. M. (1953). A Graphic Procedure in the Chemical Interpretation of Water Analysis. US Geological Survey Groundwater Note, 12.
63. Wilcox, L. V. (1948). Classification and Use of Irrigation Waters. U.S. Department of Agriculture, Washington Dc, 962.



© Author(s) 2023. This work is distributed under <https://creativecommons.org/licenses/by-sa/4.0/>



Designing a device for measuring the velocity of liquid flowing in open channels

Hüseyin Mutlu^{*1}, Emre Kaygusuz²

¹Mersin University, Mechanical Engineering Department, Türkiye

²Bingol University, Mechanical Engineering Department, Türkiye

Keywords

Measuring
Velocity
Open Channel
Device

Research Article

DOI: 10.31127/tuje.1115850

Received: 12.05.2022

Accepted: 07.07.2022

Published: 31.08.2022

Abstract

Water flow systems in open channels are designed according to certain levels. Flow rate increases in open channels can bring many disasters. Therefore, it is necessary to routinely measure flow in open channels. In addition to rivers and streams, open channels are used in many areas in city life. If open channels are not checked regularly, floods may occur in sudden rains and human life may be endangered. Practical problems like measurement, control and linearization of mechanical outputs can be solved within the context of function generation problem. In this work, an exemplary design associated with the measurement of water velocities in open channels and the resulting apparatus has been shown. To test its performance, velocities have been compared with those obtained by the constructed prototype. The results have been observed to be consistent with each other.

1. Introduction

Mechanism is a mechanical arrangement that is used to transfer motion and force or used to advance the points of an object on certain trajectories [1]. In the design of lever mechanisms, it is desirable that the rotational, oscillating and sliding movements of the output lever be a function of time, or a function of the movement of the input lever. For example; high temperature, pressure, toxic gas and chemicals, working under excessive loads, in unfavorable and dangerous environments for human health, in control events such as performing the measurement and inspection function with a remote control [2] or, on a conveyor line, while the conveyor is in motion, a motion programming event such as bottle closing, returning, taking the next cap is made possible by solving the lever mechanisms within the scope of function generation [3]. The linearization of nonlinear mechanical outputs is also considered within the scope of function synthesis [4].

Water is the most important element of food production, and the easiest and most cost-efficient way to transport it through open-channel [5]. An open channel is a waterway, canal or conduit in which a liquid

flow with a free surface [6]. Open channels had created by nature conditions or built by humans. Open channels are used in rain water channels and wastewater treatment plants. Measuring the velocity of liquid flowing in open channels are routinely made on many rivers in the world to provide information on flow. Velocity measurements are made in open channels due to needs such as protecting clean water resources, recording the processes in the industrial area, and taking precautionary measures against adverse natural events such as sudden floods.

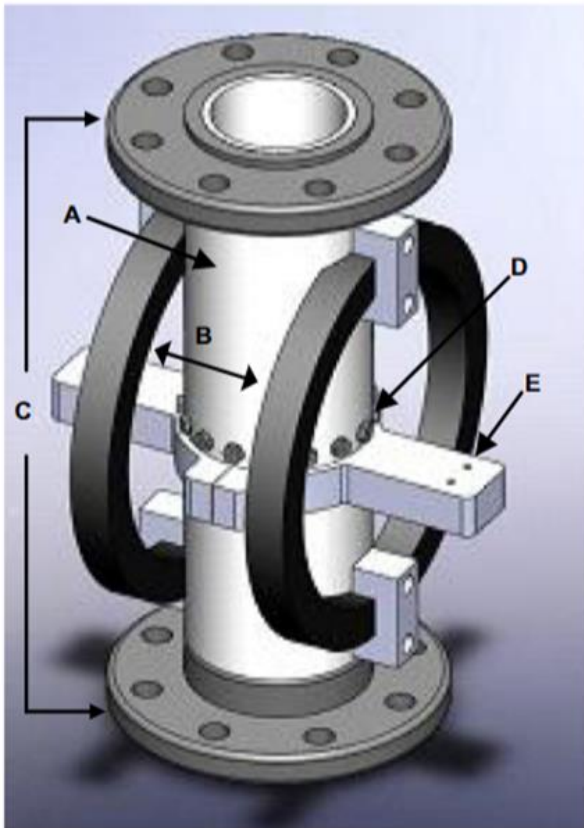
In recent years, new theoretical approaches have been studied for the measurement of flow velocity in open channels, which is an old problem. A sharp crested triangular weir was recently studied based on two theoretical models, a weir theory (Model I) and critical flow approach (Model II) [7]. Flow measurement using a triangular broad crested weir theory and experimental validation studied recently [8]. Theoretical approach studied based on the application of dimensionless energy equation applied between a section taken in the approach channel and the weir under critical flow conditions [9,10].

* Corresponding Author

(huseyinmutlu@yahoo.com) ORCID ID 0000-0002-4770-2873
(emre_kygsz@windowlive.com) ORCID ID 0000-0001-9356-2149

Cite this article

Mutlu, H., & Kaygusuz, E. (2023). Designing a device for measuring the velocity of liquid flowing in open channels. Turkish Journal of Engineering, 7(3), 259-265



A: Meter Body
 B: Helmholtz Coil
 C: Flanges
 D: Electrode Array
 E: Cable Support

Figure 1. Electromagnetic flow meter setup design [11]

Leeungcalsatien and Lucas [11] designed an electromagnetic flow meter. Electromagnetic flow meters (EMFM) which had shown in Fig.1. widely using in industries for measuring velocity of liquid flows.

Goal et al. [12] studied open channel flow measurement of water by using width contraction shown in Fig. 2. Experiments on that study were conducted on sharp edged constricted flow meters having four types of width contractions namely 2:1, 1.5:1, 1:1 and 90° in the direction of flow. The device having contraction 2:1 is the most efficient one as it allows maximum critical submergence [12].

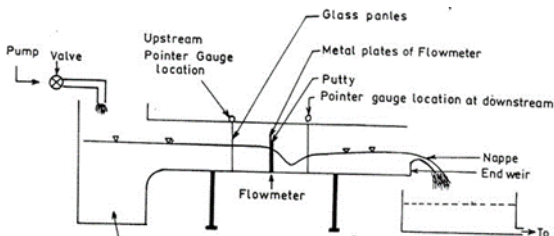


Figure 2. Experimental setup for open channel flow measurement of water by using width contraction [12]

Bolognesi et al. [13] studied measurement of surface velocity in open channels using a lightweight remotely piloted aircraft system (RPAS) shown in Fig. 3. The RPAS was used both with ground control points (GCPs) for orientation of the photographic images and without

GCPs. The data analysis showed that the RPAS provides valid results even without GCPs [13].

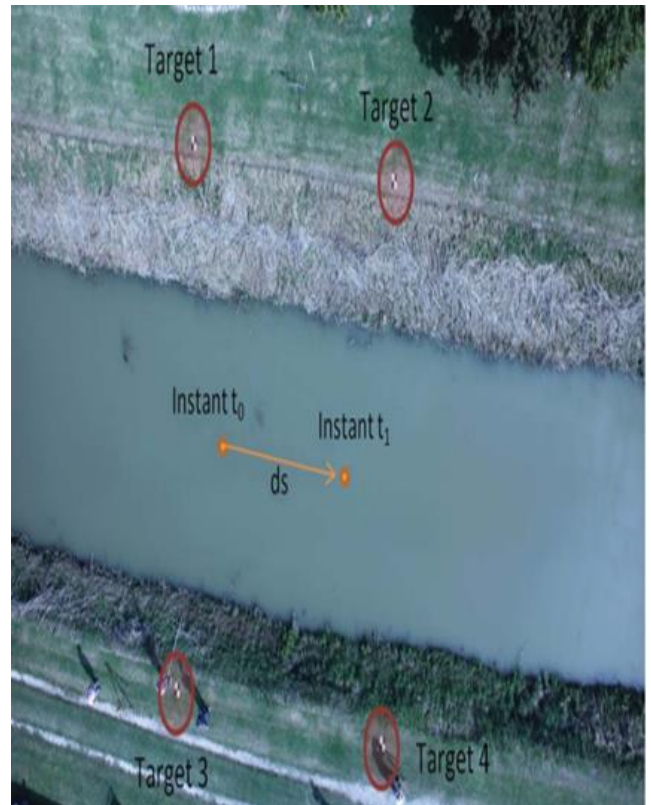


Figure 3. Layout of the test site for surface velocity measurement using the RPAS (Fossa Masi channel) [13]

Figuérez et al. [14] studied an enhanced treatment of boundary conditions for 2D Reynolds Averaged Navier–Stokes (RANS) streamwise velocity models in open channel flow. Results suggest that the influence of the free surface boundary layer has a significant impact on the results for both the streamwise velocity and boundary shear stress in windy conditions [14].

In this study, an exemplary application associated with the measurement of water velocities in open channels has been shown, and the resulting apparatus has been constructed and tested under laboratory conditions.

2. Method

There are too many 4 and 6 bar mechanism designs to produce a desired function. It is possible to obtain different designs that produce the desired function by changing the design parameters that require arbitrary selection or by choosing the method applied in the design differently. This means that we have a better chance of meeting certain criteria required from the mechanism. For example, if it is important to achieve very low structural errors, the mechanisms that best meet these criteria are selected from among the designs. If the dimensions of the mechanism are required to be compatible with each other, appropriate designs are selected.

In order to produce different designs that will produce the same function with the program packages in this study, the data in the program input set must be

changed systematically. While doing this, it may be necessary to play with the parameters that affect the design results the most. In this study, the program dataset was modified to select the mechanisms that best met the structural error and size criteria.

In practice, problems such as measurement, control, linearization of non-linear mechanical outputs can be considered within the scope of function synthesis. An example application of measuring the average flow rate of water in an open channel, which is one of such problems encountered in practice, tested under laboratory conditions.

In order to measure the water flow rate in an open channel, a device that converts the water velocity to angular displacement must be selected and the functional relationship between the water velocity and the angular displacement must be found experimentally or theoretically. For this, a suspension arm with a spherical object and mass m on it, as shown in Fig. 4.

When the spherical object at the end of the suspension arm seen in Fig. 4 is immersed in water, the water hitting the sphere at a certain speed creates a force proportional to the cross-sectional area of the sphere. The moment created with respect to point O is balanced by the mass m on the suspension arm and the weight of the suspension hair. In order to eliminate the effect of buoyancy, which causes instabilities in the system, the weight of the spherical body is chosen equal to the buoyancy force. According to these, the force created by the water velocity on the sphere is written as:

$$F = C_d \frac{v^2}{2} A \tag{1}$$

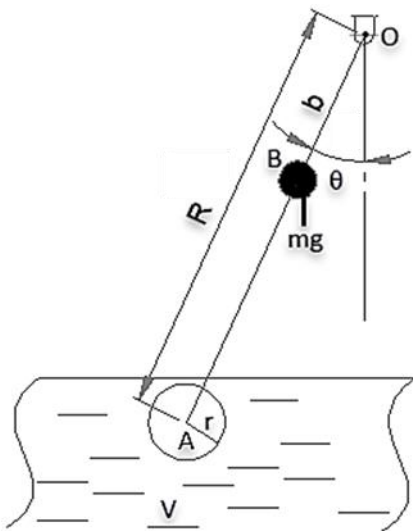


Figure 4. A device for measuring the water flow rate in an open channel

When the force balance is written with respect to the O point of the suspension arm under the influence of (1) force (C_d : Drag coefficient, A : cross-sectional area of the sphere, V : Velocity in equation (1)), the relationship between the water flow rate and the angle (θ) of the suspension arm with the horizontal becomes as follows:

$$V = k\sqrt{\tan \theta}, k = \sqrt{\frac{2bmg}{RC_d\pi r^2\rho}} \tag{2}$$

The constant k in equation (2) is a quantity dependent on the density of water and the mass and geometry of the suspension arm. Equation (2) does not include all parameters that affect the event in the measurement of water flow rate. For example, bearing frictions, axial misalignments arising from manufacturing, and additional forces occurring on the part of the suspension arm that enters the water do not cover. Instead of (2) equation, it would be more realistic to establish the relationship between θ angle and velocity at certain water velocities experimentally in laboratory facilities.

For this reason, by establishing the apparatus in Fig. 4, another apparatus with a pump, in which different flows are obtained in rectangular and open channels used as an experiment set in the laboratory, was used in order to determine the angle (θ) velocity (V) relationship. In the setup, different flow rates are provided by creating a dam at different heights in front of the channel and changing the depth of the flow.

In the setup of the assembly shown in Fig. 4, the selection of dimensions and the determination of the balancing mass m were made by taking into account the available possibilities. According to these, a hollow spherical object made of light plastic material with a radius of $r=2$ cm available in the market was added to the end of a selected $b=21$ cm long suspension arm. The inside of the spherical body is completely filled with water, eliminating the effect of the buoyancy of the water. The mass m added to the suspension arm was determined experimentally in such a way that the ball cannot come out of the water when the suspension arm is immersed in the water in the channel at the maximum flow rate. The different water flow rates obtained in the experiments were determined by means of a water velocity measuring instrument called “MULINE” with a rotating propeller. Water gage was used to immerse the suspension arm perpendicular to the flow. The results of a series of experiments carried out in the laboratory under these conditions are presented in Table (Table 1).

As can be seen in Table (Table 1), the maximum velocity value of 29.4 cm/sec is obtained against the deflection of the pendulum arm of maximum 16 degrees. For two degrees of deviation, the velocity is 12.64 cm/s. Accordingly, the working range of the velocity measuring device to be made will vary between 12 cm/s and 30 cm/s.

Table 1. Experimental water flow velocity (V) and suspension arm deviation angle (θ) values

θ (°)	θ (rad)	Velocity(V) cm/min
2	0.0349	12.64
4	0.0698	15.82
5	0.0873	18.00
8	0.1396	21.65
10	0.1745	24.30
16	0.2792	29.40

The suitability of a quadratic polynomial for the relationship between angle (θ) and velocity (V) in Table 1 was demonstrated by the least squares method. Accordingly, the quadratic polynomial obtained with the help of the values in table (Table 1) is as follows: [15].

$$V = -138.50\theta^2 + 112.60\theta + 8.90 \quad (3)$$

The graph consisting of the expression in equation (3) and the experimental results (Table 1) is shown in Fig. 5. As seen in the graph, all experimental points are very close to the curve in expression (3). Therefore, (3) the velocity (V) angle (θ) relation is appropriate.

For the design of the 4-bar mechanism that will produce the function in the expression (3), a computer program package containing the "SUBREGION" method [16] was used. Theoretical statements regarding the design of the 4-bar mechanism with the subregion method within the scope of function synthesis are

presented in this study. Accordingly, the inputs and outputs of the computer program package used for the design are as follows.

Here, DPS, DAL, respectively, the amount of rotation of the input and output arm, X_0, X_N is the first and last value of the definition range of the generated function, PS_0 , in degrees, the angle of the input arm that starts the calculations, the allowed error in E solution, N required for numerical integration, an even integer greater than 2, the number of intervals, the upper bound integer entering an NI sequential solving technique, the inputs PJ_0 and $(P_j(k), k=1,2,3,4,5)$ are the lower range limits used in the subregion method in degrees.

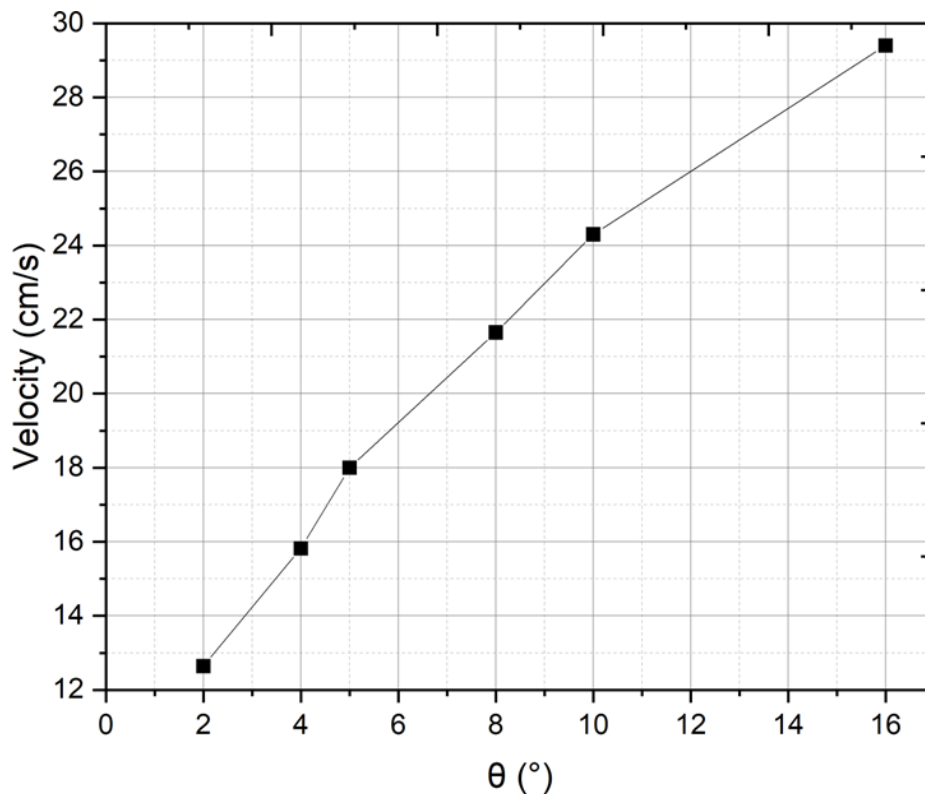


Figure 5. Variation of water flow velocity with respect to suspension arm deviation angle θ

Design results from the program:

Input arm starting angle	$\psi_0 = 354.8^\circ$
Output arm starting angle	$\alpha_0 = 76.50^\circ$
Input arm length	$x_1 = 0.8124$
Connecting rod length	$x_2 = 0.6767$
Output arm length	$x_3 = 0.5396$
Fixed arm length	$x_6 = 1$

2.1. Application of Subregion Method to 4-Bar Mechanism in Function Synthesis

The common point of many analytical methods developed is to consider the difference (error) between the desired function and the function produced by the mechanism as the objective function and to minimize this error in a certain operating range. Therefore, the idea of optimization is present in many of the methods. Methods have different names according to the mathematical approaches used in minimizing the objective function (error function). The most used ones are; The exact point

method [17], the subregion method [18], the Galerkin method [1], the least squares method [19] can be counted.

The equation of motion that connects the input arm rotation angle (ψ) of a 4-bar mechanism to the output arm rotation angle α can be written as follows using Fig. 6:

$$G(x_i, \psi, \alpha) = 0, i = 1, \dots, 5 \quad (4)$$

Here, x_i are the unknown kinematic quantities, which are used in the function synthesis design of the 4-bar mechanism and are maximum 5 [20]. These dimensions are the arm lengths as x_1, x_2, x_3 and the starting angles of the entry and exit arm ($x_4 = \psi_0, x_5 = \alpha_0$).

For the design of the 4-bar mechanism to produce a continuous function of the form $Y=f(X), X_0 \leq X \leq X_n$, (4) the equation of motion $\psi_0 \leq \psi \leq \psi_n$ by dividing it into 5 subregions, in each subdomain the integral of (1) if the condition of being zero is written [21],

$$\int_{\psi_{k-1}}^{\psi_k} G(X_i, \psi, \alpha) d\psi = 0, \quad i, k=1, \dots, 5 \quad (5)$$

In the expression (5), called the subregion method, (ψ_{k-1}, ψ_k) 's indicate the sub-region boundaries within the (ψ_0, ψ_n) range of motion.

By establishing a linear relationship between the mechanism and the independent and dependent

variables $(\psi, \alpha), (Y, X)$ of the mechanism and the produced function, and substituting the integral in the equation (5), the set of nonlinear equations with 5 unknowns is found as follows.

$$Z_2 d_k + Z_3 C_k + Z_1 I_{k-J_k} = 0, \quad k=1, \dots, 5 \quad (6)$$

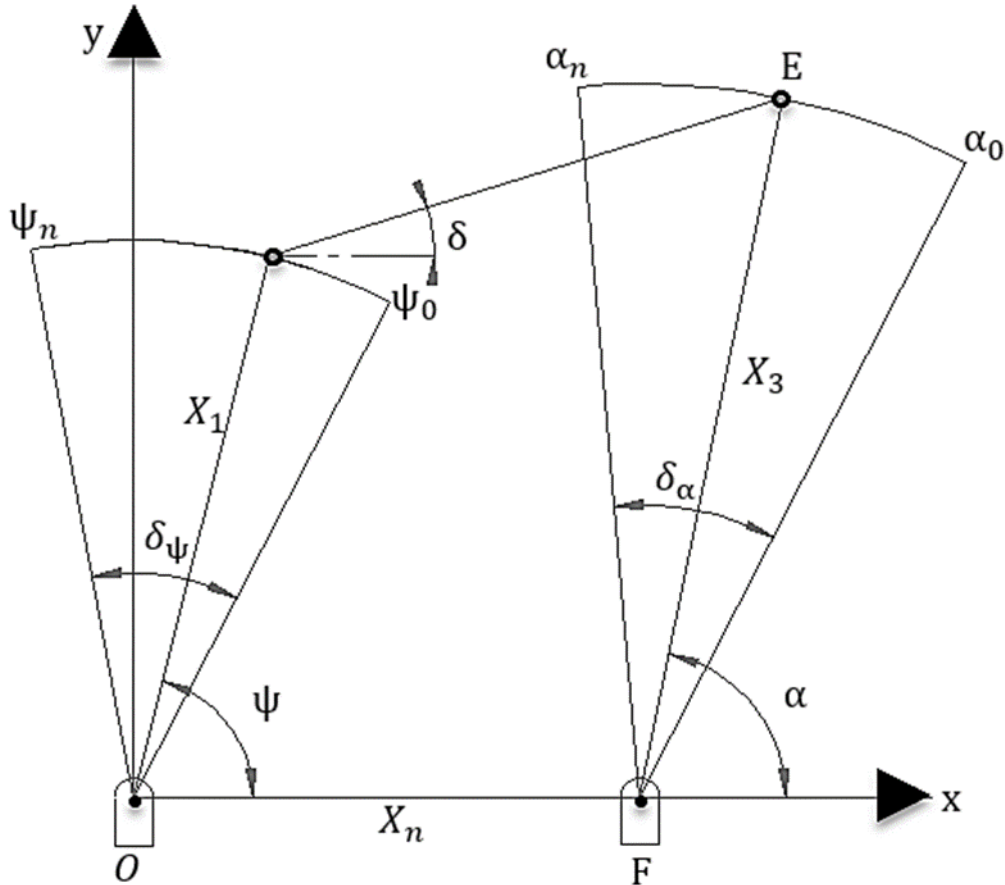


Figure 6. Function synthesis parameters of the 4-bar mechanism

Here, $Z_1 = 1/X_1, Z_2 = (1+x_1^2 + x_3^2 - x_2^2)/(x_1 x_3), Z_3 = 1/X_3$; $d_k, C_k, I_k, J_k, \psi_0, \alpha_0$ are the coefficients depending on the unknown input and output arm initial angles. If the set of equations (6) is solved using sequential iteration methods for 5 unknown parameters, the 4-bar mechanism is designed to produce the desired function.

3. Designing Velocity Measuring Setup

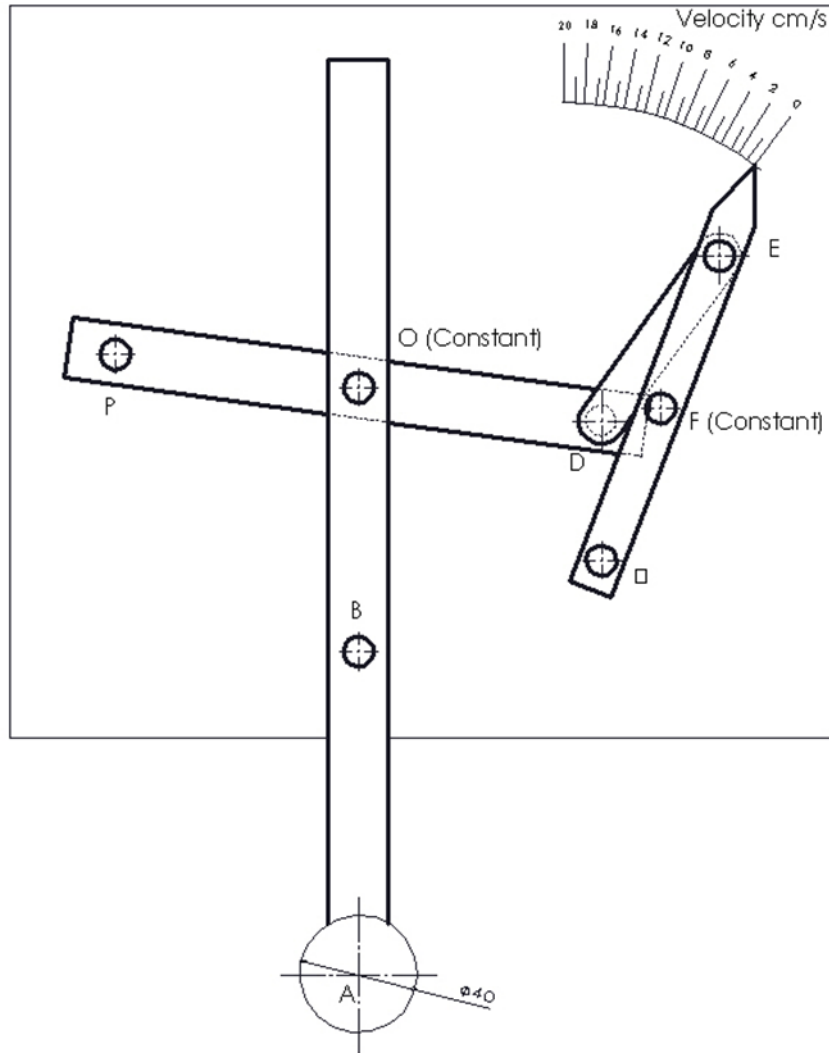
It is seen that the 4-bar mechanism size ratios obtained as a result of the design are suitable for production. These dimensions were found as a result of the body (fixed arm) length assuming 1 unit. For this reason, the mechanism lengths can be changed as desired in accordance with the purpose.

In this study, when the body length is taken as 10 cm, the appropriate design values are obtained by multiplying the other dimensions by 10. As a result of the 4-bar design formed under these dimensions, the structural error distribution, which is the difference between the function produced by the mechanism and the function given in the expression (3), is examined.

The 4-bar mechanism was designed in accordance with the results of the design, and the pendulum arm in Fig. 4 was mounted, and the velocity measuring device in Fig. 7 was obtained. In the design of the 4-bar mechanism, the inlet and outlet arms are statically balanced with the help of additional masses (P and Q). Thus, the effect of additional moments on the pendulum arm due to the mechanism's own weight is eliminated. Thanks to a linearly calibrated angle dial, the velocity values measured from the output arm of the 4-bar mechanism are shown. In Fig. 7, $OD = 8.1$ cm, $DE = 6.7$ cm, $EF = 5.4$ cm, $OF = 10$ cm, and the diameter of sphere A is 4 cm.

4. Conclusion

In order to test this setup, measurements were made at various velocities in the open channel available in the laboratory with the other velocity measuring instrument "MULINE" and the values obtained were compared. As a result, it was determined that the relative error between the "MULINE" and the velocity measuring device produced in Fig. 7 and the measured velocities did not exceed 2%.



Acknowledgement

Acknowledgements of support for the project/paper/author are welcome.

Author contributions

Hüseyin Mutlu: Methodology, **Emre Kaygusuz:** Writing-Original draft preparation, Investigation, Writing-Reviewing and Editing.

Conflicts of interest

The authors declare no conflicts of interest.

References

1. Akçalı, İ. D., & Dittrich, G. (1989). Function Generation by Galerkin Method, *Mech Mach, Theory*, 24(1), 39-43.
2. Akçalı, İ. D. (1986). Altbölge Yöntemiyle 4-çubuk Mekanizmalarının Fonksiyon Üretme Olanakları, *Tubitak II Ulusal Makine Teorisi Sempozyumu*, G.Antep ODTÜ, 14-26.
3. Uicker, J. J., Pennock, G. R., & Shigley, J. E. (2017). *Theory of Machines and Mechanisms Fifth Edition*, McGraw-Hill Inc., New York.
4. Erdman, A. G., & Midha, A. (1973). Man-Made Mechanism Models Multiply Mental Motivation, *Proceedings 3rd Applied Mechanism Conference*, s.3.1-3.21.
5. Conde, G., Quijano, N., & Ocampo-Martinez, C. (2021). Modeling and control in open-channel irrigation systems: A review, *Annual Reviews in Control*, (51), 153-171, ISSN 1367-5788, <https://doi.org/10.1016/j.arcontrol.2021.01.003>.
6. Chanson, H. (2004). *Environmental Hydraulics of Open Channel Flows*, Butterworth-Heinemann, 3-10, ISBN 9780750661652, <https://doi.org/10.1016/B978-075066165-2.50033-3>.
7. Vatankhah, A. R., & Khamisabadi, M. (2019). General stage-discharge relationship for sharp-crested power-law weirs: analytical and experimental study. *Irrigation and Drainage*, 68(4), 808-821.
8. Achour, B., & Amara, L. (2022). Flow measurement using a triangular broad crested weir theory and experimental validation, *Flow Measurement and Instrumentation*, (83), 102088, ISSN 0955-5986.

9. Achour, B., & Amara, L. (2021). Discharge coefficient for a triangular notch weir theory and experimental analysis Larhyss J. (46), 7-19 a.
10. Achour, B., & Amara, L. (2021). Theoretical discharge coefficient relationship for a contracted triangular notch weir. experimental analysis for the special case of the 90-degree V-notch. Larhyss Journal (46), 89-100.
11. Leeungculsatien, T., & Lucas, G. P. (2013). Measurement of Velocity Profiles in Multiphase Flow Using a Multi-Electrode Electromagnetic Flow Meter." Flow Measurement and Instrumentation, 31, 86-95. <https://doi.org/10.1016/j.flowmeasinst.2012.09.002>.
12. Goel, A., Verma, D. V. S., and Sangwan, S. "Open Channel Flow Measurement of Water by Using Width Contraction." Vol. 9, No. 2, 2015, p. 7.
13. Bolognesi, M., Farina, G., Alvisi, S., Franchini, M., Pellegrinelli, A., & Russo, P. (2017). Measurement of Surface Velocity in Open Channels Using a Lightweight Remotely Piloted Aircraft System. Geomatics, Natural Hazards and Risk, 8(1), 2017, 73-86. <https://doi.org/10.1080/19475705.2016.1184717>.
14. Figuérez, J. A., Galán, Á., & González, J. (2021). An Enhanced Treatment of Boundary Conditions for 2D RANS Streamwise Velocity Models in Open Channel Flow. *Water*, 13(7), 1001. <https://doi.org/10.3390/w13071001>.
15. Aktaş, Z. (1984). Oncül, H., Ural s., Sayısal Çözümleme, ODTÜ-Bilgisayar Mühendisliği Bölümü, Ankara.
16. Mutlu, H. (1990). Fonksiyon Sentezine Modüler Yaklaşım, Ç.Ü. Fen Bilimleri Enstitüsü Makine Mühendisliği Anabilim Dalı Master Tezi. Adana.
17. Hartenberg, R. S., & Denavit, J. (1980). Kinematic Synthesis of Linkages, McGraw-Hill Inc. New York.
18. Akçali, İ. D., & Lindholm, I. C. (1979). A Novel Method for the 4-bar Function Generation, V. World Congress on Theory of Machines and Mechanisms, Montreal.
19. Akçali, İ. D. (1977). *Subdomain-Least squares method of synthesizing six-bars for mechanizing functions*. Kansas State University.
20. Akçali, İ. D. (1995, August). Modular approach to function generation. In *Ninth World Congress on the Theory of Machines and Mechanisms, Milan, Italy, Aug* (pp. 1440-1444).
21. Akçali, İ. D. (1987). Design of Slider-Crank Mechanism for Function Generation. In *Proc. 7 World Congress on Theory of Machines and Mechanism* (pp. 119-124).



© Author(s) 2023. This work is distributed under <https://creativecommons.org/licenses/by-sa/4.0/>



Investigating the historical building materials with spectroscopic and geophysical methods: A case study of Mardin Castle

Lale Karataş*¹ 

¹Mardin Artuklu University, Mardin Vocational School of Higher Education, Department of Architecture and Urban Planning, Türkiye

Keywords

Historical building
Materials
Material properties
Basic physical properties
Limestone

Research Article

DOI: 10.31127/tuje.1145711

Received: 19.07.2022

Accepted: 19.08.2022

Published: 31.08.2022

Abstract

Today, the building materials form the historical buildings are being exposed to various deteriorations increasingly due to different causes. Many historical masonry constructions in the world are on the edge of extinction due to the increasing frequency and changing models of material deterioration. The materials as close as possible to the original materials in terms of their chemical compositions and physical properties are required in the reconstruction and maintenance of the buildings that have historical importance. In addition, the properties of the materials used in the historical buildings are generally not known with a sufficient accuracy. This causes misapplications in case of emergencies, and also may lead to future potential greater damages on the building. The lack of data regarding the engineering properties of these buildings causes long-term damages on the buildings due to inappropriate conservation methods and materials. Therefore, it is necessary to investigate the properties of certain materials for application in the renewal of the historical buildings. Within this context, in this study the construction materials of Mardin Castle, which is located in Mardin Province, Turkey and existing for centuries as the symbol of the city, are investigated and its properties are reached. Experimental research methods were used in the study. Primarily, the castle structure was examined on-site by field study and sampling was carried out from the areas determined. The samples were analyzed via various spectroscopic and geophysical methods, and various findings were achieved. Relatively variable and high levels of salinization were determined in the findings regarding the average values in stone samples of Mardin Castle's Fortification Walls. Results of the research document the conservation status regarding Mardin Castle and provide an experimental base and also a theoretical support for the conservation of historical buildings in Turkey; and present indicative suggestions to establish conservation schemes of the historical buildings.

1. Introduction

The historical buildings are the most important elements that ensure the sustainability of the cultural heritage by witnessing the changes in culture and civilization [1-2]. However, today the building materials, which form the historical buildings, are being exposed to various deteriorations increasingly due to various causes. Stone building materials are affected by many deterioration mechanisms that are controlled by various factors such as the mineral composition, textural properties, pore / capillary structure, temperature, moisture, and exposure time with the environment that determines the complex physical, chemical and biological transformation processes [3-9]. A significant increase

has been observed in abrasion rates of stone materials also with the air pollution increasing since the Industrial Revolution [10]. Today, damages caused on the cultural heritage are increased by increasing air pollution, human activities, and particularly by the release of the pollutants related with the industry, heating and traffic to the atmosphere [11-17]. Furthermore, also the great increase in CO₂ emission and the associated climate change in the last 150 years have negative impacts on the cultural heritage in various aspects [18]. It was seen that the global warming has increased the incidents causing the formation of harmful salines that affect the porous stone in the entire Central and North Europe [19-25]. Likewise, it was seen that advanced bioactivity of

* Corresponding Author

^{*}(lalekaratas@artuklu.edu.tr) ORCID ID 0000-0001-8582-4612

Cite this article

Karatas, L. (2023). Investigating the historical building materials with spectroscopic and geophysical methods: A case study of Mardin Castle. Turkish Journal of Engineering, 7(3), 266-278

photosynthetic (micro) organisms (eg; cyanobacteria) with increasing CO₂ and the biological degradation, in which the most (micro) organisms are increased, are increased with the climate change [26]. For instance, colours of the stones have changed and foliation has been observed [27].

It is well known that also water plays a primary role in the deterioration processes of historical stones and mortars. Water causes disintegration, surface erosion, and cracking through the freezing – dissolution or wetting – drying circles within the pores by acting as a medium for the atmospheric pollutants such as sodium and nitrate that are increasing due to the reasons explained above. Furthermore, water may also carry the soluble salines, which trigger the crystallization between the pores and dissolution of the stones [9,28].

Increase of the material deteriorations on the stone materials and buildings by all these reasons has increased the need for the applications regarding the documentation and monitoring of material deterioration on the stone buildings. Today, unmanned aerial vehicle (UAV) and lidar technology can play important roles on documentation [29-31]. UAV and Lidar technology has been frequently used to document cultural heritage [32-34].

The resistance of the construction materials can be explained by the competent / incompetent status of the physical properties within the determined standards. Through the physical tests applied (such as hardness, unit volume weight, water absorption capacity, and porosity), it may be possible to determine whether the construction materials (particularly stone / rock) maintain their original qualities or to what extent they drifted away. Ultrasonic techniques are used in determining the dynamic properties of the rocks. These techniques are being used increasingly in construction technology due to the ease of application and non-destructiveness. The ultrasonic speed (SV) measurements, which are particularly being applied extensively on the rocks, provide important data also for the historical materials. The saline contents of the materials, which form the buildings, provide information that may be deemed as indicators on the physical status of the buildings. Salines, which are present within the content of different construction materials naturally or which are carried onto the surface or into the pores of the materials via the water by dissolving in water later as a result of capillary effect, provide information about the chemical changes that may occur both within the own structure of the material and within the structure of the other materials they interact.

In recent years, spectroscopy is also being used increasingly as an analytic technique for the researches on historical and cultural works to determine the stone building materials [35]. Spectroscopy is used to investigate the construction materials such as natural stones and mortars in architectural heritage and generally saline crystallization and black Shell formation, which are their deterioration types [36]. As an important example; in the study of Lodi et. al [37], it is aimed to obtain information about the composition of the mortar and stone materials, their conservation status and possible changing processes in situ on the samples

received from a historical building in Venice via spectroscopy. It was concluded that the mortar and saline accumulations existing on the stone surfaces of the building have been crystallized very quickly due to the interaction of the abrasive atmospheric gases often with the nitrates and similar products.

Many historical masonry constructions in the world are on the edge of extinction due to the increasing frequency and changing models of material deterioration. The initial steps to set up an appropriate conservation treatment plan require the conservator to 1) determine the deterioration status through the microscopic and chemical analysis and 2) monitor the progress of deteriorations in time to determine the intensity and ratios [38].

The materials, which are as close as possible to the original materials in terms of their chemical compositions and physical properties, are needed in the reconstruction and maintenance of the buildings that have historical importance [39-40]. In addition, the properties of the materials used in the historical buildings are generally not known with a sufficient accuracy. This causes misapplications in case of emergencies, and also may lead to future potential greater damages on the building. The lack of data regarding the engineering properties of these buildings causes long-term damages on the buildings due to inappropriate conservation methods and materials [41]. Therefore, it is necessary to investigate the properties of certain materials for application in the renewal of the historical buildings. Within this context, in this study it is aimed to document the construction materials, to determine the material problems, and to present conservation suggestions through the studies carried out by spectroscopic and geophysical methods on the materials of Mardin Castle's Fortification Walls. The construction materials of Mardin Castle, which is located in Mardin Province, Turkey and existing for centuries as the symbol of the city, are investigated and its properties are reached as a result of the study. The findings of the study do not only reflect the conservation status of the historical building in real terms, but also provide an experimental base and theoretical support for the conservation of the historical buildings in Turkey. It presents indicative suggestions to establish conservation schemes of the historical buildings and enriches the maintenance and reinforcement evaluation status of the historical buildings.

Within this scope, initially information regarding the working area is presented in the section below. Then, the method followed in the study is described and the findings are presented. In the next stage, various results are achieved by comparing the findings of the study with the data obtained in the literature. In the conclusion section of the study, various conservation suggestions are presented regarding the building.

1.1. Location and importance of the study area

Mardin settlement, which has the characteristic of monumental city today, is consisted of two elements. These are Mardin Castle and the essential settlement developed on the plinth of the castle. The Castle is located

on the thin-long plane on a hill having a height of 1200 metres. This plane is in a size of 800 m in east-west direction, and of 150 m in the widest place and of 30 m in the narrowest place in North –south direction. The Castle gives the impression of a natural formation, since it has been built so as to involve the existing rocks with its walls and towers. Entry is made to the castle, where the defence capacity was strengthened, from a point that nearly centres area, on which the castle is placed, from the South, to the extent allowed by the topography. This entrance is accessed through a ramp, which steepens gradually, and stairs located at the end of it [42] (Fig. 1).

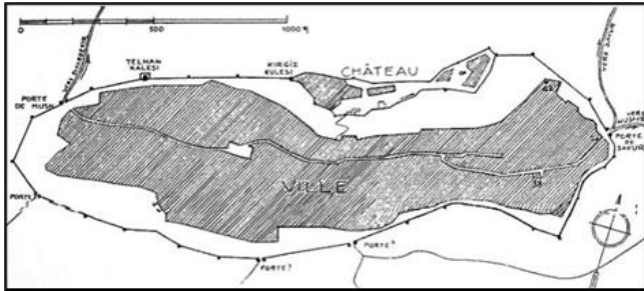


Figure 1. Plan of Mardin city walls charted by Gabriel [42]

Access to the main entrance door of the Castle from the historical settlement located on the South slope of Mardin Castle is made from a central point allowed by the topography. Firstly, the historian Ammianus Marcellinus has mentioned the Mardin Castle, which has gain reputation as a place hard to occupy along the history, in the IV. Century AC. Mardin Castle has begun to be mentioned in the historical records after a long time by Arabic scholars only from the X. century. In this period, Mardin Castle has been called Şahin Castle or Karga Castle. In 1471, it has been mentioned by the Merchant Barbaro, who has come to Mardin, in his memories that the castle had walls exceeding 12 m. and it was accessed by the stairs, and there had been nearly 300 houses within the interior castle. As of XVI. Century, according to Evliya Celebi, it has been reported that the Castle has gone under many repairs, and grain has been stored in its caves and cellars, and there had been water cisterns.

The Castle has been found by Niebuhr, who has come to Mardin in XVIII. Century, as undamaged enough, but neglected; according to the observations of Niebuhr, it has been estimated that nearly 200 houses were present, of which 80 could be habitable. In 1891, according to the records of Cuinet, it has been reported that there were 4991 houses in total within the castle and the city. Some monumental structures in Mardin Castle, in a ruin status, and the “mansion” structure as an example of the civil architecture have been emphasized in the studies conducted by Gabriel in the region in 1930. Today, the mansion structure, which has been documented by Gabriel, is destroyed. The visible relics belong to the Castle’s Mosque, which is placed just above the castle entrance and thought to be built in XV. Century, within the period of Akkoyunlular over the Artuqid building and to the Hızır Mosque, which is believed to belong to the period of Khalif Ömer.

The Mardin city, which has been developed on the plinth of the castle, is among the rare Anatolian cities that

have conserved the traditional city texture. Today, the entire region, in which the Castle and the old neighbourhoods that the traditional city texture is conserved are placed, remains within the urban archaeological site. The greatest factor in the conservation of the traditional city texture is definitely the ethnical building features of the neighbourhoods, which have been conserved within the historical process (“Fig. 2”).

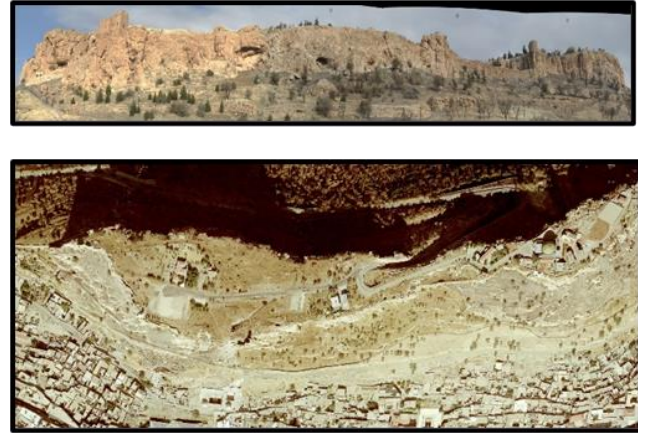


Figure 2. Mardin Castle

2. Method

Construction materials of Mardin Castle’s Fortification Walls were investigated with various methods within the scope of the research. Experimental research methods were used in the research. Primarily, the castle structure was examined on-site by field study and sampling was carried out from the areas determined. The samples were analyzed via various spectroscopic and geophysical methods, and various findings were achieved.

In the first stage of the research, physical tests, which aim to determine the unit volume weight and porosity properties, were applied on the stone/rock and ceramic (brick) samples. In the second stage, total saline content of the stone and brick samples of the fortification walls were determined conductometrically. Afterwards, the water-soluble saline types (phosphate and carbonate) and the environmental pH values of the samples (stone and brick) were determined quantitatively. It was found that the saline contents of the samples, which reflect the basic environmental conditions, demonstrated carbonation in high values, via the spot saline tests. Aggregate particle distribution values were obtained by the total aggregate and binding agent ratios and the aggregate granulometrics by acidic aggregate / binding agent analysis in the samples of mortar and plaster. Rock and mineral content, texture, status, distribution, particle sizes of the samples were investigated by petrographic fine section optical microscope analysis. Chemical content of all structural samples of the Castle were determined by PED-XRF analysis. Cementation Index data was used in order to determine the type of limestone in the mortars and plasters (“Fig. 3”).

Experiments, which were conducted under the research, are stated below, in summary.

- Documentation (Photographing), Coding and Cataloguing (Material Grouping) Studies
- Physical Tests (Unit Volume Weight, Water Absorption Capacity (WAC), Porosity, Schmidt Hardness, Ultrasonic Speed)
- Conductometrical Analysis (Amount of Total Water-Soluble Saline)
- Saline Type Tests (SO_4^{2-} , Cl^- , PO_4^{3-} , CO_3^{2-} , NO_3^- and NO_2^-)
- Aggregate / Binding Agent Tests
- Granulometric Analysis in Aggregates (Particle Size Distribution)
- Petrographic Fine Section Optical Microscope Analysis
- X-Ray Fluorescence Analysis (M-XRF)
- X-Ray Fluorescence Analysis (PED-XRF)

1. Documentation (Photographing), Coding and Cataloguing (Material Grouping) Studies
2. Physical Tests (Unit Volume Weight, Water Absorption Capacity, Porosity, Schmidt Hardness, Ultrasonic Speed)
3. Conductometrical Analysis (Total Amount of Water-Soluble Saline)
4. Saline Type Tests (SO_4^{2-} , Cl^- , PO_4^{3-} , CO_3^{2-} , NO_3^- and NO_2^-)
5. Aggregate / Binding Agent Analysis
6. Granulometric Analysis in Aggregates (Particle Size Distribution)
7. Petrographic Fine Section Optical Microscope Analysis
8. X-Ray Fluorescence Analysis (M-XRF)
9. X-Ray Fluorescence Analysis (PED-XRF)

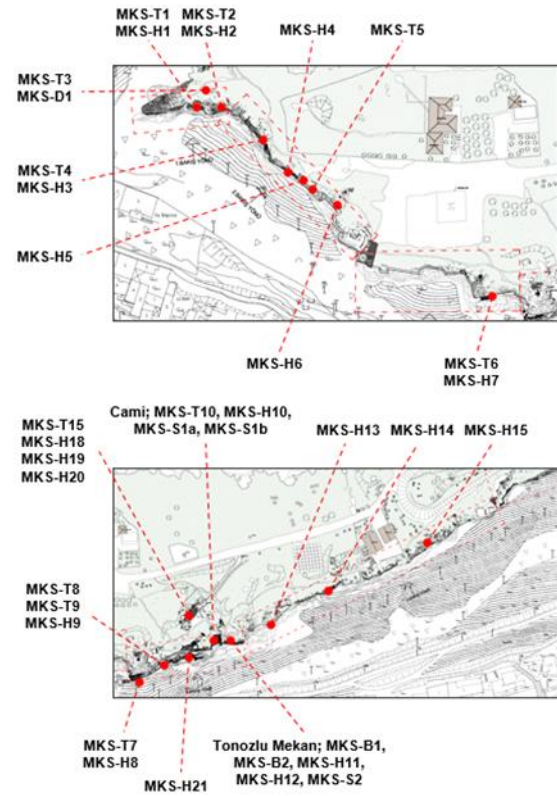
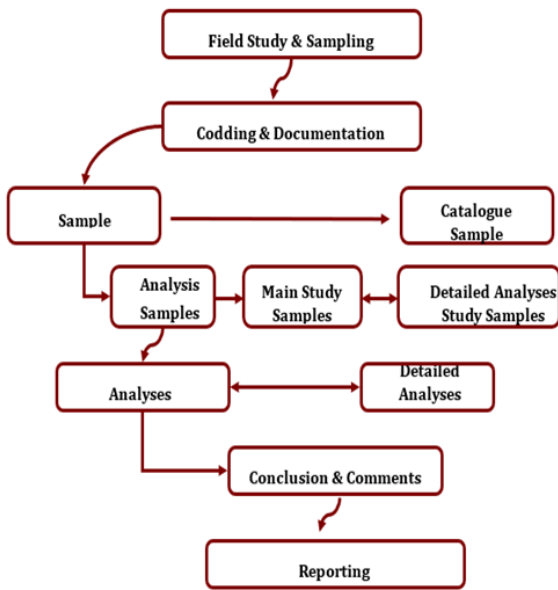


Figure 3. Material Investigation Methodology of Mardin Castle's Fortification Walls

2.1. Constructional material groups of Mardin Castle's fortification walls

Firstly, castle structure was investigated on site, and places determined on the structure were coded and sampling was carried out. Places, where the samples were taken on the Castle, are stated in "Fig. 4". Materials taken from the coded places were grouped. Material groups are shown in "Fig. 5". Analyses applied on the material groups are described in "Table 1".

Table 1. Analyses applied on the material groups during the research

Material Group	Applied Analyses / Tests
Stone / Rock Samples	1, 2, 3, 4, 7, 9
Ceramic Samples	1, 2, 3, 4, 7, 9
Mortar Samples	1, 5, 6, 7, 9
Plaster / Plaster Layer Samples	1, 5, 6, 7, 9
Soil Sample	1, 3, 4, 9
Lime Layer Sample	1, 9

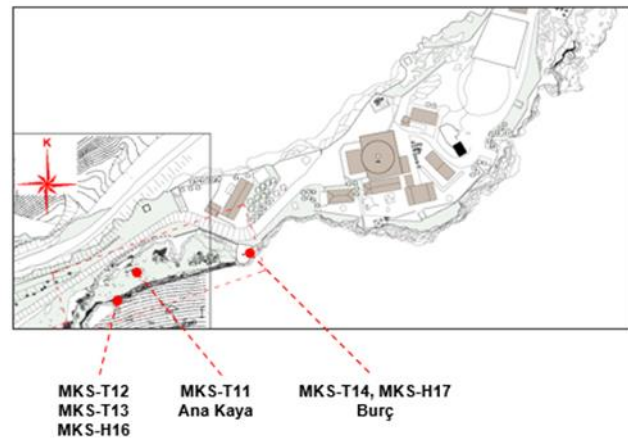


Figure 4. Coding of the Samples taken from the Castle on the layout plan

Material Group Code	Material Group Descriptions	Number of Main Samples
MKS-T	Stone / Rock Samples	25
MKS-B	Ceramic (Brick) Samples	2
MKS-H	Mortar Samples (From Stone/Brick Pointing and Debris Fillings)	31
MKS-S	Plaster/Plaster Layer Samples	3
MKS-D	Soil Sample	1
MKS-Z	Lime Layer Sample	1

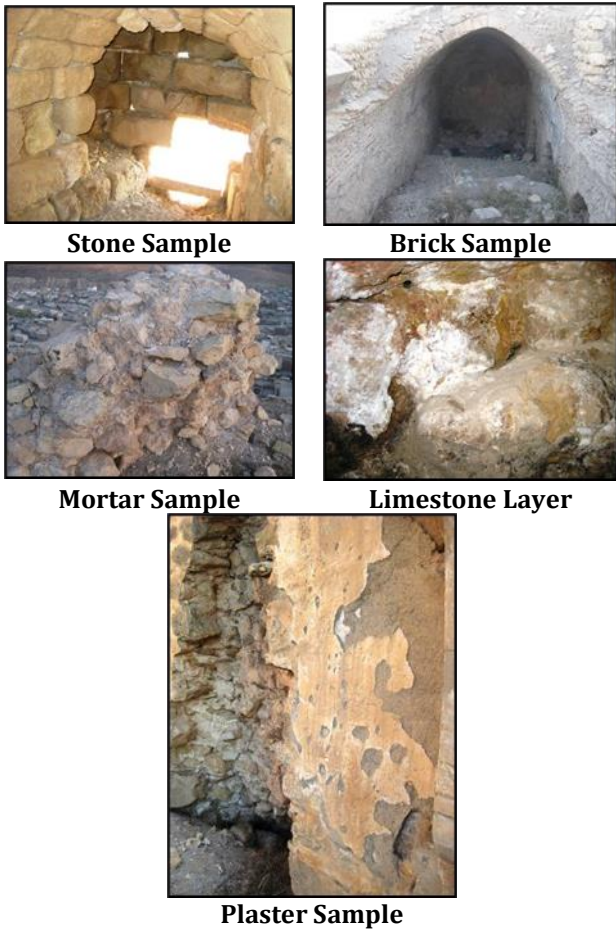


Figure 5. Constructional Material Groups of Mardin Castle's Fortification Walls

3. Results

3.1. Physical Tests

3.1.1. Unit Volume Weight, WAC and Porosity

Physical statuses of the materials were determined through the physical tests applied on the stone/rock and brick samples of Mardin Castle's Fortification Walls. Since the sample amount required to conduct the standard physical tests (standard samples of 5-10 cm³; RILEM, 1980) was not possible in terms of the standard applications, the test applications were conducted on the stone pieces taken by sampling. Basic physical tests,

which aim to determine the unit volume weight, water absorption capacity and porosity, and hardness (Schmidt and ultrasonic speed (SV) measurement tests were applied on the stone samples. For the basic physical tests, unit volume weights (wet/dry UVW, g/cm³), water absorption capacities (%WAC) and porosity (%P) values were determined by means of the dry weights taken directly, archimedes (within water) and saturated weights (watery weight, which it is ensured to reach to the pores under 50 torr pressure in distilled water) of the samples ("Table 2" and "Fig. 6-7"). Stone samples have physical properties changing depending on the natural rock structures, and all samples have physical properties changing depending on the environmental properties. The samples having low unit volume weights and high porosities with their structural properties are those in a more incompetent status. The stone samples of the fortification walls are among the limestone rock types. Among the stones, MKS-T5, MKS-T6 and MKS-T10 (Biosparitic Limestone) samples are those having the lowest competency and MKS-T9 (Argillaceous Limestone) is the one having the highest competency (Table 2).

Table 2. Unit volume weights (wet/dry UVW, g/cm³), Water absorption capacity (%WAC) and porosity (%P) values

Samples	UVW-I (g/cm ³)	UVW-K (g/cm ³)	WAC (%)	P (%)	Type
MKS-T1	2.60	2.35	3.96	9.33	R. Limestone
MKS-T2	2.73	2.34	6.07	14.20	A. Limestone
MKS-T3	2.61	2.20	7.18	15.79	A. Limestone
MKS-T4	2.75	2.35	6.16	14.46	A. Limestone
MKS-T5	2.43	1.95	10.20	19.89	B. Limestone
MKS-T6	2.50	1.93	11.81	22.80	B. Limestone
MKS-T7	2.66	2.40	4.01	9.63	Travertine
MKS-T8	2.69	2.31	6.10	14.11	A. Limestone
MKS-T9	2.72	2.63	1.26	3.32	A. Limestone
MKS-T10	2.51	1.99	10.57	21.00	B. Limestone
MKS-T11	2.68	2.40	4.34	10.43	A. Limestone
MKS-T12	2.70	2.53	2.50	6.32	A. Limestone
MKS-T13	2.66	2.47	2.90	7.18	A. Limestone
MKS-T15	2.55	2.49	1.00	2.50	Travertine
MKS-T16	2.52	2.34	3.15	7.37	R. Limestone
MKS-T17	2.49	2.13	6.78	14.43	R. Limestone
MKS-T18	2.54	2.28	4.46	10.18	A. Limestone
MKS-T19	2.62	2.31	4.96	11.48	A. Limestone
MKS-T20	2.66	2.54	1.77	4.49	A. Limestone
MKS-T21	2.59	2.45	2.21	5.40	A. Limestone
MKS-T22	2.30	1.99	6.92	13.76	A. Limestone
MKS-T23	2.57	2.33	4.07	9.48	A. Limestone
MKS-T24	2.52	2.02	9.80	19.83	B. Limestone
MKS-T25	2.67	2.51	2.42	6.08	A. Limestone
MKS-B1	2.30	1.39	28.19	39.30	Brick
MKS-B2	2.26	1.38	27.92	38.65	Brick

B. Limestone: Biosparitic Limestone, A. Limestone: Argillaceous Limestone, R. Limestone: Recrystallized Limestone

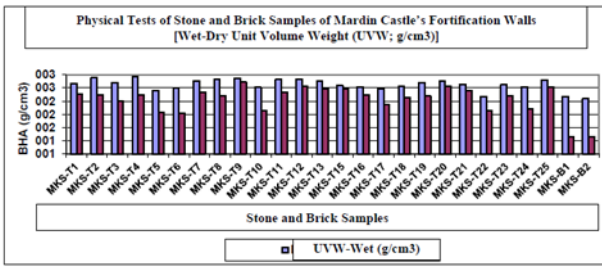


Figure 6. Unit volume weights (wet/dry UVW, g/cm³)

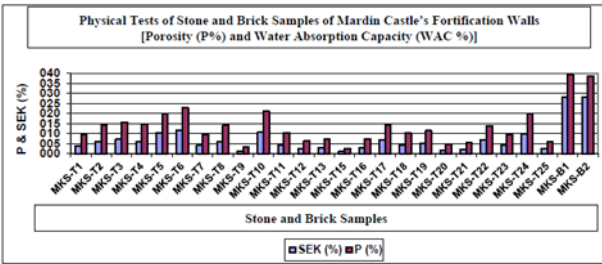


Figure 7. Water absorption capacity (%WAC) and porosity (%P) values

3.1.2. Hardness Test

Schmidt Hammer is used to determine the hardness value of the rocks. The hardness value determined is used in UCS estimation and classification of the rocks. However, this method cannot be applied on very soft or very hard rocks. During the test, attention was paid to maintain the hammer always in a vertical position on the rock. In the test, strokes were made on the 5 points on the rock surface, and average hardness values were obtained. Digital Proseq brand Schmidt Hammer was used in the measurement. Schmidt Hammer measurement results of the stone samples (limestone) of Mardin Castle’s Fortification Walls supported the basic physical tests. Stone hardness of MKS-T3 sample is higher than the other samples (26.3), and hardness of MKS-T1 stone sample is lower (22.0). If we evaluate in general, stone hardness of the samples are very close to each other (“Table 3” and “Fig. 8”).

Table 3. Stone hardness measurement tests

Samples	M 1	M 2	M 3	M 4	M 5	Average
MKS-T1	21.0	22.0	22.0	22.3	22.5	22.0
MKS-T2	23.0	24.6	25.8	26.3	26.8	25.3
MKS-T3	25.7	25.9	26.2	26.3	26.5	26.1
MKS-T4	24.0	24.2	25.0	25.2	25.3	24.7
MKS-T8	25.3	25.3	25.4	25.5	25.7	25.4
MKS-T20	22.0	23.1	23.7	24.0	24.5	23.5

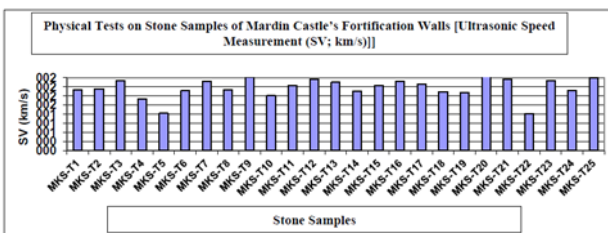


Figure 8. Hardness Test

3.1.3. Ultrasonic Speed Measurement Test

Measurements were taken by using Matest C372N Model High-Performance Ultrasonic Test Device. SV measurements conducted on the stone samples, taken from Mardin Castle’s Fortification Walls are presented in Table 4c over the average values. It could be determined in the measurements that some of the limestone samples were more porous and in the stage of deterioration. Among the samples, those having higher SV (km/s) values are more competent. This is in compliance with the data, which reflects the basic physical properties of the same samples. Within the sample set, MKS-T22 sample has the lowest competency and MKS-T20 sample has a higher competency (“Table 4” and “Fig. 9”).

Table 4. SV measurements of the limestone samples

Samples	SV (µs)	SV (km/s)	Samples	SV (µs)	SV (km/s)
MKS-T1	41.6	2.00	MKS-T14	42.2	1.96
MKS-T2	41.3	2.03	MKS-T15	39.7	2.15
MKS-T3	38.0	2.31	MKS-T16	57.0	2.28
MKS-T4	46.3	1.71	MKS-T17	39.3	2.19
MKS-T5	58.7	1.23	MKS-T18	47.6	1.94
MKS-T6	42.1	1.97	MKS-T19	46.5	1.90
MKS-T7	38.2	2.29	MKS-T20	54.2	2.44
MKS-T8	41.7	2.00	MKS-T21	41.0	2.35
MKS-T9	36.9	2.42	MKS-T22	59.1	1.22
MKS-T10	44.5	1.81	MKS-T23	38.0	2.31
MKS-T11	39.7	2.15	MKS-T24	32.6	1.99
MKS-T12	39.6	2.36	MKS-T25	40.4	2.40
MKS-T13	38.6	2.25	Average	43.4	2.07

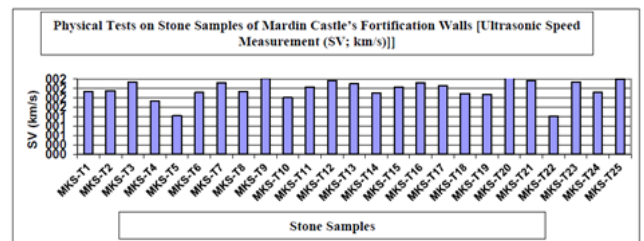


Figure 9. Ultrasonic speed measurement test values

3.2. Conductometrical Analysis (Total Amount of Water-Soluble Saline)

The total amount of water-soluble saline present in the structure (pores) of the stone and ceramic (brick pieces) samples of Mardin Castle’s Fortification Walls was determined quantitatively (“Table 5” and “Fig. 10”). For the designation of total saline measurement in the samples; sample of 5 grams, which was taken into 25 ml of water, was centrifuged for 1 hour and standard sodium hexametaphosphate was added over it after filtering. Total saline contents of the samples prepared were recorded conductrometrically via the conductometer (with Neukum Series 3001 brand conductivity/pH/heat meter). In the widest meaning, the saline content within the materials is caused by the environment of the samples, by the petrographic rock properties for the

stones / rocks or natural or metabolous (deteriorated) physical / chemical properties of the materials. The total saline content of stone /rock samples of Mardin Castle's Fortification Walls varies between 0.48-3.22% (average 1.53) and is between 0.27% and 1.22% for brick samples ("Table 5" and "Fig. 10"). Excessively variable and high levels of salination were determined in stone samples in terms of average values. Among the stone sample set, low salination was determined in MKS-T10 (limestone) sample (0.48%), and very high salination was determined in MKS-T22 (limestone) sample (3.22%) ("Table 5"). For MKS-T22 sample, this refers to a very advanced level of salination.

Table 5. Total Amount of Water-Soluble Saline

Samples	SS (%)	Samples	SS (%)
MKS-T1	0.65	MKS-T15	2.26
MKS-T2	0.83	MKS-T16	2.01
MKS-T3	1.04	MKS-T17	2.29
MKS-T4	0.86	MKS-T18	1.66
MKS-T5	2.04	MKS-T19	1.10
MKS-T6	2.85	MKS-T20	0.95
MKS-T7	1.98	MKS-T21	0.84
MKS-T8	1.40	MKS-T22	3.22
MKS-T9	1.50	MKS-T23	1.73
MKS-T10	0.48	MKS-T24	0.97
MKS-T11	0.99	MKS-T25	0.62
MKS-T12	2.10	MKS-B1	0.27
MKS-T13	1.17	MKS-B2	1.22
MKS-T14	2.82	Stone Average	1.53

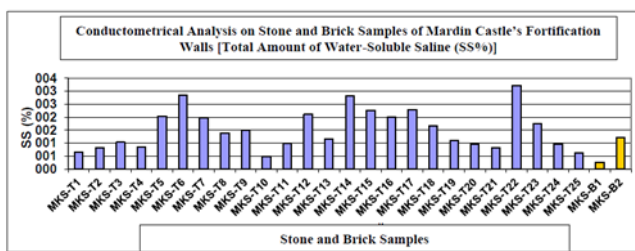


Figure 10. Total Amount of Water-Soluble Saline

All samples of Mardin Castle's Fortification Walls are open to the impact of high salination. The impact of the climatic circle is important at this point (Table 6). When long-term weather conditions of March in Mardin is considered, on average 10.7 days per month is rainy (Table 6). The heavy rains between December and April in Mardin are relatively higher than the summer season. Average temperature is 8.3°C in March and hours of sunshine are 6.1 hours during the day (Table 6). Formation of relatively humid environmental conditions were observed in the stone samples, which have been exposed to water accumulation with the heavy side rains, during the sampling carried out in the last period of the winter season, which was rainy and in which the sun

showed its face less. This causes an impact, which accelerates the deterioration on the stones. The humid environment formed on the stones causes the limestone stratification, which occurs with the recrystallization of the salines dissolved by lichenification /vegetation on the stone surfaces, with the impact of microclimate, and high salination associated with this, and reveal of destructive effect of salination on the stones (dissolution, disintegration).

3.3. Analysis of Saline Type (Water-Soluble Saline Types in Stones and Ceramics)

Types and amounts of the salines determined by the standard (Merck) spot saline type tests are presented in Table 7, and environmental pH values are presented in Table 7 and Graphic 7.

pH Distribution in the Samples: It was determined that the pH values of the stone/rock samples investigated (independent from the rock type) vary between 7.03 – 8.66, pH values of brick samples are between 7.81 and 7.95, of soil sample is 8.33 and of limestone layer sample is 6.64. The samples investigated have a poor basic feature in general, on the other hand the limestone layer sample has a more acidic feature than the other samples (Table 7 and Graphic 7).

Carbonate Test (CO32-): It helps to determine the binding agent containing lime in mortar and plasters. It is used in determining the combination of stones containing carbonate (marble, travertine, limestone, etc.) and calcified surfaces in stones/rocks. Carbonation varying between 11.2 - 80 mg/L was found in the samples. The high carbonate content determined in the soil sample, which represents the reservoir (80 mg/L), is a criterion for the other materials (Table 7).

Phosphate Test (PO43-): The impact of agricultural activities (fertilization containing phosphate), animal (defecation) or vegetable residues, sewage or household wastes may be caused by transportation of food deposits, directly or indirectly, from the soil reservoir to the material by moisture, in the vicinity of the wastes or picnic sites. Furthermore, high phosphate content is observed in rock structures or mortars and plasters with organic (plant – straw) content, and also in the materials that are exposed to the effects of lichenification on the surfaces with intense humidity.

Although it is determined in relatively low amounts in only 2 of the stone samples of the Castle (0.20), higher amounts of phosphate were determined in brick, soil, and limestone layer samples ("Table 6" and "Fig. 11").

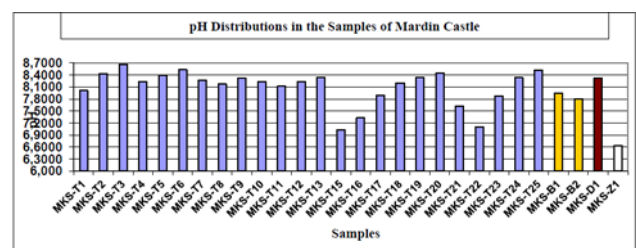


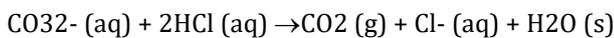
Figure 11. Saline Type Analysis (Water-Soluble Saline Types in Stone and Ceramics)

Table 6. Values of Saline Type Analysis

	Phosphate (PO ₄ ³⁻)	Carbonate (CO ₃ ²⁻)	pH
MKS-T1	-*	11.2*	8.01**
MKS-T2	-	40	8.44
MKS-T3	-	80	8.66
MKS-T4	-	19.2	8.23
MKS-T5	-	19.2	8.40
MKS-T6	-	40	8.53
MKS-T7	-	59.2	8.26
MKS-T8	-	19.2	8.17
MKS-T9	-	40	8.32
MKS-T10	-	59.2	8.23
MKS-T11	0.20	19.2	8.12
MKS-T12	-	40	8.24
MKS-T13	-	40	8.34
MKS-T15	-	19.2	7.03
MKS-T16	-	19.2	7.33
MKS-T17	-	19.2	7.90
MKS-T18	-	59.2	8.20
MKS-T19	-	11.2	8.35
MKS-T20	-	59.2	8.45
MKS-T21	-	19.2	7.63
MKS-T22	-	11.2	7.10
MKS-T23	0.20	11.2	7.88
MKS-T24	-	59.2	8.33
MKS-T25	-	80	8.52
MKS-B1	0.20	59.2	7.95
MKS-B2	0.40	40	7.81
MKS-D1	0.80	80	8.33
MKS-Z1	0.20	19.2	6.64

3.4. Aggregate / Binding Agent and Granulometrical Analyses

Samples, which were subjected to dry weighing initially in order to determine the aggregate and binding agent parts of 20 mortar and 2 plaster layers samples taken from Mardin Castle’s Fortification Walls, were treated with diluted acid (HCl of 5%) in order to refine them from binding agent contents (all carbonate content; CO32-) later (1).



After the mortar and plaster layer samples, which were separated from lime and all carbonate contents (binding agent) by the filtering, washing, and drying procedures) and where the aggregate part was obtained, are dried at room temperature, and total binding agent and aggregate amounts in terms of weight were obtained by subjecting to re-weighing (“Fig. 12”). Aggregate

particle distributions were determined (granulometrical analysis) by applying systematic sieving to the aggregates of the samples (which do not contain carbonate) (“Fig. 13”). All mortar and plaster samples, which allowed this analysis, were subjected to the abovementioned analyses (TS 3530 –Particle Size Distribution Designation – Sieving Method).

Supportive fine section optical microscope analyses and acidic aggregate / binding agent analyses were detailed, and amounts, types and distribution of aggregate and binding agent were obtained in mortars and plasters, and the samples were grouped (Table 7, Fig. 12-13).

When the aggregate content of 20 mortar and 2 plaster layers samples of Mardin Castle’s Fortification Walls, independent from being original or repaired, are reviewed in detail, it was found that the aggregate structure of majority of the analysed mortars were consisted of coarse particles (500-1000 µm; containing coarse sand and small stone pieces). Besides, an aggregate mixture formed by the aggregates collectively, which demonstrates an average and more balanced distribution (63-500 µm), were also present in the pointing stuff and mortar samples.

Table 7. Aggregate / Binding Agent and Granulometrical Analyses

Samples	<63 µm	>63 µm	>125 µm	>250 µm	>500 µm	>1000 µm
MKS-H1	13.47	9.07	14.02	22.18	31.39	9.86
MKS-H3	12.35	9.55	15.67	24.36	35.41	2.66
MKS-H4	11.03	8.44	13.71	24.05	37.07	5.69
MKS-H5	10.65	9.31	15.24	24.53	33.05	7.23
MKS-H8	13.60	9.38	11.64	18.85	32.95	13.58
MKS-H9	14.76	9.22	13.30	20.62	34.73	7.37
MKS-H10	19.10	10.51	13.52	19.65	24.84	12.38
MKS-H11	15.64	6.92	10.50	17.65	36.10	13.18
MKS-H12	15.02	9.60	16.84	25.98	26.33	6.22
MKS-H14	12.34	4.97	8.57	14.86	20.77	38.48
MKS-H15	10.86	7.23	12.13	22.17	30.65	16.96
MKS-H16	15.80	11.29	15.39	20.87	25.89	10.76
MKS-H18	11.56	8.10	13.35	21.50	29.38	16.11
MKS-H21	15.98	7.12	10.61	17.24	29.57	19.49
MKS-H24	14.44	8.59	12.53	17.76	29.09	17.60
MKS-H26	13.97	8.18	13.47	22.14	26.91	15.33
MKS-H27	16.10	9.10	15.60	25.02	27.99	6.20
MKS-H29	17.20	7.93	11.92	17.79	33.54	11.62
MKS-H30	14.55	4.20	8.49	16.55	32.78	23.43
MKS-H31	16.45	5.47	10.09	18.68	35.48	13.84
MKS-S1a	46.62	11.55	12.17	13.86	2.81	13.00
MKS-S1b	7.30	10.71	20.97	18.48	38.49	4.05
Mortar Average	14.24	8.21	12.83	20.62	30.70	13.40

Table 8. Granulometrical analysis on the aggregates of mortar and plaster samples

Samples	TB (%)	TA (%)	Samples	TB (%)	TA (%)
MKS-H1	93.63	6.37	MKS-H16	89.93	10.07
MKS-H3	85.57	14.43	MKS-H18	90.37	9.63
MKS-H4	87.94	12.06	MKS-H21	91.77	8.23
MKS-H5	88.04	11.96	MKS-H24	89.46	10.54
MKS-H8	90.54	9.46	MKS-H26	92.24	7.76
MKS-H9	92.41	7.59	MKS-H27	92.83	7.17
MKS-H10	91.82	8.18	MKS-H29	94.49	5.51
MKS-H11	96.63	3.37	MKS-H30	97.97	2.03
MKS-H12	92.98	7.02	MKS-H31	97.93	2.07
MKS-H14	87.45	12.55	MKS-S1a	96.16	3.84
MKS-H15	88.32	11.68	MKS-S1b	75.03	24.97
Mortar Ave.		91.62	8.38		

Macro-physical structures and particle types of the aggregates obtained after acidic treatment on the mortars of Mardin Castle's Fortification Walls were examined under binocular microscope. It was seen that the macro-physical structures of the aggregates of the samples contained a relatively heterogeneous aggregate length and diversity, which do not have an aggregate type preferred as a result of the certain sieving. It was seen that the aggregate content of the mortars were consisted of the aggregates in rich variety and in compliance with the local formation (limestone), of which the density is rounded.

3.5. Fine Section Optical Microscope Analysis

Thin sections (stone/rock, ceramic (brick and tile) and mortar samples) were prepared so as to show all layers from outside to inside ("Table 7") Fine sections of the samples were investigated by using LEICA Research Polarizing Microscope DMLP Model optical microscope having bottom and top illumination.

Table 9. Fine Section Optical Microscope Analysis Stone/Rock and Ceramic Samples

Stone Sample Groups	Rock Type	Hardness (Mohs)	Explanations
Stone Gr1a	Biosparitic Limestone	2.5 - 3	Fossil and fossil shells, which are in a nature affected by hydrothermal solutions, are present.
Stone Gr1b	Recrystallized Limestone	2.5 - 3	Contains calcite and dolomite.
Stone Gr1c	Argillaceous Limestone	2.5 - 3	Primarily calcite, and partly quartz and limonite minerals form the structure in silt particle size.
Stone Gr2	Travertine	2.5 - 3	Micro breaks / cracks in the structure, which was formed by hot water precipitation were filled with re-crystallized calcites. In addition, aragonite and limonite are also present in the structure.

Stone Sample Groups
 Stone Gr1a : MKS-T5, MKS-T6, MKS-T10, MKS-T14 and MKS-T24
 Stone Gr1b : MKS-T1, MKS-T16 and MKS-T17
 Stone Gr1c : MKS-T2, MKS-T3, MKS-T4, MKS-T8, MKS-T9, MKS-T11, MKS-T12, MKS-T13, MKS-T18, MKS-T19, MKS-T20, MKS-T21, MKS-T22, MKS-T23 and MKS-T25
 Stone Gr2 : MKS-T7 and MKS-T15

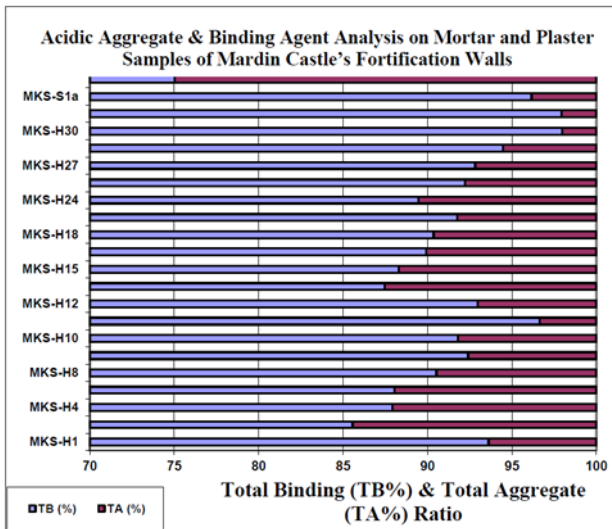


Figure 12. Aggregate and binding agent analysis on mortars and plasters

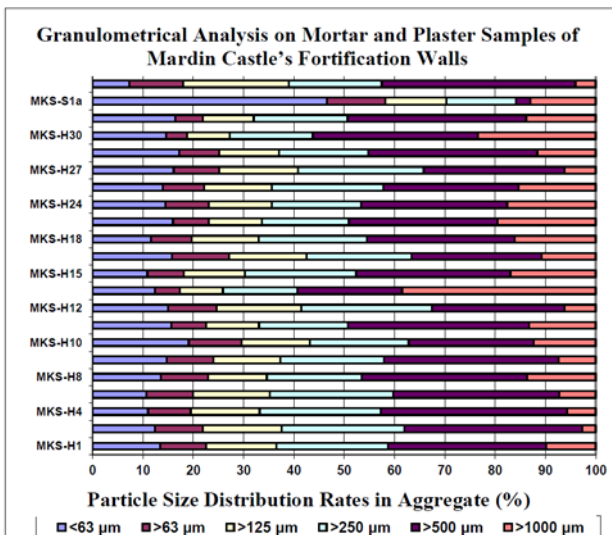


Figure 13. Granulometrical analysis on the aggregates of mortar and plaster samples

3.6. X-Ray Fluorescence (PED-XRF) Analysis

Chemical compositions of stone/rock, brick, soil, lime layer, mortar and plaster samples of Mardin Castle's Fortification Walls were obtained by PED-XRF analysis ("Table 8" and "Fig. 14").

Table 10. PED-XRF analysis values

Element	MKS-T1	MKS-T5	MKS-T8	MKS-T11	MKS-T16	MKS-T20	MKS-T24
Na ₂ O	0.075	0.080	0.079	0.078	0.088	0.074	0.074
MgO	15.47	0.07	6.76	15.65	15.43	16.70	0.03
Al ₂ O ₃	0.64	0.12	2.15	0.01	0.24	0.04	0.16
SiO ₂	4.16	0.52	12.64	0.71	1.57	1.32	0.61
P ₂ O ₅	0.027	0.080	0.054	0.438	0.026	0.160	0.009
SO ₃	0.20	0.08	0.17	0.14	3.44	0.22	0.12
Cl	0.045	0.010	0.019	0.049	0.041	0.041	0.022
K ₂ O	0.009	0.007	0.648	0.007	0.009	0.007	0.007
CaO	34.80	61.27	40.81	34.10	30.97	33.45	61.86
MnO	0.011	0.003	0.020	0.012	0.010	0.015	0.004
Fe ₂ O ₃	0.46	0.06	2.04	0.20	0.22	0.19	0.08
LOI*	44.92	37.91	34.79	48.72	47.82	47.88	37.82

Element	MKS-Z1	MKS-D1	MKS-B1	MKS-B2
Na ₂ O	0.180	0.073	0.071	0.074
MgO	21.34	4.70	4.71	4.55
Al ₂ O ₃	0.02	3.28	7.58	7.68
SiO ₂	0.01	15.98	36.90	35.37
P ₂ O ₅	0.074	0.811	0.836	0.835
SO ₃	42.39	0.31	0.34	0.46
Cl	0.061	0.025	0.020	0.023
K ₂ O	6.121	0.615	2.709	2.933
CaO	4.39	34.80	20.74	20.05
MnO	0.002	0.062	0.096	0.107
Fe ₂ O ₃	0.04	2.41	5.74	6.35
LOI*	25.98	36.80	19.73	20.93

Chemical compositions of mortar and plaster samples of Mardin Castle’s Fortification Walls were determined by PED-XRF analysis (“Table 7”). Mortar properties of the samples selected among the mortar and plaster sample groups determined by fine section optical microscope analyses were investigated per aggregate structures. Composition features of the mortar and plaster samples, which were investigated independent from their repair or original qualities, were evaluated by Cementation Index data. Cementation Index (CI) is the ratio of the part dissolved in acid to the part dissolved in bases. Mortars containing lime are classified as fat mortar (FM) and hydraulic mortar (ZHK, OHK and HK) depending on the aggregate content and type. For the mortars, the fat mortars having a total aggregate content less than 5% are the mortars having high levels of lime, thus high levels of CaO (Table 16). Mortars having a total aggregate content more than 5% are the mortars having low CaO levels, thus having hydraulic characteristic. In the composition of this type of mortars rates of silicium

(SiO₂), aluminium (Al₂O₃) and iron (Fe₂O₃) are high. Cementation Index (CI) values of the mortars and plasters are provided in ‘Table 8’. When the competency properties of the mortar and plaster samples are evaluated, it is seen that the samples contain low amounts of aggregate and have low hydraulic features (“Fig. 14”). Competence of the mortar and plaster samples is very poor and they are close to disintegration.

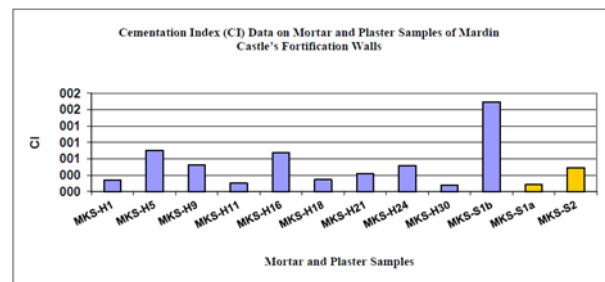


Figure 14. X-Ray Fluorescence (PED-XRF) Analysis Cementation Index Data on Mortars

4. Discussion

Constructional materials of Mardin Castle's Fortification Walls were investigated by various methods.

The first finding that must be emphasized is all samples of Mardin Castle's Fortification Walls are exposed to the effect of high salination. In stone samples, relatively variable and high levels of salination were observed in terms of the average values. The impact of the climatic circle is important at this point (Table 6). When long-term weather conditions of March in Mardin are considered, on average 10.7 days per month is rainy. The heavy rains between December and April in Mardin are relatively higher than the summer season. Average temperature is 8.3°C in March and hours of sunshine are 6.1 hours during the day. Formation of relatively humid environmental conditions were observed in the stone samples, which have been exposed to water accumulation with the heavy side rains, during the sampling carried out in the last period of the winter season, which was rainy and in which the sun showed its face less. This causes an impact, which accelerates the deterioration on the stones. The humid environment formed on the stones causes the limestone stratification, which occurs with the recrystallization of the salines dissolved by lichenification /vegetation on the stone surfaces, with the impact of microclimate, and high salination associated with this, and reveal of destructive effect of salination on the stones (dissolution, disintegration). This finding supports the finding obtained by De Ferri et. al [9] in their studied that water causes disintegration, surface erosion, and cracking through the freezing – dissolution or wetting – drying circles within the pores by acting as a medium for the substances such as sodium and nitrate, and carries the soluble salines, which trigger the crystallization between the pores and dissolution of the stones.

Although it is determined in relatively low amounts in only 2 of the stone samples of the Castle, higher amounts of phosphate were determined in brick, soil, and lime layer samples. In addition, the excessive amounts of various substances such as salines and phosphates show that it supports the finding of Sabbioni et. al. [25] in their studies stating that global warming causes the formation of harmful salines, which affects the porous stones in the entire Central and North Europe, and Turkey also supports this finding within this context.

5. Conclusion

In this study, properties of the construction materials and material problems were determined through the studies via spectroscopic and geophysical methods conducted on the materials of Mardin Castle's Fortification Walls. The research is significant in terms of determining the materials and material problems for Mardin Castle's Fortification Walls, which is located in Mardin Province, Turkey, and which survives for centuries as the symbol of the city, and presenting the conservation suggestions. The findings of the study do not only reflect the conservation status of the historical

building in real terms, but also provide an experimental base and theoretical support for the conservation of the historical buildings in Turkey. It presents indicative suggestions to establish conservation schemes of the historical buildings and enriches the maintenance and reinforcement evaluation status of the historical buildings.

In the findings, it is seen that salinization is present on the stone samples of Mardin Castle's Fortification Walls, at very variable and high levels, in terms of the average values. This results, which was obtained in the study, match particularly with the findings in the world literature obtained in the studies conducted on the stone structures, stating that the salinization factor is very high [19-24]. It leads to saline crystallization, shell formation, patinas, and alveolization in pores and cracks. Within this context, primarily it is necessary to prevent the factors, which causes salinization on historical structures.

The original mortars must be conserved on the fortification walls. Lime mortar in compliance with the original mortar content must be used in repairs. In pointing and debris fillings, and in completing the missing parts it is appropriate to use a mixture of 30% lime, 50% ground aggregate, which is sieved, washed, having local (stream bed) material, which does not contain carbonate content, and which the aggregate distribution is in compliance with the original mortars (in an aggregate structure of consisted of 30% on average of rough silt/sand mixture having maximum 1-2 mm of particles and 70% having particles of 63-1000 µm and 2% having particles <63 µm) and aggregate of 15% having silt/clay size and local (containing lime) stream bed material, and 5% of lime mortar containing clay in pozzolanic nature.

It is also possible to use ready-to-use special hydraulic lime, which is produced intended for restoration, in mortar repairs. It is not definitely recommended to use materials containing cement (classic, white or coloured with pigments) in any stage of repair mortar.

The structural stones of the fortification walls are limestone in different sub-types intensely in the research studies. Structural stones are rocks, which belong to the local formation that may be obtained within the vicinity. In repair stage, it is recommended to carry out trial applications for the recommended mortar and plaster contents, and to analyze separately for determining the compliance of the stones/rocks to be selected with the recommended materials.

Acknowledgement

Sampling from the structure and the experiments were carried out by Mardin Metropolitan Municipality.

Conflicts of interest

The authors declare no conflicts of interest.

References

1. Ma, S., Wang, L., Bao, P. (2022). Study on Properties of Blue-Brick Masonry Materials for Historical Buildings. *Journal of Renewable Materials*, 10(7), 1961–1978.
2. Alyilmaz, C., Yakar, M., & Yilmaz, H. M. (2010). Drawing of petroglyphs in Mongolia by close range photogrammetry. *Scientific Research and Essays*, 5(11), 1216-1222.
3. Normal 1/88 (1990). Alterazioni macroscopiche dei materiali lapidei: lessico, Macroscopic alteration of stone materials: glossary. Comas Graphica, Rome.
4. Franke, L., Schumann, I., Van, H. R., Van der, K. L., Naldini, S., Binda, L., Baronio, G., Van Balen, K., & Mateus, J. (1998). Classification of damage patterns found in brick masonry. protection and conservation of european cultural heritage. Research Report European Commission, 8(2), Stuttgart: Fraunhofer IRB, Verlag.
5. Henriques, M. A., Delgado-Rodrigues, J., Aires-Barros, L., & Proença, N. (2004). Materiais Pétreos e similares : terminologia das formas de alteração e degradação. In: ICT Informação técnica, Patologia e reabilitação das construções, ISBN: ITPRC 2, 39.
6. VDI 3798 (1998). Untersuchung und Behandlung von immissionsgeschädigten Werkstoffen, insbesondere bei kulturhistorischen Objekten. Die Graphische Dokumentation. VDIRichtlinien, 1-27.
7. Fitzner, B. (2002). Damage diagnosis on stone monuments—in situ investigation and laboratory studies. In Proceedings of the International Symposium of the Conservation of the Bangudae Petroglyph, Seoul National University, 29–71, Seoul, Korea,
8. Jo, Y. H., & Lee, C. H. (2014). Quantitative modeling of blistering zones by active thermography for deterioration evaluation of stone monuments. *Journal of Cultural Heritage*, 15(6), 621–627.
9. de Ferri, L., Lottici, P. P., Lorenzi, A., Montenero, A., & Salvioli-Mariani, E. (2011). Study of silica nanoparticles–polysiloxane hydrophobic treatments for stone-based monument protection. *Journal of Cultural Heritage*, 12(4), 356-363.
10. Winkler, E. (1997). *Stone in Architecture: Properties, Durability*, 3rd edition, Springer, Berlin.
11. Corvo, F., Reyes-Trujeque, J., Valdés C., Villaseñor F., Cuesta O., Aguilar, D. & Quintana, P. (2010). Influence of air pollution and humidity on limestone materials degradation in historical buildings located in cities under tropical coastal climates. *Water Air and Soil Pollution*, 205, 359-375. Doi:10.1007/s11270-009-0081-1.
12. Fort, R., Alvarez de, B., & López de, A. M. C. (2004). The efficiency of urban remodelling in reducing the effects of atmospheric pollution on monuments, *Air Pollution and Cultural Heritage*, ed. C. Saiz-Jimenez, Balkema, Amsterdam, 225–232.
13. Moroni, B., Pitzurra, L., & Poli, G. (2004). Microbial growth and air pollutants in the corrosion of carbonate building stone: Results of laboratory and outdoor experimental tests. *Environmental Geology*, 46, 436–447.
14. Spezzano, P. (2021). Mapping the susceptibility of UNESCO World Cultural Heritage sites in Europe to ambient (outdoor) air pollution. *Science of The Total Environment*, 754(), 142345–. doi: 10.1016/j.scitotenv.2020.142345
15. Webb, A. H., Bawden, R. J., Busby, A. K., & Hopkins, J. N. (1992). Studies on the effects of air pollution on limestone in Great Britain. *Atmospheric Environment*, 26(2), 165-181.
16. Alptekin, A., & Yakar, M. (2021). 3D model of Üçayak Ruins obtained from point clouds. *Mersin Photogrammetry Journal*, 3(2), 37-40.
17. Kanun, E., Alptekin, A., & Yakar, M. (2021). Cultural heritage modelling using UAV photogrammetric methods: a case study of Kanlıdivane archeological site. *Advanced UAV*, 1(1), 24-33.
18. Sesana, E., Gagnon, A. S., Ciantelli, C., Cassar, J. & Hughes, J. J. (2021). Climate change impacts on cultural heritage: a literature review, *WIREs Climate Change*, 12 e710.
19. Abousshook, M., Park, H. D., Gouda, M., Mazen, O., & El-Sohby, M. (2022). Determination of durability of some Egyptian monument stones using digital image analysis, Proceedings of the 10th IAEG Congress, Engineering Geology for Tomorrow's Cities, Nottingham, UK, The Geological Society of London, 80, 110.
20. Bradley, S. M. & Middleton, A. P. (1988). A study of the deterioration of Egyptian limestone sculpture. *J Am Inst Conserv*, 27(2), 64–86. <https://doi.org/10.2307/3179403>.
21. Cardell, C., Delalieux, F., Roumpopoulos, K., Moropoulou, A., Auger, F., & Van Griekena, R. (2003). Salt-induced decay in calcareous stone monuments and buildings in a marine environment in SW France. *Construction and Building Materials*, 17, 165–179.
22. Fahmy, A., Molina-Piernas, E. & Martínez-López, J. (2022). Salt weathering impact on Nero/Ramses II Temple at El-Ashmonein archaeological site (Hermopolis Magna), Egypt. *Herit Sci*, 10, 125. <https://doi.org/10.1186/s40494-022-00759-6>
23. Navarro, R., Pereira, D., de Arévalo, E. F., Sebastián-Pardo, E. M., & Rodríguez-Navarro, C. (2021). Weathering of serpentinite stone due to in situ generation of calcium and magnesium sulfates. *Construction and Building Materials*, 280, 122402. <https://doi.org/10.1016/j.conbuildmat.2021.122402>.
24. Rothert, E., Eggert, T., & Cassar, J. (2007). Stone properties and weathering induced by salt crystallization of maltese globigerina limestone. In: Prikryl R, Smith B J (ed) *Building stone decay: from diagnosis to conservation*. Geological society, Special publications, London, 271, 189–198.
25. Sabbioni, C., Brimblecombe, P., & Cassar, M. (2010). The atlas of climate change impact on European cultural heritage: scientific analysis and management strategies (No. 19). London: Anthem Press.
26. Viles, H. A. & Cutler, N. A. (2012). Global environmental change and the biology of heritage structures, *Global Change Biol*. 18 2406–2418.

27. McCabe, S., Smith, B., Adamson, C., Mullan, D., & McAllister, D. (2011). The 'greening' of natural stone buildings: quartz sandstone performance as a secondary indicator of climate change in the British Isles?. *Atmospheric and Climate Sciences*, 1(04), 165-171.
28. Graedel, T. E. (2000). Mechanisms for the atmospheric corrosion of carbonate stone. *Journal of the Electrochemical Society*, 147(3), 1006-1009.
29. Korumaza, A. G., Korumaz, M., Dulgerlera, O. N., Karasaka, L., Yıldız, F., & Yakar, M. (2010). Evaluation of laser scanner performance in documentation of historical and architectural ruins, a case study in Konya. *International Archives of Photogrammetry, Remote Sensing and Spatial Information Sciences*, 38(5), 361-366.
30. Yilmaz, H. M., Yakar, M., Mutluoglu, O., Kavurmaci, M. M., & Yurt, K. (2012). Monitoring of soil erosion in Cappadocia region (Selime-Aksaray-Turkey). *Environmental Earth Sciences*, 66(1), 75-81.
31. Mirdan, O., & Yakar, M. (2017). Tarihi eserlerin İnsansız Hava Aracı ile modellenmesinde karşılaşılan sorunlar. *Geomatik*, 2(3), 118-125.
32. Alptekin, A., Çelik, M. Ö., & Yakar, M. (2019). Anıtmezarın yersel lazer tarayıcı kullanarak 3B modellenmesi. *Türkiye Lidar Dergisi*, 1(1), 1-4.
33. Alptekin, A., Fidan, Ş., Karabacak, A., Çelik, M. Ö., & Yakar, M. (2019). Üçayak Örenyeri'nin yersel lazer tarayıcı kullanılarak modellenmesi. *Türkiye Lidar Dergisi*, 1(1), 16-20.
34. Alptekin, A., & Yakar, M. (2021). 3D model of Üçayak Ruins obtained from point clouds. *Mersin Photogrammetry Journal*, 3(2), 37-40.
35. Casadio F, Daher C, Bellot-Gurlet L. Raman Spectroscopy of cultural heritage Materials: Overview of Applications and New Frontiers in Instrumentation, Sampling Modalities, and Data Processing. *Top Curr Chem (Cham)*. 2016 Oct;374(5):62. <https://doi.org/10.1007/s41061-016-0061-z>.
36. Kramar, S., Urosevic, M., Pristacz, H., & Mirtič, B. (2010). Assessment of limestone deterioration due to salt formation by micro-Raman spectroscopy: application to architectural heritage. *Journal of Raman Spectroscopy*, 41(11), 1441-1448.
37. Lodi, G.C., De Ferri, L. & Pojana, G. (2017). Spectroscopic characterization of historical building materials: The case study of the Biblioteca Nazionale Marciana (Venice, Italy). *Journal of Raman Spectroscopy*, (), -. doi:10.1002/jrs.5290
38. Kottke, J. (2009). An Investigation of Quantifying and Monitoring Stone Surface Deterioration Using Three Dimensional Laser Scanning. Master's Thesis, University of Pennsylvania, Philadelphia, PA, USA.
39. Pavlíková, M., Pavlík, Z., Keppert, M., & Černý, R. (2011). Salt transport and storage parameters of renovation plasters and their possible effects on restored buildings' walls. *Construction and Building Materials*, 25(3), 1205-1212.
40. Pavlík Z, Vejmelková E, Pavlíková M, Keppert M, Černý S. C., Cassar M., Brimblecombe P., Tidblad J., Kozłowski R., Drd'acký M., Saiz-Jimenez C., Grontoft T., Wainwright I. & Ari'no X. (2006). Global climate change impact on built heritage and cultural landscapes. In *International Conference on Heritage, Weathering and Conservation*, HWC; R. Fort, M. Alvarez de Buergo, M. Gomez-Heras and Vazquez-Calvo Eds. London: Taylor & Francis, 395- 401.
41. Wonganan, N., Athisakul, C., Mahasuwanchai, P., Tanchirapat, W., Sahamitmongkol, R., & Leelataviwat, S. (2021). Ancient materials and substitution materials used in Thai historical masonry structure preservation. *Journal of Renewable Materials*, 9(2), 179-204.
42. Alioğlu, E. F. (2000). *Mardin Şehir Dokusu ve Evler*, İstanbul.



© Author(s) 2023. This work is distributed under <https://creativecommons.org/licenses/by-sa/4.0/>